

A Photochemical Model Based on a Scaling Analysis of Ozone  
Photochemistry

by

Bruce Ainslie

B.Sc. (Eng), Queen's University, 1989  
M.Sc., The University of British Columbia, 1991

A THESIS SUBMITTED IN PARTIAL FULFILMENT OF  
THE REQUIREMENTS FOR THE DEGREE OF

DOCTOR OF PHILOSOPHY

in

THE FACULTY OF GRADUATE STUDIES

(Department of Earth and Ocean Sciences)

We accept this thesis as conforming  
to the required standard

THE UNIVERSITY OF BRITISH COLUMBIA

September 21, 2004

© Bruce Ainslie, 2004

Vitruvius says that small models are of no avail for  
ascertaining the effects of large ones; and I here  
propose to prove that this conclusion is a false one.

LEONARDO DA VINCI, *Notebooks* (about 1500 A.D.)

# Abstract

A scaling-level model of a photochemical mechanism has been developed and integrated into an air quality model used to study ozone formation in an urban environment.

A scaling analysis was used to capture the internal workings of a photochemical mechanism using the OZIPR trajectory model to simulate a smog chamber for a wide range of precursor concentrations and a variety of environmental conditions. The Buckingham Pi method of dimensional analysis was used to express the relevant variables in terms of dimensionless groups. These grouping show maximum ozone, initial NOx and initial VOC concentrations to be made non-dimensional by the average  $NO_2$  photolysis rate ( $j_{av}$ ) and the rate constant for the NO- $O_3$  titration reaction ( $k_{NO}$ ); temperature by the NO- $O_3$  activation energy ( $E/R$ ) and time by the cumulative  $NO_2$  photolysis rate ( $J$ ). The analysis shows dimensionless maximum ozone concentration can be described by a product of powers of dimensionless initial NOx concentration, dimensionless temperature ( $\theta(T)$ ) and a similarity curve ( $f$ ) directly dependent on the ratio of initial VOC to NOx concentration ( $R$ ) and internally dependent on the cumulative  $NO_2$  photolysis rate:

$$\frac{[O_3]_{max}}{j_{av}/k_{NO}} \propto \left( \frac{[NOx]_o}{j_{av}/k_{NO}} \right)^a \theta(T)^b f(R; J).$$

When Weibull transformed, the dimensionless model output cluster onto two line segments. This is interpreted as a break in the scaling and can be understood in terms of a change in governing feedback mechanisms separating low- and high-NOx chemistry regimes. The similarity relationship can be modeled by two Weibull distributions using four parameters: two describing the slopes of the line segments ( $\alpha_1, \alpha_2$ ) and two giving the location of their intersection ( $\beta, \lambda$ ):

$$f(R; J) = 1 - \exp \left\{ -\lambda \left( \frac{R}{\beta(J)} \right)^{\alpha(R)} \right\}$$

$$\text{where } \alpha(R) = \frac{\alpha_2 - \alpha_1}{2} \tanh(R - \beta(J)) + \frac{\alpha_1 + \alpha_2}{2}$$

A fifth parameter ( $\gamma$ ) is used to normalize the model output. The most important parameter,  $\beta$ , the VOC to NOx ratio at the scaling break, defines a characteristic process scale for ozone photochemistry. The scaling analysis, similarity curve and parameterization appear to be independent of the details of the chemical mechanism, hold for a variety of VOC species and mixtures and are applicable over a wide range of VOC and NOx concentrations. The similarity relationship is used to

generalize ozone-precursor relationships in terms of four rules governing ozone production ( $P(O_3)$ ), to quantify NOx-inhibition and define isopleth slope. The scaling framework is used to study VOC reactivity, explore the scaling properties of a simple reaction mechanism and collapse a wide range of smog chamber measurements onto a single similarity curve.

To complement the scaling analysis, a meteorological model and an emissions inventory were developed. These were incorporated into an air quality model used to explore the sensitivity of a regional ozone plume to environmental conditions and precursor concentrations. The air quality model consisted of a series of box models being advected by the mean wind, for a single day, where photochemistry of the precursors emissions was modeled using the similarity relationships developed from the scaling analysis. The chosen domain was the Lower Fraser Valley B.C., a complex coastal region that experiences moderate ozone episodes during summertime fair-weather conditions.

Emission fields were developed using published emission totals, four land-use categories and generic temporal emissions curves and were found to be comparable with fields based on more detailed inventories. Wind observations (speed and direction), from 53 stations, on a typical episode day, were interpolated to produce hourly wind fields. Mixing depths were determined using a simple slab model incorporating the interpolated wind fields and measured heat fluxes. The most problematic aspect of the model was determining the effects of pollutant build up in the boundary layer, prior to the modeling day. This was handled by emitting precursors into the boundary layer and advecting them, without chemical reactions, until steady state concentrations were reached. These were dependent on the choice of background concentrations used to initialize the pre-conditioning scheme and were set so resulting boundary layer NOx and VOC concentrations were in agreement with the limited available data and peak ozone concentrations were typical of recent episodes.

In departure from previous modeling studies, model validation was not through point by point analysis of model output and observations but through high level comparison of model sensitivity with a range of modeling techniques and observations. The model appears to capture ozone sensitivity to meteorological conditions and precursor concentrations; justifying its use as a screening tool.

The model suggests: the region to be VOC limited; projected emissions reductions may not improve present episodic ozone concentrations; larger than anticipated reductions in NOx emissions, without equivalent additional VOC reductions, could increase episodic concentrations and future emissions reductions, stemming from TIER 2 LDV standards, which target NOx emissions to a greater extent than VOC emissions, may not result in appreciable changes in episodic ozone concentrations. These conclusions are intended to guide comprehensive modeling studies.

# Contents

Abstract . . . . .	iii
Contents . . . . .	v
List of Tables . . . . .	xii
List of Figures . . . . .	xiv
Acknowledgements . . . . .	xviii
<b>1 Preface . . . . .</b>	<b>1</b>
1.1 Aim of thesis . . . . .	1
1.2 Scope of thesis . . . . .	2
<b>I Development of the WEX Model . . . . .</b>	<b>4</b>
<b>2 Introduction . . . . .</b>	<b>5</b>
2.1 Ground level ozone . . . . .	5
2.1.1 Effects of ozone . . . . .	6
2.1.2 Air quality standards and ozone . . . . .	6
2.1.3 Meteorology and ozone . . . . .	7
2.1.4 Emissions and ozone . . . . .	7
2.2 Fundamentals of Ozone Photochemistry . . . . .	7
2.2.1 Photochemical Cycle of $NO$ , $NO_2$ and $O_3$ . . . . .	8
2.2.2 Radicals . . . . .	8
2.2.3 Reaction Chains . . . . .	10
2.2.4 Photochemical Ozone Production in the Presence of VOCs and $NO_x$ . . . . .	10
2.2.5 Summary of Ozone photochemistry . . . . .	11
2.2.6 Photochemistry and poetry . . . . .	13
2.3 Approaches to Modeling Ground Level Ozone . . . . .	13
2.3.1 Trends and Correlation Techniques . . . . .	14
2.3.2 Eulerian Grid Based . . . . .	15
2.3.3 Complementary Methods . . . . .	16
2.4 Summary . . . . .	18
<b>3 Scaling Analysis of Ozone Photochemistry . . . . .</b>	<b>19</b>
3.1 Introduction . . . . .	19
3.2 Scaling Analysis . . . . .	20
3.2.1 What is a scaling analysis? . . . . .	20

---

3.2.2	Key Concepts . . . . .	20
3.2.3	Scaling Analysis Methods . . . . .	23
3.2.4	Scaling and Photochemical Modeling . . . . .	25
3.3	Scaling Analysis of a NO <sub>x</sub> -only System . . . . .	27
3.3.1	NO <sub>x</sub> -only Photochemical System . . . . .	27
3.3.2	Relevant Variables . . . . .	27
3.3.3	Variable Dimensions . . . . .	28
3.3.4	Key Variables . . . . .	28
3.3.5	Pi-Groups . . . . .	29
3.3.6	Alternative Pi-Groups . . . . .	29
3.3.7	OZIPR Model Output . . . . .	30
3.3.8	Universal Curve . . . . .	33
3.3.9	Analytic Expression . . . . .	34
3.4	Propene-NO <sub>x</sub> System . . . . .	35
3.4.1	Ozone response surface . . . . .	36
3.4.2	Dimensional Considerations . . . . .	37
3.4.3	Propene . . . . .	40
3.4.4	OZIPR Simulations . . . . .	40
3.4.5	Similarity Relationship . . . . .	41
3.4.6	Weibull Distribution . . . . .	41
3.4.7	Scaling break and Lognormal Parameterization . . . . .	43
3.4.8	Analogy with Richardson number and Surface Stability . . . . .	44
3.4.9	WEX Model . . . . .	46
3.4.10	Ozone-precursor relationships in the NO <sub>x</sub> Limited Region . . . . .	48
3.5	Summary . . . . .	51
<b>4</b>	<b>Domain of Applicability for the Scaling Relationship . . . . .</b>	<b>53</b>
4.1	Introduction . . . . .	53
4.2	Scaling Methodology . . . . .	54
4.2.1	General simulation conditions . . . . .	54
4.2.2	Determination of test matrix size . . . . .	54
4.2.3	Selection of base concentrations and number of nodes . . . . .	55
4.2.4	Determining WEX parameters . . . . .	57
4.2.5	Statistical measures of agreement . . . . .	58
4.3	Scenario I – RADM2 VOC Classes . . . . .	58
4.3.1	Simulations with Methane, Ethane and Higher Alkanes . . . . .	59
4.3.2	Simulations with Ethene and other Alkenes . . . . .	61
4.3.3	Simulations with Aromatics . . . . .	65
4.3.4	Simulations with Carbonyl compounds . . . . .	65
4.3.5	Simulations with the Non-reactive class . . . . .	67
4.3.6	Simulations with VOC Mixtures . . . . .	67
4.3.7	Summary of RADM2 simulations . . . . .	67
4.4	Scenario II – Other Mechanism . . . . .	68
4.4.1	CB-IV Mechanism . . . . .	68
4.4.2	SAPRC-90 Mechanism . . . . .	69
4.4.3	Summary for Scenario II . . . . .	70
4.5	Scenario III – Varying Temperature . . . . .	70

4.5.1	Gross Influence of Temperature On Maximum Ozone Concentration	71
4.6	Scenario IV – Varying J	72
4.6.1	Parameterizing the similarity relationship	73
4.6.2	Translations and rotations of the similarity relationship	74
4.7	Scenario V – Effect of peak actinic flux	76
4.8	Scenario VI – Varying T and J	79
4.8.1	Variability of WEX parameters with $J$ and $T$	80
4.8.2	‘Universal’ Similarity relationship	82
4.8.3	Universal Propene Curve	85
4.8.4	Scatter Plots	86
4.8.5	Summary	87
4.9	Scaling Limits	87
4.9.1	Precursor Scaling Limits	89
4.10	Conclusion	93
<b>5</b>	<b>Scaling Break and Ozone Photochemistry</b>	<b>95</b>
5.1	Introduction	95
5.2	The Temporal Variability of Ozone	95
5.2.1	Temporal variability of $NO$ , $NO_2$ and $O_3$ for a single simulation	95
5.2.2	Reactive Odd Nitrogen ( $NO_y$ )	97
5.2.3	Isopleth Plot and Stock Simulations	97
5.3	Ozone Production	100
5.3.1	Step function model for ozone production	103
5.3.2	Maximum ozone concentration	105
5.3.3	IER and Step function model	106
5.3.4	PSP production	108
5.3.5	Quadratic Model for Ozone Production	110
5.3.6	Weibull Model	111
5.3.7	Quadratic with Asymptotic Decay	113
5.3.8	Production models with initial $NO_x$ dependence	115
5.3.9	Links between scaling break and regime change	117
5.3.10	WEX temporal ozone profile	118
5.4	Feedback Mechanisms and Ozone Photochemistry	119
5.4.1	Positive Feedback Loop	119
5.4.2	Negative Feedback Loops	121
5.5	Scaling Break and Low- $NO_x$ chemistry	123
5.5.1	Low- $NO_x$ chemistry	124
5.5.2	Low- $NO_x$ negative feedback loop	126
5.5.3	Scaling break and governing chemical processes	126
5.6	Feedback Loops and the similarity relationship	127
5.6.1	Acceleration Phase	128
5.6.2	Low- $NO_x$ Saturation Phase	128
5.7	Scaling Break and Ridgeline	128
5.7.1	Regulatory Basis for Ridgeline	129
5.7.2	Geometrical Basis for Ridgeline	130
5.7.3	Process Basis for Ridgeline	130
5.8	Relationship between Scaling break and other parameters	131

5.8.1	Scaling break Ridgeline and Chain Length ( $\chi_{OH}$ ) . . . . .	131
5.8.2	Scaling break and fraction of $HO_2^{\bullet}$ radicals that react with NO ( $f_{HO_2+NO}$ ) . . . . .	132
5.8.3	Scaling break and $OH^{\bullet}$ reactivity ( $k_{OH}$ ) . . . . .	133
5.8.4	Scaling Break and environmental conditions . . . . .	134
5.9	Summary . . . . .	134
<b>6</b>	<b>Chemical Processes and the WEX Parameters . . . . .</b>	<b>135</b>
6.1	Introduction . . . . .	135
6.2	WEX Scaling Parameter $a$ . . . . .	137
6.2.1	NOx Inefficiency . . . . .	137
6.2.2	Range of $a$ -values . . . . .	138
6.2.3	Response surface sensitivity to $a$ . . . . .	139
6.2.4	Sensitivity of $a$ to RADM2 modifications . . . . .	139
6.3	WEX Scaling Parameter $\gamma$ . . . . .	141
6.3.1	NOz speciation and $\gamma$ . . . . .	141
6.3.2	Peak Ozone and PAN and $HNO_3$ Formation . . . . .	142
6.3.3	Gamma and Isoleth shape . . . . .	143
6.3.4	Variability of $\gamma$ . . . . .	144
6.3.5	$\gamma$ RADM2 Experiments . . . . .	144
6.4	Geometric Parameter $\lambda$ . . . . .	145
6.4.1	Sensitivity of isopleth shape to $\lambda$ . . . . .	146
6.4.2	Sensitivity of $\lambda$ to RADM2 modifications . . . . .	146
6.5	Geometric Parameter $\alpha_1$ . . . . .	147
6.5.1	Sensitivity of the ozone response surface to $\alpha_1$ . . . . .	148
6.5.2	Ozone Isoleth Slope . . . . .	148
6.5.3	NOx-inhibition and $\alpha_1$ . . . . .	149
6.5.4	WEX and NOx Inhibition . . . . .	151
6.5.5	Range of $\alpha_1$ -values . . . . .	152
6.5.6	Sensitivity of $\alpha_1$ to RADM2 modifications . . . . .	153
6.5.7	NOS scaling regime . . . . .	154
6.6	Geometric Parameter $\alpha_2$ . . . . .	154
6.6.1	Sensitivity of ozone isopleths to $\alpha_2$ . . . . .	154
6.7	Conclusion . . . . .	155
<b>7</b>	<b>Evaluation of the WEX model using smog chamber data . . . . .</b>	<b>157</b>
7.1	Introduction . . . . .	157
7.2	Smog chambers . . . . .	158
7.2.1	Smog chamber design . . . . .	158
7.2.2	Chamber limitations . . . . .	159
7.3	Comparing the WEX model to smog chamber data . . . . .	160
7.3.1	CSIRO Data set . . . . .	162
7.3.2	IER Analysis . . . . .	162
7.3.3	WEX Analysis of temporal ozone concentrations . . . . .	164
7.3.4	WEX analysis of maximum ozone concentration . . . . .	166
7.4	Conclusion . . . . .	168

<b>8</b>	<b>VOC Reactivity – An Example of Scaling in Ozone Photochemistry</b>	170
8.1	Introduction	170
8.2	VOC Reactivity	171
8.2.1	Incremental Reactivity	171
8.2.2	Maximum Incremental Reactivity	173
8.2.3	Relative Incremental Reactivity	174
8.2.4	RADM2 simulations of RIR	175
8.3	Concerns about VOC Reactivity Scales	177
8.4	GRS Mechanism – An Example of an Ideal VOC Reactivity Scale	178
8.4.1	Ozone Isopleths and NO <sub>x</sub> -inhibition	178
8.4.2	Reaction Mechanism	179
8.4.3	Scaling and VOC reactivity	181
8.4.4	Radical Production and VOC reactivity	184
8.5	Conclusion	184
8.6	Summary for Part I	185
<b>II</b>	<b>Application of the WEX Model</b>	<b>186</b>
<b>9</b>	<b>Incorporating WEX into a Photochemical Model</b>	187
9.1	Introduction	187
9.2	Modeling Domain	189
9.2.1	General Air Quality in the LFV	190
9.3	Meteorology of Ozone Episodes in the LFV	192
9.4	Previous Modeling	193
9.5	Interpolation of the Wind Fields	195
9.5.1	Interpolation	195
9.5.2	Divergence Reduction	196
9.6	Development of Back Trajectories	196
9.6.1	Limitations of the Trajectories	197
9.7	Parameterizing Mixed Height	198
9.7.1	Mixing Height Results	200
9.8	Emissions	202
9.8.1	Comparison with a Detailed Episode Specific Inventory	204
9.9	Speciation of VOCs	206
9.10	Boundary Layer Processes	207
9.10.1	Deposition	207
9.11	Initial Boundary Layer Concentrations	209
9.11.1	Residual Layer Concentrations	210
9.11.2	Initial Surface Concentrations	211
9.12	Developing WEX parameters	211
9.13	Predicted Ozone Concentrations	212
9.14	Temporal Behaviour	213
9.15	Conclusions	215

---

<b>10 Model Results and Discussion</b> . . . . .	217
10.1 Sensitivity to Meteorological Parameters . . . . .	217
10.1.1 Temperature . . . . .	218
10.1.2 Residual layer concentrations . . . . .	219
10.1.3 Actinic Flux . . . . .	221
10.1.4 Wind Fields . . . . .	222
10.1.5 Back Trajectories . . . . .	223
10.1.6 Mixing Depths . . . . .	223
10.2 Sensitivity to Emissions . . . . .	225
10.2.1 Backcast emissions for 1985 . . . . .	226
10.2.2 Future scenario under Tier 2 automotive standards . . . . .	226
10.2.3 Speciation . . . . .	227
10.3 LFV Ozone Isopleths . . . . .	228
10.4 Discussion . . . . .	231
10.5 Conclusions . . . . .	234
10.6 Summary for Part II . . . . .	235
<b>11 Conclusions</b> . . . . .	236
<b>Bibliography</b> . . . . .	241
<b>A Buckingham Pi Method of Dimensional Analysis</b> . . . . .	257
A.1 Buckingham Pi Theorem . . . . .	257
<b>B OZIPR Trajectory Model</b> . . . . .	260
B.1 Overview . . . . .	260
B.2 Model Set-up . . . . .	260
<b>C RADM2 Chemical Mechanism</b> . . . . .	263
C.1 Overview . . . . .	263
C.2 Stable Inorganic Species . . . . .	263
C.3 Stable Organic Species . . . . .	263
C.4 Organic and Inorganic Radicals Species . . . . .	264
<b>D Composite Weibull Models and the WEX Model</b> . . . . .	267
D.1 Overview . . . . .	267
D.2 Weibull Distribution and Failure Rates . . . . .	267
D.2.1 Three Parameter Weibull . . . . .	268
D.3 Multimodal Analysis . . . . .	269
D.3.1 Sectional Model . . . . .	269
D.3.2 Mixed Model . . . . .	270
D.3.3 Multiplicative Model . . . . .	270
D.3.4 Competing Risk Model . . . . .	270
D.4 WEX Model . . . . .	271

---

<b>E</b>	<b>Weibull and Isopleths Plots for Various VOC compounds</b>	273
E.1	RADM2 Classes	273
E.1.1	Alkanes	273
E.1.2	Alkenes	275
E.1.3	Aromatics	276
E.1.4	Carbonyls	277
E.1.5	Non-reactive	278
E.1.6	Mixtures	279
E.2	CB-IV Mechanism	280
E.3	NRC Mechanisms	281
<b>F</b>	<b>Some Mathematical Definitions of the Ridgeline</b>	282
F.1	The ridgeline	282
F.2	Ridgeline based on ozone sensitivity to ratio of VOC to NO <sub>x</sub>	282
F.3	Ridgeline based minimum gradient along an ozone response surface	283
F.4	Ridgeline based minimum isopleth curvature	284
F.5	Conclusion	284
<b>G</b>	<b>Development of the Simple Emissions Inventory</b>	285
G.1	Spatial Emission Masks	286
G.2	Emission Sources	286
G.2.1	Mobile Source Emissions	286
G.2.2	Area Sources	288
G.2.3	Point Sources	289
<b>H</b>	<b>Physical Geography of the Modeling Domain</b>	291
<b>I</b>	<b>CART Decision tree for the LFV</b>	294
<b>J</b>	<b>Glossary of Acronyms and Abbreviations</b>	296

# List of Tables

3.1	Units and dimensions for maximum ozone and its dimensional factors. . . . .	28
3.2	Variable ranges and number of treatments for the OZIPR simulations of the NO <sub>x</sub> -only photochemical system. . . . .	31
3.3	Initial conditions and maximum ozone concentration for three NO <sub>x</sub> -only OZIPR simulations have similar $\Pi_2$ values. . . . .	32
3.4	Physical quantities which affect ozone concentrations in a smog chamber. . . . .	38
3.5	Ozone-precursor relationships in the NO <sub>x</sub> -limited region. . . . .	50
4.1	A description of scenarios used to explore the universality of the similarity relationship. . . . .	54
4.2	Values of the six WEX parameters for each of the RADM2 classes and two urban mixtures. . . . .	68
4.3	A comparison of WEX parameter values for the ARB mixture using the RADM2 and CB-IV chemical mechanisms. . . . .	69
4.4	Date, average and total actinic fluxes, as measured by NO <sub>2</sub> photolysis rates, for the five RADM2 simulations used to investigate the sensitivity of the similarity relationship on actinic flux. . . . .	73
4.5	Test conditions for simulations with different latitudes but identical $J$ -values. . . . .	77
4.6	WEX parameter values for the YVR and LAX simulations. . . . .	79
4.7	WEX parameter values for the YVR and LAX simulations. . . . .	81
4.8	Scatter plot statistics. . . . .	87
4.9	OLT precursor scaling domains. . . . .	89
5.1	Scaling break and R-value of OH-chain maximum for seven RADM2 classes and two urban mixtures. . . . .	131
5.2	Fraction of HO <sub>2</sub> <sup>•</sup> that reacts with NO scaling break for various RADM2 classes and mixtures. . . . .	132
6.1	Baseline and modified parameters for WEX generated isopleths. . . . .	137
6.2	Comparison of OLT parameters for the original and modified RADM2 mechanism. . . . .	140
6.3	Comparison of OLI parameters for the original and modified RADM2 mechanism. . . . .	145
6.4	Comparison of XYLE parameters for the original and modified RADM2 mechanism $\gamma$ . . . . .	147
6.5	RADM2 classes ranked by $\alpha_1$ . . . . .	153
6.6	Comparison of OLT parameters using the original and modified RADM2 mechanism. . . . .	153
7.1	Test conditions for the 20 CSIRO smog chamber experiments. . . . .	163
7.2	Summary of statistics for the IER and WEX scatter plots. . . . .	164
7.3	WEX parameters and power law exponents used to fit the CSIRO data. . . . .	166
8.1	Various measures for VOC reactivity. . . . .	171

---

9.1	Occurrence of Episodes in the Lower Fraser Valley. . . . .	192
9.2	Emissions categories in the simple emissions inventory. . . . .	204
9.3	Speciation of VOCs used in the LFV photochemical simulations. . . . .	208
9.4	WEX parameters used in the LFV photochemical simulations. . . . .	212
C.1	RADM2 Chemical Species List for Inorganic Compounds. . . . .	264
C.2	RADM2 Chemical Species List for Organic Compounds. . . . .	265
C.3	RADM2 Chemical List for Radicals Species. . . . .	266
G.1	Spatial allocation of emissions in the simple emissions inventory. . . . .	290
H.1	Meteorological Stations within the modeling domain. . . . .	292
H.2	Mapping of RPN Landuse classes to WEX landuse classes. . . . .	293
H.3	Land use corrections for friction velocity and kinematic heatflux . . . . .	293

# List of Figures

2.1	Schematic of ozone photochemistry. . . . .	12
3.1	Schematic showing two separate approaches to performing a scaling analysis. . . . .	25
3.2	Dimensionless maximum ozone concentration versus dimensionless initial NO concentration for 5 different initial $NO$ to $NO_2$ ratios. . . . .	32
3.3	Dimensionless steady-state ozone concentration scaled by the initial ratio of $NO$ to $NO_2$ as a function of dimensionless initial $NO$ concentration. . . . .	33
3.4	Scatter plot showing $\Pi_1/\Pi_3$ using Eq. (3.6) versus Eq. (3.12) for five different $\Pi_3$ levels. . . . .	35
3.5	Ozone response surface as a function of initial VOC and NOx concentration. . . . .	37
3.6	Schematic of the fast $NO-NO_2-O_3$ cycle and the slower radical driven cycle. . . . .	38
3.7	Dimensionless ozone scaled by dimensionless $NOx^a$ versus ratio of initial precursor concentrations ( $R$ ). . . . .	42
3.8	Procedure used to prepare OZIPR model output before Weibull transforming. . . . .	43
3.9	Scaled model output after Weibull transformation. . . . .	44
3.10	Scaled OLT model output after Lognormal and Weibull transformation. . . . .	45
3.11	Richardson number as a function of stability. . . . .	46
3.12	Ozone isopleth plot for the NOx-OLT system. . . . .	48
4.1	Distribution of $\ln(R)$ when $nodes = 41$ and $VOC_{base} = NOx_{base}$ . . . . .	56
4.2	Schematic of steps used to find WEX parameters. . . . .	58
4.3	Weibull and Isopleth plots for RADM2 class ETH. . . . .	61
4.4	Weibull transformed ETH model output versus $\ln R$ when NOx-scaling exponent ( $a$ ) is -0.2. . . . .	62
4.5	Weibull and Isopleth plots for RADM2 class OLI. . . . .	63
4.6	Weibull and Isopleth plots for RADM2 class OLI using 41 nodes. . . . .	64
4.7	Ozone isopleths for OLI showing lines of constant etc.... . . . .	66
4.8	RADM2 simulations using OLT for four different temperatures . . . . .	71
4.9	Weibull transformed dimensionless model output after scaling by dimensionless temperature $\Pi_4^b$ . . . . .	72
4.10	Dimensionless model output for the five OLT simulations after scaling by dimensionless initial NOx concentration raised to the 0.62. . . . .	74
4.11	Dimensionless model output for the five OLT simulations after scaling by dimensionless initial NOx concentration and translating so scaling break is at origin. . . . .	75
4.12	Dimensionless model output for the five OLT simulations after: scaling by dimensionless initial NOx concentration raised to the 0.62, shifting and rotating. . . . .	76
4.13	Solar zenith angle as a function of local time for Vancouver and Los Angeles . . . . .	78
4.14	NOx-scaled dimensionless maximum ozone concentration for OZIPR simulations using Los Angeles and Vancouver latitudes. . . . .	78

---

4.15	Effects of horizontal translation by $\beta$ on the 'Weibullized' and 'scaled' data. . . . .	79
4.16	Dependence of $\beta$ on temperature and actinic flux . . . . .	81
4.17	Ridgeline as a function of J and T (from Johnson (1984)) . . . . .	83
4.18	Weibull transformed model output for RADM2 simulations having five different levels of actinic flux and four different temperatures. . . . .	84
4.19	Universal similarity relationship for OLT . . . . .	85
4.20	Total actinic flux as a function of Julian day of the year for Vancouver in the summer	86
4.21	OLT scatter plots for four different actinic flux/temperature combinations. . . . .	87
4.22	Schematic of OLT modeling domains. . . . .	88
4.23	OLT similarity relationship in several scaling domains. . . . .	90
4.24	Ozone isopleths for OLT over several scaling domains. . . . .	91
4.25	Similarity relationship for different NOx-scaling exponents. . . . .	92
4.26	The OLT NOx-scaling exponent as a function of initial OLT, NOx and R. . . . .	93
5.1	Temporal evolution of ozone and other species during a simulation. . . . .	96
5.2	Ozone isopleth diagram showing isomephitic line of 0.045 ppm. . . . .	98
5.3	Temporal profiles for ozone and other species for eight simulations having initial NOx concentration of 0.045 ppm and various initial VOC concentrations. . . . .	99
5.4	Weibull transformed dimensionless ozone concentrations for the isomephitic simula- tions. . . . .	101
5.5	Simple step model function for ozone production. . . . .	103
5.6	Three members of a family of step-model functions for ozone production. . . . .	104
5.7	Ozone profiles for the three step function VOC concentrations. . . . .	105
5.8	Ozone production, concentration and maximum concentration curves for a family of four different initial VOC concentration using a step-function model. . . . .	107
5.9	Family of production curves for quadratic model. . . . .	110
5.10	Ozone production, concentration and maximum ozone concentration for four initial VOC concentrations using the parabolic model of ozone production. . . . .	112
5.11	Modified parabolic curve with hyperbolic tail. . . . .	113
5.12	Ozone production, concentration and maximum ozone concentration for four initial VOC concentrations using the parabolic model with hyperbolic tail. . . . .	114
5.13	Ozone concentration as a function of cumulative $NO_2$ photolysis rate for nine different initial NOx and VOC conditions. . . . .	116
5.14	Links between scaling break and regime change. . . . .	118
5.15	Ozone concentration versus time for a series of nine smog chamber simulations. . . . .	120
5.16	Ozone concentration versus time for SAPRC smog chamber simulation EC237. . . . .	121
5.17	Positive Feedback loop for ozone production. . . . .	122
5.18	The effects of $HNO_3$ production on the reactivity of a photochemical system. . . . .	123
5.19	Negative Feedback loop for ozone production. . . . .	123
5.20	Loss of odd oxygen by various pathways. . . . .	125
5.21	Second controlling or negative feedback loop for ozone production. . . . .	126
5.22	Relationship between scaling break and underlying photochemical processes. . . . .	127
5.23	Generalized ozone profile showing Lag, Acceleration and Low-NOx regimes. . . . .	129
5.24	OH-chain length and $f_{HO_2}$ for the Stock urban mixture. . . . .	132
5.25	Scaling break as a function of OH-reactivity. . . . .	133
6.1	Schematic representation of the four WEX geometric parameters. . . . .	136
6.2	The effects of changing $a$ on ozone response surface. . . . .	140

6.3	Scatter plot of $\gamma$ versus $O_3/NO_z$ for six RADM2 classes and two urban mixtures. . . . .	142
6.4	Speciation of final $NO_z$ for seven RADM2 classes and two urban mixtures. . . . .	143
6.5	The effects of changing $\gamma$ on ozone response surface. . . . .	144
6.6	The effects of changing $\lambda$ on ozone response surface. . . . .	147
6.7	The effects of changing $\alpha_1$ on ozone response surface. . . . .	148
6.8	The effects of changing $\alpha_1$ on ozone isopleth slope. . . . .	150
6.9	Relationship between isopleths tilting and packing. . . . .	151
6.10	Dependence of $NO_x$ -inhibition on the three WEX parameters: $a$ , $\lambda$ and $\alpha_1$ . . . . .	152
6.11	The effects of changing $\alpha_2$ on ozone response surface. . . . .	155
7.1	Observed and modeled ozone concentrations for two different smog chamber experiments. . . . .	161
7.2	Comparison of the IER model and the CSIRO smog chamber data. . . . .	165
7.3	Comparison of the WEX model and the CSIRO smog chamber data. . . . .	167
7.4	Maximum ozone concentration from the CSIRO smog chamber experiments and the corresponding WEX model. . . . .	168
8.1	IR for OLT calculated using the RADM2 mechanism and the WEX model. . . . .	173
8.2	Relative incremental reactivities for the 12 RADM2 classes in the Stock mixture based on OZIPR simulations and the WEX model. . . . .	177
8.3	Weibull and isopleth plots for three different ROCs using the GRS mechanism. . . . .	182
8.4	Weibullized plots of OLT and ALD with normal, twice and half the $k_{OH}$ rate constants. . . . .	183
9.1	The Lower Fraser Valley. . . . .	190
9.2	Modeling domain. . . . .	191
9.3	Typical ozone plume in the LFV. . . . .	192
9.4	500 hPa geopotential heights over the Northeastern Pacific Ocean on August 10 <sup>th</sup> 2001. . . . .	194
9.5	Sea-level pressure over the Northeastern Pacific Ocean on August 10 <sup>th</sup> 2001. . . . .	194
9.6	Four back trajectories derived from the interpolated wind fields and MC2 model output. . . . .	199
9.7	Calculated mixing heights at four different hours. . . . .	201
9.8	Calculated mixing heights at two different times along transect T1. . . . .	202
9.9	Calculated mixing heights at two different times along SW-NE transect T2 . . . . .	203
9.10	Spatial pattern of VOC emissions at 1600 LST based on simple inventory. . . . .	205
9.11	Spatial pattern of $NO_x$ emissions at 1600 PST based on simple inventory. . . . .	205
9.12	Comparison of VOC emissions between the simple inventory and the episode specific emissions inventory. . . . .	207
9.13	Comparison of $NO_x$ emissions between the simple inventory and the episode specific emissions inventory. . . . .	208
9.14	Ozone plume based on simple model. . . . .	213
9.15	Observed ozone plume at 1800 on August 10 <sup>th</sup> . . . . .	214
9.16	Predicted and observed ozone concentrations at various stations on August 10 <sup>th</sup> 2001. . . . .	215
10.1	Ozone plume after decreasing all temperatures 5°C. . . . .	218
10.2	Ozone plume after increasing all temperatures 5°C. . . . .	219
10.3	Ozone plume based using a clean residual layer. . . . .	220
10.4	Modeled surface ozone concentrations at 1500 PST July 19 <sup>th</sup> using the MC2-CALGRID modeling system. . . . .	221
10.5	Ozone plume using WEX parameters for a September 10 <sup>th</sup> day. . . . .	222

---

10.6	Ozone plume resulting from a 1.5× increasing in wind speed. . . . .	223
10.7	Ozone concentrations using MC2-based trajectories. . . . .	224
10.8	Ozone concentrations using MC2-based trajectories and mixing heights. . . . .	225
10.9	Ozone concentrations based on 1985 emissions levels. . . . .	227
10.10	Ozone concentrations based on projected future Tier 2 LDV emission standards. . . . .	228
10.11	Ozone plume using WEX parameters based on SMOKE speciation. . . . .	229
10.12	Region wide ozone isopleths as a function of anthropogenic VOC and NOx emissions. . . . .	230
10.13	Observed ozone concentrations in the LFV on June 21 <sup>st</sup> , 2004. . . . .	233
D.1	A ‘bathtub’ curve showing changing failure rates with increasing use. . . . .	268
D.2	A comparison of four different methods of fitting model output with different 2-Weibull models. . . . .	272
E.1	Weibull and Isopleth plots for RADM2 class HC3. . . . .	273
E.2	Weibull and Isopleth plots for RADM2 class HC5. . . . .	274
E.3	Weibull and Isopleth plots for RADM2 class HC8. . . . .	274
E.4	Weibull and Isopleth plots for RADM2 class OL2. . . . .	275
E.5	Weibull and Isopleth plots for RADM2 class OLT. . . . .	275
E.6	Weibull and Isopleth plots for RADM2 class XYLE. . . . .	276
E.7	Weibull and Isopleth plots for RADM2 class TOLU. . . . .	276
E.8	Weibull and Isopleth plots for RADM2 class HCHO. . . . .	277
E.9	Weibull and Isopleth plots for RADM2 class KET. . . . .	277
E.10	Weibull and Isopleth plots for RADM2 class ALD. . . . .	278
E.11	Weibull and Isopleth plots for RADM2 class NR. . . . .	278
E.12	Weibull and Isopleth plots the urban ARB mixture. . . . .	279
E.13	Weibull and Isopleth plots the Stockwell urban mixture. . . . .	279
E.14	Weibull and Isopleth plots for CB-IV classes PAR+OLE. . . . .	280
E.15	Weibull and Isopleth plots for urban mixture using the CB-IV mechanism. . . . .	280
E.16	Weibull and Isopleth plots for SAPRC class OLE1. . . . .	281
E.17	Weibull and Isopleth plots for urban mixture using the SAPRC mechanism. . . . .	281
I.1	CART regression tree for Rocky Point Park (T9). . . . .	295

---

# Acknowledgements

First and foremost, I would like to thank my supervisor, Dr. D. G. Steyn for his encouragement, guidance and intellectual support. I must also thank my examining committee, Drs. A. Bertram, I. G. McKendry and R. B. Stull who were always available for timely advice and insight.

A number of organizations provided funding for this research: the Sustainable Development Research Institute (SDRI) provided funding in the form of research assistantships, the University of British Columbia (UBC) through a University Graduate Fellowship, the department of Earth and Ocean Sciences (EOS) through teaching assistantships in addition to funds for conference travel and finally Dr. Steyn provided support from his grants for both research and several conference visits.

I would like to recognize Dr Gail Tonnesen, at the University of California Riverside, for her help with the OZIPR model and her answers to all my inquiries concerning process analysis. I gratefully acknowledge the advice and model output provided by Dr. Martilli and the encouragement and support from Dr. Rucker, Pascal Hägeli and Christian Reuten. I am indebted to Luca Delle Monache for his discussions and emissions data. This research was also advanced by valuable comments and discussions from all faculty and students in the Atmospheric Science Programme. I would like to thank everyone at SDRI, and especially Drs. Charmichael and Robinson, for the wonderful opportunity I had working on the QUEST integrated assessment model.

Special thanks goes to Matt Wilkins for his help with C-programming and matters pertaining to the Linux operating system and to the EOS computer staff who were invaluable in keeping my computer going. I must acknowledge the patience of Jersey and Sheena, who must have found the long days in the office very trying.

And lastly, my greatest debt of gratitude goes to my wife Margaret for her unwavering support over the last five years. Truly, greatest of them all.

---

# Chapter 1

## Preface

### 1.1 Aim of thesis

This thesis deals with ground level ozone, a relatively recent problem but now pervasive in many urban centres (United Nations Environmental Programme, 1992). Controlling this problem, like many environmental issues, has been slow, costly and difficult (National Research Council, 1991). As I will show, ozone forms as a result of complex interactions between emissions (both natural and anthropogenic), atmospheric processes and photochemical reactions. Each process is complex (with its own fields of expertise), incompletely characterized and central to ozone formation.

Furthermore, improving ground level ozone requires linking knowledge about its formation (science) to choices society makes about present and future economic development and social behaviour (policy). But the future is unknown and can follow many courses. Thus, properly protecting future air quality is inherently inexact and unpredictable.

Both this complexity and uncertainty present a tension for those trying to model ozone formation: on the one hand, a model is required that is sensitive to the intricacies of weather, photochemistry and human actions (via emissions) while on the other hand, a model is required that can succinctly and quickly explore many possible futures. This tension leads to two distinct classes of models: comprehensive 'black box' models, whose behaviours are difficult to understand, and due to their complexity and costs, preclude examining large numbers of possible futures; and less exact models, containing many approximations, which nonetheless succinctly describe ozone formation while elucidating important processes.

Finally, while scientific inquiry should be objective, subjectivity inevitably creeps into every investigation, principally through the investigator's values and beliefs (Meadows and Robinson, 1985). So, I state my personal bias here: I believe the air pollution meteorology community needs to make better use of 'simple, sophisticated' models in order to complement more comprehensive ones.

With this in mind, the aim of this thesis is to develop a concise way of describing ozone formation, in polluted urban environments, that furthers understanding about the complex photochemical

processes.

Specifically, this thesis distills the essential processes within a detailed photochemical mechanism in order to build a simple model of ozone formation. Concisely, it models a model to build a model. While this sounds academic, I will show the utility and importance of this work. That is, I develop more than just a meta-model – the methods produce a novel and powerful way of characterizing the behaviour of a photochemical system. This leads to the thesis' second, subtler and wider aim – to engage the air pollution modeling community in debate about the proper use and selection of models.

In operational terms, this thesis addresses two simple questions:

- How much detail is necessary to capture ozone sensitivity to VOC and NO<sub>x</sub> emissions in a particular region?
- Given that a model is only as strong as its weakest link, what level of detail is justified in each modeling component?

Answers to these questions, indirectly addressed throughout the thesis, come in focus in Chapter 10.

## 1.2 Scope of thesis

The thesis is broken into two parts: Part I develops a model for ozone photochemistry while Part II makes use of the model. This division also has an heuristic/prognostic split: in Part I, I use my model to understand ozone formation while in Part II, I use the model to predict ozone concentrations.

In the next Chapter, I introduce the problem of ground level ozone. Principally, I discuss the health and environmental impacts of ozone and the extent of the problem. I introduce the complex nature of ozone photochemistry and show its formation is further complicated by local emissions and by both large and small scale meteorological processes. I outline existing methods used to model ozone formation and show the importance of different modeling approaches.

In Chapter 3, I introduce scaling methods, used to build my model, and present a limited set of results. In Chapter 4, I continue my scaling analysis and show its range of validity. The model is used to understand ozone formation in terms of feedback loops in Chapters 5 and 6. In Chapter 7, I compare my model with smog chamber results and discuss the difficulties associated with such comparisons. Chapter 8, the last of Part I, explores the concept of incremental reactivity and uses the model to show the limitations of a simple chemical mechanism.

In Part II, I couple my chemical model with a simple meteorological model to build a photochemical model of ozone formation (Chapter 9). I then model an ozone episode in the Lower Fraser Valley, British Columbia (Chapter 10). Final conclusions and ideas for future work are presented in Chapter 11.

While my model has been tested using an episode in the LFV, and many of the examples used to illustrate ideas have also been drawn from this region, it is expected that techniques developed herein should be applicable to other regions. Finally, to make the presentation of ideas clearer, secondary and background material has been placed in appendices while acronyms and abbreviations are listed in the glossary (Appendix J).

## **Part I**

# **Development of the WEX Model**

## Chapter 2

# Introduction

### 2.1 Ground level ozone

Ozone, a triatomic form of oxygen, is found naturally in the stratosphere, a region of the atmosphere extending between 10 and 50 km above the surface of the earth, where it forms the ozone layer; absorbing ultraviolet radiation. It also occurs naturally in the troposphere as the result of exchange from the stratosphere (Lelieveld and Dentener, 2000) or through photochemical reactions involving naturally occurring oxides of nitrogen ( $\text{NO}_x$ ) and volatile organic compounds (VOCs) (Crutzen, 1995).<sup>1</sup> Background tropospheric ozone concentrations are usually low – only a few tens of parts per billion (ppb) compared with stratospheric levels of about 10000 ppb. While there has been great concern about observed decrease in stratospheric ozone (World Meteorological Association, 1998), concentrations of tropospheric ozone appear to be increasing (Logan (1985), Volz and Kley (1988), Altshuller and Lefohn (1996)). Surface observations in remote European locations show an increase in background ozone concentrations of between 1 and 2% per year (Janach, 1989) largely due to increased anthropogenic emissions (Hough and Derwent, 1990). Additionally, increasing tropospheric ozone levels may affect the oxidizing capacity of the atmosphere and hence the chemical lifetimes of many species (Thompson, 1992) and also play a role in anthropogenic climate change (Mickley et al., 1999).

Of interest in this thesis are high ozone concentrations, observed in densely populated urban and suburban areas, and often found in combination with other harmful pollutants such as: nitric acid ( $\text{HNO}_3$ ), carbon monoxide ( $\text{CO}$ ), nitrogen dioxide ( $\text{NO}_2$ ), hydrogen peroxide ( $\text{H}_2\text{O}_2$ ), peroxyacetylnitrate ( $\text{PAN}$ ) and fine particulate matter ( $\text{PM}_{2.5}$ ). First identified in the Los Angeles region in the 1940s (National Research Council, 1991), high ozone and its related pollutants (called smog) are now found in virtually every large urban area – in 1998, 130 million people in the U.S. alone lived in areas violating federal ozone standards (Lin et al., 2001). Furthermore, ground level ozone has become a regional issue with elevated concentrations, from different urban areas, merging

---

<sup>1</sup>More precisely, it is produced via photochemical reactions of oxides of nitrogen and radicals with VOCs acting as a radical source.

into large scale plumes (Schere and Hidy, 2000). The main concern with ground-level ozone is its deleterious effects on human health and vegetation.

### 2.1.1 Effects of ozone

#### Health

Ozone is an oxidant of biological tissue. Exposure to elevated levels causes inflammation of the specialized cells which line the respiratory tract (Harte, 1991). Symptoms of exposure include: chest pain, lung and nasal congestion, and eye and nose irritation (Horvath and McKee, 1994). Numerous studies have linked exposure to high ozone levels with increased emergency room visits (Delfino et al., 1997), school absenteeism (Gilliland et al., 2001), reduced lung function (Brauer et al., 1996) and also as a trigger for asthmatics (Friedman et al., 2001). Furthermore, responsiveness is known to be sensitive to age: Petroschevsky et al. (2001) report an increase in illness risk for individuals 65 years and older while Burnett et al. (2001) have shown negative health impacts for children less than two years of age. Finally, studies have shown that long-term exposure leads to diminished lung function and chronic respiratory symptoms (Galizia and Kinney, 1999).

#### Environmental

Ozone exposure also affects vegetation. Ozone uptake during respiration results in tissue damage and reduced plant growth (Runeckles, 2002). Most major North American agricultural crops show reduced yields after exposure to elevated ozone levels (Lesser et al., 1990). In fact, it is estimated that ozone, either alone or in combination with other pollutants, accounts for approximately 90% of crop losses from air pollution in the US (Heck et al., 1982). The estimated value of lost produce, due to ozone exposure, in the Lower Fraser Valley B.C., was \$ 9 million in 1986 (Runeckles, 2002). Plant response to ozone appears to depend more on the magnitude of the ambient concentration than exposure time (National Research Council, 1991), an important consideration when setting air quality standards (Heck and Cowling, 1997).

### 2.1.2 Air quality standards and ozone

To protect public health and welfare, ozone exposure standards have been set. In Canada, National Ambient Air Quality Objectives (NAAQOs) set a maximum one hour average acceptable ozone level at 82 ppb. A new, Canada wide standard (CWS), to be implemented by 2010, sets a goal of 65 ppb for the 4<sup>th</sup> highest 8-hour reading, averaged over three consecutive years (Canadian Council of Ministers of the Environment, 2000). In the US, the 1997 Clean Air Act Revision (CAAR97)

sets a standard of 82 ppb averaged over 8 hours for the third highest reading averaged over 4 years (Environmental Protection Agency, 1997). The statistical nature of these standards reflects the natural variability of ozone to external influences – principally meteorological conditions – and accounts for rare or unusual events that might cause excessively high concentrations in otherwise acceptable areas (Ott, 1994).

### 2.1.3 Meteorology and ozone

Elevated ozone levels are typically associated with slow moving high pressure systems producing clear skies, elevated temperatures and stagnant conditions (National Research Council, 1991). But local conditions also enhance ozone formation: mountains restrict horizontal circulation (Millan et al., 1997), weak thermal driven winds, produced in coastal locations, recirculate but do not vent pollutants (Steyn, 1996), high altitudes increase solar radiation (Fast and Zhong, 1998) and semi-permanent subsidence in subtropical latitudes limits vertical mixing (Lu and Turco, 1995). Thus, ozone formation is sensitive to both large and small scale meteorological processes<sup>2</sup>.

### 2.1.4 Emissions and ozone

Ozone is not directly emitted but is a secondary pollutant formed via chemical reactions involving precursor pollutants. Both the biogenic (Guenther et al., 2000) and anthropogenic (Placet et al. (2000), Sawyer et al. (2000)) precursor sources show great spatial and temporal variability. Quantifying these emissions is difficult and presents a major source of uncertainty in understanding ozone formation (National Research Council, 1991). Furthermore, future anthropogenic emissions are largely driven by both technological innovation and regulatory practices, both of which are difficult to predict (Intergovernmental Panel on Climate Change, 2001).

## 2.2 Fundamentals of Ozone Photochemistry

The link between ozone production and the irradiation of mixtures of NO<sub>x</sub> and VOCs was first established in the 1950s (Haagen-Smit, 1952). Since that time, a great deal of effort has been directed at understanding the exact chemical processes involved. Complicating this research is the multitude of different VOC species typically found in a polluted environment, and the extremely large number of ways these species can react — it is estimated that an explicit treatment of ozone formation would

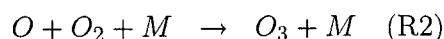
---

<sup>2</sup>While meteorology can play an indirect role, by producing conditions conducive to ozone formation or by limiting dispersion, it can also play a direct role through the transport of ozone rich stratospheric air to the surface (Holton et al., 1995).

contain more than 20,000 reactions involving several thousand reactants and products (Dodge, 2000). A brief description of ozone formation is given below.

### 2.2.1 Photochemical Cycle of $NO$ , $NO_2$ and $O_3$

To begin, ozone formation for the simplest photochemical system – one that involves only  $NO_x$  and ozone – is discussed. The process begins with photolysis of  $NO_2$ , at wavelengths  $< 424$  nm, producing a single oxygen atom that combines with oxygen to produce ozone:



where  $M$  represents a third molecule which stabilizes the formation of  $O_3$  by absorbing excess energy. Reaction (R2) is the only reaction that produces ozone in the troposphere (Seinfeld and Pandis, 1998). The  $NO$  formed in (R1) can react with ozone to regenerate  $NO_2$ :



Although ozone is produced from the photolysis of nitrogen dioxide (R1), the subsequent titration of ozone by nitric oxide (R3) limits ozone formation resulting in a balance between ozone production and titration called the photostationary state<sup>3</sup>:

$$[O_3]_{pss} = \frac{j[NO_2]_{ss}}{k_{NO}[NO]_{ss}} \quad (2.1)$$

where  $j$  –  $NO_2$  photolysis rate (1/sec)

and  $k_{NO}$  –  $NO$  titration rate ( $cm^3/(molecules \cdot sec)$ )

Most anthropogenic  $NO_x$  emissions occur as  $NO$  (Jacobson, 1999) and ozone concentrations based solely on Eq. (2.1) are lower than observed in urban atmospheres. To produce elevated ozone levels, another oxidation pathway is needed to convert  $NO$  to  $NO_2$  without consuming ozone. It is the oxidation of VOCs by radicals which provides such an alternate path.

### 2.2.2 Radicals

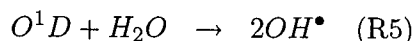
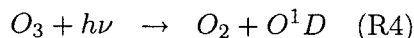
In the atmosphere, temperatures, pressures and gas concentrations are so low that generally the only reactions which proceed at appreciable rates are those involving at least one radical species (Jacob, 1999). Radicals are ubiquitous compounds with an unpaired electron in their outer shell (Turco,

<sup>3</sup>Implicit in this relationship is the assumption that the oxygen atom reacts so quickly that it is always in a steady state with  $[NO_2]$

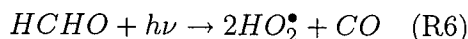
2002). Due to the unpaired electron, radicals are extremely reactive. The most important radicals in the photochemical production of ozone are the hydroxyl radical ( $OH^\bullet$ )<sup>4</sup> and the hydroperoxy radical ( $HO_2^\bullet$ ). Special mention should also be made of atomic oxygen. In its excited state ( $O(^1D)$ ), it has all its electrons paired up (so technically it is not a radical) but is still very reactive while in its ground or triplet state,  $O$  (or more formally  $O(^3P)$ ) is a radical with two unpaired electrons (and should technically be called a *biradical*). A complete understanding of the role radicals play in producing ozone requires an investigation into the radical life-cycle, namely: initiation, propagation and termination.

### Radical Initiation

Radicals have high free energies and as a result, radical formation from non-radical sources requires energy. This production, called initiation, is typically a photolysis process (Jeffries, 1995). An important source of new  $OH^\bullet$  radicals is the photolysis of ozone producing atomic oxygen in its excited state ( $O(^1D)$ ) (Jeffries and Tonnesen, 1994). The excited oxygen atom can subsequently produce two hydroxyl radicals after reacting with a water molecule:



An important source of hydroperoxy radicals is the photolysis of formaldehyde:

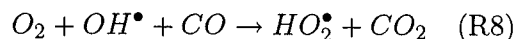


### Radical Propagation

Radicals are propagated when a reaction produces as many radicals as it consumes (Jeffries and Tonnesen, 1994). Propagation creates chains, allowing a single radicals to react many times (Seinfeld and Pandis, 1998). One of the most important propagation reactions involves the conversion of nitric oxide to nitrogen dioxide by the hydroperoxy radical:



Another important propagation reaction involves the oxidation of carbon monoxide by the hydroxyl radical:

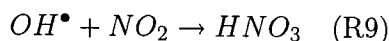



---

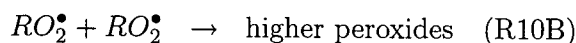
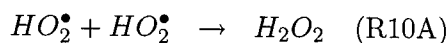
<sup>4</sup>Radical species are denoted by a superscripted 'dot' unless otherwise noted

## Radical Termination

Reactions that incorporate radicals into stable products and stop the propagation chain are called termination reactions. The most important termination reaction is:



which consumes both nitrogen dioxide and the hydroxyl radical (Jeffries and Tonnesen, 1994). Another important class of termination reactions involves two radicals reacting together. An example is the formation of hydrogen peroxide from two hydroperoxy radicals:



### 2.2.3 Reaction Chains

A reaction is said to be elementary if it occurs in a single step with no detectable reaction intermediates. In many instances, reactions that appear to be elementary occur in more than one step with radical reactions providing the intermediate steps (Pannetier and Souchay, 1967). A composite reaction involves more than one elementary reaction. If, in a composite reaction, certain intermediates are consumed in one step but regenerated in another, then the reaction is called a chain reaction or cycle. Chain reactions always involve initiation, termination and two or more propagation steps (Pannetier and Souchay, 1967). Ozone photochemistry is best viewed from the perspective of reaction chains.

### 2.2.4 Photochemical Ozone Production in the Presence of VOCs and NO<sub>x</sub>

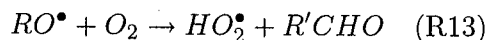
Ozone formation begins by hydroxyl attack on the VOC. For simplicity, the VOC is often expressed using two components: as a generic grouping of hydrogen, carbon and oxygen atoms – which is called the root and identified as *R*, and a single extra hydrogen (*H*). The hydroxyl radical abstracts a hydrogen atom to produce a water molecule while the remnants of the VOC (the root) reacts with oxygen to produce a peroxy radical ( $RO_2^\bullet$ ). These two reactions can be expressed in a single step:



Next, the peroxy radical reacts with the nitric oxide to produce nitrogen dioxide and the oxy radical ( $RO^\bullet$ ) in a propagation step:



The above reaction allows the conversion of  $NO$  to  $NO_2$  without the loss of ozone while propagating the radical. The oxy radical then reacts with oxygen to produce a new VOC ( $R'CHO$ ) called a carbonyl compound (where the  $R'$  represents a new root) and the hydroperoxy radical:



The carbonyl may itself photolyze to produce more radicals (in what is called a branching reaction). Finally, the hydroperoxy radical can convert more  $NO$  to  $NO_2$  while recreating the  $OH^{\bullet}$  radical:



This last hydroxyl radical can then proceed to initiate another attack on a second VOC. The net effect of reactions (R11) to (R14) is two  $NO$  to  $NO_2$  conversions through the loss and then recreation of the hydroxyl radical. As in the photostationary state, ozone is produced through the photolysis of  $NO_2$  and the combining of atomic oxygen with molecular oxygen (R2). The nitric oxide formed in R1 is available for further conversion by peroxy radicals (reactions (R12) or (R14)) and is called 'old NO' to distinguish it from fresh emissions of  $NO$ . Without the loss (titration) of ozone with  $NO$  (R3), ozone concentrations can build to high levels<sup>5</sup>. While the above reactions show the importance of radicals in producing elevated ozone concentrations, termination reactions (R9, R10A and R10B) slow ozone production by stopping radical propagation by incorporating them into stable products.

Figure 2.1 shows a schematic of the reaction pathways in the photochemical production of ozone in a polluted urban environment. In the Figure, the rectangles highlight the role of radicals. The four rectangles form a box which reveals the radical's catalytic nature; participating in reactions without being consumed. The circles show the role of the NOx emissions; continuously cycling between  $NO$  and  $NO_2$ . The two diamonds show the end products of the two termination sequences. Finally, the zig-zag lines show the photolysis reactions.

### 2.2.5 Summary of Ozone photochemistry

Photochemical production can be viewed as two interconnected cycles: one involving NOx, the other VOC. In the first cycle, VOCs are consumed, producing secondary VOCs (for example carbonyl compounds) which rejoin the pool of available VOCs. In principle, repeated consumption of these secondary VOCs eventually leads to simpler and simpler compounds as hydrogen atoms are removed

<sup>5</sup>Polluted environments can record ozone concentrations as high as 200 to 400 ppb (National Research Council, 1991). This can be compared with typical background levels ranging between 30 to 50 ppb in rural areas of the United States and Europe (Logan, 1985).

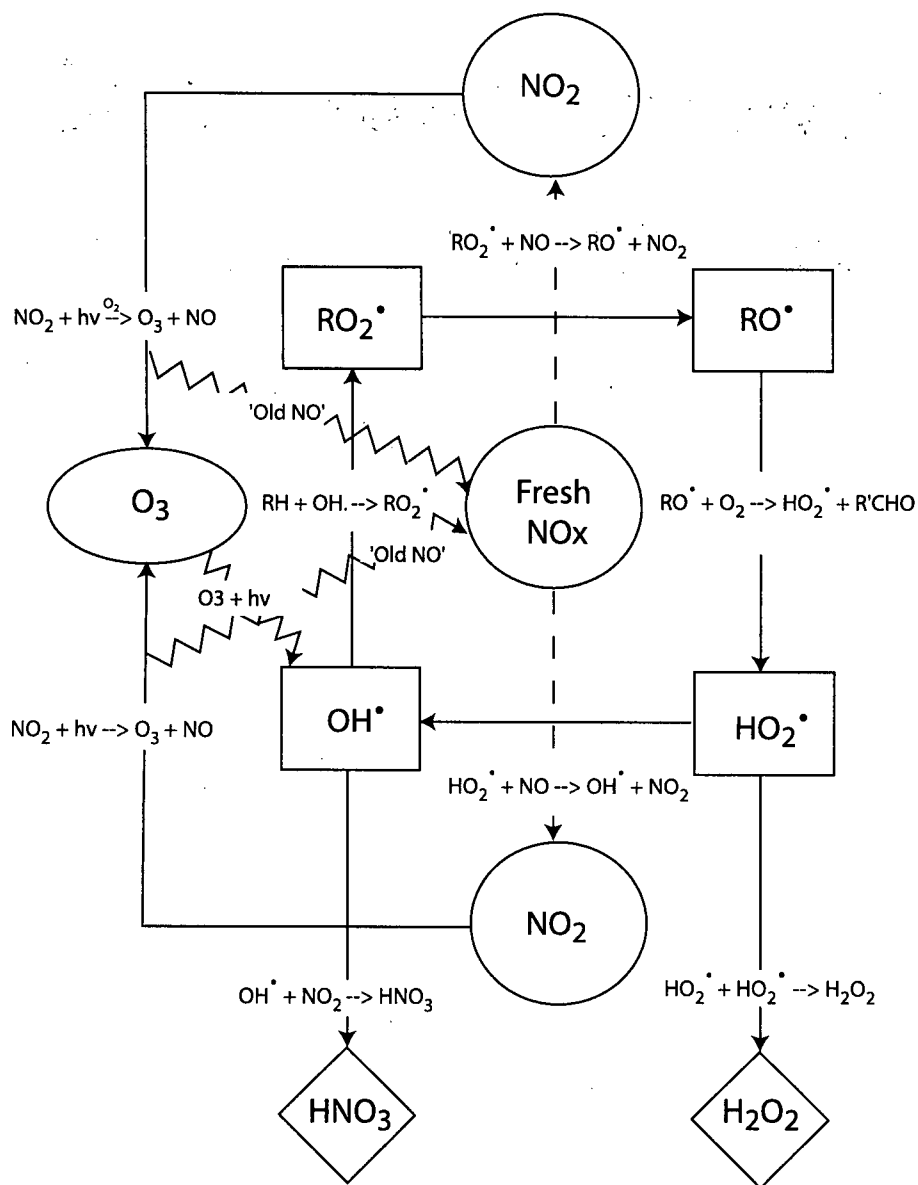


Figure 2.1: Schematic of ozone photochemistry showing the cycling of both NO<sub>x</sub> and radicals.

to form water molecules and carbon atoms to form  $\text{CO}_2$ . In practice, not all VOCs are converted to water and  $\text{CO}_2$ ; some are removed by deposition, others remain unprocessed.

The second cycle involves the interconversion of NO<sub>x</sub> between  $\text{NO}$  and  $\text{NO}_2$  (reactions (R1), (R3), (R12) and (R14)) coupled with the gradual conversion of NO<sub>x</sub> to other nitrogen products (i.e. reaction R9) which eventually terminates photochemical activity. With ozone production depending on both cycles, production is limited by whichever precursor is in greatest demand – intuitively a ‘law of the minimum’ (Sillman, 1993). Determining which precursor governs ozone production is

the central challenge of this science.

### 2.2.6 Photochemistry and poetry

To illustrate the cyclical nature of photochemical reaction chains, I have written a poem. It parodies a poem by Jonathan Swift – made famous by the physicist L. F. Richardson – who also parodied it to describe the nature of turbulence.

So, Nat'ralists observe, a Flea  
Hath smaller Fleas that on him prey;  
And these have smaller still to bite 'em;  
And so proceed ad infinitum:  
JONATHAN SWIFT, *On Poetry: A Rhapsody* [1733]

Big whorls have little whorls  
That feed on their velocity,  
And little whorls have lesser whorls  
And so on to viscosity.  
LEWIS F. RICHARDSON, *Weather Prediction by Numerical Process*, (Cambridge, 1922)

Big VOCs produce little VOCs  
In reactions radicals pursue,  
And little VOCs produce lesser VOCs  
And so on to cee-oh-two ( $CO_2$ ).  
BRUCE AINSLIE *Vancouver*, 2003

## 2.3 Approaches to Modeling Ground Level Ozone

Improvements to air quality have been largely driven by public pressure on governments to develop national standards and introduce air quality management plans. While in the last 25 years these strategies have reduced the number of episodes with extreme concentrations, they have been less successful at reducing the number of days when ozone levels exceed the standards (Scherre and Hidy, 2000). Furthermore, with Canada and the US introducing new standards at levels closer to

background concentrations, it is expected that the number of ozone exceedances will increase (Lin et al. (2001), Saylor et al. (1998)).

Thus, there is a continuing need to study ground level ozone and different methods have been developed to satisfy different needs. For instance, while the question of ozone sensitivity to VOC or NO<sub>x</sub> has been largely driven by the need to inform public policy<sup>6</sup>, there is an increasing effort to study the problem from a purely scientific view (Sillman, 1999). Furthermore, the need to forecast short term ozone concentrations requires different approaches than predicting the future levels. I briefly discuss techniques used to forecast short term ozone levels (which I call trends and correlation techniques), to model ozone sensitivities to emissions (principally Eulerian grid based models) and various methods used to complement these models. I will show the limitations of each and highlight the need for proper model selection.

### 2.3.1 Trends and Correlation Techniques

As public concern about air pollution increases, there is a growing need for air quality agencies to produce public health notifications in the form of one- or two-day ozone (or air quality) forecasts. These short term forecasts often need only predict ozone exceedances or general air quality indices (AQI). These are an overall measure of air quality achieved by comparing measured concentrations of various pollutants against their respective air quality objectives and then converting these relative concentrations to a number on an AQI scale. This allows different pollutant levels to be compared on a common scale ranging from *0-25 or good* with concentrations near background levels to *100+ or very poor* with concentrations posing significant health risks.

Perhaps the simplest way to produce these forecasts is with persistence – future ozone levels will be the same as today's. This method succeeds because many atmospheric variables (Wilks, 1995), including ozone (Robeson and Steyn, 1989), display serial correlation. For example, Robeson and Steyn (1989) have used persistence (along with Julian day of year) to develop a probability forecast for ozone concentration in the Lower Fraser Valley (LFV) B.C.. One draw back of this method is its inability to predict the beginning or end of an exceedance (Environmental Protection Agency, 1999). As an improvement, forecasts often relate future ozone levels to more easily forecast predictor variables. For example, Taylor (1992) has suggested that ozone levels will reach exceedance levels in the LFV if the summertime 850 mb temperatures are greater than 10°C.

Forecasts using several predictors along with a set of rules to group ozone concentrations based on meteorological conditions lead to a more robust model. Such a Classification and Regression

---

<sup>6</sup>In the U.S., to comply with the Clean Air Act, states are required to demonstrate the effectiveness of proposed management plans through the use of models – effectively turning them into legal tools (Jeffries, 1995).

Tree (CART) model has been used by Burrows et al. (1995) to predict ozone concentrations in the LFV. Related to CART models are artificial neural networks which use a complex set of weights and functions to relate predictor variables to ozone concentrations. The analysis allows for non-linear relationships; well suited to the underlying non-linear photochemical processes (Comrie, 1997). Finally, surface meteorological observations can be regressed against historic ozone concentrations to build statistical models for daily maximum ozone concentrations. Robeson and Steyn (1990) used this method to develop a regression model for maximum ozone concentration using daily maximum temperature and the previous days ozone concentration.

While all of these simple models are adequate for forecasting next day ozone levels, all relate future ozone concentrations to meteorological conditions – not emissions. As a result, these models might serve as a basis for short term policy decisions (i.e. restricting car use during poor air quality days) but cannot serve as a basis for improving air quality where knowledge of ozone sensitivity to emissions is required.

### 2.3.2 Eulerian Grid Based

The best means of determining ozone sensitivity to precursor emissions is through the use of Eulerian grid based models (Russell and Dennis, 2000). These models use a fixed Cartesian grid over a domain of interest, to produce an array of discrete cells at which the relevant equations describing the motion and chemical evolution of the pollutants are numerically solved. They require spatially and temporally resolved meteorological and emissions fields as inputs. The models account for horizontal and vertical transport processes as well as spatial variability of emissions, land use and topography (Seinfeld, 1988).

These models are typically not used to forecast short term ozone levels<sup>7</sup> but rather to explore the consequences of economic development and policy decisions on future air quality. Unfortunately, the future is not fixed but largely free for our own creating (Robinson, 1988) and many futures can be envisioned, not all having similar air quality<sup>8</sup>. Thus, there is a need for modeling a large set of future scenarios. Furthermore, since ozone levels are strongly influenced by meteorology (McKendry, 1994), there is a need to model a variety of synoptic conditions. However, in many instances, future air quality is explored only using meteorological conditions from a single 'design day'. A more appropriate modeling strategy is one that models many future scenarios using a

---

<sup>7</sup>Environment Canada is developing an operational photochemical model for daily ozone forecasts (Pudykiewicz and Koziol, 1999).

<sup>8</sup>This marks a big difference between models that are sensitive to emissions and those that are sensitive to meteorology – in these, choice about future weather is not an option whereas choice about future emissions is.

variety of meteorological conditions. Unfortunately, the sheer complexity and cost of these models often precludes performing large numbers of simulations. As a result, a variety of modeling methods have been developed to complement these models.

### 2.3.3 Complementary Methods

Broadly speaking, there are three different techniques to compliment Eulerian grid models: observationally based methods (OBM), process analysis and semi-empirical models (SEM). Generally, OBM corroborate Eulerian grid models, process analysis elucidates model behaviour and SEM screen for interesting scenarios requiring a more detailed analysis.

#### Observational Based Methods

OBM use ambient measurements to infer ozone sensitivities and production rates. OBMs can be subdivided into two classes: methods that make use of ambient VOC, NO<sub>x</sub> and CO and those based on secondary reaction products (Sillman, 1999).

In the first class, the original idea was to use the morning ratio of VOC to NO<sub>x</sub> concentrations to infer ozone sensitivity. This method has since been shown to be unreliable (Wolfe and Korsog, 1992). Chameides et al. (1992) suggested using an  $OH^\bullet$ -reactivity weighted VOC to NO<sub>x</sub> ratio as an indicator of ozone sensitivity which has been used by Cardelino and Chameides (1995) to build a model for ozone sensitivity using ambient VOC, NO<sub>x</sub> and CO measurements. Another OBM determines ozone sensitivity using ambient ozone and NO<sub>x</sub> concentrations to calculate the extent that NO<sub>x</sub> emissions have reacted to from secondary products (Blanchard et al. (1994) and Chang et al. (1997)). Unfortunately, ozone concentrations at any location represent the cumulative effects of local production in an air mass over the course of several hours, while the above methods determine sensitivity of local ozone production rates (Sillman, 1999).

The second class uses long-lived 'indicator' species, like nitric acid and hydrogen peroxide, to infer ozone sensitivity (Milford et al. (1994), Sillman (1995) and Lu and Chang (1998)). In this approach, NO<sub>x</sub>-sensitive conditions coincide with high concentrations of certain 'indicator' species while VOC-sensitive conditions coincide with low values. Because these methods are based on concentrations of long lived species, it is expected that results are indicative of air mass sensitivity as opposed to local sensitivity.

## Process Analysis

To understand the mechanisms responsible for modeled concentration changes, a diagnostic tool has been developed that tracks the chemical and mechanical processes that control ozone formation (Jeffries and Tonnesen, 1994). Air quality models calculate concentrations by solving the mass continuity equations for each species. The mass continuity equations relate the time rate of change of concentration to the various chemical and mechanical processes that bring about the chemical changes. Typically, only resulting concentrations are retained after the calculations and not the contribution of each process. Process analysis modifies the numerical solvers in order to integrate the rates of individual reactions and physical processes over time. These integrated rates, representing the production and loss of each species by various reactions and processes, are then used to understand the behaviour of the Eulerian grid model. This method has also been used to determine indicator species which are sensitive to both local ozone production rates (Tonnesen and Dennis, 2000a) as well as ozone concentration (Tonnesen and Dennis, 2000b).

## Semi-Empirical Models

In order to develop simple models of ozone formation which are sensitive to emissions, much research has been devoted to understanding the photochemical system in terms of a small set of variables. Typically, this research makes use of experimental data from reaction vessels or smog chambers, where possible confounding effects of meteorology and emissions are more easily controlled, to empirically fit ozone concentrations to initial precursor concentrations. Shen et al. (1977) used reaction vessel experiments to find a relationship for maximum ozone concentration as a function of initial NO<sub>x</sub> and a unknown function of the initial ratio of VOC to NO<sub>x</sub>. Subsequent computer simulations by Sakamaki et al. (1982) corroborated these findings. Chang and Rudy (1993) obtained a similar relationship and by finding a parameterization for the unknown function, were able to predict maximum ozone concentration as a function of initial precursor concentration. Their model, however, had only limited success in predicting ozone concentrations outside of regions where ozone is sensitive to NO<sub>x</sub>.

Along a similar line, Johnson (1984) developed a set of functional relationships for ozone formation based on the analysis of smog chamber data. However these relationships, while providing an intuitive understanding of ozone photochemistry, predict a constant ozone production efficiency (number of ozone molecules produced for each NO<sub>x</sub> molecule consumed) in disagreement with field studies (Blanchard, 2000).

Finally, Azzi et al. (1992) have used smog chamber data to develop a highly parameterized set

---

of chemical reactions, involving only a few species, called the Generic Reaction Set (GRS). This scheme has been coupled with a meteorological model to produce a screening tool (Venkatram et al., 1994). However, the GRS has been shown to over predict ozone concentrations in situations where NO<sub>x</sub> is in short supply (called NO<sub>x</sub>-limited conditions) severely restricting its use in a screening tool (Tonnesen and Jeffries, 1994).

The goal of this thesis is to develop a semi-empirical model for ozone formation in a NO<sub>x</sub>-VOC system, in terms of a small set of variables, which can be used as a screening tool as well as understand ozone photochemistry in both NO<sub>x</sub> and VOC limited conditions.

## 2.4 Summary

Exposure to elevated ozone concentrations presents an ongoing threat to public health and welfare. The basic science behind ozone formation is complex and incompletely understood. Regulating the problem involves making predictions about the future which adds further uncertainty. This leads to a fundamental dilemma: while comprehensive grid models are the best means of studying this problem, they are costly to run, difficult to evaluate and by no means perfect. Finally, a thorough analysis requires examining a large set of future scenarios and meteorological conditions – a task for which Eulerian grid models are ill suited. The best way around this dilemma is to use comprehensive grid models in conjunction with various other complementary models. In this thesis, I will first develop and then evaluate such a complementary model based on a scaling analysis of ozone precursor relationships.

## Chapter 3

# Scaling Analysis of Ozone Photochemistry

### 3.1 Introduction

In this chapter, I present a scaling analysis of ozone photochemistry. Methods and results developed in this chapter are central to the whole thesis: the remaining chapters in *PART I* build on results introduced here while chapters in *PART II* use these results to build a simple model of ozone photochemistry which includes meteorological processes.

I begin this chapter by introducing various concepts central to scaling: measurements systems, dimensional homogeneity, dimensionless groups and similarity. These concepts form the basis of a systematic method of performing a scaling analysis called the Buckingham Pi theorem. I start by using this method to investigate the relationship between maximum ozone concentration and initial NO<sub>x</sub> concentration, actinic flux and temperature for the simplest photochemical system: one that has only initial NO and NO<sub>2</sub>. I perform this preliminary analysis for two reasons: to introduce the important concepts using a simpler system and, as it will be shown, since this system is amenable to an exact mathematical analysis, to show the strength and weakness of a scaling analysis.

I then perform a scaling analysis of a photochemical system comprised of a single VOC and NO<sub>x</sub>. I use the Buckingham Pi analysis to find a simple relationship which describes the dependence of maximum ozone concentration to initial VOC and NO<sub>x</sub> concentration. Parameterization of this relationship reveals a surprising behaviour of the photochemical system which is the study of Chapters 5 and 6.

I conclude this chapter with a comparison of my parameterization, obtained via a scaling analysis, with other parameterizations of ozone photochemistry.

## 3.2 Scaling Analysis

### 3.2.1 What is a scaling analysis?

The central tenet of scaling is: within limited ranges, the dependence of a system (object(s) including physical properties and forces acting on it (them)) on absolute size are slight and the behaviour of a system at one size can be used to inform at another. A scaling analysis is a method of study based on this concept. Unfortunately, in many instances this concept does not hold. There are reasons why mice aren't the size of elephants or mountains 100 km high (Haldane (1985)). In these cases, there are important absolute sizes in nature which cannot be ignored. In many cases, 'size' does not have to be a length or weight but may turn out to be a simple combination of these or even a more complex combination of forces, sizes and other properties. As a result, the term scale is often used to describe this generalization of size.

A central belief in the physical sciences is that physical laws should hold at all sizes (Schroeder, 1991). However, for complex systems, the relative importance of different forces may change with size. As a result, it often appears (to first order) that different laws hold at different scales. Whenever a complex system does not show different behaviour across different scales, a 'similarity relationship' arises.<sup>1</sup> In such instances, the complex system can be described using a simple statistical or geometrical framework where highly specific physical laws are not necessary. The identification of the appropriate scales (both the correct combination of forces, sizes, etc. which identifies the equivalence and the limits under which equivalence holds) is the first task of a scaling analysis.

While similarity relationships often provide simple descriptions of complex phenomena, one of the most interesting and challenging aspects of a scaling analysis is understanding why complex systems can be described in simple terms when many entirely different physical processes are occurring. In many cases, such *a posteriori* analysis reveal the prime importance of a specific process. It is the intention of this thesis to describe the photochemical production of ground-level ozone in terms of similarity relationships without the need for specific chemical or atmospheric processes. Also, this analysis will identify specific processes which are of prime importance to ozone production in urban environments.

### 3.2.2 Key Concepts

In this section, I outline key concepts related to scaling analysis. I distinguish between dimensional analysis (to be defined shortly) and scaling analysis; a general form of analysis which may

---

<sup>1</sup>The term similarity is used to stress that, while systems may share similar behaviours, they are not identical.

include dimensional analysis. Many of the key concepts are related to the fundamental notion of measurement and how the physical world is described by quantitative means.

### Measurement Systems

The act of measuring involves a comparison between an object (or phenomena) to be measured and a standard. Standards define measurement units which are further sub-divided into fundamental and derived units. Fundamental units are an arbitrary set of standards which form the ‘building blocks’ of a measurement system and derived units are obtained from the fundamental units based physical relationships (Barenblatt, 1996). For example, if length and time are chosen as fundamental units then a derived measurement unit for velocity could be defined by a uniform motion in which one unit of length is traversed in one unit of time. In the SI (*Système International*) system, there are seven fundamental units of measurement used to quantify all physical properties: mass, length, time, temperature, electric current, luminosity intensity and amount of substance. While this is the most common system, others exist, some having a different choice of fundamental units of measurement (i.e. the British Engineering System includes force as a fundamental unit). Regardless of choice of fundamental units, all measurement systems must be able to quantify all physical properties using some combination of their fundamental units.

### Dimension

A physical quantity measured in two different measuring systems may have different numerical values (i.e. speed of sound in *SI* and in the *cgs* measurement systems) and the change in its numerical value is determined by its dimensions. For example, if the unit of measurement for length is decreased by a factor of  $L$  (between measurement systems) and time by a factor of  $T$ , then the numerical values for velocity will be a factor of  $LT^{-1}$  larger and the dimension of velocity is given by  $[LT^{-1}]$ . A quantity whose numerical value is the same in all measurement systems is said to be *dimensionless*. All other quantities are called *dimensional*.

### Dimensional Homogeneity

One implicit assumption in any mathematical expression of a physical relationship is that separate terms represent physical quantities of the same kind. This requires every term to have the same dimensional formula and is called the *principle of dimensional homogeneity* (Bridgman, 1937). An implication of this principle is that physical laws must be independent of the measurement system used to describe them (Bridgman, 1937). This invariance to measurement system imposes con-

straints on the form that dimensional variables can take in an physical relationship when expressed as mathematical equations.

### Dimensional Analysis

Dimensional analysis is a method of reasoning that uses the principle of dimensional homogeneity to simplify mathematical functions which express physical laws (Barenblatt, 1996). In this thesis, I will make use of dimensional analysis to derive a simple relationship for maximum ozone concentration and initial precursor concentrations.

### Dimensionless Groups

Any combination of physical quantities whose numerical value (i.e. measurement) is the same for every measurement system is called a dimensionless group. Such groups are of prime importance in scaling analysis and often given physical interpretations. For example, in fluid dynamics a commonly used dimensionless group is the Reynolds number:

$$Re = \frac{UL}{\nu}$$

where  $U$  is a typical velocity (in  $m/s$  say),  $L$  a typical length (in  $m$ ) and  $\nu$  the dynamic viscosity (in  $m^2/s$ ). This group can be viewed as measuring the relative importance of inertial forces to viscous forces. In a scaling analysis, it is often these groups which determine the 'size' or scale of a phenomena; for instance a fluid flow is classified as turbulent or laminar based on the size of  $Re$ .

### Similarity

Closely related to the concept of scaling is similarity. This is the equivalence of different phenomena based on the equality of a particular dimensionless group. For example, in a fluid flow, dynamic similarity of two different flows implies the equivalence of their Reynolds numbers. Similarity justifies the use of results drawn from experiments with small scale physical models in the design of ships and aircraft.

### Self-similarity

Associated with similarity is self-similarity. Some phenomena appear the same under magnification. The classic example is the branching nature of a fern leaf. The branching produces leaves that replicate of the entire plant. Furthermore, little leaves on each leaf can be viewed as smaller versions of the larger leaf. In nature, this kind of replication has limits (i.e. at the molecular level) whereas

mathematically, the pattern repeats ad infinitum. Wherever self-similarity holds, the phenomena has no preferred scale.

### Power Laws

A power law is a relationship between two or more variables where one variable is expressed as a constant times the other raised to a fixed power. It is represented as a linear relationship on a log-log plot. Power laws have a special behaviour under scaling:

$$\begin{aligned}\text{If } f(x) &= ax^b \\ \text{then } f(\lambda x) &= a(\lambda x)^b \\ &= \lambda^b f(x)\end{aligned}$$

i.e. scaling of the independent variable returns a scaled version of the dependent variable with the same scaling exponent. Such laws are self-similar and hence true on all scales. It is for this reason that power laws are often found in scaling analysis.

### 3.2.3 Scaling Analysis Methods

There are different methods used to perform a scaling analysis. The selection of a particular method often depends on how well the system can be analytically described or how well it can be observed. Below is a description of two common methods used in a scaling analysis: Buckingham Pi Theory and Scale Analysis. Both methods use similar concepts, often yield the same results, and in fact complement one another.

#### Buckingham Pi Theory

This is a systematic method of dimensional analysis in which all the relevant physical variables of a phenomena are placed into dimensionless groups (Bridgman, 1937). Mathematically, the theory exploits the principle of dimensional homogeneity and the fact that the number of relevant dimensionless groups must equal the number of original variables less the number of fundamental dimensions (Bluman and Anco, 2002). As a result, the order of a problem can often be reduced.

#### Scale Analysis

This method of analysis makes use of the governing equations relevant to the system to determine appropriate scales (Glickman, 2000). Each term in the governing equations is made dimensionless using typical values for all fundamental dimensions. The resulting dimensionless terms are then

compared. The smaller terms are ignored and the remaining terms are used to model the system. The remaining terms become the relevant dimensionless groups (or intrinsic scales) for the phenomena. Often different scales are necessary to account for different ranges of the physical quantities (for instance increasing fluid velocity may change a thermal system from a free convection to a forced convection regime). Examples of this method include: the development of Prandtl's equations for fluid flow in a boundary layer (Hinze, 1975), the development of the quasi-geostrophic equations in atmospheric physics (Dutton, 1976) or the analysis by Jackson and Steyn (1994) of gaps winds in a channel.

Figure 3.1 shows a schematic of how both approaches fit into to an investigation of a complex phenomena. The Buckingham Pi approach feeds off the observations and numerical analysis. Data obtained from these investigations are used to determine the relevant variables and design experiments. The arrows could in fact go both ways, as the Buckingham Pi analysis can be used to determine data collection needs. The scale analysis makes use of the governing equations. Both methods establish a select set of dimensionless groups. The end result of both analyses is a description of a simpler system in terms of dimensionless groups. While a mathematical analysis of the simpler system may still not be possible, the scaling analysis is still of value. By making use of the dimensionless groups, the number of independent experiments is reduced. Furthermore, observations or output from numerical models can be simplified by expressing results in terms of the dimensionless groups.<sup>2</sup>

The final stage of a scaling analysis involves fitting an empirical curve to the 'data' (observations or output from numerical models) in order to describe the relationship between groups. If the data fall on a single universal curve or a set of curves showing similar characteristics, then a *similarity relationship* is said to hold. The scaling analysis gives neither the relationship between the dimensionless groups nor the form of the equations (Stull, 1988). This must be found via trial and error or physical insight. For example, given a similarity relationship, one can often infer the relationship between variables or the dominant processes based on its mathematical form (i.e. inverse square law, exponential decay, etc..) and a few simple principles (conservation of energy, central limit theorem, etc..). This type of reasoning has been used by West et al. (1997) to explain the nature of allometric scaling laws in biology.

---

<sup>2</sup>A classic example of how dimensionless groups simplify experimental results was given by von Karman who reduced a set of experimental results, giving the internal friction of various fluids under a set of different conditions, and presented as a set of curves and tables, to a single curve (Barenblatt, 1996).

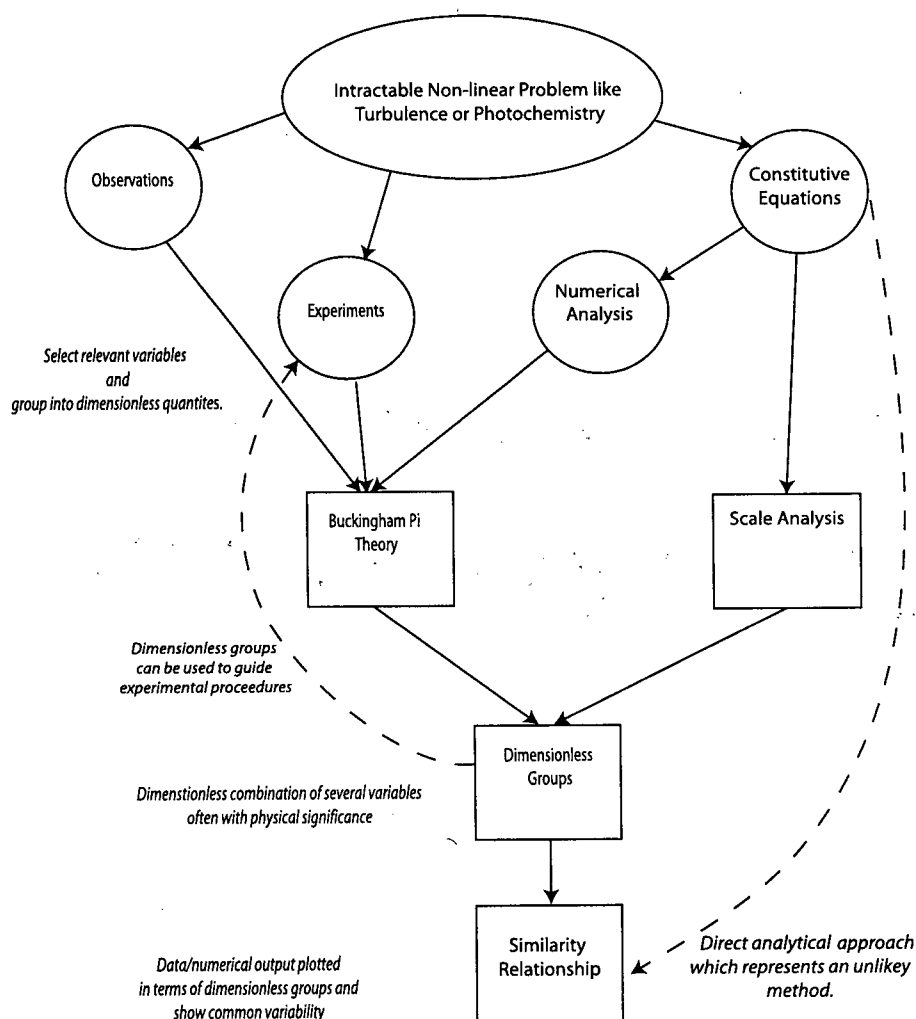


Figure 3.1: A schematic showing how different approaches to studying an intractable non-linear problem lead to formulation of relevant dimensionless groups.

### 3.2.4 Scaling and Photochemical Modeling

A scaling analysis will be used to study the relationship between modeled maximum ozone concentration and initial precursor concentrations. First, however, I would like to show how scaling methods are already extensively used in modeling episodes of elevated ground level ozone. In such models, scaling methods appear in each of the three major model components: emissions, meteorology and photochemistry.

## Emissions

The emissions component of an integrated photochemical model calculates the flux of pollutants for all major sources, throughout the simulation and across the domain of interest. Except for large industrial point sources, in-situ emissions rates are seldom measured. Instead they are inferred by relating laboratory measured emission rates to a surrogate whose spatial and temporal distribution is better characterized (National Research Council, 1991). For instance, in most urban centers, vehicle emissions are the dominant source of VOC and NO<sub>x</sub> emissions (National Research Council, 2000). Vehicle kilometers traveled (*VKT*) is used as the surrogate and laboratory measured emission rates ( $EF_{mobile}$ ) are used to determine emissions ( $\mathcal{E}_{mobile}$ ) i.e.:

$$\mathcal{E}_{mobile}(kg) = VKT(km) \times EF_{mobile}(kg/km)$$

Interestingly, while *VKT* might be easier to measure than in-situ emissions, it too, is seldom measured. Instead, *VKT* is assumed to scale with road size, temporal traffic patterns and driving patterns (National Research Council, 2000). As emission inventories become more detailed, mobile source emissions are further sub-divided based on: mean vehicle speed, vehicle age and vehicle type. Similar scaling methods are used for the other emission sources. In general, since emission inventories reflect the individual and collective actions of a society, and since there are no simple mathematical relationships describing these actions, emissions inventories consist almost entirely of scaling relationships based on more easily calculated surrogates.

## Meteorology

In the meteorological component, local dispersion of pollutants by turbulent mixing is often not explicitly modeled but calculated using similarity relationships. These relationships scale turbulent mixing with: height, wind speed, surface heating and temperature structure of the atmospheric boundary layer (Arya, 1999).

## Chemistry

Finally, scaling relationships are also used in the chemistry component. As mentioned before, modern photochemical mechanisms condense the complex chemical processes into a smaller set of reactions involving a limited number of species (Dodge, 2000). To achieve this condensation, organic compounds are grouped into manageable sets of VOC classes based on similarity of reactivity and emission rates (Stockwell et al., 1990). In essence, this thesis extends the scaling of VOCs, based on reactivity and emission rates, to a scaling of VOC-NO<sub>x</sub> reactivity based on initial concentrations,

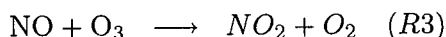
temperature and actinic flux. I begin by studying a simpler NO<sub>x</sub>-only photochemical system before moving to more complex VOC-NO<sub>x</sub> mixtures.

### 3.3 Scaling Analysis of a NO<sub>x</sub>-only System

In this section, I use the Buckingham Pi method of dimensional analysis to study ozone production in a photochemical system having only *NO* and *NO*<sub>2</sub>. An overview of the Buckingham Pi method is given in Appendix A. I use this simple system to develop my methods which I extend in the following section. The scaling analysis produces an expression for maximum ozone concentration as a function of initial NO<sub>x</sub> concentration and different environmental conditions (temperature and actinic flux). I compare it with an analytical model to show the success and limitations of the scaling analysis.

#### 3.3.1 NO<sub>x</sub>-only Photochemical System

Consider a chemical system involving the following two reactions<sup>3</sup>:



where I assume that reaction *R2* proceeds so quickly that *R1* and *R2* can be written as a composite reaction *R1a*. As mentioned in Chapter 2, the steady state concentration of *NO*<sub>2</sub>, *NO* and *O*<sub>3</sub> is given by:

$$[\text{O}_3]_{pss} = \frac{j[\text{NO}_2]_{pss}}{k_{NO}[\text{NO}]_{pss}} \quad (3.1)$$

Equation (3.1) describes the steady state ozone concentration in terms of the *NO*<sub>2</sub> photolysis rate and NO-titration rate and depends on the steady state *NO* and *NO*<sub>2</sub> concentrations. A scaling analysis will be used to relate **maximum** steady state ozone concentration to the **initial** *NO* and *NO*<sub>2</sub> concentrations. It will also examine the dependence of maximum ozone concentration on actinic flux and temperature.

#### 3.3.2 Relevant Variables

To start the scaling analysis, consider a smog chamber of volume *V* containing an initial amount (in moles) of *NO* (*N*<sub>NO</sub>) and *NO*<sub>2</sub> (*N*<sub>NO<sub>2</sub></sub>) at a temperature *T* irradiated by a time varying spectral

<sup>3</sup>A more realistic description for a NO<sub>x</sub>-only photochemical system would also include reactions driven by the ubiquitous radicals. For simplicity, I ignore these and treat (*R1a*) and (*R3*) as a complete description of the photochemistry.

Variable	Description	Units	Dimension
$V$	Chamber volume	$cm^3$	$length^3$
$N_{O_3}$	Maximum amount of ozone	<i>molecules</i>	<i>number</i>
$N_{NO}$	Initial amount of $NO$	<i>molecules</i>	<i>number</i>
$N_{NO_2}$	Initial amount of $NO_2$	<i>molecules</i>	<i>number</i>
$j_{pk}$	Peak $NO_2$ -photolysis rate constant	$sec^{-1}$	$time^{-1}$
$A$	$NO$ - $O_3$ collision frequency	$cm^3(molecules \cdot s)^{-1}$	$length^3(number \cdot time)^{-1}$
$E$	$NO$ - $O_3$ activation energy	$J \cdot molecule^{-1}$	$mass \cdot length^2 \cdot time^{-2} \cdot number^{-1}$
$kT$	average translational molecular energy	$J \cdot molecule^{-1}$	$mass \cdot length^2 \cdot time^{-2} \cdot number^{-1}$

Table 3.1: *Units and dimensions for maximum ozone and its dimensional factors.*

actinic flux  $I(\lambda, t)$  for duration  $\Delta t$ . It is expected that the maximum amount (in moles) of ozone ( $N_{O_3}$ ) will depend on  $N_{NO}$  and  $N_{NO_2}$ . Guided by Eq. (3.1), I expect  $N_{O_3}$  to also depend the actinic flux via the  $NO_2$  photolysis rate. While, this rate is a complex function of wavelength, spectral intensity, absorption cross-section and quantum yield (Finlayson-Pitts and Pitts, 1999), I assume for a constant ozone column abundance and particulate loading, the rate is determined solely by the solar zenith angle. Furthermore, assuming that  $O_3$ ,  $NO_2$  and  $NO$  adjust their concentrations faster to changes in  $I(\lambda, t)$  than  $I(\lambda, t)$  changes with time, then the length of time the mixture is irradiated should be unimportant. These last two assumptions also suggest that maximum ozone formation should be dependent on the peak photolysis rate constant ( $j_{pk}$ ). Finally,  $N_{O_3}$  is a function of the  $NO$  titration rate. This in turn depends on the reaction activation energy ( $E$ ), the average molecular translational energy ( $kT$  where  $k$  is the Boltzmann constant) and the molecular collision rate (also called the frequency factor ( $A$ )).

In all, I expect  $N_{O_3}$  to be a function of seven factors: chamber volume ( $V$ ), initial  $N_{NO}$  and  $N_{NO_2}$ , peak  $NO_2$  photolysis rate ( $j_{pk}$ ), ozone- $NO$  collision rate ( $A$ ), activation energy ( $E$ ) and molecular translational energy ( $kT$ ).

### 3.3.3 Variable Dimensions

The fundamental dimensions for maximum ozone and its seven independent factors are given in Table 3.1. In all, the problem contains four fundamental dimensions: *length*, *time*, *mass* and *number of atoms or molecules*.

### 3.3.4 Key Variables

Because this system has four dimensions, four 'key variables' are required to non-dimensionalize the problem. These can be any of the variables from Table 3.1 subject to the following restrictions:

- There must be as many key variables as fundamental dimensions
- All of the fundamental dimensions must be represented by the key variable
- The key variables cannot be arranged into a single dimensionless group

The chamber volume ( $V$ ), peak photolysis rate constant ( $j_{pk}$ ), activation energy ( $E$ ) and frequency factor ( $A$ ) form an appropriate selection since they contain all dimensions and no single dimensionless group can be formed from them.

### 3.3.5 Pi-Groups

Next, the remaining four variables ( $N_{O_3}$ ,  $N_{NO}$ ,  $N_{NO_2}$  and  $T$ ) are made dimensionless using the key variables. The resulting dimensionless variables, called Pi-groups after the engineering scientist Buckingham who developed the technique (Buckingham, 1914) are:

$$\pi_1 = \frac{N_{O_3}}{V \cdot j_{pk}/A}, \quad \pi_2 = \frac{N_{NO}}{V \cdot j_{pk}/A}, \quad \pi'_3 = \frac{N_{NO_2}}{V \cdot j_{pk}/A}, \quad \pi'_4 = \frac{kT}{E} \quad (3.2)$$

### 3.3.6 Alternative Pi-Groups

The theorem allows new Pi-groups to be chosen from the original groups provided that the number of groups remains the same, all variables are represented and no Pi-groups can be formed from any other group (Stull, 1988). By taking advantage of this option, I form the following Pi-groups:

$$\pi_1 = \frac{N_{O_3}}{V \cdot j_{pk}/A}, \quad \pi_2 = \frac{N_{NO}}{V \cdot j_{pk}/A}, \quad \pi_3 = \frac{N_{NO_2}}{N_{NO}}, \quad \pi_4 = \exp\left\{\frac{E}{kT}\right\} \quad (3.3)$$

The relationship between maximum amount of ozone, for a simple photochemical system defined by (R1a) and (R3), and its relevant variables should now be expressible by four dimensionless groups; a reduction in the order of the problem by four i.e.:

$$\begin{aligned} N_{O_3} &= F(V, N_{NO}, N_{NO_2}, j_{pk}, kT, E, A) && \text{Dimensional} \\ \pi_1 &= \hat{f}(\pi_2, \pi_3, \pi_4) && \text{Dimensionless} \end{aligned}$$

While recasting the problem in terms of Pi-group has simplified the problem, the function relationship between Pi-groups must still be empirically determined using observations or numerical modeling. However, to aid in the search, a suitable form for the relationship can be guessed. To this end, I suggest the following functional relationship:

$$\Pi_1 = \pi_1/\pi_4 = f(\pi_2/\pi_4, \pi_3/\pi_4) \quad (3.4)$$

By rewriting in this form, dimensionless number concentrations can be expressed in a simpler manner. For dimensionless ozone:

$$\Pi_1 = \frac{\pi_1}{\pi_4} = \frac{N_{O_3}}{\frac{V \cdot j_{pk}}{A \exp\{-E/(kT)\}}} = \frac{[O_3]_{max}}{j_{pk}/k_{NO}} \quad (3.5)$$

where  $[O_3]_{max}$  ( $= N_{O_3}/V$ ) is the maximum ozone concentration and  $k_{NO}$  ( $= A \exp\{-E/kT\}$ ) is the Arrhenius rate constant for reaction (R3)<sup>4</sup>. Similar expressions for dimensionless NO and NO<sub>2</sub> are found using  $\Pi_2 = \pi_2/\pi_4$  and  $\Pi_3 = \pi_3/\pi_4$ . To test this form, model output was generated.

### 3.3.7 OZIPR Model Output

Numerical simulation of a NO<sub>x</sub>-only photochemical system (defined exclusively by reactions R1a and R2) were carried out using a box model with a constant temperature, no dilution and the initial NO and NO<sub>2</sub> initially uniformly mixed before the start of irradiation. The initial ozone concentration was set to zero. The simulations used actinic flux levels appropriate to Vancouver B.C. (Latitude 49.25° N and Longitude 123.15° W) for a time interval beginning at 8:00 a.m. and ending at 7:00 p.m. (Pacific Standard Time). Parametrization of the NO<sub>2</sub> photolysis rate with solar zenith was taken from the RADM2 (Stockwell et al., 1990) chemical mechanism. A matrix of simulations was run for 15 different NO<sub>x</sub> levels, five different  $[NO_2]_o/[NO]_o$  ratios, four temperatures and five Julian dates for a total of 1500 simulations. The Julian dates, ranging between June 21<sup>st</sup> and September 15<sup>th</sup>, were chosen to provide a uniform spacing of  $j_{pk}$ -values while the temperature range was chosen to be representative of maximum summertime temperatures in the LFV, B.C. (Steyn et al., 1999). The simulated NO<sub>x</sub> concentrations range from values typical of remote locations to values found in urban and suburban boundary layers (National Research Council, 1991). Finally, the low end of the  $[NO_2]_o/[NO]_o$  range corresponds to typical ambient conditions in the LFV (Jiang et al., 1997a) while the upper end represents ratios typical of raw vehicle exhaust (Lenner, 1987).

Table 3.2 lists the ranges and number of treatments for each variable. I have recorded the NO<sub>x</sub> range using concentration units (in ppm) for two reasons: this form is the easiest to use based on the final  $\Pi$ -groups and it is the conventional way of describing the relative amount of substance in air pollution meteorology.

The numerical solver OZIPR (Tonnesen, 2000) was used to simulate the reactions. OZIPR is a research-oriented version of EPA's OZIP (Ozone Isopleth Plotting Package) computer modeling program. This is a simple trajectory model useful for relating ozone concentrations to different precursor concentrations and environmental conditions. A more complete description of the model

<sup>4</sup>The Boltzmann constant ( $k$ ) is not to be confused with the rate constant ( $k_{NO}$ ) which will always appear with a subscript.

Variable	Range (units)	Number of Treatments
Temperature	293-308 (K)	4
Peak Photolysis	0.00738-0.00895 (1/sec)	5
Initial $NO_x$ concentration	0.00010-1.5000 (ppm)	15
Initial ratio of $NO_2$ to $NO$	0.124-1.94	5

Table 3.2: Variable ranges and number of treatments for the OZIPR simulations of the  $NO_x$ -only photochemical system.

is given in Appendix B. Photochemistry was simulated using the RADM2 chemical mechanism (Stockwell et al., 1990). A complete description of this mechanism is given in Appendix C. From each simulation, maximum ozone concentration was recorded (which indeed coincided with peak  $NO_2$  photolysis rate). The relevant variables were made dimensionless using Eq. (3.4).

In Figure 3.2, dimensionless maximum ozone concentration ( $\Pi_1$ ) has been plotted against dimensionless initial  $NO$  ( $\Pi_2$ ) for the various different initial  $[NO_2]_o/[NO]_o$  ratios ( $\Pi_3$ ). From this graph, the model output falls onto five distinct curves. Each tends to an asymptotic value as  $\Pi_2$  becomes large. Furthermore, it appears that this asymptotic value corresponds to the  $\Pi_3$ -value. This suggests plotting  $\Pi_1/\Pi_3$  versus  $\Pi_2$  to obtain a single ‘universal’ curve. Figure 3.3 shows such a plot where the five curves have now almost collapsed onto a single curve. The collapse is best for the high and low  $\Pi_2$  values but there is still some spread between the curves for  $\Pi_2 \in (5, 20)$ . A line of best fit has been drawn through the data which represents the empirically derived similarity relationship (discussed next).

To understand the significance of this plot, consider three OZIPR simulations, all for a latitude of  $49.25^\circ N$  having the following initial conditions:

1. A temperature of  $35^\circ C$  with an actinic flux appropriate for June 21<sup>st</sup> and starting with initial  $[NO]_o = 0.51$  ppm and  $[NO_2]_o = 0.99$  ppm.
2. A temperature of  $20^\circ C$  for August 10<sup>th</sup> with initial  $[NO]_o = 0.63$  ppm and  $[NO_2]_o = 0.63$  ppm.
3. A temperature of  $25^\circ C$  for August 27<sup>th</sup> with initial  $[NO]_o = 0.56$  ppm and  $[NO_2]_o = 0.19$  ppm.

The corresponding dimensionless  $NO$  concentrations ( $\Pi_2$ ) are nearly identical: 29.6, 30.0 and 30.7. As a result, the analysis suggests that the corresponding ratios of  $\Pi_1/\Pi_3$  should be nearly identical and indeed they are: 0.91, 0.92 and 0.94. However, there are different ways to produce a constant  $\Pi_1/\Pi_3$  ratio: and in this case, because of the large range in  $[NO_2]/[NO]$  ratios (1.94, 1.00, 0.33),

$[NO]_o$ (ppm)	$[NO_2]_o$ (ppm)	T (K)	$k_{NO}$ (ppm/sec)	Date	$j_{pk}$ (1/s)	$[O_3]_{max}$ (ppb)	$\Pi_2$	$\Pi_3$	$\Pi_1$	$\Pi_1/\Pi_3$
0.51	0.99	308	0.52	June 21	0.00895	30.4	29.6	1.94	1.77	0.91
0.63	0.63	293	0.41	August 10	0.0086	19.1	30.0	1.00	0.92	0.92
0.56	0.19	298	0.45	August 27	0.00819	5.7	30.7	0.33	0.31	0.94

Table 3.3: Initial conditions and maximum ozone concentration for three  $NO_x$ -only OZIPR simulations have similar  $\Pi_2$  values.

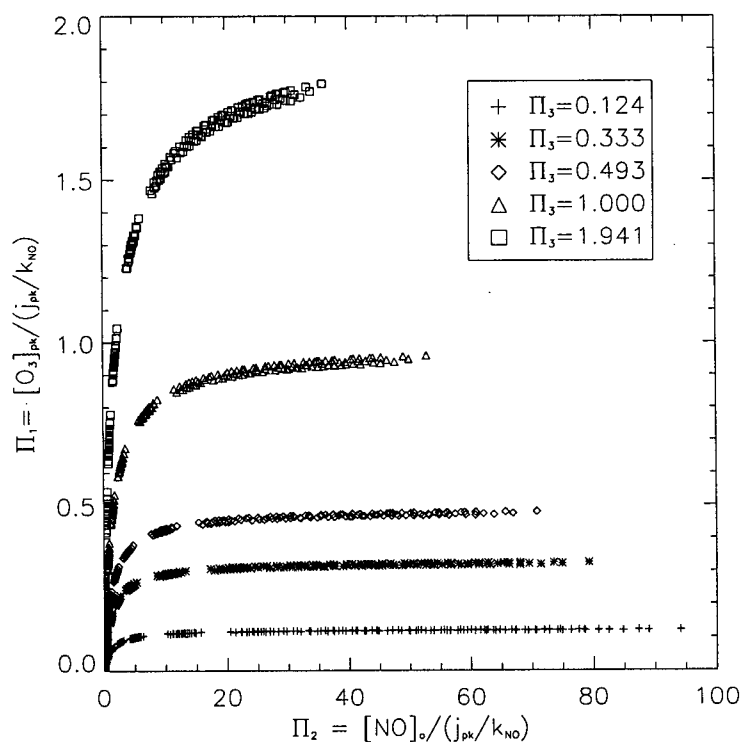


Figure 3.2: Dimensionless maximum ozone concentration versus dimensionless initial  $NO$  concentration ( $\Pi_2$ ) for 5 different initial  $NO_o$  to  $NO_2$  ratios. Values of  $\Pi_2$  reflect different initial  $NO$  concentrations,  $k_{NO}$  rates (via different temperatures) or  $j_{pk}$  values (via different Julian dates).

there is a large range in maximum ozone values: 30.4, 19.1 and 5.7 ppb. Table 3.3 summarizes these three simulations. Thus a wide range of ozone concentrations, arising from a wide range of simulations conditions, are nonetheless considered equivalent from a scaling perspective.

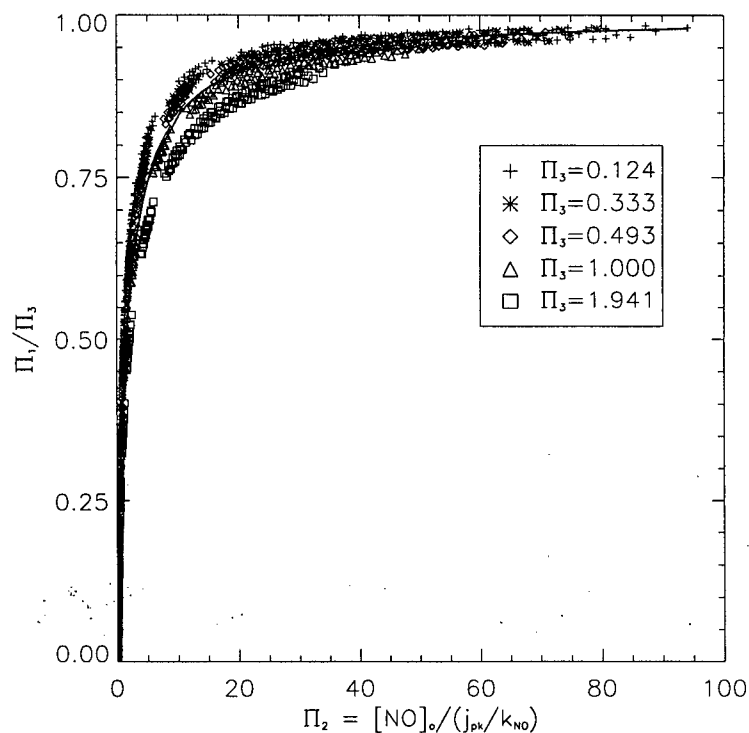


Figure 3.3: Dimensionless steady-state ozone concentration scaled by the initial ratio of  $NO$  to  $NO_2$  as a function of dimensionless initial  $NO$  concentration. Also plotted is the ‘universal’ similarity relationship  $\Pi_1/\Pi_3 = 0.5 \left\{ (\Pi_2^2 + 6\Pi_2 + 1)^{1/2} - (\Pi_2 + 1) \right\}$ .

### 3.3.8 Universal Curve

By trial and error, a curve which fits the dimensionless model output has been found:

$$\frac{\Pi_1}{\Pi_3} = 0.5 \left\{ (\Pi_2^2 + 6\Pi_2 + 1)^{1/2} - (\Pi_2 + 1) \right\} \quad (3.6)$$

Equation 3.6 shows that as  $\Pi_2$  gets large,  $\frac{\Pi_1}{\Pi_3} \rightarrow 1$ . This implies that for large enough initial  $NO$  concentration:

$$[O_3]_{max} \approx \frac{j_{pk}[NO_2]_o}{k_{NO}[NO]_o} \quad (3.7)$$

This expression is similar to Eq. (3.1) except now **maximum** ozone concentration is related to **initial**  $NO_x$  concentrations. In essence, with enough initial  $NO$  (or high  $k_{NO}$  (via high temperatures) or small  $j_{pk}$  (via little actinic flux)), the resulting maximum ozone concentration is achieved with very little change in the initial ratio of  $NO_2$  to  $NO$ .

### 3.3.9 Analytic Expression

It is possible, from this simple system, to derive an analytic expression for maximum ozone concentration as a function of the initial NO<sub>x</sub> concentrations (Seinfeld and Pandis, 1998). This is achieved by introducing two additional constraints to equation 3.1. The first is the conservation of nitrogen, namely:

$$[NO](t) + [NO_2](t) = [NO]_o + [NO_2]_o \quad (3.8)$$

and the second a stoichiometric balance of O<sub>3</sub> with NO :

$$[NO]_o - [NO](t) = [O_3]_o - [O_3](t) \quad (3.9)$$

(i.e. both O<sub>3</sub> and NO are consumed and produced in a fixed proportion) Using these constraints, the steady state ozone concentration (when initial ozone concentration is set to zero ([O<sub>3</sub>]<sub>o</sub> = 0)) is:

$$[O_3]_{pss} = -\frac{1}{2} \left( [NO]_o + \frac{j}{k_{NO}} \right) + \frac{1}{2} \left\{ \left( [NO]_o + \frac{j}{k_{NO}} \right)^2 + 4 \frac{j}{k_{NO}} [NO_2]_o \right\}^{1/2} \quad (3.10)$$

Maximum steady state ozone concentration (for fixed NO, NO<sub>2</sub> and temperature) occurs when  $j$  is a maximum i.e.:

$$\frac{d[O_3]_{pss}}{dt} = 0 \quad \text{when} \quad \frac{dj}{dt} = 0 \quad (3.11)$$

Using Eq. (3.11) and rewriting Eq. (3.10) using dimensionless groups gives an exact relationship between Pi-groups:

$$\begin{aligned} \frac{[O_3]_{max}}{j_{pk}/k_{NO}} &= -\frac{1}{2} \left( \frac{[NO]_o}{j_{pk}/k_{NO}} + 1 \right) + \frac{1}{2} \left\{ \left( \frac{[NO]_o}{j_{pk}/k_{NO}} + 1 \right)^2 + 4 \frac{[NO]_o}{j_{pk}/k_{NO}} \cdot \frac{[NO_2]_o}{j_{pk}/k_{NO}} \right\}^{1/2} \\ \text{or } \Pi_1 &= -\frac{1}{2} (\Pi_2 + 1) + \frac{1}{2} \left\{ (\Pi_2 + 1)^2 + 4\Pi_2 \cdot \Pi_3 \right\}^{1/2} \end{aligned} \quad (3.12)$$

Equation 3.12 shows that it is not possible to express  $\Pi_1/\Pi_3$  as a function of  $\Pi_2$  only. Thus it is not possible to express the dependence of maximum ozone concentration on  $[NO]_o$ ,  $[NO_2]_o$ ,  $T$  and  $j$  by a single curve. Therefore, the 'universal' curve (Eq. 3.6) represents an approximation of the true relationship, obtained as an empirical fit to the OZIPR model output. However, while not exact, Eq. (3.6) provides a simple means of describing ozone formation in this system which is valid over a wide range of conditions. In Figure 3.4, I have plotted  $\Pi_1/\Pi_3$ , obtained via Eq. (3.12) versus  $\Pi_1/\Pi_3$  from Eq. (3.6), for the same range of parameter values as given in Table 3.2. Also plotted is the 1 : 1 line, representing perfect agreement between the two equations. From the Figure, it is apparent that the 'universal' curve over-predicts when  $\Pi_3 > 1$ , under-predicts when  $\Pi_3 < 1$ , however in these instances the discrepancy is less than 10%. Finally the two equations show perfect agreement when  $\Pi_3 = 1$ .

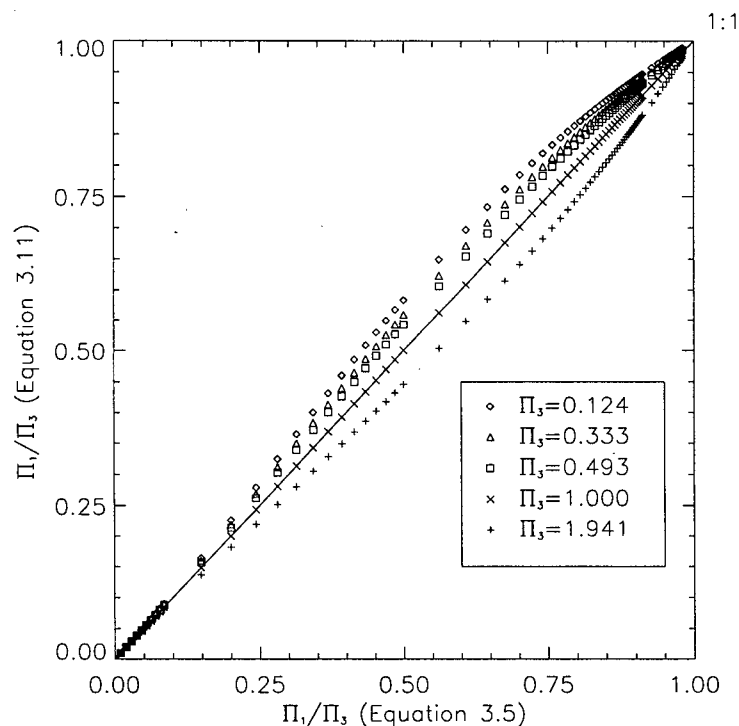


Figure 3.4: Scatter plot showing  $\Pi_1/\Pi_3$  using Eq. (3.6) versus Eq. (3.12) for five different  $\Pi_3$  levels. Also shown is the 1 : 1 line.

In most cases, an exact expression like Eq. (3.12) is not available and similarity methods provide the best means of describing the complex system in simpler terms. In the next section, I look at a more complex photochemical system where an exact relationship for ozone dependence on initial precursor concentration cannot be found and similarity methods must be used.

### 3.4 Propene-NO<sub>x</sub> System

In this section, I use the Buckingham Pi method of dimensional analysis to analyze a photochemical system involving a single VOC species and NO<sub>x</sub>. The analysis considers only the dependence of maximum ozone on initial precursor concentrations. A more detailed analysis, involving different VOCs, VOC mixtures and varying environmental conditions is postponed until the next chapter.

I start the analysis with a qualitative description of an ozone response surface; highlighting the complex dependence of maximum ozone on initial precursor concentration. The analysis then proceeds with a consideration of the important processes and variables which govern ozone formation in a VOC-NO<sub>x</sub> system. This is followed by the selection of appropriate Pi-groups, numerical simu-

lations and the eventual plotting of a similarity relationship. Parameterization of this relationship introduces results and methods which are central to much of this thesis. The section finishes with a comparison of ozone-precursor relationships.

### 3.4.1 Ozone response surface

The dependence of ozone formation on initial amounts of VOC and NO<sub>x</sub> is most easily seen by plotting contours of maximum ozone against initial precursor concentrations. Such a response surface (plotted in Figure 3.5) is referred to as an ozone isopleth diagram and is generated by performing a larger number of photochemical simulations with varying initial VOC and NO<sub>x</sub> concentrations while keeping all other variables constant (Seinfeld and Pandis, 1998). Since isopleth diagrams are a concise way to depicting the effects of changing VOC or NO<sub>x</sub> concentrations on peak ozone concentrations, they have also been used to quantitatively develop control strategies (National Research Council, 1991).

The ozone response surface highlights the complex behaviour of maximum ozone on both the absolute and relative levels of VOC and NO<sub>x</sub>. For example, consider the two arrows in Figure 3.5. In the region marked by the lower arrow, maximum ozone levels initially increase as initial NO<sub>x</sub> concentrations increase. At a critical ratio of VOC-to NO<sub>x</sub>, the maximum ozone level reaches a peak and then starts to decrease as NO<sub>x</sub> concentrations are further increased (as indicated by the upper arrow). The location of peak maximum ozone forms a ridgeline, defined as the location where the sensitivity of maximum ozone to changing NO<sub>x</sub> concentrations is zero i.e.:

$$\frac{\partial [O_3]_{max}}{\partial [NO_x]_o} = 0 \quad (3.13)$$

This ridgeline definition is somewhat arbitrary; one could equally define the ridgeline as the location where maximum ozone shows equal sensitivity to changing NO<sub>x</sub> and VOC concentrations. The significance of different ridgeline definitions is investigated in chapter 4. The region below the ridgeline, called the NO<sub>x</sub> limited region (NLR), has ozone production limited by low NO<sub>x</sub> availability. Above the ridgeline, maximum ozone increases with increasing VOC levels and is called the VOC limited region (VLR). The objective of the scaling analysis is to find a simple mathematical description of this complex behaviour.

While precursor concentrations are the most important factors in determining maximum ozone concentrations, other factors also influence the photochemistry. One group of factors, which I call environmental factors, includes temperature and actinic flux. In this chapter, I include these in the selection of the dimensionless groups but postpone an investigation of their influence until the next chapter. Another group, which I call mechanical factors, includes deposition, entrainment and

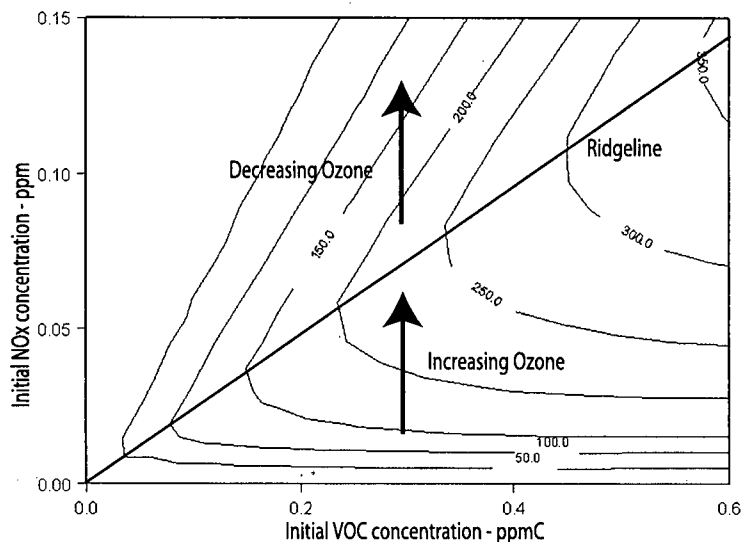


Figure 3.5: Ozone response surface as a function of initial VOC and  $NO_x$  concentration. Isopleth show maximum ozone concentration in ppb. A ridgeline separates the surface into two regions: one shows an increase in ozone for an increase in initial  $NO_x$  (marked by the lower arrow), the other a decrease (upper arrow).

dilution. I do not include these in the scaling analysis but I examine their influence in Part II.

In order to eliminate the possible confounding effects of both the mechanical and environmental factors, I simulate a smog chamber where dilution and entrainment are not present and deposition can be accounted for. Smog chambers are essentially large reaction vessels where emission, temperature, humidity and sunlight can be accurately controlled and the confounding effects of the real atmosphere can be removed (Finlayson-Pitts and Pitts, 1999). These chambers are not without their own complicating influences which I address in Chapter 7.

### 3.4.2 Dimensional Considerations

For the VOC- $NO_x$  system, the presence of VOCs suggest radical driven chemistry, as outlined in Chapter 2, will be important. As mentioned before, the net effect of the radical driven chemistry is to slowly convert  $NO$  to  $NO_2$  without consuming  $O_3$ . This slower cycle is interconnected with the fast cycling of  $NO_x$  between  $NO$  and  $NO_2$ . Figure 3.6 shows a schematic of the two cycles where the fast cycle is comprised of reactions (R1a) and (R3) and the slow cycle is characterized by  $NO$ -to- $NO_2$  conversion via the  $HO_2^\bullet$  radical; a product of  $OH^\bullet$  attack on VOCs. The presence of a fast and slow cycle suggest this problem will have several characteristic scales.

Drawing on the results from the  $NO_x$ -only scaling, I expect the maximum amount of ozone

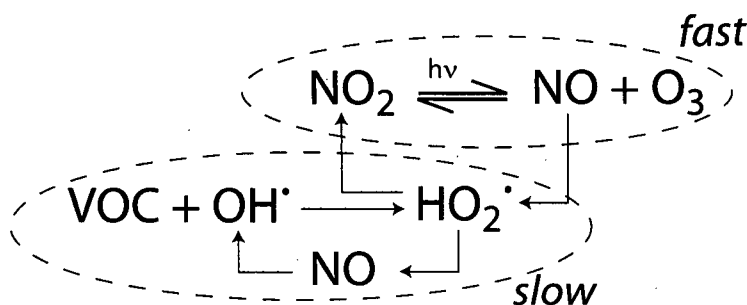


Figure 3.6: Schematic of the fast  $\text{NO}-\text{NO}_2-\text{O}_3$  cycle and the slower radical driven cycle (adapted from Seinfeld and Pandis (1998)).

Variable	Description	Units	Dimensions
$V$	Chamber volume	$\text{m}^3$	$\text{length}^3$
$N_{\text{O}_3}$	Maximum amount of ozone	moles	number
$N_{\text{NO}_x}$	Initial amount of $\text{NO}_x$	moles	number
$j_{av}$	Average $\text{NO}_2$ photolysis rate constant	$\text{sec}^{-1}$	$\text{time}^{-1}$
$A_{\text{NO}}$	$\text{NO}-\text{O}_3$ collision frequency	$\text{cm}^3(\text{molecules} \cdot \text{s})^{-1}$	$\text{length}^3(\text{number} \cdot \text{time})^{-1}$
$E_{\text{NO}}$	Activation energy for $\text{O}_3 + \text{NO}$ titration	$\text{J} \cdot \text{molecule}^{-1}$	$\text{mass} \cdot \text{length}^2 \cdot \text{time}^{-2} \cdot \text{number}^{-1}$
$N_{\text{VOC}}$	Initial amount of VOC	moles	number
$\Delta t$	Length of test	sec	time
$A_{\text{OH}}$	$\text{VOC} - \text{OH}$ collision frequency	$\text{cm}^3(\text{molecules} \cdot \text{s})^{-1}$	$\text{length}^3(\text{number} \cdot \text{time})^{-1}$
$E_{\text{OH}}$	Activation energy for $\text{VOC} + \text{OH}^\bullet$ reaction	$\text{J} \cdot \text{molecule}^{-1}$	$\text{mass} \cdot \text{length}^2 \cdot \text{time}^{-2} \cdot \text{number}^{-1}$
$kT$	Average molecular translational energy	$\text{J} \cdot \text{molecule}^{-1}$	$\text{mass} \cdot \text{length}^2 \cdot \text{time}^{-2} \cdot \text{number}^{-1}$

Table 3.4: Smog chamber scaling parameters

( $N_{\text{O}_3}$ ) to be a function of the chamber volume ( $V$ ) and molecular translational energy ( $kT$ ) as well as the ozone titration activation energy ( $E_{\text{NO}}$ ) and molecular collision rate ( $A_{\text{NO}}$ ). Because of the fast cycling between  $\text{NO}$  and  $\text{NO}_2$ , it is likely that the total amount of the two ( $N_{\text{NO}_x}$ ) will be an important factor. The presence of the slower cycle suggests that maximum amount of ozone formed may not coincide with peak actinic flux. As a result, the average  $\text{NO}_2$  photolysis rate constant ( $j_{av}$ ) should be a better measure of the actinic flux than the peak photolysis rate constant ( $j_{pk}$ ).

The slow cycle is characterized by the length of time the mixture is irradiated ( $\Delta t$ ), the initial amount of VOC ( $N_{\text{VOC}}$ ), the activation energy of the  $\text{VOC}-\text{OH}^\bullet$  attack ( $E_{\text{OH}}$ ) and the collision rate for this reaction ( $A_{\text{OH}}$ ). Thus the problem has eleven different factors having four separate fundamental dimensions: length, time, mass and amount of substance. Table 3.4 summarizes the relevant variables and their dimensions.

Four key variables ( $kT$ ,  $V$ ,  $j_{av}$  and  $A_{\text{NO}}$ ), containing all the fundamental dimensions, have been

chosen to non-dimensionalize the remaining variables which yields the following seven (11 variables - 4 fundamental dimensions) dimensionless groups:

$$\begin{aligned} \pi &= \frac{N_{O_3} A_{NO}}{V j_{av}}, & \pi'_1 &= \frac{N_{VOC} A_{NO}}{V j_{av}}, & \pi_2 &= \frac{N_{NOx} A_{NO}}{V j_{av}}, \\ \pi_3 &= j_{av} \Delta t, & \pi_4 &= \frac{E_{OH}}{kT}, & \pi_5 &= \frac{E_{NO}}{kT}, & \pi_6 &= \frac{A_{NO}}{A_{OH}} \end{aligned} \quad (3.14)$$

For Arrhenius type reactions,  $A_{NO}$  and  $A_{OH}$  are independent of temperature, their ratio becomes a constant and so  $\pi_6$  will not influence the functional form of the similarity relationship and so can be ignored. Finally, I form a new pi-group ( $\pi_1$ ) by dividing  $\pi'_1$  by  $\pi_2$ .

Dimensionless analysis then suggests the relationship between maximum ozone and its governing variables can be expressed by:

$$\pi = \hat{f}(\pi_1, \pi_2, \pi_3, \pi_4, \pi_5) \quad (3.15)$$

where  $\hat{f}^5$  is an unknown function of only five factors. This marks the end of the formal analysis. Further simplifications to the problem must be made through trial and error or by physical insight.

Drawing on the results of the NOx-only scaling, I use  $\pi_5$  to write  $\Pi = \pi/\pi_5$  and  $\Pi_2 = \pi_2/\pi_5$ . I express the dimensionless activation energy ( $\pi_4$ ) in an exponential form ( $\Pi_4 = \exp[-\frac{E_{OH}}{k}(\frac{1}{T} - \frac{1}{T_{ref}})]$ ) where  $T_{ref}$  is a arbitrary reference temperature chosen to be 25°C. I further assume that  $\pi_5$  has only a temperature dependence that is captured by  $\Pi_4$  and so the direct dependence of this group can be ignored. Finally, to be consistent in my notation, I set  $\Pi_3 = \pi_3$ .

Thus, I hope to find a relationship between maximum ozone and its governing variables having the following form:

$$\begin{aligned} \Pi &= f(\Pi_1, \Pi_2, \Pi_3, \Pi_4) \quad \text{or} \\ \frac{[O_3]_{max}}{j_{av}/k_{NO}} &= f\left(\frac{[NO]_o}{j_{av}/k_{NO}}, \frac{[VOC]_o}{[NOx]_o}, j_{av} \Delta t, \exp\left[-\frac{E_{OH}}{k}\left(\frac{1}{T} - \frac{1}{T_{ref}}\right)\right]\right) \end{aligned} \quad (3.16)$$

To further simplify the functional form, a power law dependence for  $\Pi_2$  is hypothesized. There is no *a priori* reason for such a selection; justification occurs when the data collapse onto a common 'universal' curve (Arya, 2001). However, the work of Chang and Rudy (1993), Blanchard et al. (1999), and Johnson (1984) all suggest that maximum ozone concentrations scales with a power of initial NOx concentration. Another consideration is that dimensional analysis only resolves power functions (Bridgman, 1937).

With this in mind, Eq. (3.17) can be rewritten:

$$\frac{\Pi}{\Pi_2^a} = f(\Pi_1, \Pi_3, \Pi_4) \quad (3.17)$$

<sup>5</sup>I use  $\hat{f}$  (and later  $f$ ) as generic labels for the unknown function. These are different functions than those found in the NOx-only scaling analysis.

where  $a$  is an unknown exponent. The unknown function is now only dependant on three dimensionless groups. To keep the analysis simple, I will initially let only  $\Pi_1$  vary. I examine the scaling behaviour for this simple case before extending the analysis to include varying actinic flux and temperature. Also, I examine only a single VOC, an alkene, in this section. In the next chapter, other VOCs are analyzed.

### 3.4.3 Propene

I use propene as the sole VOC due to its relatively simple chemistry, its high reactivity and because it is often used as a benchmark for comparing VOC reactivities (National Research Council, 1991). Unfortunately, in the RADM2 mechanism (Stockwell et al., 1990) propene is not specifically modeled. In this mechanism, alkenes are represented using 3 species: ethene (ETH), a surrogate for terminal alkenes (alkenes with a double bond attached to a carbon at the end of the molecule) called OLT and a third (OLI) used to represent internal alkenes, cyclic alkenes and dienes. The OLT surrogate generalizes the behaviour of terminal alkenes and reacts with  $OH^\bullet$  and  $O_3$  with the same rate constants as propene (Stockwell et al., 1990). Therefore, it is expected that results obtained for OLT will be representative of propene.

### 3.4.4 OZIPR Simulations

To generate model output, a matrix of simulations was run using the OZIPR (Tonnesen, 2000) trajectory model. The test matrix consisted of 121 simulations created by independently varying initial OLT and NO<sub>x</sub> concentrations in 10% increments. The range of initial OLT concentrations was between 0.0 and 0.6 ppm while the NO<sub>x</sub> range was 0.0 to 0.15 ppm. The simulation conditions were similar to those outlined in Section 3.3.7, namely: start time was 7:00 a.m. (PDST) and end time was 6:00 p.m. (PDST), and there was neither dilution, entrainment nor deposition. However, these simulations were run with a constant temperature of 25°C, a 'total' dimensionless actinic flux of  $\Pi_3 = 347$  (corresponding to Vancouver B.C. in mid-summer (August 3)) and an initial NO<sub>2</sub> to NO ratio of 0.250. These simulations produced an overall maximum modeled ozone concentration of 348 ppb.

Model output consisted of maximum ozone concentration along with initial VOC and NO<sub>x</sub> concentrations. However, before the model output was analyzed, some simulations were excluded. Whenever initial NO<sub>x</sub> concentration was zero (and  $\Pi_1$  infinite), the RADM2 mechanism produced no ozone. These trivial simulations were removed. In addition, whenever the initial OLT concentration were zero ( $\Pi_1 = 0$ ), the RADM2 mechanism produced low ozone concentrations, independent

of OLT, representing ozone formation in a NO<sub>x</sub>-only system. Since the scaling analysis is concerned with VOC-NO<sub>x</sub> systems, these simulations were also excluded. After these removals, 100 simulations remained to determine  $f(\Pi_1, \Pi_2, \Pi_3)$ .

### 3.4.5 Similarity Relationship

Using Eq. (3.17), modeled maximum ozone concentration was made dimensionless and scaled by a power of dimensionless NO<sub>x</sub> i.e.:

$$\frac{[O_3]_{max}}{j_{av}/k_{NO}} / \left( \frac{[NOx]_o}{j_{av}/k_{NO}} \right)^a \quad (3.18)$$

It was found that with a value of  $a = 0.6$ , model output, when plotted using Eq. (3.18) as a function of  $\Pi_1$  (which is conventionally denoted by the variable  $R$ ), collapsed onto a single common curve (Figure 3.7); suggesting success in the scaling analysis.

The sigmoid shape of this curve suggests that it may be modeled by the cumulative distribution of a probability function. The idea for such parameterization was guided by Chang and Rudy (1993) who, after scaling ozone by  $NOx^{0.5}$  (and normalizing by a constant), found that the function:

$$\phi(R) = 1 - \exp \left\{ -aR^b \right\} \quad (3.19)$$

fit their (scaled but not dimensionless) data well. This expression, chosen because of its simple functional form (Chang and Rudy, 1993), can be expressed as the cumulative distribution of a Weibull probability distribution after the transformation  $b = \alpha$  and  $a = \beta^{-\alpha}$  i.e.:

$$\phi(R) = 1 - \exp \left\{ -(R/\beta)^\alpha \right\} \quad (3.20)$$

That is, without realizing it, they found that a Weibull distribution was a suitable choice for modeling their results.

### 3.4.6 Weibull Distribution

I have also chosen to use a Weibull distribution to parameterize my similarity relationship, not because I believe ozone formation is a Weibull process but rather because the Weibull distribution has a closed form inverse which provides an easy check for the suitability of the model. To check the suitability of the Weibull distribution, the NO<sub>x</sub>-scaled and dimensionless model output must first be normalized. This normalization represent the last of several manipulations of the model output that I perform in order to parameterize the similarity relationship. Figure 3.8 summarizes all these manipulations. I refer to the final scaled and normalized model output as simply the 'scaled data'.

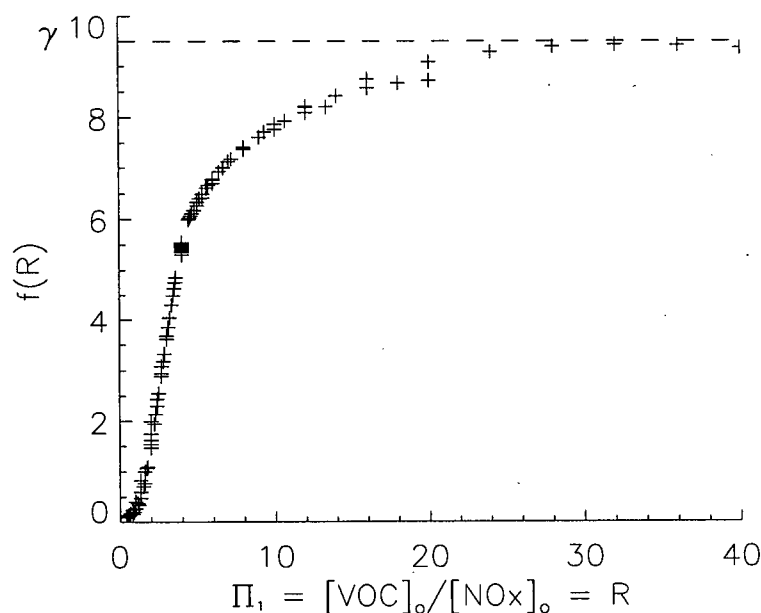


Figure 3.7: Dimensionless ozone scaled by dimensionless initial  $\text{NO}_x^a$  versus ratio of initial precursor concentration ( $R$ ). Model output from RADM2 (Stockwell et al., 1990) simulations using OLT as the sole VOC, a constant temperature of  $25^\circ\text{C}$  and a total dimensionless actinic flux of  $J = 347$ .

Once normalized, the Weibull transformation was applied to the ‘scaled data’:

$$W(f(R)) = \ln \left( \ln \left( \frac{1}{1 - f/\gamma} \right) \right) \quad (3.21)$$

where  $\gamma$  is the normalizing constant based on Eq. (3.18). I will refer to the Weibull transformed ‘scaled data’ and the ‘Weibullized data’. To test the suitability of the Weibull model,  $W(f(R))$  was plotted against  $\ln R$ , expecting that the 100 data points would cluster onto a single straight line.

Figure 3.9 shows the plot of the ‘Weibullized data’ as a function of  $\ln R$ . From this figure, it is evident that the ‘Weibullized data’ collapses not onto **one** but **two** straight lines, which separates the similarity relationship into two regions characterized by a change in slope at  $\ln R = 1.3$  ( $R = 3.7$ ). This shift hints at a change in governing chemical process; perhaps evidence of the change in ozone sensitivity to changing  $\text{NO}_x$  concentration across the ridgeline.

Included in the figure are two boundaries separating the figure into three regions: Region I, lies to the right of the break and regions IIa, IIb to the left. From the Figure, it appears that for small  $\ln R$ , that there is more scatter in the ‘Weibullized data’. The scatter in these low  $\ln R$  values, associated with simulations having low initial OLT concentrations, suggests a different scaling, perhaps one similar to the scaling of the  $\text{NO}_x$ -only systems. The transition is highlighted by the

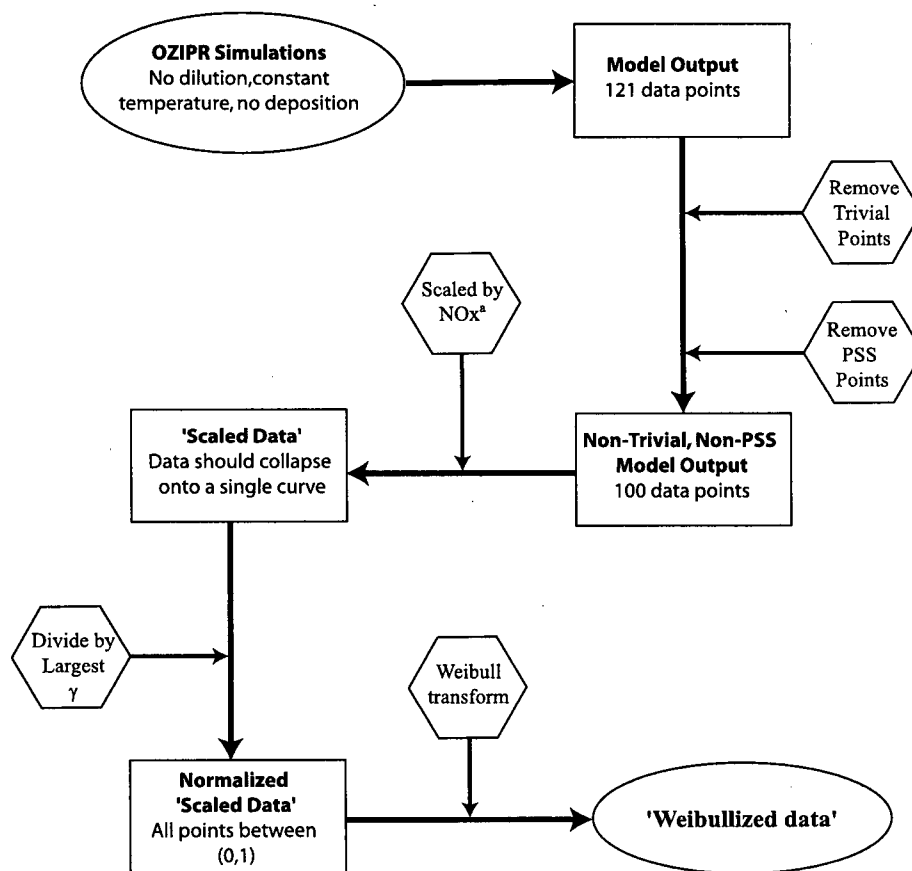


Figure 3.8: Procedure used to prepare OZIPR model output before Weibull transforming.

boundary between regions IIa and IIb. It is difficult to objectively place this boundary and further investigation is required to better define it.

### 3.4.7 Scaling break and Lognormal Parameterization

To show that the scaling break is not a by-product of the Weibull transformation, a lognormal distribution was used to fit the data. To test the effects of using the lognormal distribution to parameterize the similarity function, dimensionless OLT model output was transformed using the inverse error (*ERFI*) and inverse complementary error function (*ERFCI*). Such a transformation will take data drawn from a lognormal distribution and produce a straight line when plotted as a function of  $\ln(R)$ . Figure 3.10 shows the results of the OLT model output after this transformation. The transformed model output clusters around two lines segments with a break occurring at roughly  $\ln(R) \approx 1.4$ . Also shown is the same model output after Weibull transforming. Both transformations show model output clustering onto two line segments with a break at roughly the same  $\ln R$ -value.

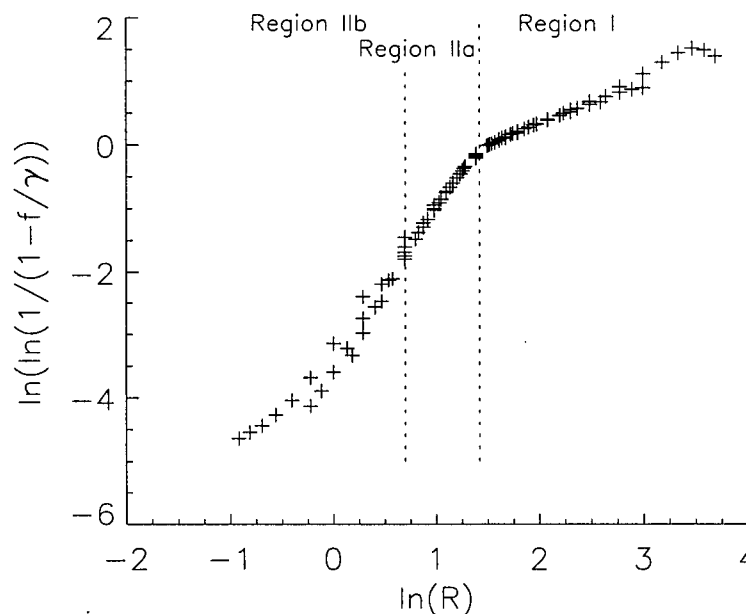


Figure 3.9: Scaled model output after the Weibull transformation. Also shown are two vertical lines separating the plot into three regions. The dashed line at  $R = 3.7$  indicates the shift in slopes and the second dashed lines marks the region of increased scatter.

This suggests the scaling break is not an artifact of the Weibull model. For the remainder of this thesis, I use the Weibull model to parameterize all of my similarity relationships because of its simple form.

### 3.4.8 Analogy with Richardson number and Surface Stability

The form of the 'Weibullized data' in Figure 3.9 suggests strong similarities with another figure also obtained via a scaling analysis. Based on micro-meteorological observations performed in Kansas in the summer of 1968, Businger et al. (1971) examined wind and temperature profiles using dimensional analysis. One of their results was a graph, shown in Figure 3.11, of dimensionless stability (Richardson number ( $Ri$ )) versus a dimensionless height ( $\zeta$ ) defined as:

$$Ri = \frac{g\partial\bar{\Theta}/\partial z}{\bar{\Theta}(\partial\bar{U}/\partial z)^2} \quad \text{versus} \quad \zeta = -\frac{k_v g \overline{w'\Theta'z}}{\bar{\Theta}u_*^3} = \frac{z}{L} \quad (3.22)$$

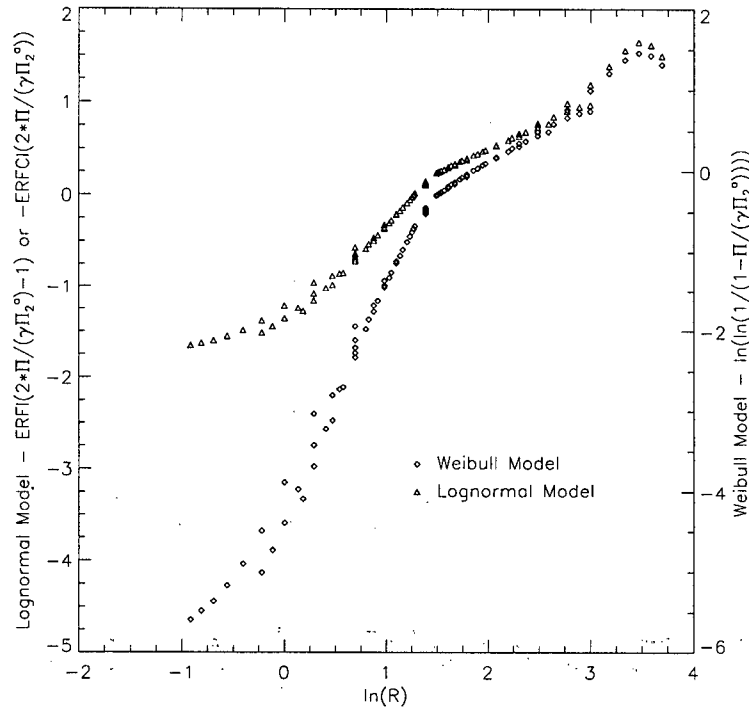


Figure 3.10: Scaled model output after Lognormal and Weibull transformation. ERFI is the inverse error function and ERFCI is the inverse of the complementary error function.

where

- $g$  — local acceleration due to gravity
- $\bar{\Theta}$  — mean temperature
- $z$  — height above ground
- $\bar{U}$  — mean horizontal wind speed
- $k_v$  — von Karman constant
- $\overline{w'\Theta'}$  — kinematic sensible surface heat flux
- $u_*$  — friction velocity
- $L$  — Monin-Obukov dimensionless length scale

In this graph, there are three striking similarities with Figure 3.9. First of all, the scaled data appears to collapse onto a single curve with a similar shape. The collapse of the data onto a common curve indicates that  $Ri$  scales with  $\zeta$ . Secondly, there appears to be a change in the slope of the curve. This can be attributed to a change in the sign of the turbulent kinematic sensible surface heat flux ( $\overline{w'\Theta'}$ ). When  $\overline{w'\Theta'}$  is positive (and  $\zeta$  is negative), turbulence is generated by the surface heating. When the flux goes negative (and  $\zeta$  goes positive), the surface becomes a

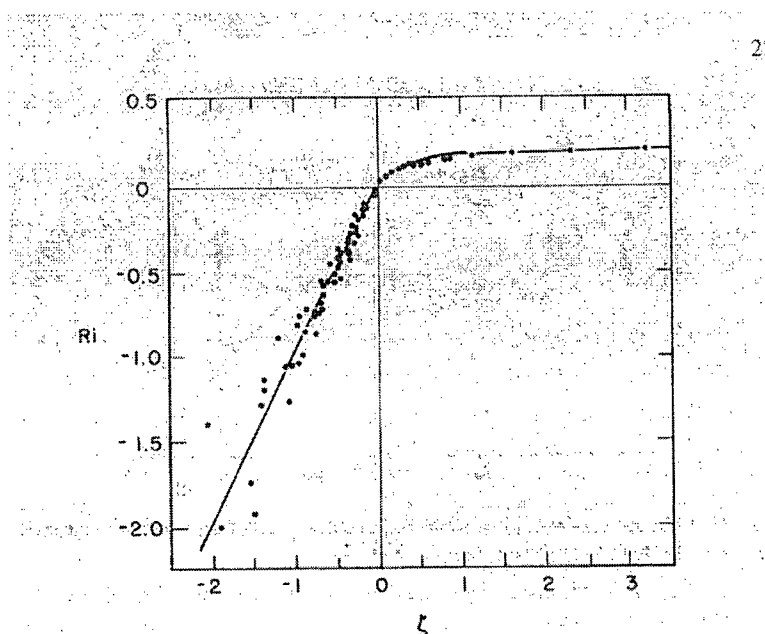


Figure 3.11: Richardson number as a function of stability (taken from *Businger et al. (1971)*).

sink for heat and buoyant turbulent energy is consumed. Hence the change in the turbulent heat flux — from a source to a sink — represents a change in physical process and produces the two distinct line segments. Finally, there is more scatter in the data for the large negative  $\zeta$  values. The increased scatter corresponds to the transition from forced convection to free convection. In the free convection regime, the appropriate velocity scale becomes the convective velocity ( $w_*$ ) and not the friction velocity ( $u_*$ ). This transition is not abrupt but gradual and hence the scaled points gradually become more scattered around the common fitted curve.

The use of  $\zeta$ ,  $Ri$  and  $L$  as scaling parameters is a central idea in micro-meteorology (Arya, 2001). The utility and physical importance of these parameters has been proven in many field studies: the 1968 Kansas Field Program (Businger et al., 1971) and various field campaigns in Australia (Garrat and Hicks, 1990).

### 3.4.9 WEX Model

A parameterization for the similarity relationship, called the WEX model, has been developed to fit the ‘Weibullized data’ and is both continuous and differentiable at the break. WEX is a contraction of Weibull-Exponential because one of the line segments in the Weibull transformed similarity relationship (Weibull plane) has slope less than one. Such a Weibull generalizes the exponential distribution. I will discuss the physical significance of the magnitude of the slopes in chapter 5.

The WEX model is:

$$\phi(R) = f(R)/\gamma = 1 - \exp \left\{ -\lambda (R/\beta)^{\alpha(R)} \right\} \quad (3.23)$$

$$= WEX(R; \alpha_1, \alpha_2, \beta, \lambda) \quad (3.24)$$

where the exponent  $\alpha(R)$  is a function of  $R$ :

$$\alpha(R) = \left( \frac{\alpha_2 - \alpha_1}{2} \right) \tanh(R - \beta) + \left( \frac{\alpha_1 + \alpha_2}{2} \right)$$

giving an expression for maximum ozone concentration:

$$\frac{[O_3]_{max}}{j_{av}/k_{NO}} = \left( \frac{[NOx]_o}{j_{av}/k_{NO}} \right)^a f(R) \quad (3.25)$$

In this model  $(\alpha_1, \alpha_2)$  represent the slopes of the two line segments in the Weibull plane and  $R = \beta$  is the R-value at their matching point. The parameter  $\lambda$  is related to the value of the 'Weibullized data' at  $R = \beta$ . When  $\alpha_1 = \alpha_2$  and  $\lambda = 1$ , the Weibull is recovered. There are other models used for fitting two Weibull functions to curves which show a break or 'dogleg'. Such curves arise frequently in the field of reliability engineering where failure rates often shows a characteristic change as a function of age. These models handle the 'dogleg' by several different means: matching two separate distributions at the break (Jiang et al., 1999), using the product of two Weibull curves (Jiang and Murthy, 1997) or using the weighted sum of different Weibulls (Jiang and Murthy, 1995b). While each of these models is capable of capturing the variability of the similarity relationship, the WEX model is a better choice in the present context because:

- It explicitly identifies the location of the break point.
- Regressing of model output to the WEX model is straight forward.
- Its four parameters can be given a physical interpretation (see Chapters 5 and 6).

A description of the various means of fitting two Weibulls is given in Appendix C.

In Figure 3.12, I have plotted ozone isopleths using the OLT OZIPR model output. Isopleths based on the WEX model (dotted lines), with parameter values of:  $\gamma = 9.5$ ,  $a = 0.60$ ,  $\lambda = 0.92$ ,  $\beta = 4.2$ ,  $\alpha_1 = 2.2$  and  $\alpha_2 = 0.72$  have also been included along with a line of constant  $R = 4.2$  (associated with the break). In addition, the ridgeline, as defined by Eq. (3.13) is also drawn. It has a value of  $R \approx 4.7$  and from this figure; it appears that the scaling break seen in Figure 3.9 occurs above the ridgeline. The WEX model gives a good fit to the model output in the VOC-limited region (IIa), around the ridgeline and especially in the NOx-limited region (I). However, in Region IIb the model starts to noticeably diverge from the OZIPR model output.

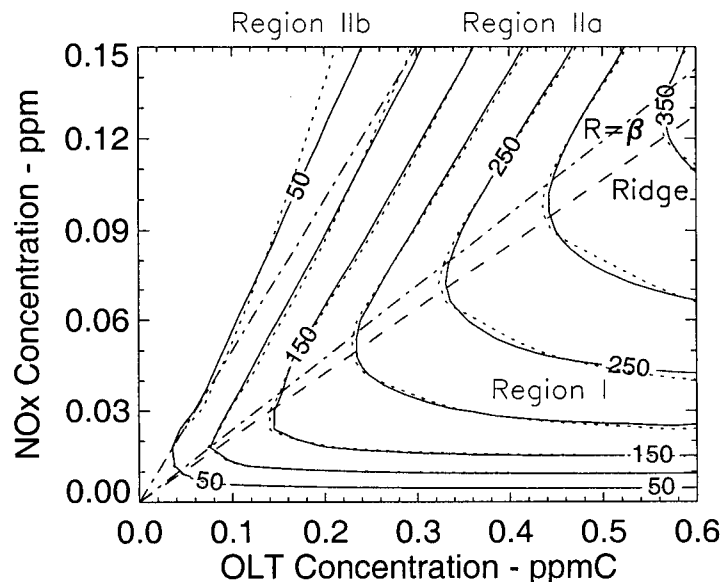


Figure 3.12: Ozone isopleth plot for  $NO_x$ -OLT system. All ozone concentrations in ppb. Solid lines are isopleths from OZIPR model. Dotted isopleths are from the WEX model. Also shown is the ridgeline (dashed line labeled Ridge) and scaling break (dot-dashed line labeled  $R = \beta$ ). Regions I, IIa, IIb have also been marked: Region I is below  $R = \beta$ , Region IIa between  $R = \beta$  and dot-dashed line and Region IIb above this second dot-dashed line.

### 3.4.10 Ozone-precursor relationships in the $NO_x$ Limited Region

The WEX model captures the behaviour of the ozone response surface over a wide range of initial precursor concentrations including: parts of VLR, around the ridgeline and in the NLR. In this final section, I compare the WEX model to other models of ozone formation in the NLR. I begin by presenting a simplification to the model, valid only in the NLR, and then compare it with other models valid in this region.

#### WEX model and $NO_x$ -only scaling

The NLR lies below the ridgeline and the scaling break (Region I in Figure 3.12) where initial VOC concentrations are larger than initial  $NO_x$  concentrations and their ratio ( $R = [VOC]_o/[NO_x]_o$ ) is greater than  $\beta$ . From Figure 3.7 as  $R$  gets large,  $f(R)$  tends asymptotically to  $\gamma$  as  $R \rightarrow \infty$  (where  $\gamma$  is the normalizing constant). The similarity function ( $\phi(R)$ ) is now independent of  $R$  and Eq.

(3.17) can be rewritten as:

$$\Pi_1 \approx \gamma \Pi_2^a \quad (\text{Dimensionless}) \quad (3.26)$$

i.e. the relationship between maximum ozone and initial precursor concentration is approximated by a simple power law. In terms of the original dimensional variables:

$$[O_3]_{max} \approx \hat{\gamma} [NOx]_o^a \quad (\text{Dimensional}) \quad (3.27)$$

$$\text{where } \hat{\gamma} = \gamma (j_{pk}/k_{NO})^{1-a}$$

I call the region of an isopleth diagram where  $f(R)$  is independent of  $R$  and Equations (3.26 and 3.27) hold, the *NOx-only Scaling region (NOS)*. This region is a sub-region of the NLR, away from the ridgeline, where isopleths are nearly parallel to the VOC axis. I now compare Eq. (3.27) with other ozone precursor models. I must point out that the other models do not make the distinction between NLR and NOS. In these models,  $[O_3]_{max}$  refers not to the maximum ozone concentration for a particular simulation but rather the highest maximum ozone concentration (what I call peak ozone concentration) that can be formed for a given initial NOx concentration.

### IER Model

The first comparison is with the IER model (Johnson, 1984) which expresses ozone formation in terms of *Primary Smog Product (PSP)* equal to the amount of ozone formed plus the amount of initial NO converted to  $NO_2$ :

$$[PSP](t) = [O_3](t) - [O_3]_o + [NO]_o - [NO](t) \quad (3.28)$$

where the  $t$  refers to concentration at time  $t$  and  $o$  refers to initial concentrations. Johnson (1984) argues that when PSP is a maximum ( $PSP_{max}$ ), ozone is also at a maximum. With initial ozone concentration zero and final  $NO$  concentration negligible, Eq. (3.28) can be rewritten:

$$PSP_{max} \approx [O_3]_{max} + f [NOx(0)] \quad (3.29)$$

where  $f$  equals the initial ratio of  $NO$  to NOx. Based on extensive smog chamber studies performed at the Commonwealth Scientific and Industrial Research Organization (CSIRO), Johnson (1984) proposed an empirical relationship between maximum PSP and initial NOx:

$$PSP_{max} = \beta [NOx(0)] \quad (3.30)$$

where  $\beta$  was found to be  $4.1 \pm 0.4$  (dimensionless). Using Eq. (3.29), equation 3.30 can be rewritten in terms of maximum ozone concentration:

$$[O_3]_{max} \approx (\beta - f) [NOx]_o \quad (3.31)$$

Model/Reference	Relationship	Parameter Values
Johnson (1984)	$[O_3]_{max} = (\beta - f)[NOx]_o$	$\beta = 4.1$
Blanchard et al. (1999)	$[O_3]_{max} = \beta[NOx]_o^{2/3} - f[NOx]_o$	$\beta = 1.9$ (when using ppm units)
Chang and Rudy (1993)	$[O_3]_{max} = \gamma[NOx]_o^{1/2}$	$\gamma = 1.03$ (when using ppm units)
WEX (for OLT)	$[O_3]_{max} = \hat{\gamma}[NOx]_o^\alpha$	$\hat{\gamma} = \gamma \cdot (j_{av}/k_{NO})^{1-\alpha} = 1.93$ (ppm units) and $\alpha = 0.6$ (for a June 21 <sup>st</sup> LFV simulation)

Table 3.5: Ozone-precursor relationships in the NOx-limited region.

This last expression gives a linear relationship between initial NOx concentration and peak ozone concentration whereas the WEX model (Eq. (3.27)) shows a power law dependence with an exponent of 0.6. The linear trend in Eq. (3.31) has generated concerns because it implies a constant ozone production efficiency (number of ozone molecules produced for each NOx molecule consumed) whereas field studies suggests that this increases as NOx decreases (Blanchard et al., 1994).

### Modification to the IER Model

The IER model has been modified by Blanchard et al. (1999) who used smog chamber data from the University of North Carolina (UNC), the Statewide Air Pollution Research Center (SAPRC) as well as photochemical box model simulations to suggest that Eq. (3.30) be replaced with:

$$SP_{max} = \beta[NOx]_o^\alpha \quad (3.32)$$

where they refer to PSP as *Smog Produced (SP)*. Or, in terms of maximum ozone concentration:

$$[O_3]_{max} = \beta[NOx]_o^\alpha - f[NOx]_o \quad (3.33)$$

where  $\beta = 1.9$  (when using ppm units) and  $\alpha = 0.66$ . While Eq. (3.33) is similar to Eq. (3.27) – both having similar NOx-exponents – Eq. (3.27) does not have the offset term ( $f[NOx]_o$ ).

### Chang and Suzio's Model

Finally, Chang and Suzio (1995) have proposed the following relationship for maximum ozone in the NLR:

$$[O_3]_{max} = \gamma[NOx]_o^{1/2} \quad (3.34)$$

with  $\gamma = 1.03$  (ppm<sup>0.5</sup>). This expression is identical to Eq. (3.27) except for the magnitude of the exponent. However, it will be shown in Chapter 6 that the value of this exponent is sensitive to VOC species.

To summarize, the WEX model predicts, in the NOS regime, maximum ozone concentration to be a function of initial NO<sub>x</sub> concentration only, consistent with Chang and Suzio (1995), Blanchard et al. (1999) and Johnson (1984). However, the WEX model gives different exponents and parameter values. Table 3.5 summarizes the ozone-precursor relationships in the NLR.

### 3.5 Summary

In this chapter, I have introduced the concept of scaling and shown that scaling methods, in various guises, already exist in Eulerian grid based photochemical models. In essence, this research represents an extension of these methods, where I have now parameterized the entire chemical mechanism.

I began my analysis with a NO<sub>x</sub>-only photochemical system and developed a simple relationship for maximum ozone concentration as a function of initial NO, NO<sub>2</sub> concentration, actinic flux (using the peak NO<sub>2</sub> photolysis rate) and temperature (via the temperature dependence of the NO-O<sub>3</sub> titration rate). This relationship compares favourably with an exact mathematical representation.

I then developed a simple parameterization (the WEX model) for maximum ozone concentration as a function initial precursor concentration for a VOC-NO<sub>x</sub> system. The parameterization, when Weibull transformed, exhibits a striking feature (a 'dogleg') which suggests the photochemical system switches governing regimes. The switch coincides closely (but not exactly) with a change in ozone sensitivity to initial NO<sub>x</sub> concentration (the ridgeline on an isopleth diagram).

The WEX model captures the complex dependence of ozone formation on initial precursor concentrations over a wide range: above, below and around the ridgeline. This represents an improvement over similar efforts by Johnson (1984), Chang and Rudy (1993) and Blanchard et al. (1999). These results suggest that over a wide range of initial precursor concentrations, and when viewed from the proper perspective (provided by the scaling analysis), the complex behaviour of an ozone response surface can be simply described.

While this model is successful at predicting maximum ozone concentrations, it raises many interesting questions, namely:

- Can the photochemistry of other VOCs and VOC mixtures be captured by a scaling relationship?
- If so, do they all show a similar 'dogleg' in their similarity relationship?
- How does varying temperature and actinic flux change the similarity relationship?

- Are these results a product of the RADM2 mechanism or are they universal to all chemical mechanisms?
- Are these results consistent with observations?
- What is the range of validity for the WEX parameterization?

Through an investigation of these questions, I hope to build an heuristic understanding of the major factors controlling ozone photochemistry. The next chapter begins this investigation.

## Chapter 4

# Domain of Applicability for the Scaling Relationship

### 4.1 Introduction

In this chapter, I explore ozone-precursor scaling relationships under a variety of conditions. I study the scaling behaviour for a variety of VOCs and VOC mixtures. In addition, to show the scaling behaviour is not an artifact of the RADM2 chemistry, two other photochemical mechanisms are used. I also examine the effects of two different environmental parameters – temperature and actinic flux – on the scaling. I vary the latter by modeling ozone formation for different days of year and different latitudes. To clarify my description of the numerical experiments, I propose the following terminology:

- A *scenario* refers to design conditions common to a number of numerical runs. These include the type of VOC, temperature and chemical mechanism.
- *Test matrix* refers to a set of numerical runs (usually 121 in total but may be more) having common design conditions (given by the scenario) but a range of initial VOC and NO<sub>x</sub> concentrations. A scenario investigating temperature effects might have five test matrices each using a different temperature.
- A *simulation* is a single numerical run with fixed initial VOC and NO<sub>x</sub> concentrations and whose actinic flux ( $J$ ) and temperature ( $T$ ) are given by the test matrix. Test matrices usually have 121 individual simulations.

To explore the universality of the scaling relationship, six different scenarios were designed to isolate the influence of various factors on the similarity relationship. The first scenario examined the influence of different VOCs on the scaling analysis. A variety of VOCs and VOC mixtures were examined. The second scenario controlled for the influence of the chemical mechanisms. OZIPR simulations were run with two different mechanisms: CB-IV (Gery et al., 1989) and a modified version of the SAPRC90 (Carter, 1990) mechanism. The third scenario looked at the

influence of temperature, the fourth Julian date, the fifth latitude while the last examined the effects of both temperature and Julian date. Table 4.1 gives a brief description of the scenarios. Before proceeding with the analysis, I must first clarify the various steps involved in performing the numerical experiments and analyzing the model output.

## 4.2 Scaling Methodology

In this section I briefly outline the steps involved in producing the scaling analysis. Steps include the selection of the simulation conditions, the determination of test matrix size and procedures used to analyze the model output.

### 4.2.1 General simulation conditions

In order to standardize the analysis, all simulations started at 7:00 a.m. and ended at 6:00 p.m. (local daylight savings time). There was no dilution, no deposition and the temperature was held at a constant value (as set out in the scenario) throughout the simulation. The initial fraction of  $NO_2$  to  $NO$  ( $f$ ) was always set at 0.25. No emissions were added; every simulation began with a well mixed charge of VOC and NOx.

### 4.2.2 Determination of test matrix size

As mentioned before, OZIPR creates a test matrix of simulations through the process of independently varying the given (or what I call base) VOC and NOx concentrations. Careful selection of the base concentrations and the matrix size is essential to properly characterizing the scaling relationship. I begin by outlining how OZIPR develops the test matrix.

Imagine a row matrix composed of VOC concentrations ranging from zero to the base value, in equal increments with the number of elements (called nodes) provided by the user. A higher value of nodes leads to smaller the increments and more elements. A matrix of initial conditions is formed from the set of all possible combinations between such a VOC row matrix and an equivalent NOx

Scenario Name	Environmental Conditions	Chemical Mechanism	VOCs
RADM2 Classes and Mixtures	Fixed	Fixed	Varying
Other Mechanisms	Fixed	Varying	Varying
Varying Temperature	Vary $T$ Fixed $J$	Fixed	Fixed
Varying Julian Date	Fixed $T$ Varying $J$	Fixed	Fixed
Varying Latitude	Fixed $T$ Varying $J$	Fixed	Fixed
Varying Temperature and Actinic Flux	Vary $T$ Vary $J$	Fixed	Fixed

Table 4.1: A description of scenarios used to explore the universality of the similarity relationship.

matrix i.e.:

$$\begin{bmatrix} \text{Matrix of initial} \\ \text{VOC}_o \quad \text{NOx}_o \end{bmatrix} = \begin{bmatrix} \frac{[\text{VOC}]_{base}}{nodes - 1} \cdot 0, \frac{[\text{VOC}]_{base}}{nodes - 1} \cdot 1, \dots, \frac{[\text{VOC}]_{base}}{nodes - 1} \cdot (nodes - 1) \end{bmatrix} \quad (4.1)$$

$$\times \begin{bmatrix} \frac{[\text{NOx}]_{base}}{nodes - 1} \cdot 0, \frac{[\text{NOx}]_{base}}{nodes - 1} \cdot 1, \dots, \frac{[\text{NOx}]_{base}}{nodes - 1} \cdot (nodes - 1) \end{bmatrix}^T$$

This matrix has  $nodes \times nodes$  elements. As an example, setting nodes to 11, creates a matrix with 121 ( $[\text{VOC}]_o, [\text{NOx}]_o$ ) pairs with individual initial VOC and NOx concentrations ranging from 0 to the base concentration in 10% increments.

Because of the importance of the ratio of initial VOC to NOx concentration ( $R$ ) in the scaling analysis, the resulting set of R-values is also worth examining. By continuing to exclude simulations where initial NOx is zero (and hence  $R = \infty$ ) and those where initial VOC is zero ( $R = 0$ ) the test matrix produces an ordered set of R-values having the following range:

$$\left\{ \left( \frac{[\text{VOC}]_{base}}{[\text{NOx}]_{base}} \cdot \frac{1}{nodes - 1} \right), \dots, \left( \frac{[\text{VOC}]_{base}}{[\text{NOx}]_{base}} \right), \dots, \left( \frac{[\text{VOC}]_{base}}{[\text{NOx}]_{base}} \cdot \frac{nodes - 1}{1} \right) \right\}$$

$$= \{ R_{base}/(nodes - 1), \dots, R_{base}, \dots, (nodes - 1) \cdot R_{base} \} \quad (4.2)$$

This set has  $(nodes - 1) \times (nodes - 1)$  elements. For example, with nodes set at 11,  $[\text{VOC}]_{base} = 10$  ppb and  $[\text{NOx}]_{base} = 2$  ppb, then  $R_{base} = 5$  and the range of R-values is (0.5, 50). Thus a larger value for nodes produces more simulations and, more importantly, a greater range of R-values. The distribution of R-values found in Eq. (4.2) is addressed in the next section.

### 4.2.3 Selection of base concentrations and number of nodes

In the last section, I examined the range of R-values and initial VOC and NOx concentration in a test matrix for a given number of  $nodes$  and base concentrations. In this section, I examine how these must be chosen in order to best capture any scaling behaviour.

*Why is it important to control the range of initial conditions and R-values?* As it will be shown, some VOCs have a low propensity to react with the  $\text{OH}^\bullet$  and high concentrations are required to produce a fixed amount of ozone. Similarly, some VOCs require a large relative abundance of VOC to NOx (R-value) in order to exhibit NOx-only scaling. To ensure that any analysis captures the full range of VOC oxidation behaviour, I propose the following objectives for  $node$  and base concentration selection:

- The test matrix should have an equal number of simulations on either side of any observed scaling break.

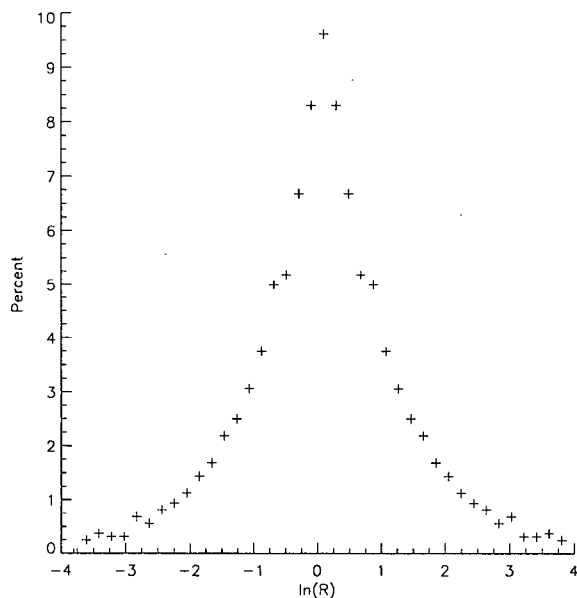


Figure 4.1: Distribution of  $\ln(R)$  when  $nodes = 41$  and  $VOC_{base} = NOx_{base}$ .

- To ensure that the model is not pushed outside of its calibrated range, the maximum modeled ozone concentration must represent realistic concentrations for a polluted urban environment.
- Simulations must include a sufficiently large range of R-values to capture the asymptotic behaviour of the similarity function  $f(R)$ .

To meet the first objective, it is necessary to study the distribution of R-values found in Eq. (4.2). For convenience, I examine the distribution of  $\ln(R)$  (since the scaling break is most evident in the Weibull plane which is plotted as a function of  $\ln(R)$ ). Consider a scenario where both the base VOC and NOx concentrations are  $1.0 \text{ ppb}$  and the number of nodes is 41. In this case, the ratio of base VOC to base NOx ( $R_{base}$ ) is also 1.0. Figure 4.1 shows the fraction of all simulations whose value of  $\ln(R)$  lie within a range spanning  $\ln(R_{base}/nodes)$  to  $\ln(R_{base} \cdot nodes)$ . From the Figure, the distribution is centered around  $\ln(R) = 0.0$  or  $R = 1.0$ ; suggesting that the ratio of base VOC to NOx must equal the expected R-value for the break in order to have an equal numbers on simulations each side of the break. Since the R-value of any scaling break is not known *a priori*, a set of trial simulation must first be performed to provide an estimate of  $R_{break}$ . Meeting this objective places one constraint on the selection of  $[VOC]_{base}$  and  $[NOx]_{base}$ .

Requiring peak maximum ozone concentration be in the range of 100-300 ppb gives a second constraint. This range is representative of elevated but not unrealistically high ozone concentrations for urban environments (National Research Council, 1991) and should not push the chemical

mechanism outside of its intended regime. I use these first two constraints to determine base VOC and NOx levels.

Finally, the third objective determines the number of nodes. In order to use the Weibull transformation, the modeled output must be normalized. The natural normalizing value, the asymptote of the similarity function, requires simulations with sufficiently large R-values. As Eq. (4.2) shows this is determined by nodes. Typically, nodes is set to 11 giving a maximum R-value of  $10 \times R_{base}$ . If, however, a VOC does not show asymptotic behaviour in that range, a larger number of nodes is required. For example, with 41 nodes, OZIPR performs a total of 1681 simulations and allows R-values to be 40 times greater than  $R_{base}$ . In this thesis only nodes sizes of 11 and 41 are used.

The above three constraints determine the selection procedure for  $[VOC]_{base}$ ,  $[NOx]_{base}$  and nodes. Figure 4.2 outlines this procedure and shows the iterative nature of the selection process. In several instances (most notably for formaldehyde), R-values for asymptotic behaviour required more nodes than the OZIPR maximum of 51. In these instances, nodes was set to 41 and base VOC and NOx concentrations were adjusted to provide reasonable peak ozone concentrations as well as a fair distribution of R-values.

#### 4.2.4 Determining WEX parameters

To objectively determine optimal values for the six WEX parameters ( $\gamma, a, \alpha_1, \alpha_2, \beta, \lambda$ ) a computer program was used. The code required initial values for the parameters which was supplied, through visual inspection of the data, from a spreadsheet program. From this first guess, the code individually varied only five of the parameters ( $a, \alpha_1, \alpha_2, \beta, \lambda$ ), searching to minimize the RMSE between OZIPR model output and WEX values. The sixth parameter ( $\gamma$ ) was calculated using the selected NOx-scaling power ( $a$ ). For each trial value of  $a$ ,  $\gamma$  was adjusted so that the maximum scaled model output was 0.99. This value was chosen because the Weibull transformation is quite sensitive to values very close to 1.0 (with 1.0 being mapped to an infinite value). Standardizing the maximum scaled ozone value also ensures a means of comparing the Weibull plots for different VOCs. To optimize the fit, each of the five parameters was varied by  $\pm 10\%$  around its first guess value. Due to scatter in some of data sets, it was decided that fitting around the ridgeline was to be a priority since this region present the most important area for identifying ozone sensitivity. To this end, for every trial  $\beta$ -value, only R-values encompasses all but the lowest 10% and highest 10% of the R-values were used to fit the data. While only 80% of the OZIPR points were used for fitting, *all* points were used to quantify the ability of the WEX model to parameterize the similarity relationship.

### 4.2.5 Statistical measures of agreement

I use the correlation coefficient between the OZIPR and WEX ozone values as a measure of agreement between the two as well as the root mean square error between WEX- and OZIPR-calculated maximum ozone concentrations for each simulation:

$$RMSE = \sqrt{\frac{1}{(nodes - 1)^2} \sum_{i=1}^{(nodes-1)^2} (OZIPR_i - WEX_i)^2} \quad (4.3)$$

### 4.3 Scenario I – RADM2 VOC Classes

To determine if the OLT scaling behaviour holds for other VOCs, a systematic analysis was performed using the RADM2 (Stockwell et al., 1990) mechanism. This mechanism does not explicitly

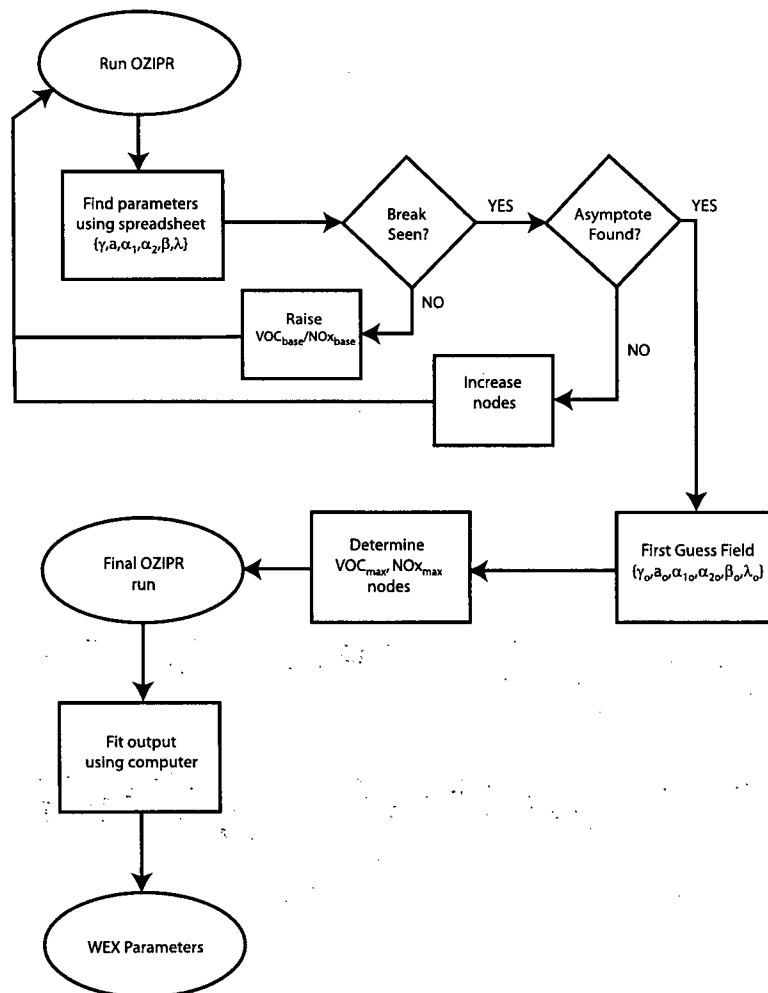


Figure 4.2: Schematic of steps used to find WEX parameters.

model every VOC since, as mentioned before, this could entail modeling over 20000 different species (Dodge, 2000). Instead, RADM2 has 14 classes of VOCs and assumes the oxidation behaviour of any VOC can be treated by one of these classes or by a linear combination of them (the 14 classes can be thought of as representing a set of basis vectors for the vector space of VOC compounds). These classes include methane, ethane, three classes for higher alkanes, ethene, terminal alkenes (alkenes with their double bonds at the end of the molecule), alkenes with internal double bonds, two classes for aromatics, aldehydes and ketones, isoprene and finally non-reactive VOCs. So, to explore the scaling behaviour of VOCs in general, a scaling analysis was performed on each of the RADM2 classes. As well, a scaling analysis was performed on two VOC mixtures considered to be representative of polluted urban environments.

For each VOC class and the two mixtures, I present results using two figures. The first figure shows model output and corresponding WEX model after Weibull transforming and in the second, results are presented in the more conventional isopleth diagram. For brevity, only a sample of the figures, covering the range of agreement between model output and WEX model, is presented in this chapter with the remaining figures placed in Appendix E.

### 4.3.1 Simulations with Methane, Ethane and Higher Alkanes

Alkanes are the most abundant VOCs found in urban environments (National Research Council, 1991). They are relatively unreactive, have low deposition rates and hence can be transported long distances (Stockwell et al., 1990). On average, methane comprises 13% of VOC emissions (moles C) while non-methane alkanes comprise 46% (Stockwell et al., 1990). To handle alkane reactions, RADM2 uses five categories. Methane (CH<sub>4</sub>) and ethane (ETH) are treated explicitly with the remaining higher alkanes sorted into three classes according to their  $OH^\bullet$ -reactivity. I did not perform a scaling analysis on methane due to its low  $OH^\bullet$ -reactivity. Its chemical lifetime is in the order of years – too long to be of importance at the urban or regional scale (Finlayson-Pitts and Pitts, 1999). It is worth mentioning however, that methane is of prime importance in the production of tropospheric ozone at the global scale. Alkanes with an  $OH^\bullet$ -reactivity less than  $5 \times 10^3 \text{ ppm}^{-1} \text{ min}^{-1}$  are represented by HC3. This class includes propane, n-butane and alcohols like ethanol and methanol. The class HC5 represents alkanes with a reactivity between  $5 \times 10^3 \text{ ppm}^{-1} \text{ min}^{-1}$  and  $1 \times 10^4 \text{ ppm}^{-1} \text{ min}^{-1}$  and includes pentanes and hexanes while those with a reactivity greater than  $1 \times 10^4 \text{ ppm}^{-1} \text{ min}^{-1}$  are represented using HC8. This last group includes long chained alkanes like n-heptane.

Due to their low reactivity, the alkanes were the hardest to scale. In Figure 4.3A, I plot the ‘Weibullized’ ETH model output (+) and corresponding WEX parameterization (solid line) as a

function of  $\ln(R)$ . In Figure 4.3B, I replot the same results as an isopleth diagram where solid lines give OZIPR isopleths (in ppb) and the dotted lines give WEX-based isopleths (also in ppb). The two dashed lines in this Figure locate the respective ridgelines based on Eq. (3.13). Similar plots for HC3, HC5 and HC8 can be found in Appendix E.

For both ETH and HC3, I had to set the number of nodes to 41 in order to capture the asymptotic behaviour and keep an equal number of simulations on both sides of the scaling break. For ETH, the scaling break appears to occur at  $\ln(R) \approx 6.5$  but it is not sharp. There appears to be more scatter in the ‘Weibullized data’ for simulations with  $\ln(R) < 6$ . For ETH and HC3, the best choice for the NO<sub>x</sub>-exponent ( $a$ ) appears to depend on the R-value. For ETH, when the exponent is chosen to be 0.7, the ‘Weibullized data’ scales for  $\ln(R) > 7$  (Figure 4.3A) but for  $\ln(R) < 7$  the correct choice appears to be -0.2 (Figure 4.4). However, choosing this lower value destroys any scaling at high R-values.

The WEX parameterization for both ETH and HC3 produce isopleths that fit the OZIPR model output in the NO<sub>x</sub>-limited region (NLR) and up to the ridgeline (Figures 4.3B and E.1A). At the ridgeline and in the VLR, WEX isopleths diverge from OZIPR isopleths. For ETH and especially HC3 it is difficult to identify a sharp break in the Weibull plots. It appears that the Weibull plots for these VOC classes are composed of a family of curves each having a break at different R-values (this is especially evident in Figure 4.4). Furthermore, the OZIPR ridgelines for these classes are curved lines whereas the WEX model produces a straight ridgeline. HC3 has a more curved OZIPR ridgeline and also shows greater scatter in its ‘Weibullized data’. Therefore, I suspected that scatter for these two classes occurs for two reasons:

- The ridgeline cannot be characterized by a line of constant R (a straight-line).
- The NO<sub>x</sub>-limited and VOC-limited regions have different NO<sub>x</sub>-scaling exponents ( $a$ ).

Neither HC5 nor HC8 appear to show scaling (Figures E.2A and E.3A). It is difficult to understand why these classes do not show scaling while ETH and HC3 do. As well, the HC5 and HC8 classes produce progressively less ozone than ETH and HC3. Since that the major chemical loss for alkanes is through  $OH^\bullet$ -attack (Atkinson, 2000), and that the  $OH^\bullet$  radical abstracts the most weakly bound hydrogen atom (Seinfeld and Pandis, 1998), then one would expect that higher alkanes, with more secondary hydrogen atoms, would produce higher ozone levels. Yet the HC8 class produces no more than 10 ppb of ozone. It is likely that greater NO<sub>x</sub> and peroxy radical loss, through the formation of organic nitrates, accounts for this discrepancy.

The ETH class is representative of VOCs that the WEX model cannot parameterize very well. The HC5 and HC8 classes the model cannot parameterize at all.

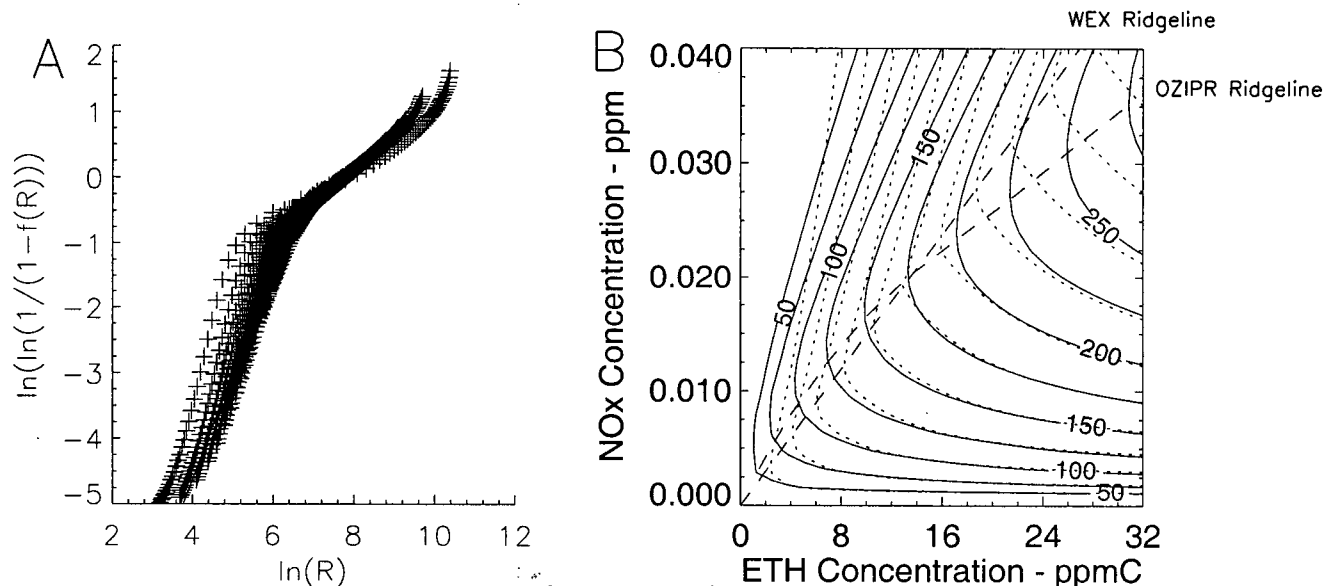


Figure 4.3: Weibull transformed OZIPR model output (+) for ETH as a function of  $\ln R$  (figure A). Solid line is WEX model. In Figure B, the same results are plotted in the more conventional form of ozone isopleths (in ppb) with OZIPR model output in solid lines and WEX model in dotted lines. The two dashed lines refer to ridgelines for the OZIPR isopleths and the WEX model. Both were found by locating the region where ozone shows no sensitivity to changing  $NO_x$ .

#### 4.3.2 Simulations with Ethene and other Alkenes

Alkenes are hydrocarbons with a single double bond. They have higher  $OH^\bullet$ -reactivities than alkanes and react readily with both ozone and the nitrate radical ( $NO_3^\bullet$ ) (Atkinson, 2000). Alkenes are constituents of gasoline and vehicle exhaust emissions (Seinfeld and Pandis, 1998). Isoprene, emitted naturally from vegetation provides another source of alkene emissions (Atkinson, 2000). Alkenes account for about 10% of nonmethane VOC concentrations in some US cities (Chameides et al., 1992). The simplest alkene, ethene ( $C_2H_4$ ), is treated explicitly by RADM2 (as OL2) because it has the lowest alkene  $OH^\bullet$ -reactivity and is typically found in higher concentrations than the other alkenes (Stockwell et al., 1990). As mentioned before, propene and other terminal alkenes are represented by the OLT class. Alkenes with an internal double bond are represented by OLI. Finally isoprene (ISO) is treated as a separate species whose reaction products are assumed to be the same as propene. Weibull transformed OZIPR model output as well as isopleth plots, for alkene classes OLI, OLT, OL2, are shown in Figures E.4, E.5 and 4.5 respectively.

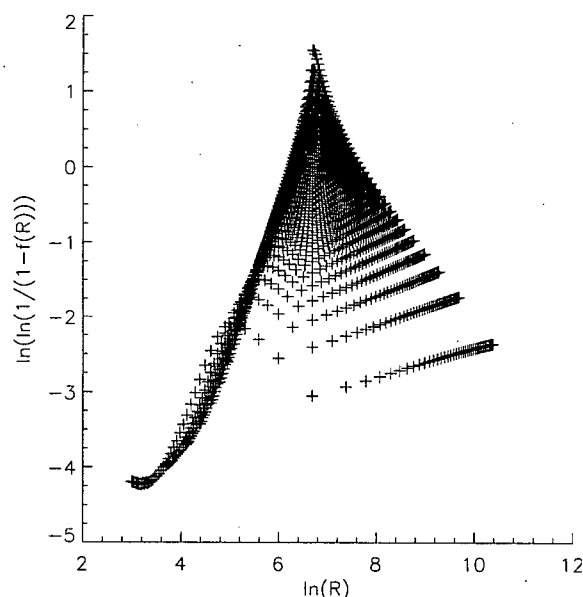


Figure 4.4: Weibull transformed ETH model output versus  $\ln R$  when  $NO_x$ -scaling exponent is (a)- 0.2. Changing the exponent to this lower value produces better scaling for  $\ln R < 7$  but destroys the scaling for  $\ln R > 7$ .

The hardest class to fit was OL2 because of its lower  $OH^\bullet$ -reactivity. For OL2, nodes was set to 41 since its scaling break occurs at  $R = 4.9$  while its asymptotic behaviour occurs at  $R \approx 200$ . Its Weibull plot (Figure E.4A) showed a fair degree of scatter below the break but less above. The WEX parameterization fits the OZIPR isopleths in the NLR and VLR but deviates around the ridgeline and for very low R-values (Figure E.4B).

The 'Weibullized data' for both OLT (Figure E.5A) and OLI (Figure 4.5A) were well captured by the WEX model with OLI showing a slightly better fit. Both classes required only 11 nodes. As seen from the isopleth plots (Figures E.4B and 4.5B), the WEX model fits the two classes well in both the NLR and VLR. The fit along the ridgeline is best for OLI but both are better than OL2. Both classes seem to show a second break at high R-values. For OLI, it appears that the 'Weibullized data' shows another break with a downward trend at  $\ln R \approx 3$ . I suspect this marks the beginning of a new regime where alkene+ $O_3$  reactions are important. This new trend, impossible to see on an isopleth diagram because ozone isopleths diagrams compress the response surface along the VOC axis at high R-values, warrants further study.

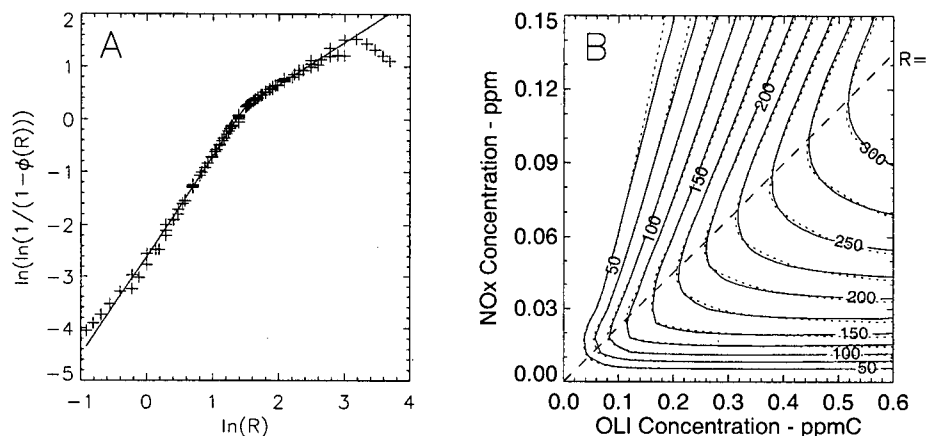


Figure 4.5: Weibull transformed OZIPR model output (+) for OLI as a function of  $\ln R$  (figure A). Solid line is WEX model. In Figure B, the same results are plotted in the more conventional form of ozone isopleths (in ppb) with OZIPR model output in solid lines and WEX model in dotted lines. The dashed line represents the scaling break  $R = \beta$ .

## Second Break

To explore this second break, the OLI simulations were rerun using 41 instead of 11 nodes with the resulting range of R-values now extending from  $1/40^{\text{th}}$  to 40 times the break (compared with  $1/10^{\text{th}}$  to 10 times in the original simulations). The Weibull plot for this larger data set is shown in Figure 4.6A where the WEX model (regressed against the *original* 11-node simulation) has been over plotted. The most important feature in this Figure is the more pronounced break in the 'Weibullized data' for  $\ln R > 3.0$  and the upward curvature for  $\ln R < -1.0$ . Both trends suggest the appearance of new scaling regimes. Values of  $\ln(R) > 3.5$  correspond to model output from simulations where the initial  $[OLI]_o$  to  $[NOx]_o$  ratio is greater than 33. At this ratio of OLI to NOx, maximum ozone concentration is strongly affected by the reaction  $OLI + O_3$ . While this regime hints at the limits to the scaling analysis, it does not represent realistic conditions for a polluted urban environment and so no attempt will be made to better understand the variability in this region.

While I was mainly interested in the second break at large R-values, increasing the number of nodes reveals a second trend, occurring at low R-values which also suggest a new scaling regime. This region represents a middle ground between NOx-only photochemistry (no VOCs and  $R = 0$ ) and an urban environment with high VOC concentrations (and moderate to high R-values). This middle ground likely has a photochemical behaviour similar to the remote or background troposphere. While it is not the intention of this thesis to study ozone photochemistry in this

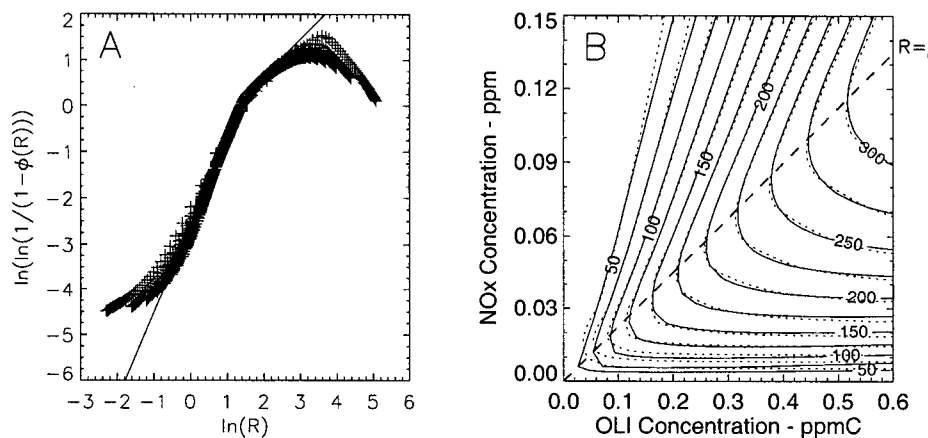


Figure 4.6: Weibull transformed OZIPR model output (+) for OLI as a function of  $\ln R$  (figure A). The same initial conditions were used to produce these simulations as in Figure 4.5 but with 41 nodes. The model output has been scaled by a larger  $\gamma$  value (8.25 versus 8.03) to accommodate slightly larger asymptotic values. The solid line is the WEX model. In Figure B, the OZIPR isopleths (solid lines and in ppb) based on the 41-node simulations whereas the WEX isopleths (dashed lines) are based on the 11 node regression. The dashed line represents the scaling break  $R = \beta$ .

region, the appearance of this trend (and the second break) raises important questions:

- What is an appropriate range for VOC, NO<sub>x</sub>, R-values and O<sub>3</sub> (and environmental conditions as well) needed to capture the variability of maximum ozone concentration in a polluted urban environment?
- Over what range of VOC, NO<sub>x</sub>, R-values and O<sub>3</sub> does the scaling analysis hold?

In essence, these questions are similar to the objectives set out to characterize the Weibull plots. Namely, precursor and ozone ranges should be set so they represent physically reasonable situations. Furthermore, since the ridgeline represents the region of greatest interest to policy makers (due to different ozone abatement strategies on either side), characterization of the ridgeline and regions immediately above and below should be of prime importance in development of a control surface. This suggests the ridgeline should be centered as nearly as possible along the main diagonal (1 : 1 line) of an isopleth diagram; requiring that ratio of maximum VOC to NO<sub>x</sub> equal the R-value of ridgeline. When the R-value of the break ( $\beta$ ) is close to the R-value for the ridgeline, the above constraint is consistent with the selection criteria developed for *nodes* and  $R_{base}$ .

In Figure 4.6B, I have plotted ozone isopleths using the WEX model (dotted isopleths) and using

OZIPR model output from the 41-node simulation where the six WEX parameters were found by a regression to the 11-node simulation. Again, the WEX model captures maximum ozone variability in the NLR, around the ridgeline and in parts of the VLR. Compare this to Figure 4.6A where the same WEX parameterization (based on the same model output) appears to show a much poorer fit. The difference is that in Figure 4.6A, extreme R-values are accentuated by the logarithmic axis, whereas in 4.6B, these regions of extreme R-values are compressed. This is best understood by examining Figure 4.7. In this Figure, OLI isopleths along with lines of constant  $R$  corresponding to:  $R_{break}$ ,  $10 R_{break}$ , and  $1/10 R_{break}$  (range R-values for an 11-node simulation) and  $40 R_{break}$  and  $1/40 R_{break}$  (41-node range of R-values) have been plotted. With 11 nodes, simulations with R-values occur in almost the entire quadrant – excluding only one part of the NLR with elevated ozone levels. From a geometrical point of view, moving to simulations with 41 nodes provides only a marginal increase in coverage and then, only in regions well removed from the ridgeline. This suggests, that in most instances, 11-node simulations are sufficient to characterize the dependence of maximum ozone on its precursors. Furthermore, since the region of interest is the ridge area, the bounds ( $1/10 R_{break}$ ,  $10 R_{break}$ ) define limits where knowledge of the similarity relationships is most beneficial and where the WEX model should capture ozone variability.

### 4.3.3 Simulations with Aromatics

Aromatic compounds are an important class of VOCs due to their high reactivity and abundance in solvents, gasoline and motor vehicle exhaust (Seinfeld and Pandis, 1998). Their chemistry is quite complex and not completely understood (National Research Council, 1991). The two RADM2 aromatic classes, XYLE and TOLU, both show distinct breaks in their Weibull plots (Figure E.7A and E.6A). XYLE shows more scatter above the ridgeline while TOLU below. Both WEX generated isopleths are in good agreement with the OZIPR results. The XYLE isopleths (Figure E.6B) show more deviation around the ridgeline but produce a good fit for both high and low R-values. TOLU (Figure E.7B) shows better agreement along the ridgeline but has more difficulty at low R-values.

### 4.3.4 Simulations with Carbonyl compounds

Carbonyl compounds have an oxygen atom joined to a carbon atom by a double bond. Two classes of carbonyls are aldehydes and ketones; aldehydes have one alkyl group joined to the carbon containing the oxygen double bond while ketones have two. Carbonyls emitted from both anthropogenic and biogenic sources, can also be formed as intermediates in the oxidation of hydrocarbons. Formaldehyde, the simplest aldehyde, a probable human carcinogen (EPA, 1988), is also a regulated emission for New Low Emission Vehicle (NLEV) in the United States (EPA, 2000). RADM2

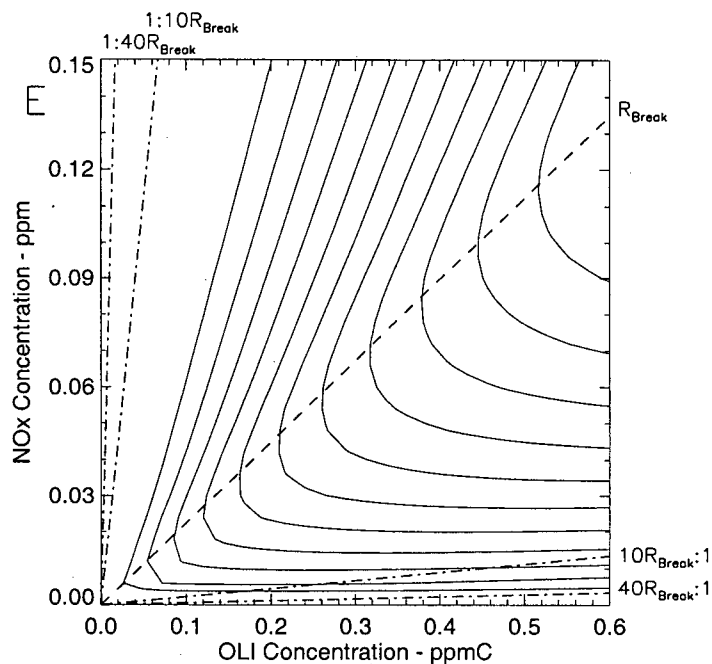


Figure 4.7: Ozone isopleths for OLI versus initial OLI and NO<sub>x</sub> concentrations. Also shown is the line  $R = \beta$  and lines corresponding to:  $10\beta$ ,  $1/10\beta$ ,  $40\beta$ ,  $1/40\beta$ .

uses three chemical classes to model carbonyls: formaldehyde (HCHO) is modeled explicitly, higher aldehydes by ALD and KET for all ketones.

Formaldehyde proved challenging to scale. Its break occurred at  $R = 4.4$  but did not show asymptotic behaviour until an R-value around 600. While very reactive, this long gap between break and asymptote is similar to behaviour shown by less reactive ETH and OL2. Properly modeling this behaviour (as set out by the objectives in section 3.2.3) would require 136 ( $600/4.4$ ) nodes or almost 20000 ( $136^2$ ) simulations – greater than the computational limits programmed into OZIPR. As a compromise, a base VOC to NO<sub>x</sub> ratio was chosen at 15 (well above  $\beta$ ). With 41 nodes, this produced R-values up to 600, including 220 simulations (out of 1600) below the break. The Weibull plot (Figure E.8A) shows the ‘Weibullized data’ clustering on a common curve when the NO<sub>x</sub>-scaling exponent is 0.75. The WEX generated isopleths (Figure E.8B) have the correct shape but underestimate maximum ozone concentrations in the NLR and overestimate them in the VLR.

Both ALD and KET (Figures E.10 and E.9) were easier to characterize; each requiring only 11 nodes. ALD shows perhaps the best fit to the ozone isopleths of all RADM2 classes (Figure E.10B)

with good agreement everywhere except at very low R-values. The KET similarity relationship is also well described by the WEX model but produce isopleths which have a slightly poorer fit in the VLR (Figure E.9B).

#### 4.3.5 Simulations with the Non-reactive class

In the RADM2 mechanism, the non-reactive class (NR) does not react; its sole use is to account for non-reacting or slow reacting VOCs in an urban airshed. This class does not appear to scale by any power of  $NOx^a$  (Figure E.11A) and is of no further concern.

#### 4.3.6 Simulations with VOC Mixtures

Two VOC mixtures, representative of polluted urban environments, were also modeled using RADM2. The first mixture was an Air Resources Board (ARB) modified version of the (Jeffries et al., 1986) analysis of the Lonneman (Lonneman, 1986) 29 city VOC canister study (Tonnesen, personal communication – hereafter referred to as the ‘ARB’ mixture). The second was a mixture that was used by Stockwell et al. (1997) in his comparison of his RADM2 model and the Regional Atmospheric Chemistry Mechanism (RACM) model and referred to as the ‘STOCK’ mixture<sup>1</sup>.

Figures E.12 and E.13 show Weibull and isopleth plots for the ‘ARB’ and ‘Stock’ mixtures. Both show the distinctive scaling break. Both similarity plots show an upward curvature for the very low R-values and a second break in the NLR. The WEX model (Figure E.12A) captures the ARB oxidation behaviour slightly better than the Stock behaviour (Figure E.13A) which shows deviations at high R-values.

#### 4.3.7 Summary of RADM2 simulations

Table 4.2 gives the numerical values of each WEX parameter used to fit each of the 14 RADM2 classes and the two urban mixtures. The RADM2 classes (with the exception of the slow reacting alkanes (HC5 and HC8)) and the two urban mixtures, show scaling. That is, when model output is described using dimensionless maximum ozone ( $\Pi = [O_3]_{max}/(j_{av}/k_{NO})$ ), dimensionless NOx ( $\Pi_2 = [NOx]_o/(j_{av}/k_{NO})$ ) and the ratio of initial VOC to NOx ( $\Pi_1 = [VOC]_o/[NOx]_o$ ), model output over a wide range of conditions show a common variability. Furthermore, when the resulting similarity relationship is Weibull transformed, all of the reactive VOC classes and the two urban mixtures (which I define as the ‘RADM2 scaling classes’) show a distinct ‘dogleg’ at R-values

<sup>1</sup>The speciation was supplied by Dr. Tonnesen (*personal communication*) and is slightly different than the one suggested in Stockwell’s paper.

	Species	$\gamma$	a	$\alpha_1$	$\alpha_2$	$\beta$	$\lambda$	RMSE (ppb)	$r^2$
Alkanes	ETH	22.40	0.70	1.60	0.49	672.0	0.54	15.4	0.99
	HC3	14.36	0.66	1.60	0.73	122.5	0.81	13.5	0.98
	HC5	7.68	0.40	0.65	0.84	1638.0	1.36	18.3	0.77
	HC8	0.45	0.43	0.00	0.00	1370.0	2.63	2.1	0.77
Alkenes	OL2	22.20	0.70	1.80	0.53	4.9	0.40	8.2	0.94
	OLI	8.03	0.57	1.90	0.81	4.5	1.29	2.6	1.00
	OLT	9.53	0.60	2.22	0.72	4.2	0.92	4.2	1.00
Aromatics	TOLU	7.77	0.48	3.10	0.69	10.1	1.29	7.0	1.00
	XYLE	7.57	0.56	1.92	0.44	5.3	1.61	6.5	1.00
Carbonyls	HCHO	40.64	0.75	1.50	0.60	4.4	0.14	9.8	1.00
	ALD	7.48	0.53	1.73	0.54	5.2	1.69	3.4	1.00
	KET	7.71	0.59	2.84	0.62	15.3	1.04	6.2	0.98
Unreactive	NR	0.16	0.35	0.00	0.00	5.0	3.00	0.3	0.98
Mixtures	ARB	8.16	0.58	2.34	0.63	8.5	1.40	3.6	1.00
	STOCK	8.15	0.57	2.68	0.59	9.4	1.40	4.5	1.00

Table 4.2: Values of the six WEX parameters for the RADM2 (Stockwell et al., 1990) classes and two urban mixtures.

near the ridgeline, suggesting that this kink is associated with a change in governing chemical process. A discussion about the significance of each parameter and its relationship to the underlying photochemical processes is postponed until the next chapter. The next section looks at ozone scaling relationships using different chemical mechanisms.

## 4.4 Scenario II – Other Mechanism

To test whether the scaling is an artifact of the RADM2 mechanism, two different chemical mechanisms were used to simulate ozone formation: CB-IV and SAPRC. These two methods use entirely different approaches to condensing the photochemistry and so observation of ozone scaling from each will strengthen the premise that complex photochemical processes can be described using a small set of variables – at least to the extent that numerical models capture the chemical processes.

### 4.4.1 CB-IV Mechanism

Grid based Eulerian photochemical models perform repeated chemical calculations at thousands of grid points at every time step. This requires a condensing of the chemistry into a compact form. There are two main methods to achieve this condensing: lumped molecule and lumped structure approach.<sup>2</sup>

The carbon bond mechanism, developed in 1976 by Systems Applications International, is an example of the lumped structure approach. In this approach, each VOC is broken into smaller reaction elements based on the type of carbon bonds it contains. For example, most single-bonded carbon atoms are treated using a carbon atom surrogate (PAR) and double-bonded carbon atoms

<sup>2</sup>In essence this thesis is a further condensing of these (condensed) mechanisms through a scaling analysis.

Parameter	RADM2	CB-IV
$\gamma$	8.2	8.3
$a$	0.58	0.62
$\alpha_1$	2.3	2.4
$\alpha_2$	0.63	0.52
$\beta$	8.5	9.6
$\lambda$	1.4	1.2

Table 4.3: A comparison of WEX parameter values for the ARB mixture using the RADM2 and CB-IV chemical mechanisms.

using a two carbon surrogate called OLE. In this way, a simple alkane like n-butane would be represented by four PAR groups based on its four alkyl groups. Similarly, propene with one alkyl group and one double bond is represented by a single PAR and OLE group. This approach captures VOC oxidation behaviour with fewer surrogate species than with the lumped molecular approach, is more compact and more easily implemented in large grid-based Eulerian photochemical models (Gery et al., 1989).

The current version of the mechanism is called CB-IV (Gery et al., 1989). Two simulations were run using CB-IV. The first used a single PAR and single OLE (to represent propene) and the second simulated the ARB urban mixture used in the RADM2 simulations with Dr. Tonnesen providing the speciation (*personal communication*). Figures E.14 and E.15 show the Weibull and isopleths plots for the PAR+OLE and ARB simulations. Both show the characteristic ‘dogleg’ in the Weibull plot and both have WEX-generated isopleths capturing the modeled ozone variability (Figures E.14B and E.15B). Table 4.3 lists WEX parameters used to fit the RADM2 and CB-IV model output for the ARB mixture.

#### 4.4.2 SAPRC-90 Mechanism

The lumped molecule approach uses particular organic compounds or generalized species to represent organics of similar oxidation characteristics (Dodge, 2000). RADM2 is an example of a lumped molecule approach. Another is the Statewide Air Pollution Research Center (SAPRC-90) mechanism of (Carter, 1990). Unlike RADM2, in this mechanism users can modify both the kinetic and mechanistic parameters of the organic chemistry. A condensed version of the SAPRC-90, called COND2243, which contains 54 chemical species and 129 reactions, was tuned for use in the Lower Fraser Valley, B.C. (LFV) by Jiang et al. (1996). This version – called CD2243V2 – was modified to reflect the region’s urban VOC profile (Jiang et al., 1996). Simulations of propene, using the CD2243V2 surrogate OLE1, and a LFV urban VOC mixture, were performed. Both Weibull plots (Figures E.16A and E.17A) are characterized by a scaling break and both WEX models fit the OZIPR isopleths well (Figures E.16B and E.17B).

### 4.4.3 Summary for Scenario II

A scaling analysis has been used to study the oxidation behaviour of different VOCs. With the exception of slow reacting alkanes and non-reacting species, all VOCs show scaling. Additionally, VOC mixtures are also amenable to this method of analysis. Furthermore, when analyzing photochemistry using different chemical mechanisms, maximum ozone shows the same scaling relationships. The WEX model is able to parameterize the scaling relationships for these VOCs and their mixtures. However, to conclude this exploration of the universality of ozone scaling, the influence of two key environmental conditions – temperature and actinic flux – must still be examined.

## 4.5 Scenario III – Varying Temperature

To explore the sensitivity of the scaling analysis to temperature, four OZIPR simulations were performed. Each had a different test temperature but all had the same actinic flux. The simulations used the RADM2 mechanism with OLT as the sole VOC. The base OLT concentration was 0.6 ppm, the base NO<sub>x</sub> was 0.15 and 11 nodes were used. Each simulation used an actinic flux appropriate to Vancouver on June 21<sup>st</sup>. The four test temperatures were 20, 25, 30 and 35°C which were held fixed throughout each simulation.

To begin the analysis, maximum ozone and initial NO<sub>x</sub> concentrations were scaled by  $j_{av}/k_{NO}$  where, due to its temperature dependence, a different value of  $k_{NO}$  was used for each simulation. This temperature dependence was determined using the RADM2 rate expression (Stockwell et al., 1990):

$$k_{NO} = 2490 \exp\{-1400/T\} \quad (4.4)$$

where  $k_{NO}$  has units of  $\text{ppm}^{-1}\text{min}^{-1}$  and temperature ( $T$ ) is in Kelvin.

Next, a common NO<sub>x</sub>-scaling exponent (found by inspection using a spreadsheet program and subsequently refined using a computer program) was used to scale the model output and is plotted in Figure 4.8A. This figure shows a family of four curves where each curve tends to a different asymptote with larger asymptotic values corresponding to the higher test temperatures. To plot these curves in the Weibull plane, the asymptotic value for the  $T = 35^\circ\text{C}$  curve was used to normalize all four sets of 'scaled data'. These were then Weibull transformed and plotted against  $\ln R$  (Figure 4.8B). This Figure shows that each curve has its break at roughly the same location ( $\ln R \approx 1.4$ ) with similar slopes both before and after the break but each differentiated by a vertical shift.

To collapse the four curves onto a single curve, a power law dependence for  $\Pi_4$  was tried where it was hoped that for some suitable exponent  $b$ , the four sets of NO<sub>x</sub> and temperature scaled maximum

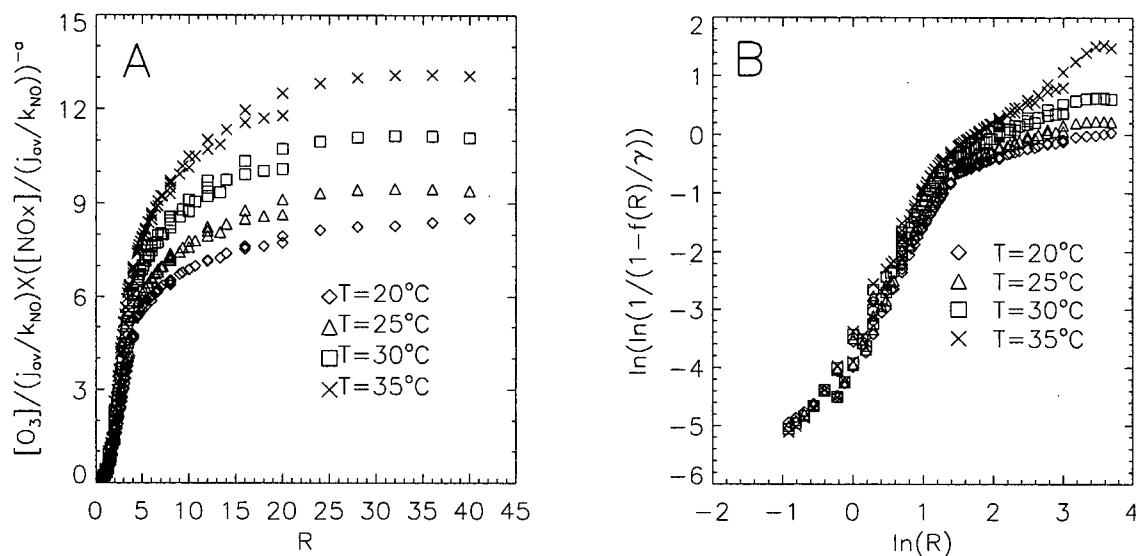


Figure 4.8: *RADM2* simulations using OLT for four different temperatures. Figure A shows NOx-scaled dimensionless maximum ozone concentration versus initial ratio of OLT to NOx concentration while Figure B shows the resulting curves after Weibull transforming.

ozone values should be expressible by a single function of  $R$  i.e.:

$$f(R) = \frac{[O_3]_{max}}{j_{av}/k_{NO}} \left( \frac{[NO_x]_o}{j_{av}/k_{NO}} \right)^{-a} \cdot \exp \left\{ -\frac{E_{OH}}{k} \left( \frac{1}{T} - \frac{1}{T_{ref}} \right) \right\}^{-b} \quad (4.5)$$

To test this hypothesis, the four family of curves shown in Figure 4.8A were further scaled by  $\Pi_4^b$ . Initially a spreadsheet program was used to estimate the best value of  $b$ . This value was then used as a first guess in a computer program which sought to optimize the RMSE between the OZIPR model output and the WEX model. In all, five WEX parameters ( $a, \alpha_1, \alpha_2, \beta, \lambda$ ) and the temperature scaling exponent  $b$  were systematically varied about their initial guess values until no new combinations could further reduce the RMSE. The method found the optimal NOx-scaling exponent to be 0.62 and the temperature exponent ( $b$ ) to be 5.89. Figure 4.9A shows the resulting four Weibull curves after scaling by  $\Pi_2^a$  and  $\Pi_4^b$ . The curves have collapsed onto a common curve with some scatter for both small and large values of  $\ln R$ . After mapping back to the similarity plane (Figure 4.9B), the family of curves has collapsed onto a single similarity relationship, with common asymptote although, again, there is some scatter in for the higher  $R$ -values.

#### 4.5.1 Gross Influence of Temperature On Maximum Ozone Concentration

In general, the system of photochemical reactions modeled by *RADM2* comprises over 150 chemical reactions each with its own temperature sensitivity. These sensitivities can be either positive and

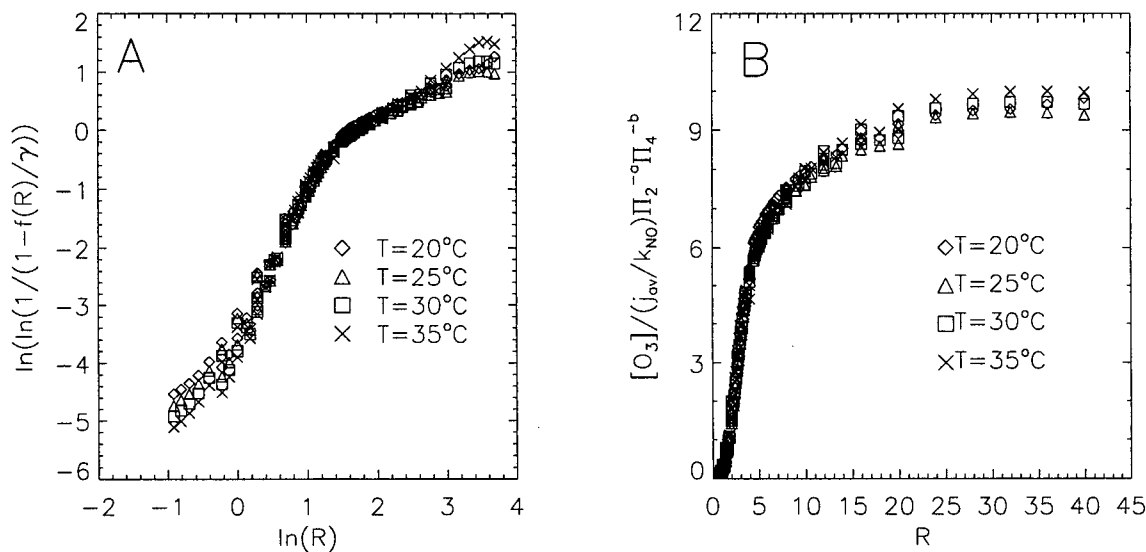


Figure 4.9: Weibull transformed dimensionless model output after scaling by dimensionless temperature  $\Pi_4^b$ . Figure A shows model output after Weibull transforming and Figure B shows the resulting similarity relationship.

negative (i.e. show an increasing rate constant with increasing temperature or a decreasing rate constant with increasing temperature). While temperature alters each reaction rate differently, it appears that the gross influence of temperature on maximum ozone concentration can be expressed by a power law involving a single temperature scaling term with an Arrhenius form i.e.:

$$\begin{aligned}\Pi_4 &= \exp\{-E_{OH}/k(1/T - 1/T_{ref})\} \\ &= \exp\{E_{OH}/k/T_{ref}\} \exp\{-E_{OH}/k(1/T)\} \\ &= A \exp\{-E_{OH}/k(1/T)\}\end{aligned}\quad (4.6)$$

Thus, the gross temperature influence ( $\Pi_4^b$ ) shows a positive temperature dependence implying that as temperature increases so does ozone concentrations consistent with statistical analysis of ozone trends (Robeson and Steyn (1990), Burrows et al. (1995)).

## 4.6 Scenario IV – Varying J

This section investigates the effects of varying actinic flux on the similarity relationship. There are many different atmospheric compounds that absorb radiation and enter an excited state. These molecules may subsequently dissociate or return to a less excited state by other means (Seinfeld and

Month	Date	$j_{av}$ (1/1000) s	$J$
September	12	5.152	204
September	2	5.758	228
August	20	6.490	257
August	3	7.247	287
June	22	8.056	319

Table 4.4: Date, average and total actinic fluxes, as measured by  $NO_2$  photolysis rates, for the five RADM2 simulations used to investigate the sensitivity of the similarity relationship on actinic flux.

Pandis, 1998). The dissociation products may react with other compounds or they may themselves undergo photolysis. While the consequences of such photochemical processes is complex, the purpose of this scenario is to quantify the gross influence of changing actinic flux on ozone formation. I accomplish this by performing five OZIPR simulations each at a constant test temperature (298 K) but varying the solar intensity. To measure the actinic flux (i.e. energy added to the system capable of driving photochemical reactions) the cumulative  $NO_2$  photodissociation rate ( $j_{NO_2}$ ) was used:

$$J = \int_{start}^{end} j_{NO_2} dt \quad (4.7)$$

The photodissociation rate coefficient has units  $sec^{-1}$  and so  $J$  is dimensionless. Implicit in this relationship is the dependence of  $j_{NO_2}$  on the solar zenith angle which in turn is a function of local time.

A fourth order polynomial was used to express the RADM2  $NO_2$  photolysis rate as a function of solar zenith angle. Next, expressions for solar zenith angle as a function of location (latitude and longitude) and date were used to express the photolysis rate as a function of local time (Stull, 2000). This allowed total actinic flux levels ( $J$ -values) to be calculated for any day of the year. Five summer dates, chosen to give an equally spaced range of  $J$ -values and encompassing the typical ozone season in Vancouver (Pryor and Steyn, 1995), are given in Table 4.4.

Numerical simulations were run using the RADM2 mechanism (Stockwell et al., 1990) with the OLT class and a base concentration of 0.6 ppm. The base  $NO_x$  concentration was 0.15 and 11 nodes were used.

#### 4.6.1 Parameterizing the similarity relationship

Dimensionless model output for each simulation was scaled by  $([NO_x]/(j_{av}/k_{NO}))^a$  where a common value of  $a = 0.62$  was found to produce the least amount of scatter between all of the five data sets. The resulting curves are plotted in Figure 4.10A. The five curves do not collapse onto a single curve but, again, appear to form a family of curves differentiated by their  $J$ -values. Next, the largest

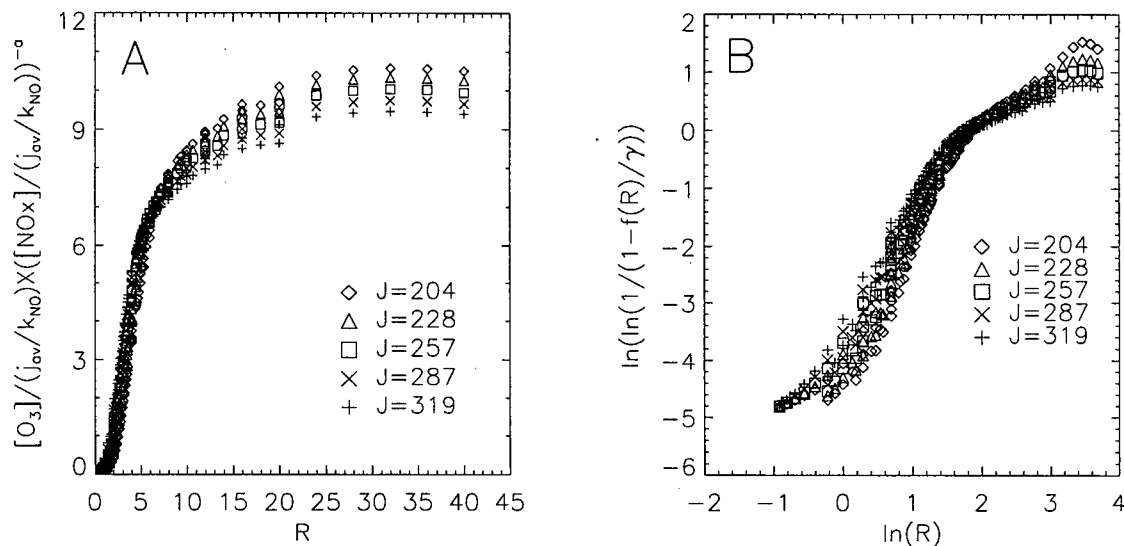


Figure 4.10: Dimensionless model output for the five OLT simulations after scaling by dimensionless initial NO<sub>x</sub> concentration raised to the 0.62 (A) and after normalizing and Weibull transforming (B).

value was used to calculate a common normalizing value  $(\gamma)^3$ . The ‘scaled data’ were then Weibull transformed and plotted against  $\ln R$  as shown in Figure 4.10B. From this figure, it is apparent that there is scatter for both large and small values of  $\ln R$  and any parameterization ( $g$ ) of this ‘scaled data’ must be a function of both  $R$  and  $J$  i.e.:

$$\frac{[O_3]_{max}}{j_{av}/k_{NO}} \left( \frac{j_{av}/k_{NO}}{[NOx]_o} \right)^a = g(R; J) \quad (4.8)$$

#### 4.6.2 Translations and rotations of the similarity relationship

Inspection of Figure 4.10B shows that for small  $\ln R$  values, the curve corresponding to the smallest actinic flux ( $J = 204$ ), lies below the others, while for the larger values of  $\ln R$ , this curve lies above the others. It appears that changing actinic flux results in a rotation about  $\ln \beta$  of the ‘Weibullized data’. To investigate this hypothesis, each curve was shifted so its scaling break occurred at the origin. In terms of the WEX parameters, this amounts to a horizontal translation by  $\ln \beta$  and a vertical translation related to  $\ln \lambda$  (which I call  $\delta(J)$ ): If the Weibull transformed similarity function is:

$$W(g(R; J)) = G(\ln R; J)$$

<sup>3</sup>Again, the normalizing parameter was set at 1/0.99 times the largest value to avoid difficulties using the Weibull transformation.

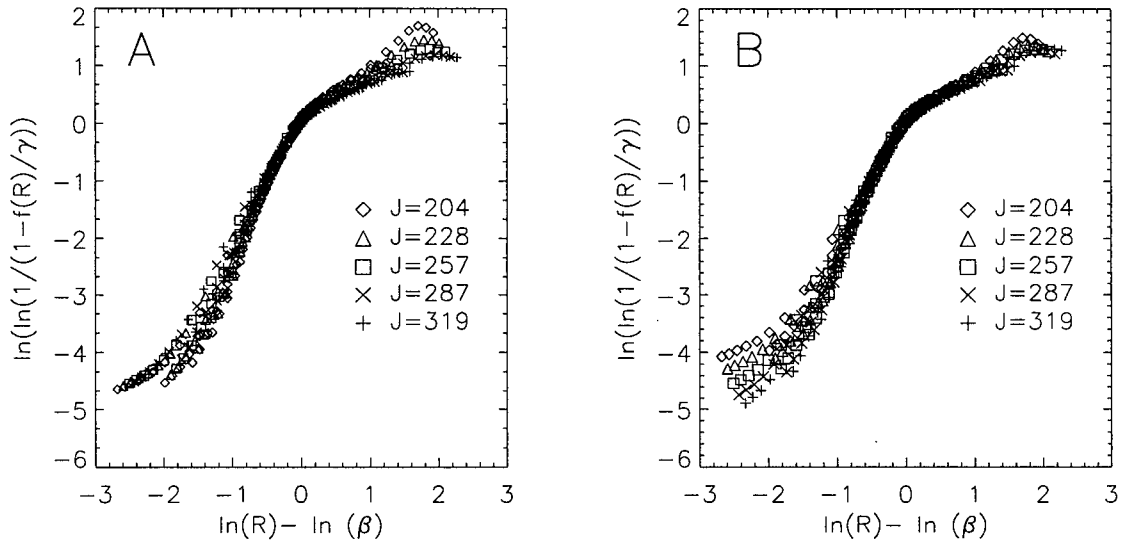


Figure 4.11: *Dimensionless model output for the five OLT simulations after: A) scaling by dimensionless initial NO<sub>x</sub> concentration and shifting to scaling break is at origin and B) further rotating about scaling break.*

then the horizontal translation and vertical translations produce a new function ( $G'(\ln R; J)$ ):

$$G'(\ln R; J) = G(\ln R - \ln \beta(J); J) - \delta(J)$$

Figure 4.11A shows the five curves after the horizontal and vertical translations where each now has its break at the origin. Although the curves are starting to collapse to a single universal curve, there is still evidence the curves have been rotated about their break point.

The transformation necessary to rotate the curves involves multiplying each to a constant. It was found that each curve required a different amount of rotation; dependent on the J-value i.e.:

$$G''(\ln R; J) = k(J) \cdot G'(\ln R; J) \quad (4.9)$$

where  $G''$  represents the rotated similarity function. The  $J = 257$  curve was used as a baseline and all of the others were rotated to match this one. Figure 4.11B, shows the effect of rotations on the five curves. Finally, these rotated and translated curves have been mapped back to the similarity plane and plotted against  $R/\beta$  in Figure 4.12. There is now less variability between the curves and the resulting similarity function is a complex function of both  $R$  and  $J$ :

$$g(R; J) = W^{-1}(k(J) \cdot (G(\ln R - \ln \beta(J)) - \delta(J)))$$

In a subsequent section I will simplify this expression.

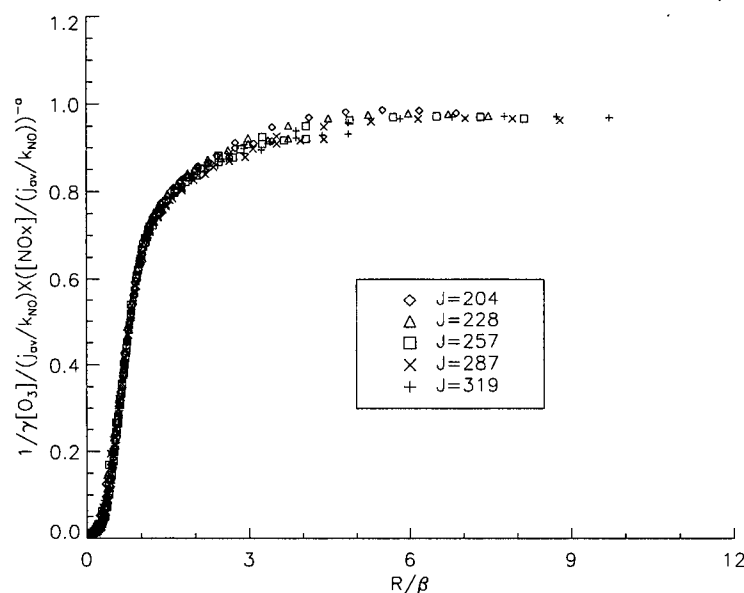


Figure 4.12: Dimensionless model output for the five OLT simulations after: scaling by dimensionless initial NO<sub>x</sub> concentration raised to the 0.62, shifting and rotating.

This analysis only gives a partial account of any actinic flux dependence.  $J$ -values are influenced by three factors: date, latitude and irradiation time. So far, I have varied  $J$  by keeping the irradiation time constant and varying the date. However, it is possible to produce actinic fluxes which have identical  $J$ -values but different peak values by changing simulation latitude and irradiation times. One question that comes to mind is: How does peak actinic flux affect the similarity relationship? If peak actinic flux has no direct influence, then OZIPR simulations with identical  $J$ -values but different  $j_{pk}$  values should produce the identical scaled dimensionless maximum ozone concentrations. If, however, peak actinic flux has a direct influence on ozone formation, then such simulations will not show identical scaled values and a new scaling parameter would be needed to capture this  $j_{pk}$  dependence. I explore these ideas in the next section.

## 4.7 Scenario V – Effect of peak actinic flux

In this scenario, OZIPR simulations were performed for two different locations: Vancouver (49.15°N) and Los Angeles (34.0°N). Simulations had the same  $J$ -values but different  $j_{pk}$  values. The longitude for both locations was adjusted to 120°W – the local prime meridian – so that both had the sun overhead at noon. Different Julian days of the year were chosen at each site so that resulting  $J$ -values were the same. Each simulation used the RADM2 mechanism (Stockwell et al., 1990) with

the OLT was the sole VOC. Throughout each simulation, the temperature was held fixed at 298 K. Table 4.5 gives the test conditions.

In Figure 4.13, Vancouver and Los Angeles solar zenith angle and the corresponding  $NO_2$  photolysis rates are shown as a function of local time. Both  $NO_2$  photolysis curves have the same area under their curves but have different peaks. The difference between the solar zenith curves is more pronounced than the difference between the photolysis rates because the  $NO_2$  photolysis rate is not sensitive to solar zenith at small zenith angles. Figure 4.13 shows the Vancouver location to have initially higher photolysis rates while the Los Angeles location has more intense photolysis around noon. The question is: *Will the higher initial actinic fluxes for the Vancouver location serve to stimulate early photochemical production (through increased radical production via inorganic sources (Jeffries and Tonnesen, 1994)) earlier and produce maximum ozone levels comparable to the Los Angeles location with its higher rates later in the day?* If so then, maximum ozone concentrations will not be sensitive to  $j_{pk}$ .

Figure 4.14A shows NOx-scaled dimensionless maximum ozone versus  $R$  for both simulations (a common NOx-exponent of  $a = 0.607$  was used). The curves show similar variability with the Vancouver curve (with maximum value of 10.16) lying slightly underneath the Los Angeles curve (maximum value of 10.24) suggesting the former has slightly more reactive conditions. Table 4.6 summarizes the WEX parameters used to fit each similarity relationship. The largest difference between parameter values is for  $\beta$ ; at the Vancouver location it is 4.86 versus 4.62 at the Los Angeles location. In order to examine the curves in the Weibull plane, both curves were normalized by the Los Angeles maximum value. Figure 4.14B shows the ‘Weibullized data’ for both curves – it appears that the two differ only by a horizontal translation. In Figure 4.15A, both curves have been translated so that their breaks occurred at  $\ln R = 0$ . In Figure 4.15B these shifted curves have been transformed back to the similarity plane where the agreement between the two curves is better (although the initial difference was not great to start with).

This analysis has shown that the dimensionless group  $J$  cannot account for all of the ozone

Location	Vancouver (YVR)	Los Angeles (LAX)
Month	August	September
Date	20	6
Latitude ( $^\circ$ )	49.15	34
Test Length (hours)	11	11
Temperature (K)	298	298
$j_{av}$ (1/s)	0.006490	0.006490
$J$	257	257
$j_{pk}$ (1/s)	0.0085	0.0089

Table 4.5: Test conditions for simulations with different latitudes but identical  $J$ -values.

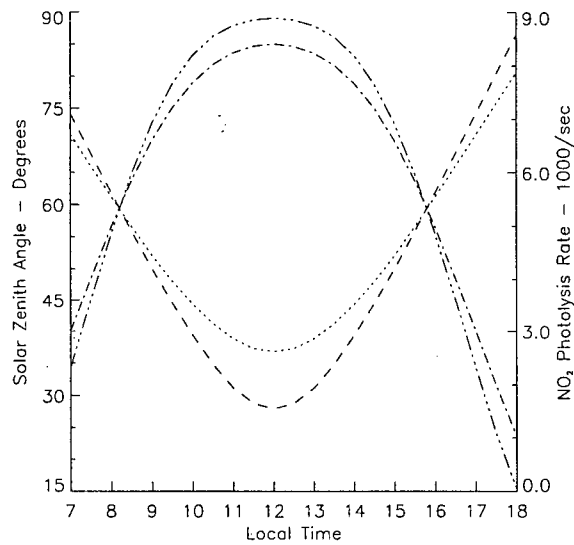


Figure 4.13: Solar zenith angle (in degrees) as a function of local time for Vancouver (dotted line) on August 20<sup>th</sup> and Los Angeles (dashed line) on September 6<sup>th</sup>. In addition,  $\text{NO}_2$  photolysis rate (1000/sec) as a function of local time for both Vancouver (single 'dot') and Los Angeles (three 'dots') are plotted.

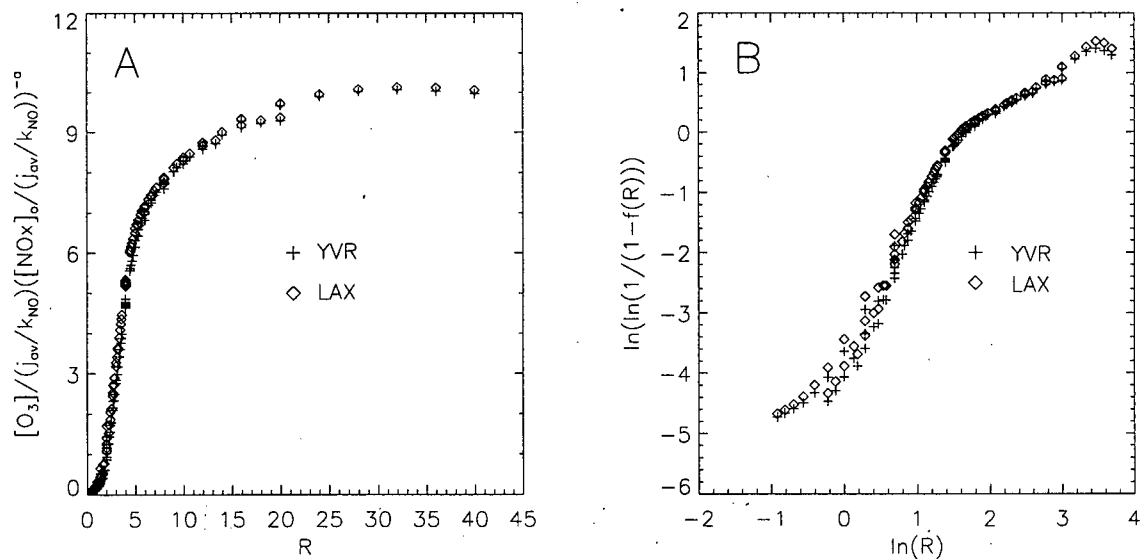


Figure 4.14:  $\text{NO}_x$ -scaled dimensionless maximum ozone concentration for OZIPR simulations using Los Angeles and Vancouver latitudes (A). Figure B shows the corresponding curves after normalizing by a common value and Weibull transforming.

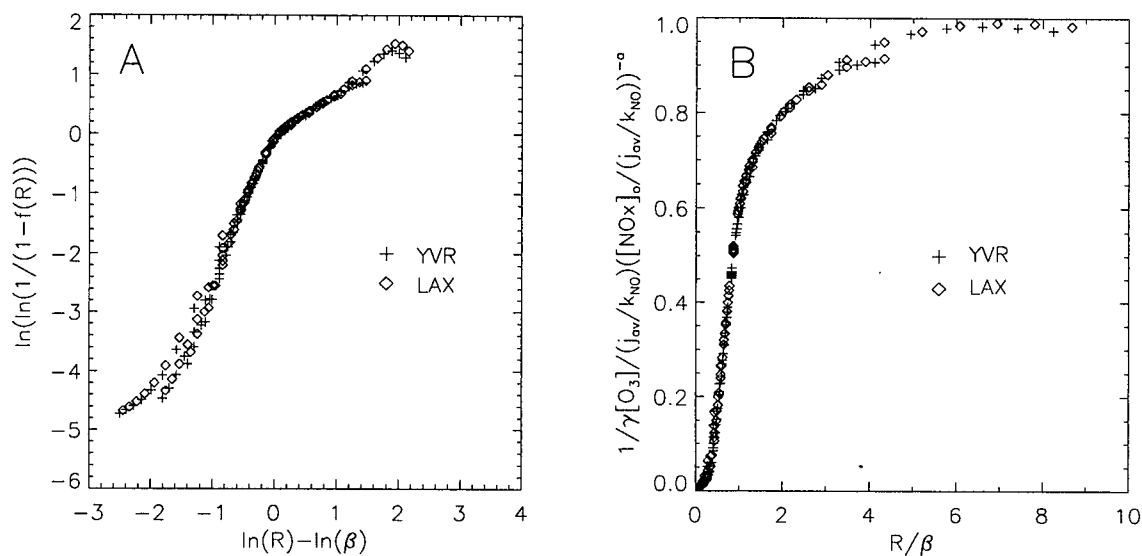


Figure 4.15: Effects of horizontal translation by  $\beta$  on the 'Weibullized' (A) and 'scaled' (B) data.

dependence on actinic flux; it does not distinguish between  $J$ -values with different peak actinic fluxes. In essence, a new scaling parameter would be needed to account for this:

$$\Pi_5 = \frac{j_{pk}}{j_{av}} \quad (4.10)$$

Since the effects caused by  $j_{pk}$  appear to be small, and do not alter the general nature of the similarity relationship, this approach will not be pursued, and the remaining simulations will use actinic flux values using a Vancouver latitude.

## 4.8 Scenario VI – Varying T and J

In this last section, a scaling analysis of ozone formation is performed using model output for 20 test matrices having four different temperatures and five different levels of actinic flux. The analysis starts by individually fitting the WEX model to each simulation and noting the variability of each

Parameter	YVR	LAX
$\gamma$	10.16	10.24
$a$	0.607	0.607
$\alpha_1$	2.39	2.31
$\alpha_2$	0.78	0.74
$\beta$	4.86	4.62
$\lambda$	0.95	0.95
RMSE	12.1	11.8

Table 4.6: WEX parameter values for the YVR and LAX simulations.

parameters value with temperature and actinic flux. Then, the dependence of  $\beta$  on  $J$  and  $T$  is parameterized and compared with results drawn from smog chamber simulations. Next a similarity relationship for maximum ozone concentration which accounts for varying initial OLT and NOx concentration, varying temperature and actinic flux is developed. Finally, scatter plots are used to show the level of agreement between this parameterization and the original model output.

#### 4.8.1 Variability of WEX parameters with $J$ and $T$

To examine the combined effects of varying both temperature and actinic flux on the scaling analysis, OZIPR simulations were performed at five different actinic fluxes and at four different temperatures. All used the RADM2 mechanism Stockwell et al. (1990) with OLT as the sole VOC. All simulations started at 7:00 a.m. and ended 11 hours later at 6:00 p.m. Again, there was neither dilution nor deposition. Each simulation had base OLT concentration of 0.6 ppm and base NOx concentration of 0.15 ppm using 11 nodes. Actinic flux levels were the same as described in Section 4.6 while temperatures corresponded to those used in Section 4.5. Table 4.7 shows WEX parameter values for each of the twenty test matrices. From this Table a few important observations are:

- The NOx-scaling exponent ( $a$ ) shows the least variability of all of the parameters.
- The normalizing parameter ( $\gamma$ ) and  $\lambda$  show a much stronger dependence on temperature than actinic flux.
- Both WEX slopes ( $\alpha_1$  and  $\alpha_2$ ) increase with increasing temperature and increasing J-values. Additionally,  $\alpha_2$  shows more sensitivity than  $\alpha_1$  to both  $J$  and  $T$ .
- The scaling break ( $\beta$ ) is almost equally dependent on temperature and actinic flux.

The behaviour of the scaling break is of special importance. As I will shortly show, it will be used to capture the  $J$ -dependence in the ‘universal’ similarity relationship. It also defines a natural scale for the ratio of initial VOC to NOx. Characterizing how this scale responds to changing environmental conditions provides valuable insight into the nature of ozone-precursor relationships. In Figure 4.16,  $\beta$ -values from Table 4.7 have been plotted as a function of  $J$ . Four separate trends, each associated with a different temperature, are apparent. A power law has been used to model each trend. Each power law uses the same exponent but a different pre-exponential factor i.e.:

$$\beta(T, J) = c_o J^{-c_1} \quad \text{where} \quad c_o = c_o(T) \quad (4.11)$$

Each curve fits the  $\beta$ -values with a correlation coefficient greater than 0.99. From this Figure, the following conclusions can be drawn:

$\gamma$					$\alpha$				
$J$	T293	T298	T303	T308	$J$	T293	T298	T303	T308
319	8.38	9.54	11.56	13.98	319	0.63	0.61	0.60	0.64
287	8.64	9.78	11.87	14.28	287	0.63	0.61	0.60	0.63
257	8.96	10.14	12.19	14.61	257	0.64	0.61	0.60	0.62
228	9.30	10.44	12.51	14.92	228	0.64	0.62	0.60	0.61
204	9.60	10.67	12.68	15.09	204	0.66	0.62	0.61	0.61

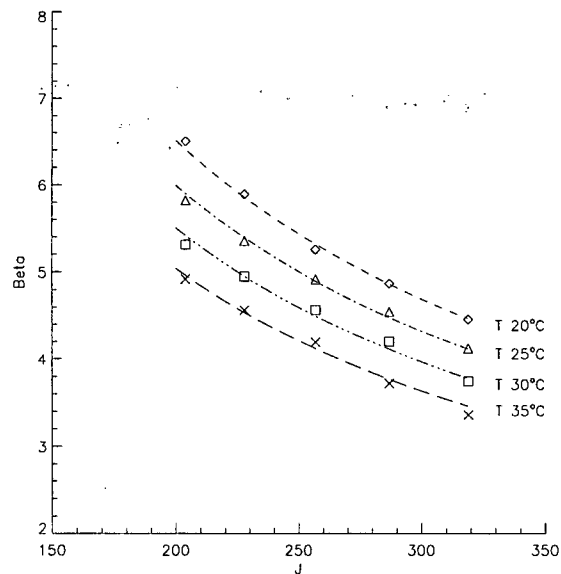
  

$\alpha_1$					$\alpha_2$				
$J$	T293	T298	T303	T308	$J$	T293	T298	T303	T308
319	2.14	2.21	2.33	2.46	319	0.65	0.73	0.80	0.85
287	2.20	2.27	2.33	2.49	287	0.66	0.74	0.79	0.88
257	2.28	2.37	2.41	2.51	257	0.71	0.77	0.82	0.87
228	2.30	2.42	2.51	2.61	228	0.73	0.83	0.86	0.89
204	2.33	2.46	2.59	2.69	204	0.78	0.90	0.93	0.95

$\beta$					$\lambda$				
$J$	T293	T298	T303	T308	$J$	T293	T298	T303	T308
319	4.46	4.12	3.74	3.36	319	0.94	0.89	0.76	0.58
287	4.87	4.55	4.20	3.72	287	0.97	0.95	0.82	0.63
257	5.25	4.92	4.57	4.19	257	0.96	0.96	0.84	0.70
228	5.89	5.36	4.95	4.57	228	0.99	0.94	0.86	0.73
204	6.50	5.82	5.31	4.92	204	0.98	0.93	0.82	0.73

Table 4.7: WEX parameter values for the YVR and LAX simulations.

Figure 4.16: Dependence of WEX parameter  $\beta$  (scaling break) on  $J$  for four different temperatures. Also shown are power-law fits to the model output where each power law is constructed to have the same exponent.

- At any  $J$ -value, increasing temperature will always decrease  $\beta$ .
- As  $J \rightarrow \infty, \beta \rightarrow 0$ . Physically, this implies that as more energy is provided to the OLT-NOx system, the ridgeline on an isopleth diagram shifts upwards. Simulations initially in the VOC

limited region become NO<sub>x</sub>-limited. And given enough irradiation, the whole response surface becomes NO<sub>x</sub>-limited.

- As  $J \rightarrow 0, \beta \rightarrow \infty$ . This is just the corollary to the above, namely, as the actinic flux is reduced, the  $\beta$  moves towards the VOC axis and NO<sub>x</sub>-limited simulations become VOC-limited. In this way, the VLR can also be considered a light-limited region (Johnson (1984)).
- The power law relationship for  $\beta$  implies there is no characteristic scale for the scaling break.

Finally, it is interesting to compare Figure 4.16 with a similar figure produced by Graham Johnson for his IER model (Johnson, 1984). This figure, reproduced here as Figure 4.17, shows emission reduction control options as a function of cumulative sunlight. He defines cumulative sunlight in the same manner as  $J$  (but bases his calculations on a latitude of 34°S). For a given actinic flux and initial VOC to NO<sub>x</sub> ratio (R-value), the plot determines if ozone production is controlled VOC or NO<sub>x</sub> emissions. To do this, one locates the point on the Figure corresponding to the expected  $J$ - and  $R$ -values. Next, using the temperature of interest, one determines if this point lies on the VOC controlled or NO<sub>x</sub> controlled side of the expected temperature's dividing line. The dividing line is in essence the ridgeline. In this way, the diagram can also be used to show the ridgeline behaviour of the as a function of  $J$  and  $T$ . This behaviour is consistent with  $\beta$ , the scaling break. I do not know how Johnson produced his plot – whether it was based on his smog chamber data, modeling or intuition. It is worth mentioning that  $\beta$  could be thought of as simply one of several regression parameters, determined by a computer, used to parameterize the behaviour of a numerical model. However, the fact that this regression parameter shows such a regular dependence on both temperature and actinic flux, consistent with observations drawn from smog chamber studies, suggests that this high level analysis captures the essence of ozone photochemistry.

#### 4.8.2 'Universal' Similarity relationship

To find a 'universal' similarity relationship for the  $T$  and  $J$  simulations, maximum ozone and initial NO<sub>x</sub> concentrations were first made dimensionless by  $k_{NO}$  and  $j_{av}$  using Eq. (4.4) and (4.7). Next, dimensionless maximum ozone was scaled by  $\Pi_2^a$  and  $\Pi_4^b$  where initial values for  $a$  and  $b$  were estimated using a spreadsheet program and the largest value was used to determine the normalizing constant ( $\gamma$ ). Next, it was assumed that these scaled and normalized points were now only a function of  $R$  and  $J$ . Furthermore, it was assumed that the  $J$ -dependence could be modeled by a horizontal shift of the Weibull-transformed data. Next, the normalized points were Weibull transformed and translated along the horizontal axis. The amount of translation was equal to  $\ln(\beta_{av})$  where  $\beta_{av}$  represents the average  $\beta$ -value for each  $J$ -level. (No temperature dependence

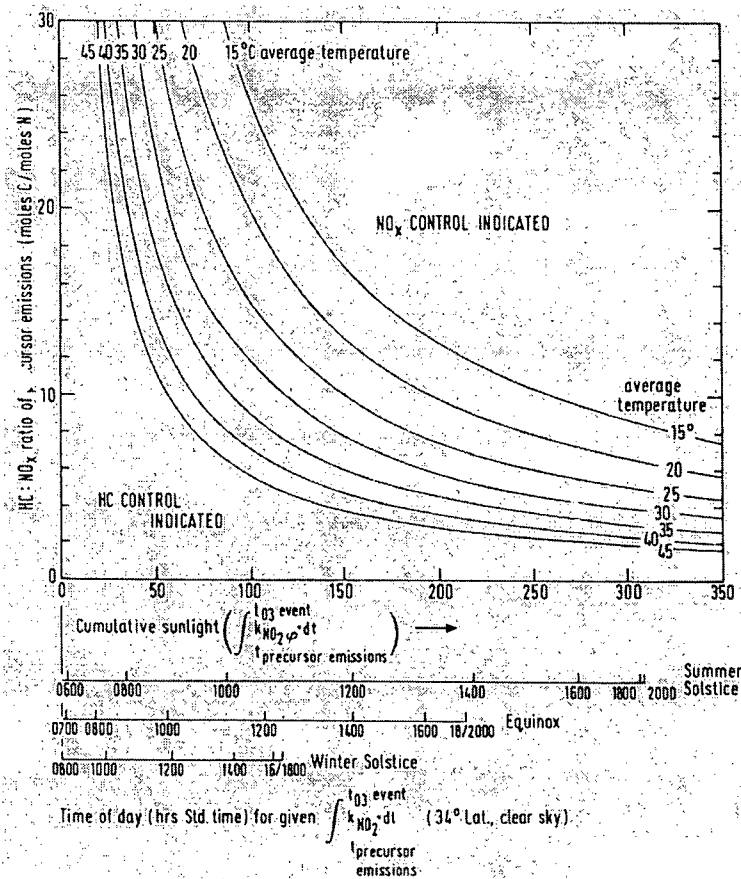


Figure 4.17: Ridgeline as a function of  $J$  and  $T$  (from Johnson (1984)).

was allowed for  $\beta$  since it was assumed that all temperature dependence was explained by  $\Pi_4^b$ ). In this way, all scenarios having a common actinic flux were shifted by the same amount – regardless of temperature. The amount of each translation was parameterized by:

$$\beta_{av} = c_0 J^{-c_1} \quad (4.12)$$

where  $c_0$  and  $c_1$  were found by regressing the temperature averaged  $\beta$ -values against  $J$ . No rotations were used to capture the  $J$ -dependence; these transformations did not appear to reduce the scatter.

Figure 4.18A shows all the data sets in the ‘Weibullized data’ after translating by  $\ln \beta_{av}$ . The Figure shows scatter for both  $\ln(R/\beta) < -1.0$  and  $\ln(R/b) > 1.0$ . One simulation in particular appeared to deviate from the others. This simulation had the lowest  $J$ -value and lowest temperature. This low flux/low temperature simulation suggests a limit to the scaling regime and is the subject of the next section. Figure 4.18B shows the same plot as 4.18A but with this simulation removed. There is a little less scatter in the  $\ln(R/\beta) > 1.0$  region now. Also plotted on this Figure, is the WEX

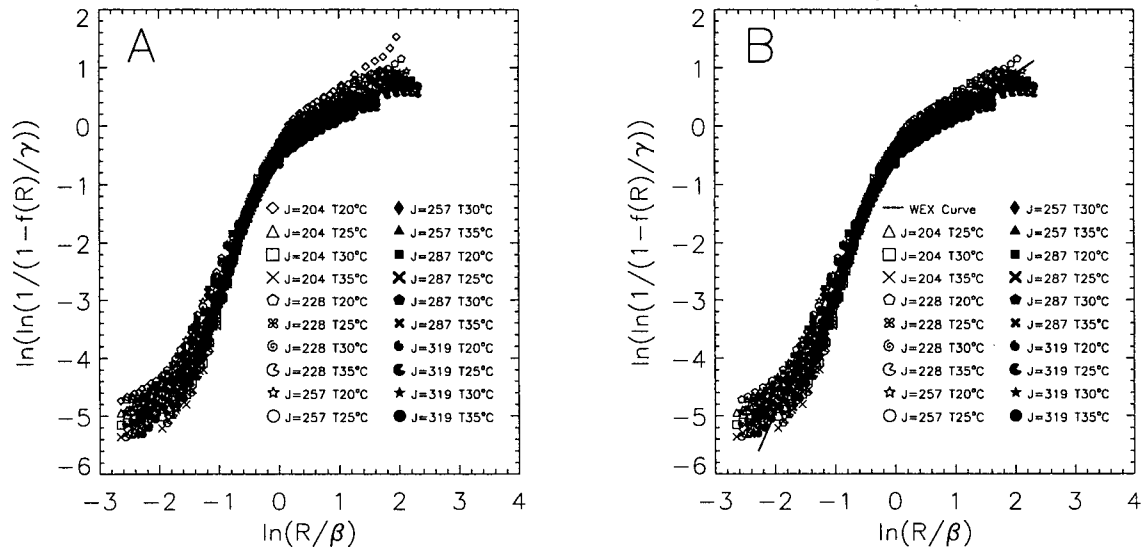


Figure 4.18: Weibull transformed model output for RADM2 simulations having five different levels of actinic flux and four different temperatures after horizontal translation by  $\ln \beta_{av}$  (A). Figure B is the same as (A) but the simulation with  $J = 204$  and  $T = 20^\circ \text{C}$  removed

curve which has been fitted to these remaining 19 test matrices. The regression was performed using a computer to calculate the scaling powers ( $a$  and  $b$ ) as well as the WEX parameters ( $\alpha_1, \alpha_2, \lambda$ ). The program required a first guess which was supplied by a spreadsheet program. The model was forced to fit more closely around the ridgeline area. To do this, the regression found WEX parameters which minimize the RMSE (between the WEX model and OZIPR model output) around an area defined by  $R/\beta \in [0.2, 5.0]$ . Again, the normalizing value ( $\gamma$ ) was determined to be  $1/0.99$  times the largest scaled value. Finally,  $\beta$ -values were not calculated in the regression since they were already imposed on the similarity relationship through the horizontal translations.

Finally, the 'Weibullized' and transformed 'data' has been mapped back to the similarity plane to give a 'universal' curve for OLT. Figure 4.19A shows that the 'universal' curve captures ozone variability for  $R$ -values less than  $R = \beta$  but shows more variability for higher  $R$ -values. In Figure 4.19B the  $J_{204}, T_{20^\circ\text{C}}$  scenario has been removed and the 'universal' WEX curve added.

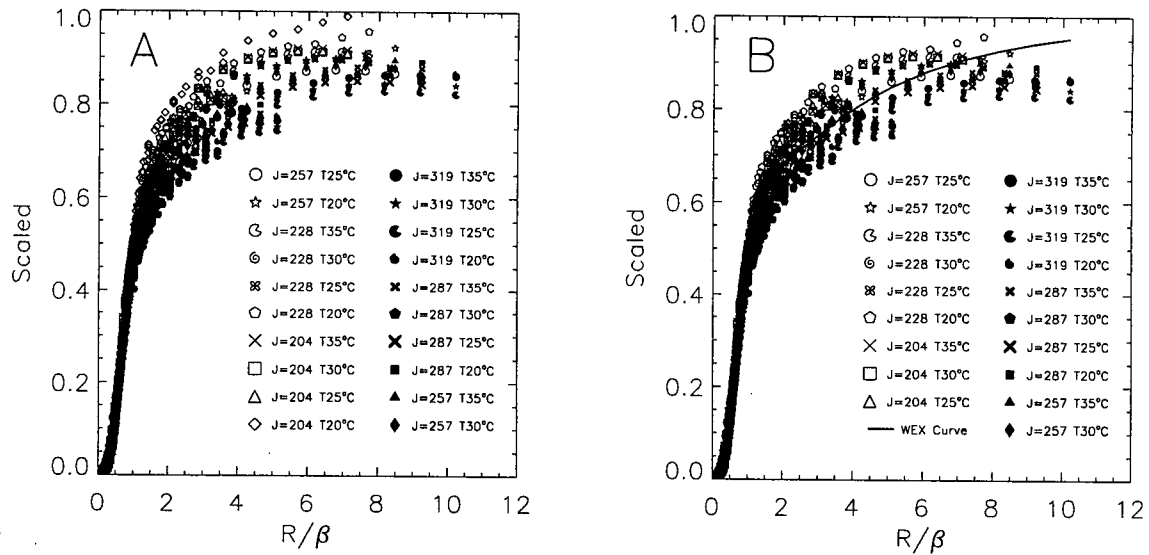


Figure 4.19: Universal similarity relationship for OLT. Figure A shows the model output after scaling and translating and Figure B replots (A) without the  $J = 204$  and  $T = 20^\circ\text{C}$  simulation and with the 'universal' WEX parameterization.

### 4.8.3 Universal Propene Curve

Based on the above analysis, the 'universal' curve OLT has the form:

$$[O_3]_{max} = \gamma \frac{j_{av}}{k_{NO}} \left( \frac{[NOx]_o}{j_{av}/k_{NO}} \right)^a \exp \left\{ -\frac{E_{OH}}{k} \left( \frac{1}{T} - \frac{1}{298} \right) \right\}^b WEX(R; \beta(J), \alpha_1, \alpha_2, \lambda) \quad (4.13)$$

and  $\beta(J) = c_o J^{-c_1}$

$$\gamma = 11.5, \lambda = 0.62, \alpha_1 = 2.5, \alpha_2 = 0.69$$

$$a = 0.65, b = 6.1$$

$$c_o = 413, c_1 = -0.81$$

This 'universal' curve captures the variability of maximum ozone concentration over a wide range of NOx and OLT concentrations, as well as a range of actinic fluxes and temperatures typical of the 'ozone season' in Vancouver B.C. A total of 8 parameters are needed to fully characterize this variability. The importance of each parameter is discussed in the next two chapters.

To make use of Eq. (4.13), one first calculates the expected environmental conditions:  $T$  and  $J$ .  $J$  can be easily calculated based on the expected total irradiation time, the station location and the day of the year. Figure 4.20 shows a contour plot of clear sky J-values for different latitudes

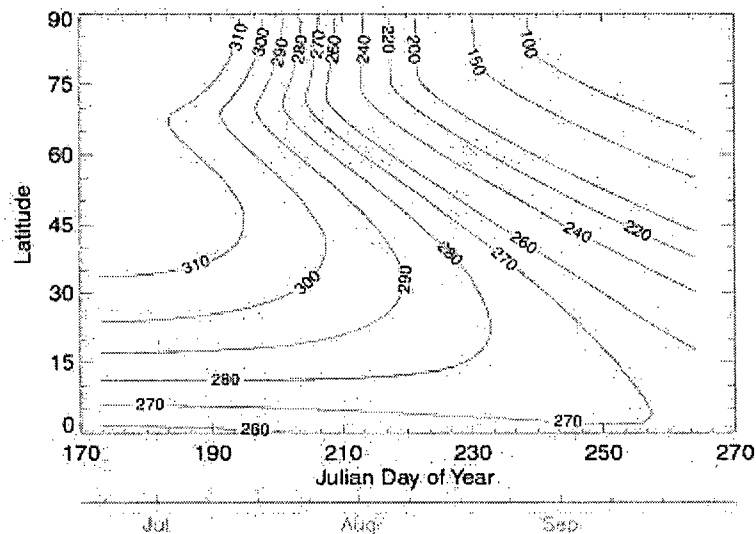


Figure 4.20: Total actinic flux (as measured by the integrated  $\text{NO}_2$  photolysis rate) as a function of Julian day of the year and latitude. The plot assumes a fixed irradiation interval starting at 7:00 a.m. (local time) and ending at 6:00 p.m. (local time).

(in the Northern Hemisphere) and days of the year (based on an irradiation time starting at 8:00 a.m. and ending at 7:00 p.m. (LST)). This plot allows  $J$  and  $j_{av}$ . Next, the expected temperature determines  $k_{\text{NO}}$  and  $\Pi_4^b$ . Finally, initial  $\text{NO}_x$  and OLT concentrations give  $R$ . Equation (4.13) can then be evaluated to predict maximum ozone concentration. The next subsection compares results predicted by Eq. (4.13) directly with OZIPR model output.

#### 4.8.4 Scatter Plots

To test the ability of the 'universal' WEX curve (Eq. (4.13)) to predict maximum ozone concentrations, it was compared with model output at 4 different temperatures/actinic fluxes combinations. Figure 4.21 shows four scatter plots of WEX-predicted ozone versus OZIPR model output. In general, the plots show most points lying close to the  $y = x$  line. The correlation coefficient for each plot is above 0.99. For each plot a line of best fit was calculated. Finally, the scatter of the data about this line was also determined. Table 4.8 outlines these statistics.

The WEX model consistently under predicts maximum ozone (by 16%) for the low actinic flux case (A). As  $J$  increases, the model tends to over predict ozone and the RMSE increases. There does not appear to be more scatter at large ozone concentrations than low ones. This is in contrast

Plot	A	B	C	D
Temperature (C)	25	30	30	35
Actinic Flux (J)	204	257	287	319
Slope	1.1571	1.0314	0.9749	0.9749
Intercept (ppm)	0.0007	0.0077	0.0101	0.0101
RMSE (ppm)	0.00790	0.01125	0.01131	0.02060

Table 4.8: Statistics for four scatter plots comparing maximum ozone concentrations predicted by the ‘universal’ WEX model (Eq. (4.13)) and OZIPR model output using the RADM2 mechanism (Stockwell et al., 1990) using OLT as the sole VOC.

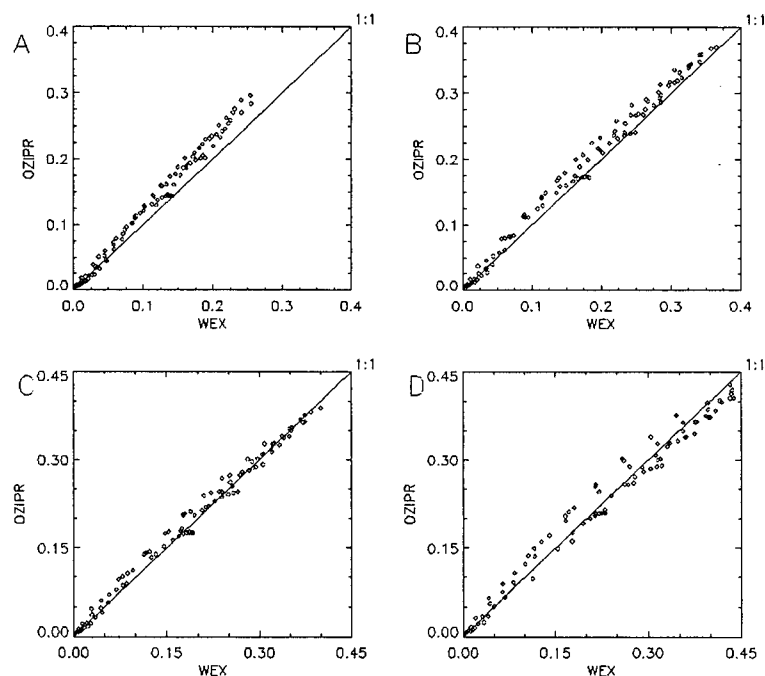


Figure 4.21: Scatter plots showing modeled maximum ozone concentrations (in ppm) based on OZIPR model output and WEX ‘universal’ curve (Eq. (4.13)) for four different actinic flux/temperature combinations: (A) J204/T25, (B) J257/T30 (C) J287/T30 (D) J319/T35.

to the shape of the ‘universal’ similarity curve which shows large scatter for large R-values.

#### 4.8.5 Summary

A scaling analysis for maximum ozone concentration, produced from an OLT-NO<sub>x</sub> system, has been performed which captures variability due to initial OLT and NO<sub>x</sub> concentrations as well as a range of temperatures and actinic fluxes typical of ozone episodes in the Vancouver, B.C. region. The

similarity relationship displays a characteristic 'break' when normalized and Weibull transformed. I find that the temperature dependence can be described by a power law. The dependence on actinic flux, captured through the  $J$ -dependence of  $\beta$ , can be viewed as a horizontal translation of the 'Weibullized data'. The similarity relationship shows a lot of scatter for  $R$ -values greater than  $\beta$  but scatter plots of maximum ozone concentration based on the 'universal' WEX curve and OZIPR model output show good agreement over the entire range of ozone concentrations. The next section investigates the range of validity of the parameterization.

## 4.9 Scaling Limits

By parameterizing the behaviour of the chemical mechanism, I fix the relative importance of competing chemical processes and (implicitly) assume that this importance does not change over a range of  $[VOC]_o$ ,  $[NOx]_o$ ,  $R$ -values, temperatures or actinic fluxes. The extent of this range, not directly determined by the scaling analysis, should be included as part of the parameterization. Outside of this scaling range, it is possible that different photochemical processes might control ozone formation, leading to a new scaling regime and a breakdown of the original parameterization. In this section, I consider the range of applicability (in terms of  $[VOC]_o$ ,  $[NOx]_o$ ,  $R$ -values) for the WEX parameterization using OLT as an example. For the WEX model to be useful, its range of applicability must overlap the range of environmental conditions typically found in polluted urban environments.

From Section 4.8, it appears that the temperature range for the OLT parameterization lies above 20°C while the actinic flux range should be such that the cumulative  $NO_2$  photolysis rates are greater than 200 (corresponding to summer dates between early March and early September for a latitude of 49°N). Therefore, it is likely that at temperatures below 20°C or  $J$ -values below 200 the WEX model (at least with its present parameter values) cannot be used to describe the relationship between maximum ozone concentration and initial precursor concentration. I will not attempt to determine an upper limit on ambient temperature since values higher than 35°C are not common in the LFV (Oke and Hay, 1998) – the region in which I model ozone formation in Part II. Furthermore, since the analysis captures ozone variability at the LFV's maximum  $J$ -value, no upper bound on this range is needed. Therefore, using the WEX parameterization in conditions with significantly higher temperatures and  $J$ -values (i.e. lower latitudes) will require further investigation.

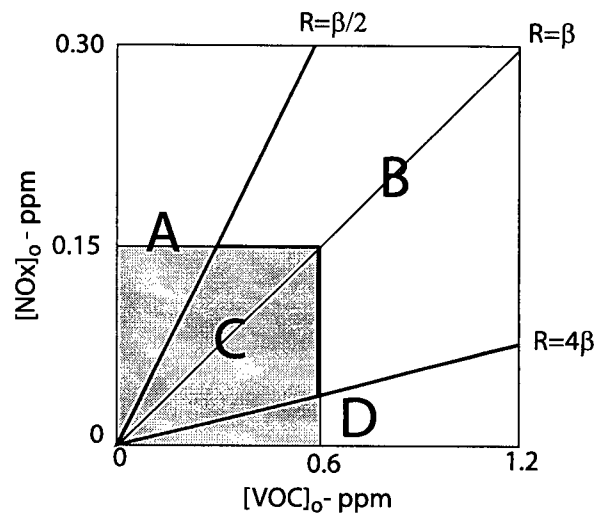


Figure 4.22: Schematic of OLT modeling domains. The shaded region gives to the original VOC and NO<sub>x</sub> range, used for the WEX parameterization, and is labeled 'C'. The large box gives the larger modeling domain. The lines  $R = 2\beta$  and  $R = 4\beta$  produce three additional regions 'A', 'B' and 'D'. Region 'A' identifies simulations have low  $R$ -values, region 'D' encompasses simulations having high  $R$ -values and region 'B' identifies those simulations having  $R$ -values in the range  $[\beta/2, 4\beta]$  but lying outside of the original domain. For completeness, the line  $R = \beta$  has been included.

#### 4.9.1 Precursor Scaling Limits

I determined the scaling limits by developing a parameterization of OLT over a limited range of initial VOC and NO<sub>x</sub> concentrations and then calculate maximum ozone concentrations for higher precursor concentrations. I compare the extrapolated values with additional model output (simulating these higher concentrations) to establish the limits of applicability. Based on the WEX model, maximum ozone concentration depends on its precursors in two ways: as a function of  $[NOx]_o$  and  $R$ . However, since  $R$  is a function of  $[VOC]_o$  and  $[NOx]_o$ , maximum ozone concentration is a function of three variables, each of which may have its own scaling limits.

A first guess for the  $R$ -range can be made by looking at the OLT model output in the Weibull plane (c.f. Figure 3.9). The increased scatter in the similarity relationship for  $\ln R > 3$  ( $R > 20$ ) and  $\ln R < 0.75$  ( $R < 2$ ) suggests that  $\beta/2 < R < 4\beta$  ( $\beta = 4.2$ ) defines an appropriate range. One would expect that a comparison of WEX generated ozone isopleths with OZIPR isopleths (c.f. Figure 3.12) would similarly give an estimate of the VOC and NO<sub>x</sub> range. However, this Figure does not show any consistent discrepancies at high VOC or NO<sub>x</sub> concentrations (it does, however, show the discrepancies at low  $R$ -values). Thus, in order to determine the VOC and NO<sub>x</sub>

Label	Range	Description
A	$R < \beta/2$	Low R-values
B	$\beta/2 \leq R \leq 4\beta$ and $[VOC]_o > 0.6$ ppm, $[NOx]_o > 0.15$ ppm	Higher $[VOC]_o$ and $[NOx]_o$ with only R-values around $\beta$
C	$\beta/2 \leq R \leq 4\beta$ and $[VOC]_o \leq 0.6$ ppm, $[NOx]_o \leq 0.15$ ppm	Original domain without high and low R-values
D	$R > 4\beta$	High R-values

Table 4.9: OLT precursor scaling domains.

ranges and improve the estimate of the R-range, OZIPR simulations were run over a much larger precursor range. Specifically, simulations were run with  $[VOC]_{base} = 1.2$  ppm and  $[NOx]_{base} = 0.3$  ppm – a doubling of the original VOC and NOx ranges. As well, 41 nodes were used in the simulations, extending the original (non-trivial) R-range from  $[0.4, 40]$  to  $[0.1, 160]$ . Figure 4.22 shows the  $[VOC]_o$  and  $[NOx]_o$  ranges for the original and modified runs. The original VOC and NOx range is highlighted by the shaded region and is labeled ‘C’. Lines  $R = 2\beta$  and  $R = 4\beta$  have also been drawn forming three additional regions ‘A’, ‘B’ and ‘D’. Region ‘A’ identifies simulations have low R-values, region ‘D’ encompasses simulations having high R-values and region ‘B’ identifies those simulations having R-values in the range  $[\beta/2, 4\beta]$  but outside of the shaded region. These regions are described in Table 4.9.

In order to compare the model output on the larger domain with the original WEX parameterization, the model output was first put into dimensionless form, scaled by  $[NOx]_o^a$  and normalized by  $\gamma$  (where values from the 11-node regression were used for  $a$  and  $\gamma$ ). To highlight the discrepancies in each of the four domains, separate comparisons are shown in Figures 4.22A,B,C and D (where the letters refer to one of the domains labeled in Figure 4.22).

Figure 4.23A shows that, for low R-values, the model output does not collapse onto a single common curve and the WEX parameterization overestimates for  $R > 0.5$ . In Figure 4.23B, the model output clusters around a common curve but shows more variability for  $R > 8$ . Figure 4.23C plots the model output in the original domain where the WEX model provides an excellent parameterization. Finally, in Figure 4.22D, model output and the WEX parameterization are compared at high R-values. Scaled model output in this domain shows great variability, with the WEX parameterization consistently overestimating.

I have also made comparisons using the more conventional isopleth diagram (Figure 4.24). There, isopleths found using the WEX parameterization (established on the smaller domain, but now extrapolated over the entire domain (dotted isopleths)) are plotted along with isopleths (solid lines) found from the OZIPR simulations. Superimposed are the boundaries of regions A,B,C and D. As was the case for the original domain (c.f Figure 3.12), for low R-values (region A), WEX isopleths have too steep a slope and overestimate the model output. In region B, the WEX model

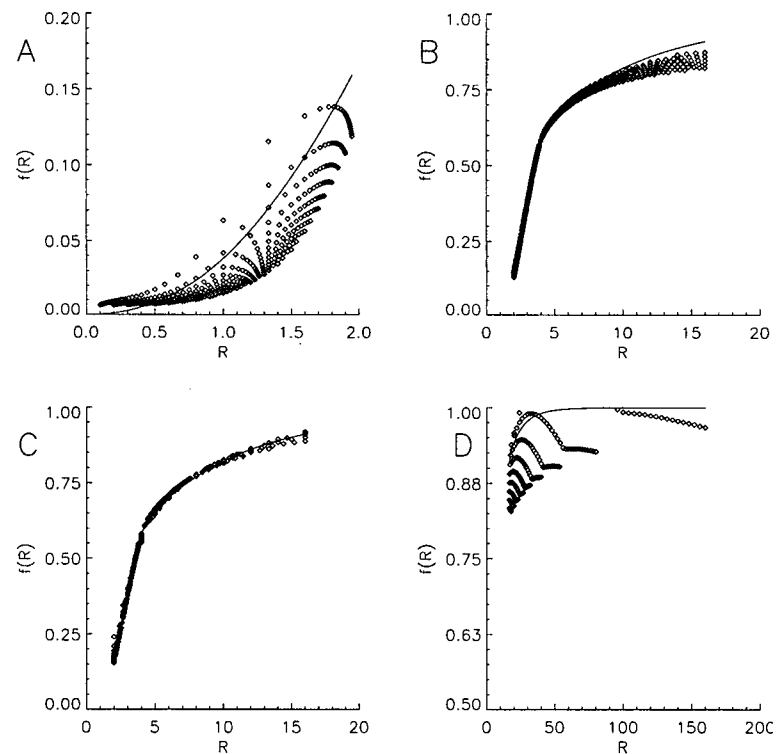


Figure 4.23: OLT similarity relationship in several scaling domains. Figures A, B, C and D refer to the different regions discussed in Table 4.9. In each Figure, the WEX parameterization is given by the solid line and model output by the diamonds

shows good agreement with the model output. However, for  $R > 8$ , the WEX mode overestimates maximum ozone concentrations. This discrepancy, not noticeable at lower VOC concentrations, suggests the similarity relationship breaks down at higher VOC concentrations. In region D, the model continues to overestimate. It appears that the OZIPR isopleths are not parallel to the VOC axis but instead gently slope upwards; a feature not captured by the asymptotic behaviour of the Weibull function.

To reduce the variability in regions A,B and D, different NO<sub>x</sub> scaling exponents were tried. In region A, when the exponent  $a$  is set to zero (i.e. making maximum ozone concentration as a function of  $R$  only) the scatter is almost completely removed (Figure 4.25A). Also shown in the Figure is the original WEX parameterization. The model output now clusters along a common curve indicating for low  $R$ -values, maximum ozone scales with  $R$  only. In Figure 4.25B, a lower value for the exponent has been tried (0.55 versus 0.60) again, reducing the scatter. Finally, it appears that an exponent value of 0.5 is the best choice for the NO<sub>x</sub> dependence for large  $R$ -values (4.25D).

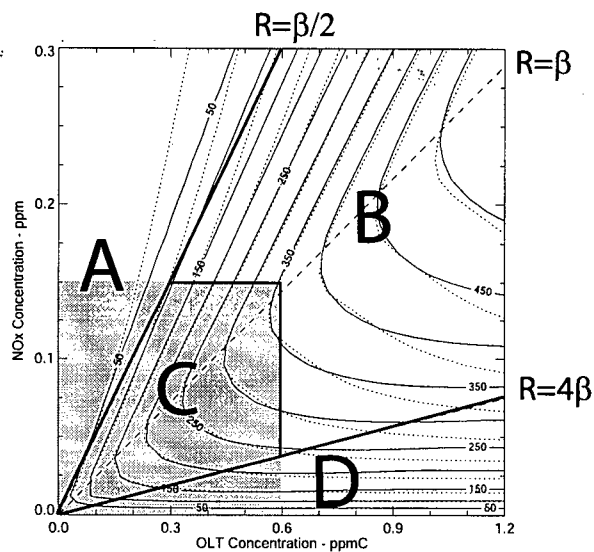


Figure 4.24: Ozone isopleths (in ppb) for OLT over several scaling domains. Dotted lines show isopleths based on the WEX model and solid lines using the model output. The shaded region represents the domain used to determine the WEX model. Regions A, B, C and D are explained in the text and in Table 4.9.

However, with this choice of exponent, there is still a large amount of scatter.

Finally, Figure 4.26 is a schematic showing the dependence of the NOx scaling exponent as a function of initial OLT, NOx and  $R$ -values. It appears that the NOx scaling exponent takes on three values based on the  $R$ -value: 0.0 at low  $R$ ,  $\approx 0.6$  for  $\beta/2 < R < 4\beta$  and 0.5 for high  $R$ . Furthermore, in the ridge area, it appears that as  $[OLT]_o$  and  $[NOx]_o$  increase, the NOx scaling exponent decreases. I have marked this transition with an arc extending between the lines  $R = \beta/2$  and  $R = 4\beta$ . While I have shown it to be an abrupt transition, I expect that it slowly decreases from one to the other. Further analysis is required to see if this decrease continues at higher precursor concentrations.

To summarize, the scaling analysis provides a means of capturing the behaviour of a chemical mechanism over a moderate range of initial VOC and NOx concentrations. However, the resulting parameterization breaks down when the ratio of initial OLT to NOx ( $R$ -value) is either very large or small. In addition, the parameterization is influenced by initial VOC concentration. Furthermore, the relationship between maximum ozone and initial NOx concentration depends on  $R$ . Despite this, the WEX parameterization, over the original limited domain, is able to predict maximum ozone concentration around the ridgeline and for a wide range of initial VOC and NOx concentrations.

While this analysis has been for a single VOC species, I expect similar trends to hold for the other VOC and VOC mixtures. Ideally, the parameterization range should be guided by  $R/\beta$ -values and

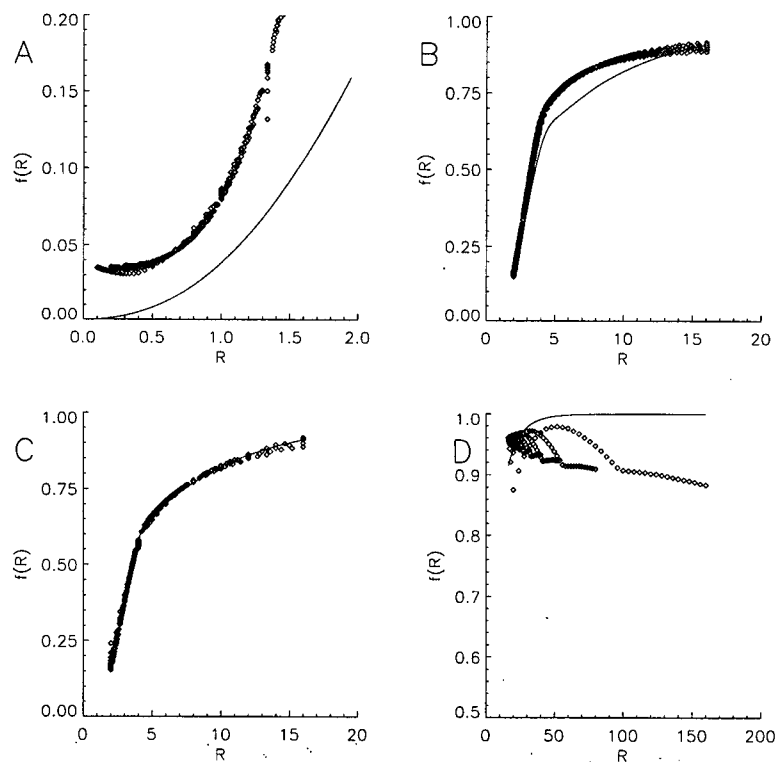


Figure 4.25: Similarity relationship for different  $\text{NO}_x$ -scaling exponents. Figures A, B, C and D refer to the regions discussed in Table 4.9. In each Figure, the original WEX parameterization is given by the solid line and model output scaled by different powers of initial  $\text{NO}_x$  concentration by the diamonds.

$[\text{O}_3]_{\max}$  found in urban environments. Unfortunately, it is difficult to determine  $\beta$  from ambient measurements, so instead, I have chosen a parameterization range centered around the scaling break that keeps the maximum ozone concentration below 300 ppb. For OLT, the maximum error produced by the WEX model in this region is 3.8 ppb or 4.0%.

## 4.10 Conclusion

In this chapter I have taken a novel approach of describing the ozone formation and shown it to be applicable for a wide range of VOC species and VOC mixtures. Furthermore the techniques prove to be independent of chemical mechanism. These techniques are also capable of capturing the variability of maximum ozone concentration on temperature and actinic flux. The analysis shows  $\gamma$  and the  $\text{NO}_x$ -scaling exponent ( $a$ ) vary with VOC species a point not considered by Blanchard et al. (1999), Chang and Rudy (1993) or Johnson (1984). Furthermore,  $\gamma$  appears to depend on

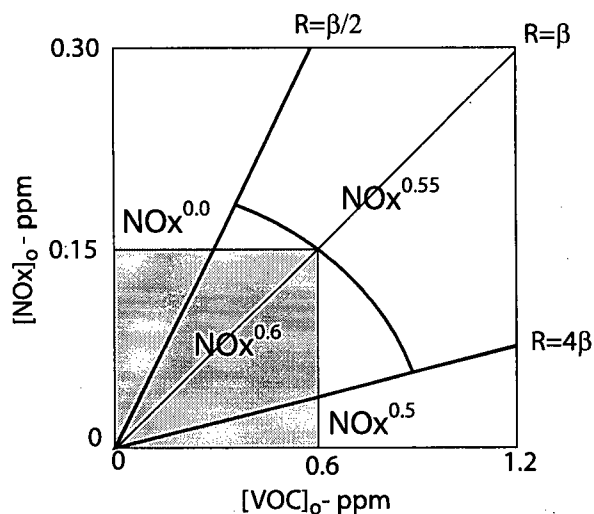


Figure 4.26: The OLT  $\text{NO}_x$ -scaling for OLT as a function of initial OLT,  $\text{NO}_x$  and  $R$ . The shaded region represents the domain used to determine the WEX model. Regions A, B, C and D are explained in the text and in Table 4.9. The arc between  $R = \beta/2$  and  $R = 4\beta$  is intended to reflect a change in exponent values from 0.60 to 0.55 and not an abrupt jump.

actinic flux which, again, has not been previously accounted for. This chapter has also shown the ranges of VOC,  $\text{NO}_x$ , temperature and actinic flux for which of the scaling analysis is valid.

In general the scaling analysis can be used in two ways: to calculate maximum ozone concentrations (using the similarity relationships) or to succinctly present data (by making use of the scaling techniques). In the next two chapters, I will outline a third application: to understand the general behaviour of a photochemical system through the interpretation of WEX parameters. A subsequent chapter will compare WEX modeled ozone concentrations with smog chamber data.

## Chapter 5

# Scaling Break and Ozone Photochemistry

### 5.1 Introduction

This is the first of two chapters which explores the physical significance of the WEX parameters. This chapter deals with the  $\beta$  – the R-value which characterizes the change in chemical regime and hence scale break in the WEX model – while the next examines the remaining five parameters. I start by examining the relationship between ozone production, ozone concentration, maximum ozone concentration and  $\beta$ . I begin with the temporal evolution of ozone concentration; showing that as the photochemistry proceeds, a fundamental shift in chemistry causes a change in the way ozone is produced. I then demonstrate that the scaling break is a manifestation of this shift. Next, I study the chemistry causing shift from a systems point of view; explaining the shift in terms of positive and negative feedback loops. Finally, I examine the relationship between the scaling break and the ridgeline,  $OH^\bullet$ -reactivity and chain length.

### 5.2 The Temporal Variability of Ozone

I begin by examining how ozone concentration varies during a single OZIPR simulation. Then, I study a sequence of simulations and show how the temporal variability of ozone, NO<sub>x</sub> and various other species is affected by the initial VOC to NO<sub>x</sub> ratio.

#### 5.2.1 Temporal variability of $NO$ , $NO_2$ and $O_3$ for a single simulation

Figure 5.1 shows the temporal evolution of ozone and various other species for a simulation using the stock urban mixture. The initial concentration of NO<sub>x</sub> was 0.045 ppm and for the VOC mixture it was 1.35 ppm (for an R-value of 30), which puts the simulation in the NO<sub>x</sub>-only scaling regime. Note that the highest ozone concentration occurs at the simulation end. It is this ozone value that would be plotted on an isopleth diagram and used to find the WEX parameters.

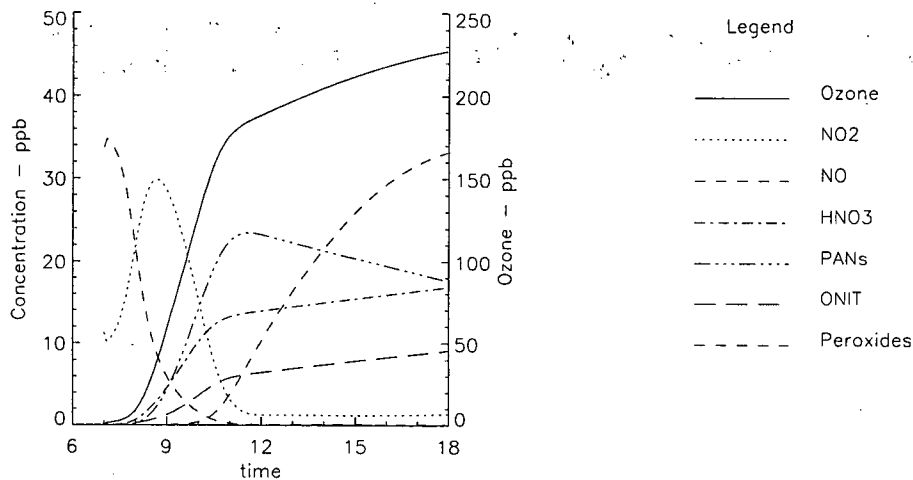
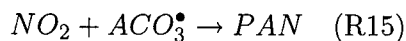


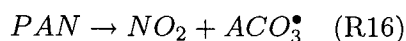
Figure 5.1: Temporal evolution of  $O_3$ ,  $NO_2$ ,  $NO$ ,  $HNO_3$ , PAN, ONIT and other peroxides for an OZIPR simulation using the Stock urban mixture. The initial  $NO_x$  concentration was 0.045 ppm and initial VOC concentration was 1.35 ppm for an  $R$ -value of 30.

The temporal variability of the various species reveals important processes, namely:

- For  $NO$ , its concentration almost immediately begins to drop. This represents the conversion of  $NO$  to  $NO_2$  by peroxy or hydroperoxy radicals (R7).
- Initially, the  $NO_2$  concentration rises (at the expense of  $NO$ ) then reaches a peak before falling. The drop in concentration coincides with the production of  $HNO_3$  (R9) and PAN.
- The ozone curve is flat until about 8:00 a.m. after which it starts to rise. This coincides with the increase in  $NO_2$  and drop in  $NO$  concentration. Ozone growth continues throughout the day but at a slower rate by late morning ( $t \approx 11:00$ ).
- The PAN concentration increases rapidly around 8:00 am and reaches a maximum around 11:00 a.m. and then decreases throughout the remainder of the simulation. This drop may be explained as follows: PAN forms as the result of a reaction between nitrogen dioxide and the acetylperoxy radical (modeled as  $ACO_3^\bullet$  in RADM2):



PAN also readily decomposes back into these products:



Both reactions occur simultaneously and are highly temperature dependent (Finlayson-Pitts and Pitts, 1999). When both  $NO_2$  and  $ACO_3^*$  are abundant, PAN readily forms. However, as  $NO_2$  becomes scarce, the balance between  $R15$  and  $R16$  shifts with more decomposition than production (low  $NO_2$  slows  $R15$ ) resulting in a PAN reduction.

- Nitric acid ( $HNO_3$ ) concentration rises rapidly before slowing around 11:00 a.m. The final concentration of  $PAN + HNO_3$ , roughly equal to the initial  $NO_x$  concentration, represents the conversion of  $NO_x$  to other nitrogen compounds.  $NO_x$ , PAN and nitric acid represents three major components of an important class of atmospheric species called reactive odd nitrogen.

### 5.2.2 Reactive Odd Nitrogen (NO<sub>y</sub>)

Reactive odd nitrogen (NO<sub>y</sub>) represents the sum of  $NO_x$  and all compounds that are the products of the atmospheric oxidation of  $NO_x$ . In the RADM2 mechanism, these include: nitric oxide ( $NO$ ), nitrogen dioxide ( $NO_2$ ), nitric acid ( $HNO_3$ ), peroxyacyl nitrates (PAN and TPAN), alkyl nitrates (ONIT), the nitrate radical ( $NO_3^*$ ), nitrous acid ( $HONO$ ) and dinitrogen pentoxide ( $N_2O_5$ ). The first five represent the most important components of NO<sub>y</sub>. In the absence of deposition and dilution,  $[NO_y]$  is conserved under photochemical reactions. Based on the simple description of ozone photochemistry given in the introduction, it is important to note that without termination reactions,  $NO_x$  acts as a catalyst; cycling between  $NO$  and  $NO_2$  (whereas the VOCs are gradually consumed). However, with termination reactions, the continuous cycling of  $NO_x$  between  $NO$  and  $NO_2$  is broken and ozone photochemistry ceases when all  $NO_x$  has been converted to other forms of NO<sub>y</sub> (Jeffries and Tonnesen, 1994). Another class of nitrogen compounds is called total reacted nitrogen (NO<sub>z</sub>) and is defined as the difference between  $NO_x$  and NO<sub>y</sub>

$$NO_z = NO_x - NO_y$$

When  $[NO_z] \approx [NO_x]_o$ , a photochemical system stops reacting. In the next chapter, I will show that partitioning of NO<sub>z</sub> between the  $HNO_3$ , PAN and ONIT determines several WEX parameters.

### 5.2.3 Isopleth Plot and Stock Simulations

To extend the analysis to include the effects of initial VOC and  $NO_x$  concentrations, I now examine a sequence of eight simulations. To keep the analysis simple, all eight simulations start with the same initial  $NO_x$  concentration but with varying initial VOC concentrations in order to provide a range of R-values above, below and along the ridgeline. I have marked the initial VOC and  $NO_x$

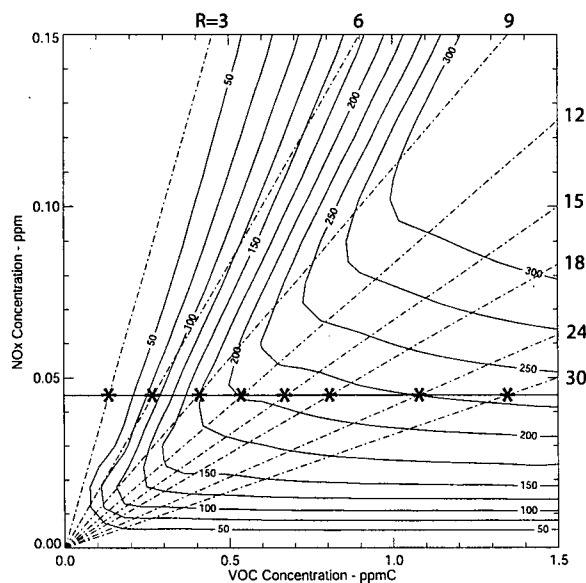


Figure 5.2: Ozone isopleth plot using the Stock urban mixture showing an isomephitic line of  $[NOx]_o = 0.045$  ppm. Also drawn are rays of constant  $R$ -values. The intersection of these rays with the isomephitic line, indicated by stars, gives the initial VOC concentrations for the eight simulations.

concentrations, for these simulations, on an isopleth diagram (Figure 5.2) along with an isomephitic<sup>1</sup> (constant NOx) line at  $[NOx]_o = 0.045$  ppm. Also drawn are rays of constant  $R$  at values: 3, 6, 9, 12, 15, 18, 24 and 30. The intersection of these rays and the isomephitic path, indicated by stars, marks the initial conditions for the eight simulations. The isopleth diagram shows simulations  $R = 3$  and 6 are above the ridgeline,  $R = 9$  is close to the scaling break ( $\beta = 9.4$ ) and the remainder are in the NOx limited region. For each simulation,  $O_3$ ,  $NO$ ,  $NO_2$ , PANs (RADM2 classes PAN + TPAN),  $HNO_3$ , ONIT (RADM2 class for organic nitrate) and peroxides (RADM2 classes  $H_2O_2$  + OP1 + OP2 and PAA) are plotted as a function of time. On each figure, ozone concentrations are given on the right-hand axis and the remaining on the left axis. The plots reveal several features which merit discussion.

To start, inspection of the  $NO_2$  concentration curve shows that increasing  $R$  (i.e. increasing initial VOC concentration) speeds up the early  $NO$  to  $NO_2$  conversion. For example, the  $NO_2$  peak occurs at 12:00 for  $R = 6$  and  $t = 9:00$  for  $R = 24$ . In all cases, the rise in ozone follows the  $NO_2$  rise; occurring earlier in the simulation for higher  $R$ -values. Also, in each simulation,  $NO$  concentrations decrease more quickly with increasing  $R$ . For all but the  $R = 3$  simulation,  $NO_2$

<sup>1</sup>I have coined this word based on the term 'mephitic air' used by Rutherford after his discovery of nitrogen in 1772

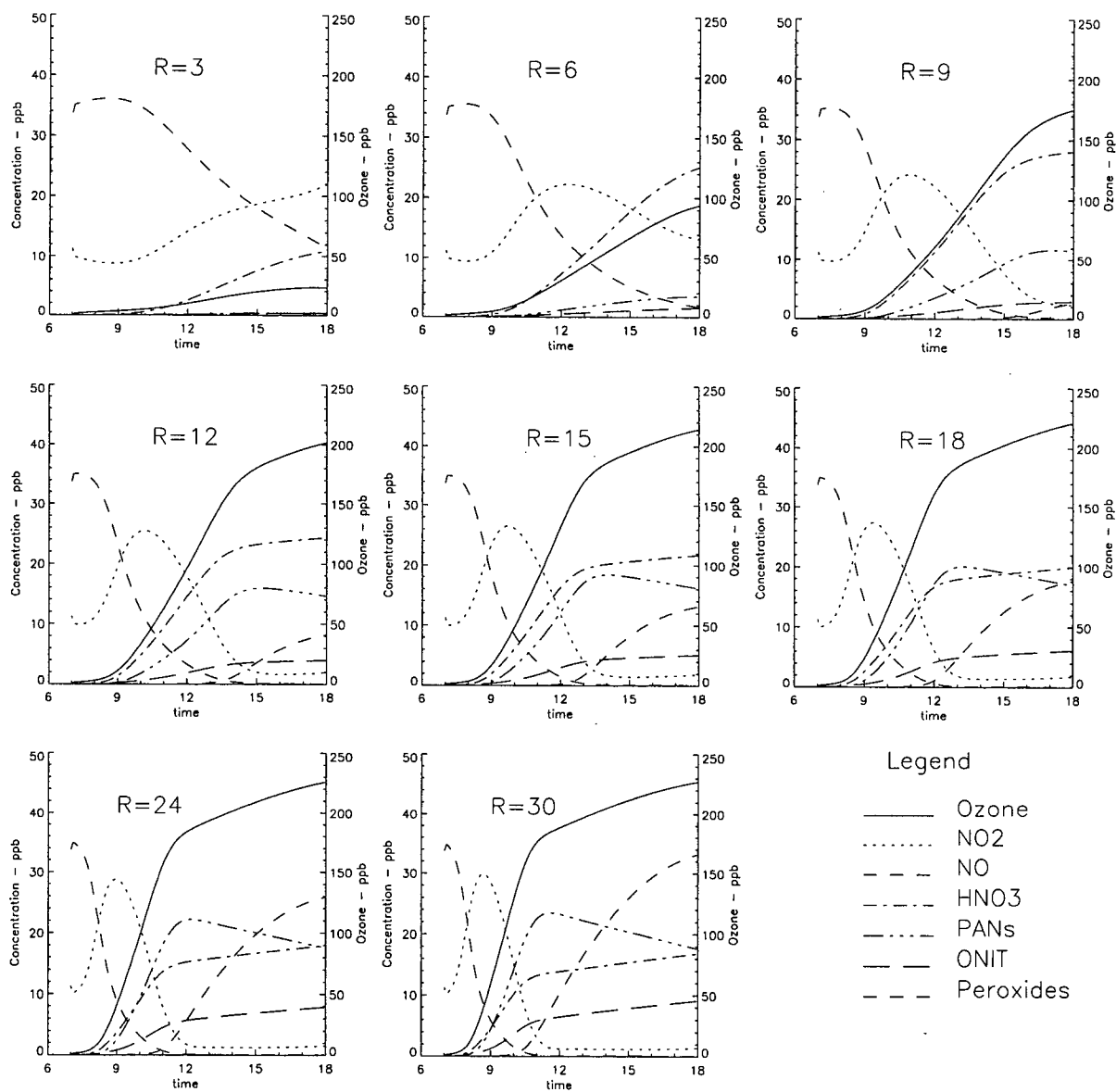


Figure 5.3: Temporal evolution of  $O_3$ ,  $NO_2$ ,  $NO$ ,  $HNO_3$ ,  $PAN$ ,  $ONIT$ , and peroxides concentrations for eight different OZIPR simulations each starting with initial  $NO_x$  concentration of 0.045 ppm but varying initial VOC concentration.

levels peak and then fall. For simulations below the scaling break ( $R > 9$ ),  $NO_2$  concentrations level off at a value around 2 ppb. The drop in  $NO$  and  $NO_2$  is matched by an increase in  $HNO_3$  for simulations with  $R > 9$  and by an increase in  $HNO_3$ , PANs and ONIT for the higher R-values. Finally, at the higher R-values, production of peroxides becomes noticeable.

Secondly, in all simulations, ozone concentration increases monotonically and the maximum

value increases with increasing R-value until  $R \approx 24$  where it remains roughly constant. This represents the NOS regime where maximum ozone concentration is now a largely a function of initial NOx concentration only. For simulations below the scaling break, the ozone temporal variability shows a marked decrease in growth rate towards early afternoon. Close inspection shows this slowing down coincides with the leveling off of  $NO_2$  at its low value. Thus it appears that once  $[NO_2] \approx 0$  (nitrogen dioxide concentrations do not go exactly to zero due to a steady state that is reached with PAN and the nitrate radical), ozone growth slows but does not cease. Inspection also shows that this change in growth rate occurs earlier with increasing  $[VOC]_o$ .

Finally, for simulations with  $R > \beta$ , the ozone versus time profile is 's-shaped'; with low concentrations for the first few hours, followed by a rapid increase and then a gradual slowing down. This pattern, which resembles the similarity profile (except there **NOx-scaled dimensionless maximum** ozone was plotted as a function of **R**), suggests a Weibull transformation may reveal something about the temporal dynamics of ozone formation. In order to use this transformation, all concentrations were first normalized by a common value:  $[O_3]_{max} = 230$  ppb ( $= \gamma[NOx]_o^a$  where  $\gamma$  and  $a$  are the WEX parameters for this example). Next, each normalized profile ( $f(t)/\gamma$ ) was Weibull transformed and plotted against  $\ln(t - t_o)$  (Figure 5.4). The Figure indicates for  $R > 12$ , simulations produce a marked 'dogleg' around  $\ln(t - t_o) = 2.0$ , with the bend more pronounced and occurring sooner for greater R-values. This bend marks a change in the rate of increase of ozone concentration with time and coincides with the low  $NO_2$  condition (see Figure 5.3). There is also another bend in the time series at  $\ln(t - t_o) \approx 0$ . This break is related to conditions which are radical limited and needs more explanation. I propose that the 'dogleg' arises from a change in the way ozone is produced; reflecting a change in governing chemical process. I also propose that this change causes the observed scaling break. To prove these assertions, I use the concept of ozone production.

### 5.3 Ozone Production

Following Tonnesen and Dennis (2000b), ozone concentration can be expressed as the cumulative production of ozone over a given time period i.e.:

$$[O_3](t) = [O_3](t_o) + \int_{t_o}^t P(O_3)dt \quad (5.1)$$

where  $P(O_3)$  represents the instantaneous production of ozone. This production represents the net effect of reactions which produced ozone to those that consume it i.e.:

$$P(O_3) = \frac{d[O_3]}{dt} = \text{Ozone Produced} - \text{Ozone Consumed} \quad (5.2)$$

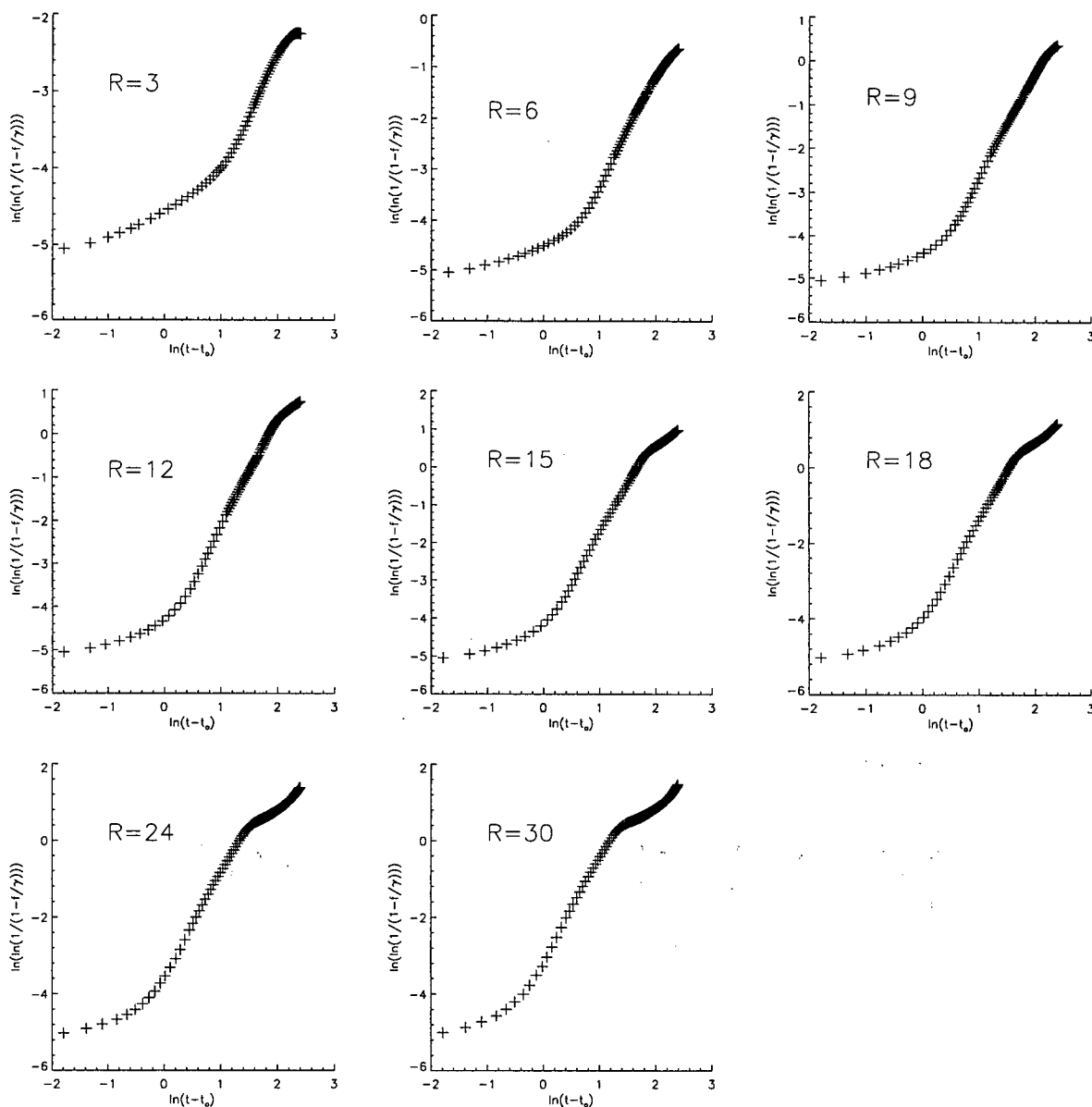


Figure 5.4: Weibull transformed dimensionless ozone concentrations (for the eight isomephitic simulations given in Figure 5.3) plotted against  $\ln(t - t_0)$ .

Determining an expression for  $P(O_3)$ , given a chemical reactions set, is a straight-forward process. For example, for the  $NO_x$ -only system, ozone is produced in R1 (with rate  $j_{NO_2}[NO_2]$ ) and consumed in R2 (with rate  $k_{NO}[NO][O_3]$ ) resulting in the following expression for ozone production:

$$P(O_3) = j_{NO_2}[NO_2] - k_{NO}[NO][O_3] \quad (5.3)$$

While expressions like Eq. (5.3) are easy to develop, even for systems involving many VOCs and radicals, evaluating them directly is usually not possible. However, expressions for  $P(O_3)$ , based on simplified photochemical systems, while not amenable to analytic evaluation, do provide useful insight into the governing chemical processes. For instance, Sillman et al. (1990), have found that when the instantaneous NOx concentration exceeds instantaneous VOC concentration:

$$P(O_3) \sim \frac{k_{OH}[VOC] (A[O_3] + B[VOC])}{k_{HNO_3}[NO_2] - C[VOC]} \quad (5.4)$$

where  $A$ ,  $B$ ,  $C$  are constants which measure the rate of radical production from ozone, aldehydes and carbonyl compounds respectively. This expression shows that ozone production increases with increasing VOC concentration and decreases with increasing  $NO_2$  concentration. When instantaneous VOC concentration exceeds NOx, they find a different approximation holds:

$$P(O_3) \sim [NO] (A[O_3] - B[VOC])^{1/2} \quad (5.5)$$

where production now shows only a slight dependence on VOC concentration and is proportional to NO concentration. Thus Sillman et al. (1990) classify ozone production into two different regimes based on the ratio of *instantaneous* VOC to NOx concentrations:

This division is also supported by Kleinman (1994) who further suggests that this separation reflects a fundamental change in photochemistry:

*'...the two types of photochemistry apparent at low and high NOx concentrations are not merely continuous differences, as NOx is varied, but instead reflects a structural change in reaction mechanism.'*

It is the intent of this chapter to prove that the scaling break arises as a result of such a structural change. There are several steps involved in the proof. To start, I propose that as the photochemical reactions proceed and NOx is removed more quickly than the VOCs, the resulting low NOx environment triggers a shift in ozone production. This shift in production affects the resulting ozone concentration (via Eq. (5.1)), gives rise to the 'dog-leg' in the ozone concentration versus time curve and ultimately alters the maximum or final ozone concentration. Next, I propose that the initial relative abundance of VOC to NOx (R-value) determines whether a switch to low-NOx conditions will occur. I will then show that these two assertions imply that a switch in ozone production causes a scaling break in maximum ozone concentration (when plotted as a function of  $R$ ) if the initial R-value is greater than a fixed value ( $\beta$ ).

I prove these assertions by constructing several simple models for ozone production, each showing two distinct production regimes. I use these models to explore how the change in production affects ozone concentration as a function of both time and initial precursor concentration.

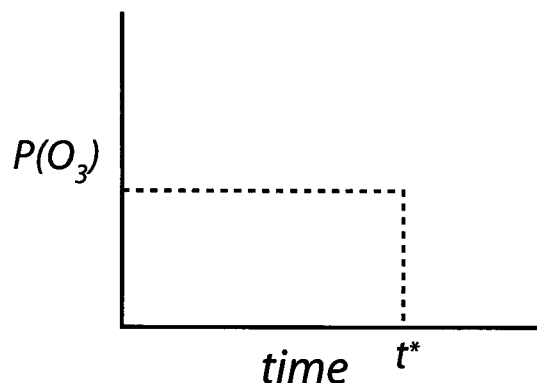


Figure 5.5: *Simple step model function for ozone production.*

### 5.3.1 Step function model for ozone production

I begin by constructing a simple model for ozone production ( $P(O_3)$ ) which shows a regime change – a step function. I use this model to show the connection between a production regime shift and the corresponding relationship for maximum ozone concentration as a function of initial VOC concentration. While this model may seem contrived, I will show that it captures interesting properties of ozone photochemistry and, in fact, represents the basis for the IER model (Johnson, 1984). In subsequent sections, I modify the model to make it more realistic.

The model, shown in Figure 5.5, has a constant  $P(O_3)$  level until time  $t^*$  at which point production drops to zero. The initial high production reflects the initially VOC-limited chemistry (analogous to the low-VOC regime in Eq.(5.4)). The drop to zero production at  $t^*$  reflects a switch to NO<sub>x</sub>-limited conditions, where all initial NO<sub>x</sub> has been converted to stable nitrogen products and production ceases (analogous to the low-NO<sub>x</sub> regime in Eq. (5.5)).

To this model, I add several features. I want to include a  $P(O_3)$ -dependence on initial precursor concentrations, and to start, I include only a VOC dependence – later a NO<sub>x</sub> dependence will be added. From Eq. (5.4), Sillman et al. (1990) show  $P(O_3)$  increases with increasing VOC concentration. To give the step function model such a VOC dependence, I construct a family of production curves with the following three properties (which, for now, I only partially justify but later generalize and discuss):

**Property I:** Motivated by Eq. (5.4), a larger initial VOC concentration produces a greater initial  $P(O_3)$  level.

**Property II:** For a greater initial VOC concentration, regime shift occurs earlier.

**Property III:** The switchover time ( $t^*$ ) is such that the area under the  $P(O_3)$ -time curve is

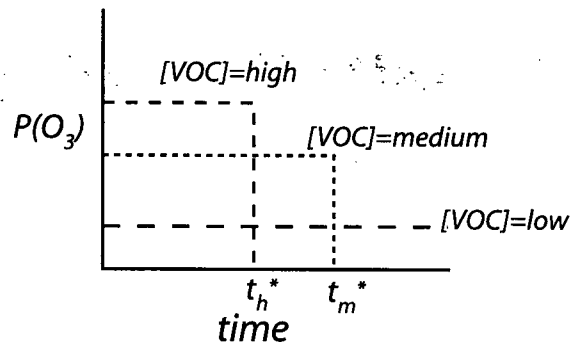


Figure 5.6: Three members of a family of step-model functions for ozone production. The high VOC switches regimes at  $t_h^*$ , the medium at  $t_m^*$  while the low VOC never switches regimes.

constant. The area under a  $P(O_3)$ -time curve represents an ozone concentration (see Eq. (5.1)) and so this rule implies production ceases when the corresponding ozone concentrations reach a fixed value, independent of VOC. This property, the hardest to justify, is explained as follows: I want the model to have the greatest maximum (peak) ozone concentration as a function of initial  $NO_x$  only. With production zero after the switchover, maximum ozone concentration becomes a constant (independent of VOC).

In Figure 5.6 I have sketched three members of a family of production curves, identified by initial VOC concentration, based on the above properties. From this Figure, the higher VOC concentration has a larger initial production but regime shift occurs sooner. The area under both the high and medium curves is constant. For the low VOC concentration, initial production rate is so low that switchover never occurs.

From a model for ozone production, ozone concentrations can be determined using Eq. (5.1). For the simple step-model function, this produces temporal profiles which increase linearly with time. If initial production is great enough and switchover occurs, then ozone concentrations reach a plateau where they remain. Figure 5.7 is a schematic of ozone concentration versus time curves for the production family given in Figure 5.6. From this Figure, higher production associated with the highest initial VOC concentration results in ozone concentrations rising quickest. However, both the medium and high VOC curves achieve the same final ozone concentration. The low VOC curve rises the slowest and never reaches the plateau.

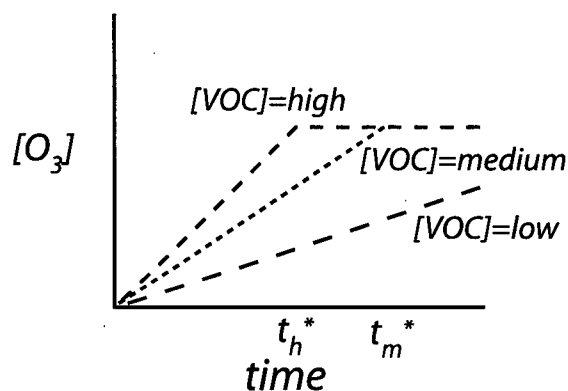


Figure 5.7: Ozone concentration curves for the three VOC given in Figure 5.6. The highest VOC reaches the plateau at  $t_h^*$ , the medium at  $t_m^*$  while the lowest never reaches a plateau.

### 5.3.2 Maximum ozone concentration

To finish the analysis, I now plot maximum ozone concentration as a function of initial VOC. However, instead of sketching curves, I numerically calculated a set of production, concentration and maximum ozone concentration curves using the step function model and typical production values. These results are *not* based on OZIPR model output. In Figure 5.8A, I start with typical production rates which I use to calculate concentrations (B) and maximum ozone concentration (C) for four initial VOC concentrations. In Figure 5.8A ozone production for the lowest initial VOC concentration ( $[VOC]_o = 1.0$  ppm) never shifts regimes, while the next highest shifts and the largest two switch progressively sooner. Integration of the production curves gives resulting ozone concentrations. Finally, in Figure 5.8C, the relationship between maximum ozone concentrations and initial VOC concentration has been plotted with two linear line segments passing through the data. The arrow running between Figures 5.8B and 5.8C indicates how the *final* ozone concentration along any curve in Figure 5.8B becomes the *maximum* concentration for that initial VOC concentration<sup>2</sup>. Thus, the step function model produces a maximum ozone/initial VOC curve which is piecewise – unlike the curved or ‘s-shaped’ curves produced from OZIPR model output. A second shortcoming of the step function model is that maximum ozone/initial VOC curve attains its maximum value rather than approaching it asymptotically.

It is worthwhile noting that the  $[O_3](t)$  versus  $t$  curve for  $[VOC]_o = 4.0$  ppb (Figure 5.8B), is geometrically similar to the  $[O_3]_{max}$  versus  $[VOC]_o$  profile (Figure 5.8C). This trend is also

<sup>2</sup>While only four curves are shown in Figures 5.8A and B, Figure 5.8C has been plotted using an additional 6 initial VOC concentrations. To avoid clutter, these extra members were not plotted in the first two graphs.

evident in the OZIPR simulations where dimensionless and scaled  $[O_3](t)$  curves, for NO<sub>x</sub>-limited conditions, show an 's-shaped' profile, similar to the shape of the WEX similarity relationship (for example, compare the  $R = 30$  plot in Figure 5.3 with the similarity function in Figure 3.7). For the step function model, this similarity arises because  $P(O_3)$  increases linearly with  $[VOC]_o$ . The corresponding parameterization for ozone as a function of time and initial VOC concentration ( $[O_3](t; [VOC]_o)$ ) is linear in both time and  $[VOC]_o$ . Had I chosen a  $P(O_3)$  production with quadratic dependence on  $[VOC]_o$ , each  $[O_3](t; [VOC]_o)$  curve would still be piecewise linear in time, but the parameterization of maximum ozone as a function of initial VOC ( $[O_3]_{max}([VOC]_o)$ ) would be quadratic for VOC concentrations that do not have a regime change and linear (constant) for those that do. Since OZIPR model output produces  $[O_3](t; [VOC]_o)$  curves which are geometrically similar to  $[O_3]_{max}([VOC]_o)$  curves, I suggest that any parameterization for the  $[O_3](t; [VOC]_o)$  should have initial VOC and time to the same power. This implies initial VOC concentration and time have the same effect on ozone concentration; increasing initial VOC concentration is equivalent to 'speeding up the clock'. I include this as a fourth property to be satisfied by a family of ozone production curves in Section 5.3.5.

So far, I have introduced a simple parameterization for ozone production and a set of rules to create a family of curves based on initial VOC concentration. I have shown that starting from the production curves, the  $[O_3]_{max}$  versus  $[VOC]_o$  relationship follows from Eq. (5.1). For the step function model, the  $[O_3]_{max}([VOC]_o)$  relationship differs from similar relationships obtained from model output: it is not 's-shaped' and it does not asymptotically approach its limiting value. While I will improve these shortcomings later, my main intention in this section is to provide the simplest basis (or essence) of ozone photochemistry. I believe that this step function model, with the properties for developing a family of curves based on initial VOC concentration, is a beginning to this end. In fact, in the next subsection, I show how the step model function generalizes the IER model.

### 5.3.3 IER and Step function model

While the step function model may seem a bit contrived, I now show that it can be used to develop the IER model (Johnson, 1984). Development of this model was guided by results for an extensive set of outdoor smog chamber experiments<sup>3</sup> and was intended to provide a simple set of formulae which quantitatively describe ozone formation (Johnson, 1984). The model predicts that initially,

<sup>3</sup>In essence my ozone model is being developed along a similar line but I am being guided by model output not smog chamber data. I will show that each is not without its own difficulties.

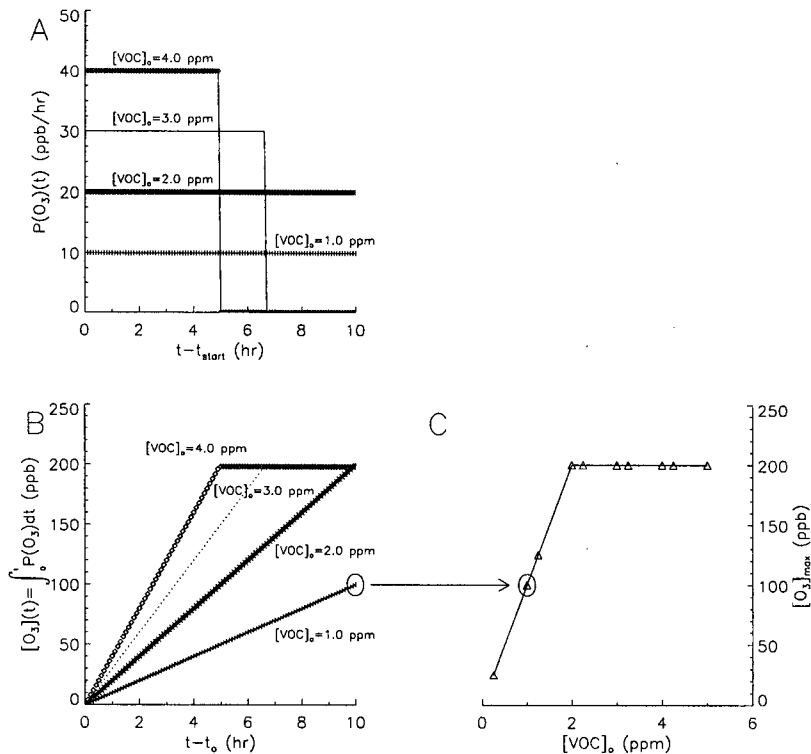


Figure 5.8: Ozone production (A), concentration (B) and maximum concentration (C) for a step function model. The arrow between Figures B and C highlights the relationship between final ozone concentration and maximum ozone concentration.

smog potential (PSP) (the sum of ozone produced and initial NO converted to  $NO_2$ ):

$$[PSP](t) = [O_3](t) - [O_3]_o + [NO]_o - [NO](t) \quad (5.6)$$

increases linearly with cumulative  $NO_2$  photolysis rate:

$$[PSP](t) = \rho(T)[VOC]_o \int_{start}^t j_{NO_2} dt \quad (5.7)$$

where  $\rho(T)$  is a temperature dependent measure of the VOC reactivity.<sup>4</sup> While the independent variable in this equation is time, the cumulative photolysis of  $NO_2$  ( $\int j_{NO_2} dt$ )— a measure of the energy added to the photochemical system — could also be used as the independent variable. By setting  $j(t) = \int j_{NO_2} dt$ , Equation 5.7 describes a linear dependence between smog potential and  $j(t)$  i.e.:

$$[PSP](j(t)) = \rho(T)[VOC]_o j(t)$$

<sup>4</sup>I have slightly modified the original notation to avoid confusion with my notation.

Differentiation of Eq. (5.7) with respect to  $j(t)$  gives PSP production rate ( $P(PSP)$ ):

$$P(PSP)(j(t)) = \frac{d[PSP](j(t))}{dj(t)} = \rho(T)[VOC]_o \propto [VOC]_o \quad (5.8)$$

Thus production is initially constant (and proportional to initial VOC concentration).

Furthermore, the model does not have smog potential growing indefinitely with  $j(t)$ . The model limits smog potential to a maximum value, independent of initial VOC concentration:  $[PSP]_{max} = \beta[NOx]_o$  which implies that at some time ( $t_{cease}$ ), smog production ceases:

$$P(PSP)(j(t_{cease})) = 0 \quad (5.9)$$

Together, Equations 5.8 and 5.9 describe a step function model for PSP production (when considered as a function of  $j(t)$ ). Furthermore, PSP production also satisfies my properties I, II, III for a family of production curves, namely:

**Property I:** This property is satisfied by Eq. (5.8) which shows initial production is greater for larger initial VOC concentration.

**Property II:** The IER model has PSP reaching a maximum value ( $\beta[NOx]_o$ ) when:

$$\rho(T)[VOC]_o j(t) \geq \beta[NOx]_o \quad (5.10)$$

Again, this implies  $P(PSP)$  goes to zero, with switchover ( $j^*$ ) occurring when:

$$j^* = j(t^*) = \frac{\beta[NOx]_o}{\rho(T)[VOC]_o} \quad (5.11)$$

which decreases with increasing  $[VOC]_o$ .

**Property III:** The left hand side of the inequality in Eq. (5.10) represents the area under a PSP production- $j_{NO_2}$  curve (when this is given by a step function), indicating that switchover occurs when a fixed area (in this case  $\beta[NOx]_o$ ) is reached.

Thus we can think of the IER model as parameterizing PSP production using a step function model which satisfies properties I, II, III of Section 4.3.1. While the IER model has been criticized for its linear dependence of maximum ozone concentration on initial NOx (Blanchard, 2000), the basis for this model (Eq. 5.7 and 5.10) is supported by environmental chamber data and current understanding of atmospheric chemistry (Blanchard et al., 1994).

### 5.3.4 PSP production

In this section, I justify the step-function nature of the IER model, and propose improvements, by examining PSP production using a simple reaction set. Consider a photochemical system which

includes the two NO<sub>x</sub>-only reactions (R1a and R3) along with the conversion of NO to NO<sub>2</sub> by peroxy radicals (R12):



Based on these three reactions ozone production remains unchanged from the NO<sub>x</sub>-only system i.e.:

$$P(O_3) = \frac{d[O_3]}{dt} = j[NO_2] - k_{NO}[NO][O_3] \quad (5.12)$$

The rate of change of NO is given by:

$$\frac{d[NO]}{dt} = j[NO_2] - k_{NO}[NO][O_3] - k_{RO_2}[RO_2^\bullet][NO] \quad (5.13)$$

Subtracting Eq. (5.12) from Eq. (5.13) gives a relationship for PSP production:

$$P(PSP) = \frac{d[O_3]}{dt} - \frac{d[NO]}{dt} = k_{RO_2}[RO_2^\bullet][NO] \quad (5.14)$$

Equation 5.14 can be used as a physical basis for the IER model and to propose improvements. Based on Eq. (5.14)  $P(PSP)$  is non-zero so long as there is initial NO and  $RO_2^\bullet$  radicals. As NO<sub>x</sub> is converted to NO<sub>z</sub>, NO concentrations drop (for example, see Figure 5.3) suggesting that  $P(PSP)$  should also decrease. This explanation does not take into account peroxy radical influences on PSP production but it does suggest that  $P(PSP)$  should show a drop from an initial state to a lower one. Equation 5.14 can be used to justify Property I: assuming the main source of peroxy radicals arises from photolysis of VOCs and  $OH^\bullet$  attack on VOCs, then higher initial VOC concentrations should lead to higher  $RO_2^\bullet$  concentrations and higher  $P(PSP)$ . I cannot justify Property II and III using Eq. (5.14) but I can use it to suggest improvements to the step function model. Namely, as the sun reaches its zenith, both VOC photolysis and  $OH^\bullet$  attack should increase with time (since the main source of  $OH^\bullet$  is the photolysis of ozone) before reaching a peak around midday (when the sun is at its zenith), and then declining throughout the afternoon. This suggests replacing the initial constant production with a production which starts at zero, increases to a maximum and then decreases. I use these ideas to improve the step-function model (and indirectly the IER model) in the next section. However, I modify my model to use  $j(t)$  as the independent variable instead of  $t$ .

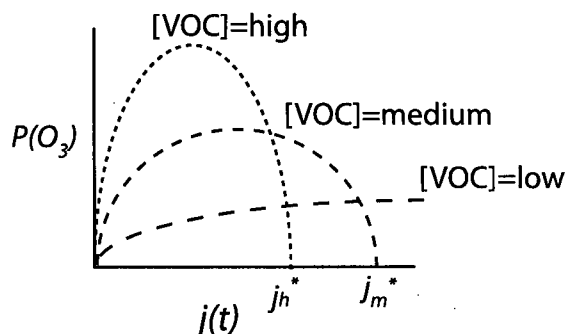


Figure 5.9: Family of production curves for three initial VOC concentrations using the quadratic model. With the high initial VOC concentration, production peaks before falling to zero at  $t_h^*$ . Production from the medium VOC concentration ceases at  $t_m^*$  while production from the lowest VOC never falls to zero.

### 5.3.5 Quadratic Model for Ozone Production

To include the effects of ozone production on changing solar zenith, I replaced the linear step function model with a quadratic version. In this configuration, production increases with  $j(t)$  until reaching a maximum after which time it decreases until reaching zero where it remains fixed (representing a switch to low production after most NO<sub>x</sub> is converted to NO<sub>z</sub>). I developed a parameterization for a family of such curves, based on my three properties:

**Property I:** Higher  $[VOC]_o$  leads to higher peak production.

**Property II:** Higher  $[VOC]_o$  leads to a quicker switch to zero production.

**Property III:** The area under each production- $j(t)$  curve is constant.

**Property IV:**  $[VOC]_o$  and  $j(t)$  are both of order two in the parameterization of  $[O_3](t; [VOC]_o)$ .

Figure 5.9 shows a schematic of three production curves based on this model. As before, integration of the production curves yields ozone concentrations and the maximum from each concentration curve then gives a single point on the  $[O_3]_{max}$  versus  $[VOC]_o$  curve. These steps have been carried in Figure 5.10: Figure (A) shows production based on typical values, (B) concentrations after integration, (C) maximum ozone versus initial VOC concentration (where, again, addition  $[VOC]_o$  levels have been included to highlight features) and (D) gives the corresponding ‘Weibullized data’ modeled by two line segments. Again, these plots are *not* based on OZIPR model output but simply the quadratic production model using typical production rates to quantify the various curves.

*Is the quadratic model an improvement over the step-function model?* To start, both the concentration curves (Figure 5.10B) and the maximum ozone curve (Figure 5.10C) are now more ‘s-shaped’,

in closer agreement with Figure 5.3 and Figure 3.7 respectively.<sup>5</sup> However, to be consistent with the model output, the concentration curves for  $[VOC]_o = 4.0$  (Figure 5.10B) should approach its limiting value in an asymptotic manner. Furthermore, while the Weibull plot shows two distinct linear segments, the zero slope of second curve is unrealistic (based on the results of Chapter 4). To eliminate both flaws will require production to asymptotically approach zero after peaking. I examine the consequences of such a parameterization in section 5.4.7.

Finally, note that the Weibull plot produces a scaling break **not** because of the local maximum in ozone production but instead because production is fixed at zero after most of the NOx conversion to NOz. For instance, the  $[VOC]_o = 2.4$  ppb production curve does not reach zero production and, consequently, its ozone maximum lies to the left of the scaling break in the Weibull plot ( $\ln 2.4 = 0.88$ ). However, this production curve reaches a maximum at  $j \approx 180$ . This suggests that the local maximum in the ozone production curve does not produce the scaling break. I explore this premise in the next section.

### 5.3.6 Weibull Model

In this section, I present a model for ozone production which shows asymptotic decay after reaching a maximum. My intention with this model is not to see how well it reproduces the OZIPR features but rather to prove that a change in curvature or a maximum in production are *not* associated with the scaling break. To do this, I created a model for production which peaks and then shows asymptotic decay. While any bounded curve, which is non-zero for all  $j(t)$ , will serve for the parameterization, I have chosen the Weibull distribution. Let the family of production curves be given by:

$$P(O_3)(j; [VOC]_o) = \frac{[VOC]_o}{\beta'} \left( \frac{[VOC]_o j}{\beta'} \right)^{\alpha-1} \exp \left[ - \left( \frac{[VOC]_o j}{\beta'} \right)^\alpha \right] \quad (5.15)$$

with corresponding ozone concentrations:

$$[O_3](j(t); [VOC]_o) = \left( 1 - \exp \left[ - \left( \frac{[VOC]_o j}{\beta'} \right)^\alpha \right] \right)$$

and maximum ozone concentration:

$$[O_3]_{max} = \left( 1 - \exp \left[ - \left( \frac{[VOC]_o J}{\beta'} \right)^\alpha \right] \right) \quad (5.16)$$

where  $J = j(t_{end})$  is a constant.

Letting  $J/\beta' = 1/\beta$ , the single Weibull model from Chapter 3 (Eq.(3.9) but now as a function of VOC instead of  $R$ ) is recovered. With maximum ozone concentration parameterized by a

<sup>5</sup>In Figure 3.7 I have plotted NOx-scaled dimensionless maximum ozone versus  $R$ . For now, I am ignoring the effects of initial NOx by assuming a constant value. As a result, the two curves plot equivalent variables.

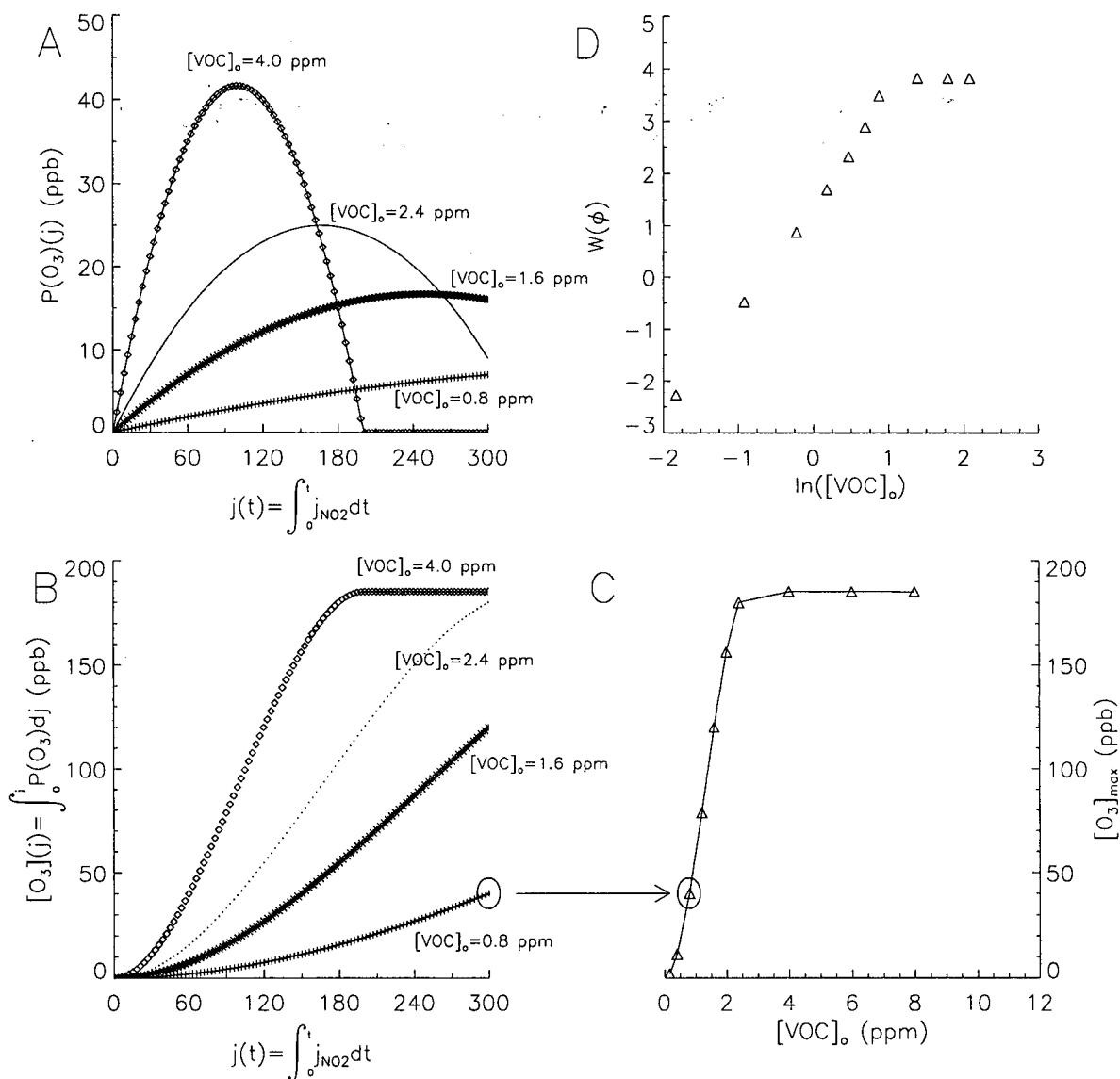


Figure 5.10: Ozone production (A), concentration (B), and maximum ozone concentration (C) for four initial VOC concentrations using a parabolic model of ozone production. Also plotted is Weibull transformed normalized maximum ozone concentration versus natural logarithm of initial VOC concentration (D).

single Weibull (Eq. (5.16)), there **cannot** be a break in the ‘Weibullized data’ – a single Weibull produces a *single* straight line upon Weibull transformation. However, such a parameterization shows both a local maximum and a change in curvature (where slope of the production-time curve switches from positive to negative). I conclude, that the scaling break is neither associated with a production maximum nor a change in production curvature – it must be associated with something

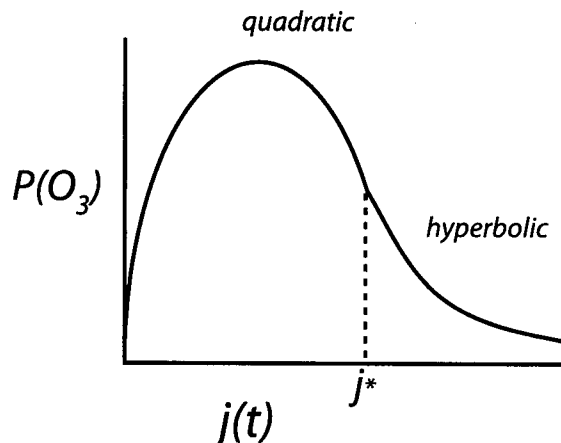


Figure 5.11: *Modified quadratic curve with hyperbolic tail. Transition occurs at  $j^*$ .*

fundamentally different. That a parameterization like Eq. (5.16) shows no scaling break but produces a ‘ridgeline’ on an isopleth diagram (see for example Figure 2 in Chang and Rudy (1993)) is also of interest and is discussed in the next chapter.

### 5.3.7 Quadratic with Asymptotic Decay

I now create a model for ozone production which shows a scaling break and has ‘Weibullized data’ showing a non-zero slope after the scaling break. In order to produce the break, the quadratic model is fitted with a hyperbolic tail. This tail represents the shift in production that occurs once most NO<sub>x</sub> is converted to NO<sub>z</sub>. I make use of the quadratic model but stress that **any** family of curves which has the desired properties (to be outlined next) will capture the key features of the OZIPR curves – there does not appear to be any physical link between the Weibull distribution and ozone formation. The model makes a transition to hyperbolic behaviour once the area under the production curve reaches a constant. In addition, the total area under the production curve is bounded. This now places two integral constraints on the model; one for total area under the production curve and the other for transition to the hyperbolic regime. Figure 5.11 sketches the model.

To create a family of production curves, I make the peak value increase with increasing initial VOC concentration and require this peak to occur sooner. Figure 5.12 shows a family of production, concentration and the corresponding maximum value and Weibull plots based on this model. Both the concentration (Figure 5.12B) and maximum value profiles (Figure 5.12C) show asymptotic behaviour. The Weibull plot (Figure 5.12D) shows results clustering onto two line segments with

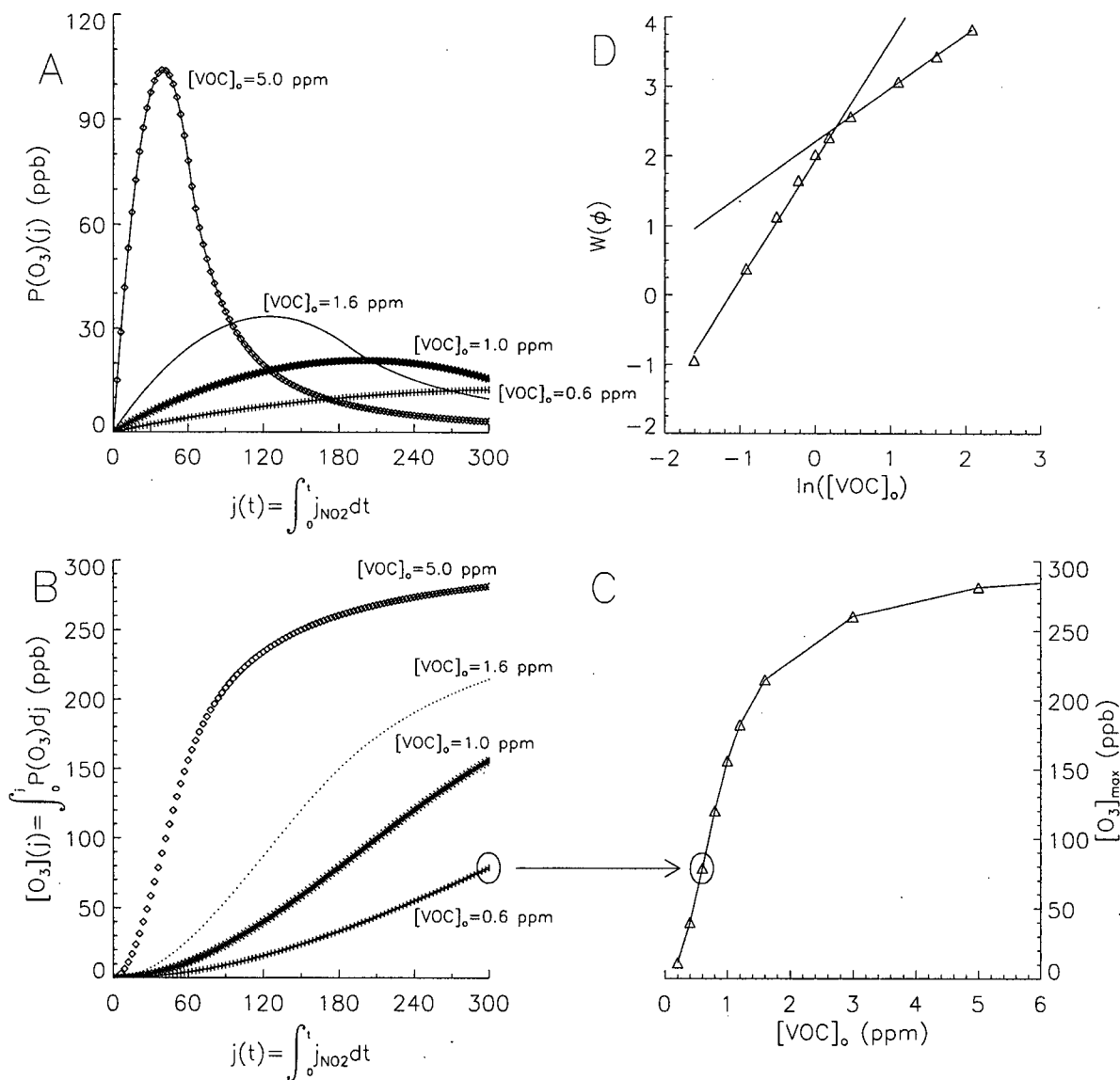


Figure 5.12: Ozone production (A), concentration (B), and maximum ozone concentration (C) for four initial VOC concentrations using the parabolic model with hyperbolic tail. Also shown is the Weibull transformed maximum ozone concentration fit by two line segments (D).

the second segment having a positive, non-zero slope. Thus, even for a quadratic parameterization for production, a Weibull distribution produces a good fit to the corresponding maximum ozone curves.

Let me summarize what I have accomplished so far. I have found that the best starting point

for developing a simple model of ozone photochemistry begins with ozone production. I find that any model for ozone production should initially increase, reach a maximum and then asymptotically decrease. Furthermore, the parameterization should have a transition to a second functional relationship in order to produce a scaling break. In addition, production should increase with increasing initial VOC concentration. Any production parameterization which has these properties will reproduce the key traits of the OZIPR model output namely:

- Ozone concentration and maximum ozone concentration curves will have an 's-shape'.
- A scaling break will be observed when maximum ozone versus initial VOC concentration is Weibull transformed.
- Maximum ozone versus initial VOC concentration curves which are well modeled by a composite of two Weibull distribution.

To complete my characterization of ozone formation, I must still include a NO<sub>x</sub> dependence.

### 5.3.8 Production models with initial NO<sub>x</sub> dependence

In this section I make explicit any NO<sub>x</sub> (and hence  $R$ ) dependence on ozone production and generalize the four properties outlined in Section 5.3.5.

I start by examining ozone concentrations from a set of nine OZIPR smog chamber simulations using the Stock urban speciation. Figure 5.13 shows the nine ozone curves plotted as a function of  $j(t)$ . All simulations have  $R$ -values greater than  $\beta$ . Along the first row, all simulations have initial an NO<sub>x</sub> concentration of 0.015 ppm, along the second 0.045 ppm and along the third 0.075 ppm. The first column of plots have a common  $R$ -value of 12, the second column 24 and the third 30. In each plot, I have also included a dashed vertical line at the approximate  $j$ -value where the concentration curve shows a slowing of growth. From these plots, a number of observations can be made:

- A switch to a slowing of ozone concentration occurs at the same  $j$ -value for simulations with identical  $R$ -values; independent of both initial NO<sub>x</sub> and VOC concentration. In addition, increasing  $R$  causes the transition to occur sooner.
- Ozone concentration at the time of switch is roughly constant for simulations with identical initial NO<sub>x</sub> concentrations; independent of initial VOC or  $R$ -values. In terms of production, this implies that for a given initial NO<sub>x</sub> concentration, switchover occurs for a fixed area under the production curve, independent of VOC or  $R$ . In addition, as initial NO<sub>x</sub> increases, ozone concentration at the switch increases.

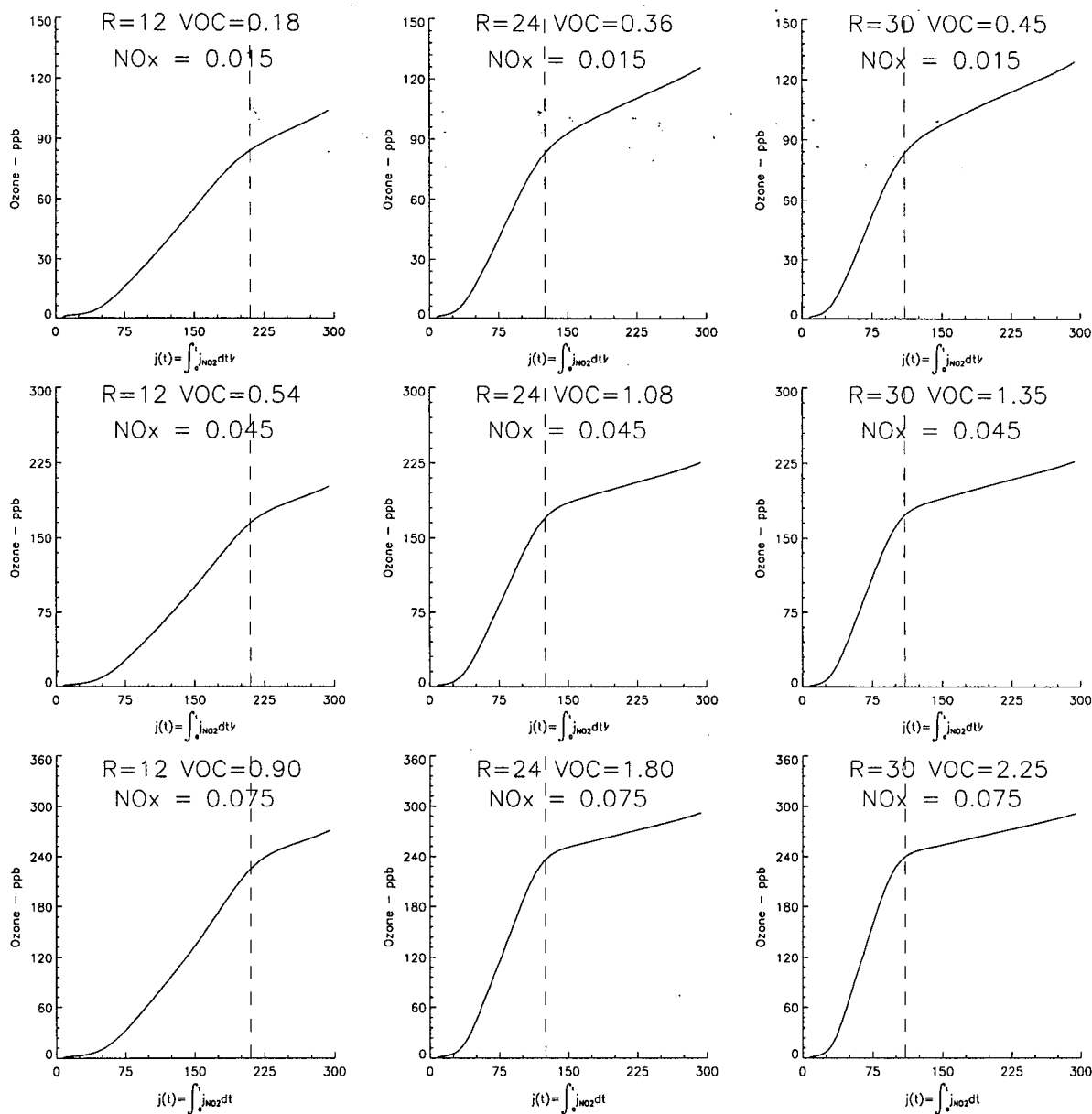


Figure 5.13: Ozone concentration as a function of cumulative  $\text{NO}_2$  photolysis rate for nine different initial  $\text{NO}_x$  and VOC conditions. Dashed lines roughly indicate the slowing of the increase in ozone concentration.

- For simulations with identical R-values, increasing initial  $\text{NO}_x$  concentration increases final ozone concentration.

In terms of ozone production, it now appears that  $P(\text{O}_3)$  should increase with both increasing  $R$  and  $\text{NO}_x$  and that the timing of the regime shift is determined by initial R-value only. These suggests the following modifications to my original parameterization properties:

**Property Ia:** Larger  $R$ -values lead to greater peak  $P(O_3)$  levels.

**Property Ib:** Larger initial  $NO_x$  concentrations lead to greater peak  $P(O_3)$  levels.

**Property II:** Larger  $R$ -values cause the transition ( $j^*$ ) to occur sooner.

**Property IIIa** The total area under the  $P(O_3)$ - $j(t)$  curve is a function of initial  $NO_x$  only.

**Property IIIb:** The area under the  $P(O_3)$ - $j(t)$  curve at the transition time is a function of initial  $NO_x$  only.

**Property IV:** The resulting parameterization for ozone concentration must have  $R$  and  $j(t)$  to the same order.

At first glance, the IER model does not appear to satisfy these properties. For example, PSP production (Eq. (5.8)) shows neither an  $R$  nor an  $[NO_x]_o$  dependence but only a VOC dependence. However, closer inspection shows the model does satisfy the above rules but, as a consequence of the way it scales maximum ozone with initial  $NO_x$  and the way production depends on  $R$ , both the  $NO_x$  and  $R$  dependence cancel – leaving what appears to be only a VOC dependence. This can be seen by rewriting the PSP production rate (Eq. (5.8), (5.9)) using  $R = [VOC]_o/[NO_x]_o$  as:

$$P(PSP) = \begin{cases} \rho(T)[VOC]_o = \rho(T)[NO_x]_o R & j < j^* \\ 0 & j > j^* \end{cases} \quad (5.17)$$

Equation (5.17) now includes an initial  $NO_x$  dependence as well as an  $R$  dependence. Production now increases with  $R$  (Ia) and  $[NO_x]_o$  (Ib), transition occurs sooner for higher  $R$  (II) and area under the production curve (both at the total (IIIa) and transition (IIIb)) is a function of  $[NO_x]_o$  ( $= \beta[NO_x]_o$ ). Finally, integration of Eq. (5.17) shows  $PSP$  is a linear function of  $j$  and  $R$  (IV).

### 5.3.9 Links between scaling break and regime change

So far in this chapter, I have set out to understand the scaling break in terms of the underlying chemistry. Along the way, I have developed two different but related ideas: the link between ozone production and the scaling break and the essential properties of ozone production. I summarize the latter first.

The fundamental basis for describing ozone formation is in terms of ozone production. A realistic parameterization for production should show  $P(O_3)$  initially increasing, reaching a peak value and then decreasing. Corresponding ozone concentration curves will then show ‘s-shaped’ behaviour. The parameterization should have two distinct regimes so that the corresponding Weibull plot has a scaling break. However, the scaling break corresponds to neither a local maximum in production nor a change in curvature – instead it stems from a change in regime. Regime change appears to occur once the cumulative production (i.e. ozone concentration) reaches a critical level. Ozone

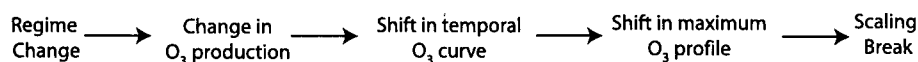


Figure 5.14: Links between scaling break and regime change.

production in the second regime should show a non-zero and asymptotically decreasing trend to generate a non-zero slope of the ‘Weibullized data’ after the scaling break.

The link between scaling break and regime shift runs like this: A change in photochemical regime causes a fundamental shift in ozone production which alters the temporal variability of the ozone concentration curve. This affects the maximum concentrations which are used to produce the  $[O_3]_{max}$  versus  $[VOC]_o$  (or more generally  $[O_3]_{max}$  versus  $R$ ) curve which, when Weibull transformed, produces the scaling break. A schematic of this logic is given in Figure 5.14. This analysis gives rise to a new question: *What is the physical basis for the regime change? For a given  $[NOx]_o$ , why does regime shift occur at a fixed ozone level?* I address these questions in the next sections.

The second major finding of this chapter has been the development of a set of properties which characterizes ozone production. I have shown that the IER model (Johnson, 1984) can be thought of as a step function parameterization for smog production ( $P(PSP)$ ) satisfying these properties. I have also used these properties to propose improvements to the IER model.

### 5.3.10 WEX temporal ozone profile

Before moving on, I present a parameterization for ozone concentration as a function of  $j(t)$  based on the WEX model. Based on the four properties for ozone production, the parameterization for maximum ozone concentration (Eq. (3.25)) can be extended, by adding a  $j$ -dependence whenever an  $R$ -dependence occurs (Property IV):

$$\frac{[O_3]}{j_{av}/k_{NO}}(j(t), R, [NOx]_o) = \gamma \left( \frac{[NOx]_o}{j_{av}/k_{NO}} \right)^a \left( 1 - \exp \left[ -\lambda \left( \frac{Rj}{\beta'} \right)^\alpha \right] \right) \quad (5.18)$$

where  $J/\beta' = 1/\beta$ . The corresponding ozone production relationship is:

$$\frac{P(O_3)}{j_{av}/k_{NO}} = \gamma \left( \frac{[NOx]_o}{j_{av}/k_{NO}} \right)^a \lambda \frac{R}{\beta'} \left( \frac{Rj}{\beta'} \right)^{\alpha-1} \exp \left[ -\lambda \left( \frac{Rj}{\beta'} \right)^\alpha \right] \quad (5.19)$$

Figure 5.15 shows 9 plots of ozone concentration versus  $j(t)$ . Each plot has model output from the RADM2 mechanism using the Stock urban speciation, along with curves based on Eq. (5.18). I must mention that new WEX parameter values were **not** found specifically for Eq. (5.18) – the same values found during the regression of maximum ozone to initial VOC and NOx were used. The  $R = 12$  and  $R = 24$  plots correspond to those in Figure 5.13 but in order to get a wider

variety of initial conditions, I have replaced the  $R = 30$  plots with three simulations below the ridgeline with  $R = 6$ . Except for the low  $R$ /low NOx plots ( $R = 6$  and  $[NOx]_o = 0.015, 0.045$  ppm), Eq. (5.18) shows good agreement with the model output. In many cases, Eq. (5.18) does not match the transition time exactly but does manage to be within  $\pm 10\% j^*$ . Notice that the final ozone concentrations are in close agreement with the model output – this is to be expected since these maximum values were the ones used in the regression of the WEX parameters. Figure 5.15 can be compared with smog chamber experiments used to validate the RADM2 mechanism. Figure 5.16 shows ozone concentrations during a smog chamber study experiment conducted at the State Wide Air Pollution Research Centre (SAPRC) in Riverside, California. Also included is the simulated ozone concentration using a version of RADM2 model which has been modified to include expected chamber effects. The simulation started with 0.476 ppm of NOx and 17.79 ppm of a complex mixture of reactive organic species (Carter and Lurman, 1991). From the Figure, the level of agreement between RADM2 and the data appears to be of the same order as Eq. (5.18) and RADM2.

## 5.4 Feedback Mechanisms and Ozone Photochemistry

In this section I explain the chemistry behind the regime change. While ozone production results from the integrated effect of a complex set of photochemical processes, Jeffries and Tonnesen (1994) suggest that it should be viewed as the interaction of two competing cycles each driven by sunlight: a radical driven organic cycle and an inorganic NO-cycle. It is the interaction of these cycles that leads to ozone production. I will describe these cycles from a slightly different perspective – using positive and negative feedback loops – and show that it is the interaction of the feedback loops that leads to the scaling break.

### 5.4.1 Positive Feedback Loop

In section 5.3.4, I showed that for a simplified set of reactions, PSP production was proportional to the product of peroxy radical concentration times NO concentration (Eq. 5.14). In a similar vein, Sillman et al. (1990) argue that ozone production is proportional to the rate of  $OH^\bullet$  attack on VOCs:

$$P(O_3) \sim k_{OH}[OH^\bullet][VOC] \quad (5.20)$$

Equation (5.20) implies production increases when  $OH^\bullet$  concentration increases. However, as mentioned in the introduction, a major source of  $OH^\bullet$  radicals is the photolysis of ozone ( $R4$  and  $R5$ ). Hence  $P(O_3)$  increases when ozone concentration increases. Thus we can say that ozone is an

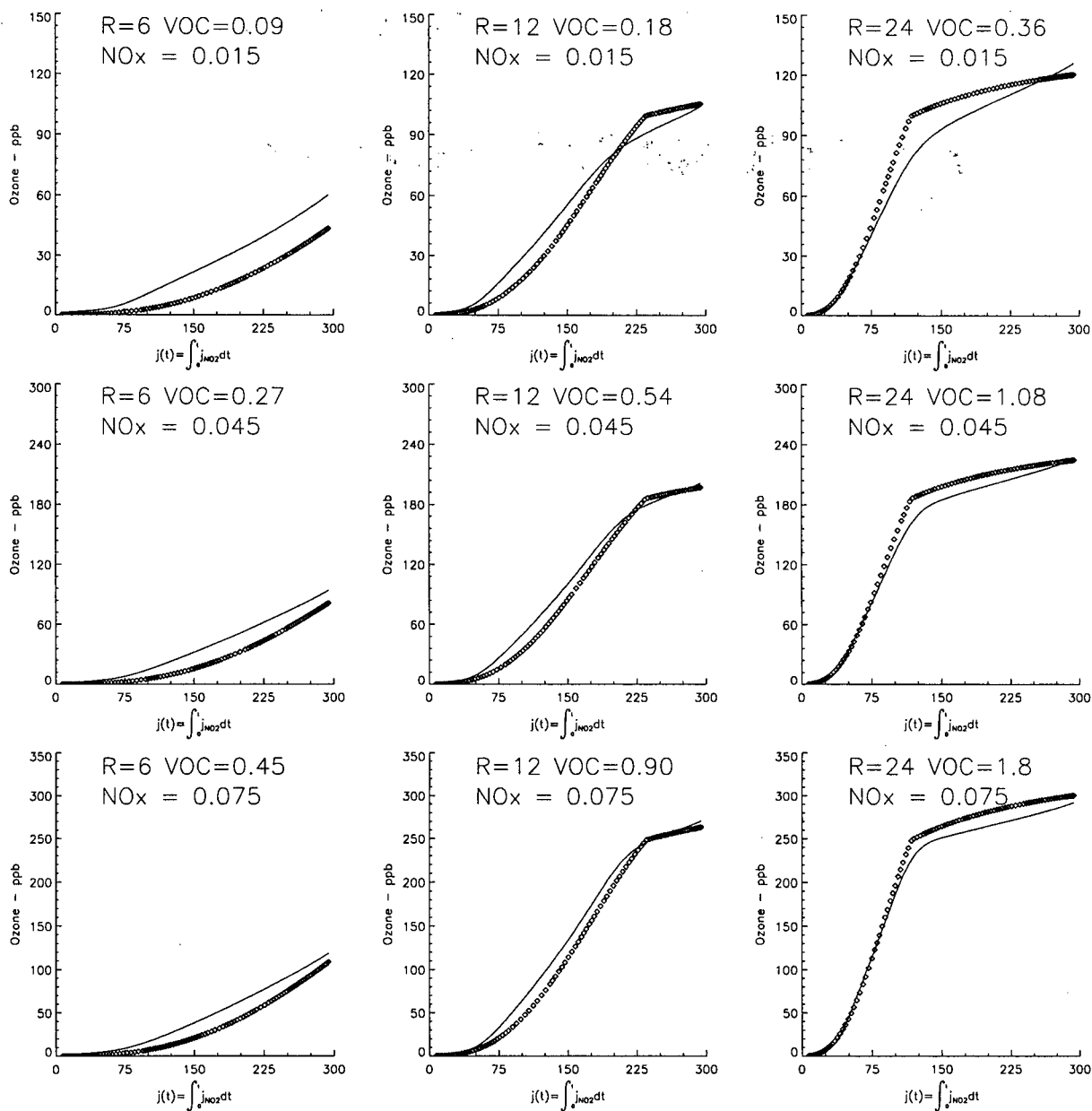


Figure 5.15: Ozone concentration versus time for a series of nine smog chamber simulations. Solid lines represent model output using the RADM2 mechanism (Stockwell et al., 1990) and circles represent results based on Eq. 5.18.

autocatalyst in its own production i.e. ozone production increases as ozone concentration increases. This is analogous to saying: *It takes money to make money.*

Figure 5.17 depicts ozone production as a positive feedback mechanism. In this schematic, ozone

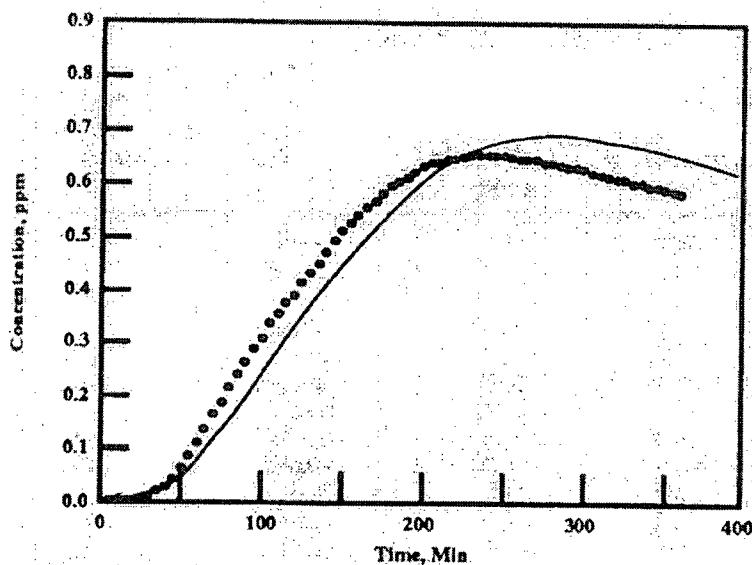


Figure 5.16: Ozone concentration versus time for SAPRC smog chamber simulation EC237. Dots are smog chamber observations and the solid line is model output using the RADM2 mechanism (Stockwell et al., 1990). Taken from Carter and Lurman (1991).

photolyzes to produce  $OH^\bullet$  radicals which attack VOCs to produce peroxy radicals. These convert  $NO$  to  $NO_2$  which then photolyzes to produce ozone. Note that each ozone photolysis can produce two  $OH^\bullet$  (reaction  $R5$ ) and each  $OH^\bullet$  can initiate two  $NO$ -to- $NO_2$  conversions. Furthermore, since the second  $NO$ -to- $NO_2$  conversion (not shown in Figure 5.17), reproduces the  $OH^\bullet$ , the original  $OH^\bullet$  can attack even more VOCs, leading to further ozone production.

#### 5.4.2 Negative Feedback Loops

Positive feedback loops cannot continue indefinitely. At some point, these amplifying processes uncover stabilizing mechanisms that limit growth. For ozone production this happens with the production of  $NO_2$ .

An interesting aspect of ozone production is that initial  $NO$  must first be converted to  $NO_2$  before ozone levels rise since surplus  $NO$  quickly titrates ozone ( $R2$ ). Thus ozone concentrations rise in response to elevated  $NO_2$  concentrations. Furthermore, high ozone levels lead to elevated  $OH^\bullet$  levels ( $R4$  and  $R5$ ). However, high  $OH^\bullet$  and  $NO_2$  concentrations favour the formation of nitric acid ( $R9$ ) – on average  $OH^\bullet$  reacts with  $NO_2$  5.5 times faster than with VOCs (Seinfeld and Pandis, 1998) – leading to increased  $HNO_3$  production ( $P(HNO_3)$ ). To see the effects of  $P(HNO_3)$  on the system reactivity, I have plotted in Figure 5.18 instantaneous  $NO_2$  and  $HNO_3$  concentration as

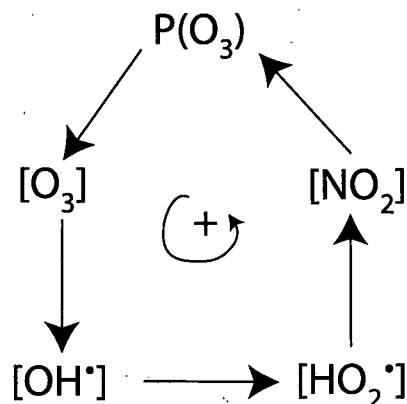


Figure 5.17: Ozone production builds ozone concentration. Photolysis of ozone gives rise to elevated hydroxyl concentrations resulting in increased attack on VOCs and enhanced peroxy concentrations. These radicals convert more  $NO$  to  $NO_2$  which leads to greater ozone production. Because each ozone photolysis can produce two hydroxyl radicals and each  $OH^\bullet$  can oxidize many  $NO$  molecules, a small initial amount of ozone can lead to a large final concentration.

well as the fraction of  $OH^\bullet$  that react with VOC (denoted as  $f_{OH+VOC}$ ) as a function of  $j$  using the RADM2 (Stockwell et al., 1990) mechanism and the Stock urban speciation with  $[VOC]_o = 1.08$  ppm and  $[NO_x]_o = 0.045$  ppm. Initially, both the  $NO_2$  concentration and  $f_{OH+VOC}$  increase as the system reacts. However,  $NO$  to  $NO_2$  conversions increase  $NO_2$  concentration to a point where  $NO_2$  competes with the VOCs for the  $OH^\bullet$  radical causing a decrease in  $f_{OH+VOC}$  and an increase in  $HNO_3$  concentration – effectively lowering the reactivity of the system. Finally, the continued removal of  $NO_2$  via  $HNO_3$  production results in sufficiently low  $NO_x$  concentrations that  $NO_2$  no longer competes effectively for  $OH^\bullet$ . This is marked by an increase in  $f_{OH+VOC}$  and by a slowing of the increase in  $[HNO_3]$ . The dynamics of the system at the resulting low  $NO_x$  concentrations (discussed in the next section) is paramount to understanding the regime change (and hence the scaling break).

To summarize, as ozone production begins to show rapid growth, it produces conditions favourable for nitric acid production. This production removes  $NO_2$  and ultimately slows ozone production. This negative feedback loop is schematically sketched in Figure 5.19.

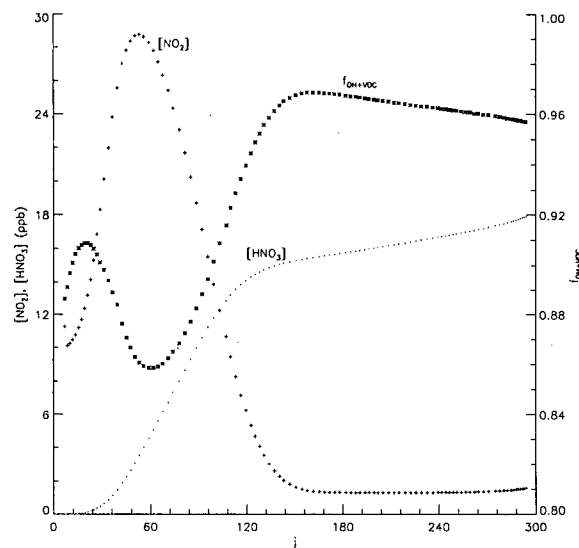


Figure 5.18: The effects of  $HNO_3$  production on the reactivity of a photochemical system.  $[NO_2]$ ,  $[HNO_3]$  and  $f_{OH+VOC}$  versus cumulative  $NO_2$  photolysis rate  $j$  for an OZIPR simulation using the RADM2 mechanism (Stockwell et al., 1990) and the stock urban mixture.

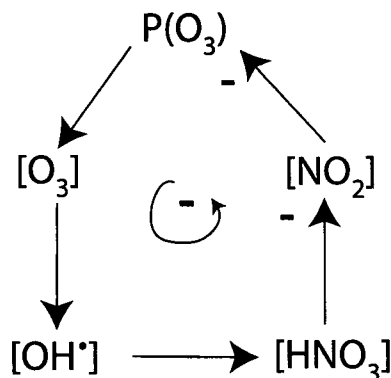


Figure 5.19: Negative Feedback loop for ozone production. As ozone levels rise, more  $OH^\bullet$  is produced via ozone photolysis. High  $OH^\bullet$  concentration coupled with high  $NO_2$  concentration favours  $HNO_3$  formation which removes  $NO_2$ ; lowering ozone production.

## 5.5 Scaling Break and Low-NOx chemistry

The main objective of this chapter is to show that the observed scaling break represents a change in chemical process. To this end, I have shown that the scaling break stems from a change in the temporal variability of ozone production. To understand this variability, I have presented ozone

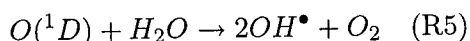
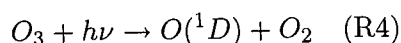
photochemistry as a dynamical system which is initially controlled by a strong positive feedback mechanism. I have then shown that as a result of this positive feedback, conditions are created which awaken a self-regulating negative feedback loop. I am now in a position to show that this negative feedback loop creates conditions favourable to a second negative feedback loop and that the switch to this new loop represents the fundamental change in chemical process that causes the scaling break.

### 5.5.1 Low-NOx chemistry

In Figure 5.18, I showed that as  $NO_2$  and  $OH^\bullet$  concentrations rise,  $HNO_3$  production follows suit which slows ozone production by removing NOx from the system, and, in the absence of fresh NOx emissions, NOx concentrations become very low. This sets up conditions similar to those found in the remote troposphere where NOx is the rate limiting precursor to ozone production (Seinfeld and Pandis, 1998). For clean background conditions over the Pacific ocean, Liu et al. (1992) have shown that  $NO$  concentrations play a critical role in determining if ozone is produced via:



(followed by  $NO_2$  photolysis (R1a) and ozone formation (R3)) or if it is consumed via:



Now, I have been modeling ozone formation in a smog chamber, with elevated VOC levels. While such elevated levels are not found in the remote troposphere, I believe that in a low-NOx environment, both the smog chamber and remote troposphere are controlled by the same processes. To prove this assertion, I examine the NOx limiting behaviour using  $OH^\bullet$ -chain length. In essence, when  $NO$  is low, the  $OH^\bullet$ -chain length is low because radicals are not propagated efficiently via R7 and R12, so that ozone photolysis can be a net loss for ozone production. For example, while ozone photolysis can produce as many as two  $OH^\bullet$  radicals, and even if most of these react with VOCs to produce  $HO_2^\bullet$  and  $RO_2^\bullet$  radicals, without sufficient  $NO$  to propagate the radicals and produce  $NO_2$ , peroxide producing reactions (R8A&B) take place and terminate the oxidation chain. In addition, as  $HO_2^\bullet$  concentrations build up (via  $OH^\bullet + VOC$  reactions), reaction R17 becomes important and presents a new sink for ozone.

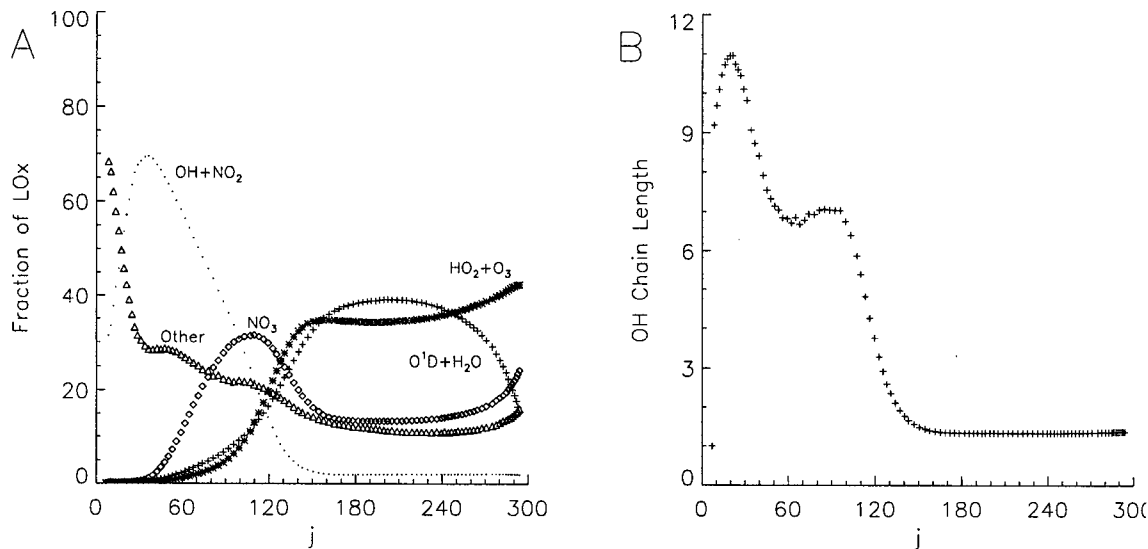


Figure 5.20: Loss of odd oxygen by various pathways for a RADM2 (Stockwell et al., 1990) using the Stock urban speciation (A) with the corresponding  $OH^\bullet$ -chain length (B).

In Figure 5.20A, I have plotted the percent of odd oxygen loss ( $LOx$ ) versus  $j$  for the RADM2 (Stockwell et al., 1990) simulation of the previous section. I consider the loss of odd-oxygen ( $O_x = O_3 + NO_2 + 2NO_3^\bullet + O(^1D) + O(^3P) + HNO_4 + 3N_2O_5 + PAN$ ) in this circumstance because  $R5$ ,  $R17$  as well as  $R9$  (formation of nitric acid) are all losses of odd-oxygen. I have partitioned  $LOx$  into five categories:  $R5$ ,  $R17$ ,  $R9$ , various reactions involving the nitrate radical and other miscellaneous reactions. From this Figure, initially the principle loss of odd oxygen is via nitric acid formation (while the 'other' loss is high at the simulation start, in absolute terms it is quite small and does not represent a significant process). As the system reacts, a point is reached where all of the five categories provide significant avenues for loss. After which, losses via  $O_3 + HO_2^\bullet$  and  $O_3 + h\nu$  dominate. To show that the loss of ozone via  $R3$  and  $R13$  does not lead to significant ozone production (via the feedback loop discussed in section 5.4.1), in Figure 5.20B, I have plotted the  $OH^\bullet$ -chain length as a function of  $j$ . From this Figure, it can be seen that the chain length is very close to 1.0 for  $j > 150$ , suggesting that few  $OH^\bullet$  radicals are recreated and  $R4$  and  $R17$  do indeed represent losses.

This supports the assertion that, like the remote troposphere, under low- $NO_x$  conditions, ozone loss via photolysis and  $HO_2^\bullet$  emerge as important processes. These new processes define a fundamentally different regime that I now show gives rise to the scaling break.

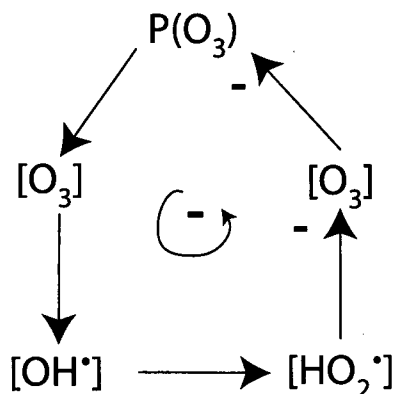


Figure 5.21: *Second controlling or negative feedback loop for ozone production. Ozone photolysis leads to new  $OH^\bullet$  radicals which, after VOC attack, produce  $HO_2^\bullet$  radicals. These react with ozone; lowering ozone production.*

### 5.5.2 Low-NOx negative feedback loop

The loss of ozone at low-NOx to *R17* represents another controlling or negative feedback loop for the photochemical system. I describe this loop as follows: initial ozone production leads to increased ozone concentrations. High ozone levels lead to high  $OH^\bullet$  concentrations which in turn lead to an abundance of  $RO_2^\bullet$  and  $HO_2^\bullet$  radicals. This  $HO_2^\bullet$  then titrates some of the abundant ozone; slowing ozone production. The cycle is schematically drawn in Figure 5.21.

### 5.5.3 Scaling break and governing chemical processes

To summarize, a shift in processes governing ozone production, brought on by low NOx conditions, leads to a marked reduction in ozone production. This change in production manifests itself in the temporal variability of ozone concentration and is most evident in the maximum values. *But what determines whether low NOx environment will occur?* Property 2 suggests a mixture's *R*-value does.

#### An aside on the significance of *R*

*R*, is the ratio of two quantities:

$$R = \frac{[VOC]_o}{[NOx]_o}$$

and to understand its significance consider the denominator: in order to reach the low NOx environment, (almost) all the initial NOx must be converted to NOz. Larger  $[NOx]_o$  implies more NOx to process. However, for the numerator, increasing  $[VOC]_o$  leads to ozone levels rising sooner and a

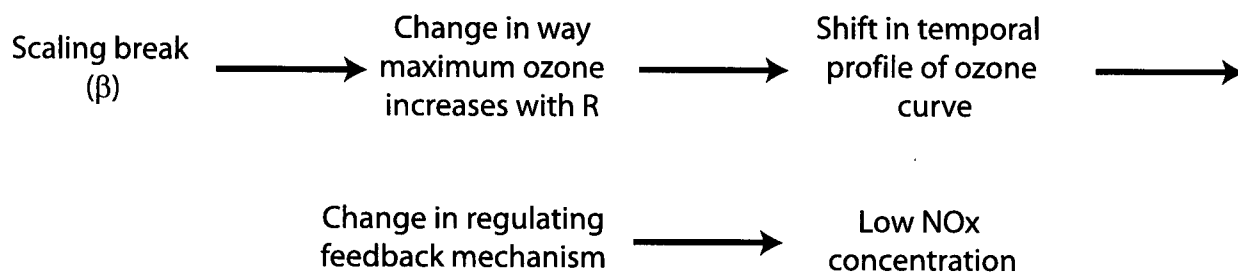


Figure 5.22: Relationship between scaling break and underlying photochemical processes. (arrows imply 'caused by')

quicker conversion of NOx to NOz (see Figure 5.3). Thus the ratio of  $[VOC]_o$  to  $[NOx]_o$  measures the processing rate for NOx to the amount of NOx to process – a quantity that varies inversely with time. Thus, I suggest that  $R$  can be thought of as a surrogate for time; a finding consistent with ozone production Property IV which indicates that  $R$  and  $j$  always appear to the same order in the parameterization of ozone concentration. And finally,  $\beta$  can be thought of as a characteristic size for this time scale.

And now, I can finish drawing the link between the scaling break and the governing chemical processes. The ratio  $R$ , a measure of the time necessary to process a fixed amount of NOx, determines whether a mixture of VOC and NOx will produce a low NOx environment before the end of irradiation. As I have already pointed out, in the low-NOx environment, ozone production slows; reducing maximum ozone concentrations. As a result, when maximum ozone concentrations are plotted as a function of  $R$  and Weibull transformed, a scaling break is observed. Figure 5.22 gives a schematic of the links between scaling break and regime shift. I must point out that the scaling break is also observed when  $[O_3]_{max}/[NOx]_o^a$  versus  $R$  is Weibull transformed. In the next chapter, I explain the significance of ratio.

## 5.6 Feedback Loops and the similarity relationship

I finish the analysis of ozone formation based on feedback processes by qualitatively describing the shape of the similarity curve. At the origin, where  $R \approx 0$ , the similarity relationship has low maximum ozone concentrations.<sup>6</sup> As mentioned in Section 5.2.1, ozone is formed only after significant  $NO$  has been converted to  $NO_2$ . As a result, for a VOC/NOx mixture with excess NOx (low  $R$ -values), a large amount of  $NO$  must first be converted to  $NO_2$ . By the time all the  $NO$  has been converted,  $NO_2$  photolysis rate may be well past its maximum and only a small amount of

<sup>6</sup>Actual similarity relationship relates  $[O_3]_{max}/[NOx]_o^a$  to  $R$  which is equal to (within a constant)  $[O_3]_{max}/[O_3]_{ult}$  where  $[O_3]_{ult}$  is the ultimate ozone that can be formed for a given amount of NOx.

ozone may be produced. Low ozone production leads to little radical initiation and photochemical process cannot tap into the positive feedback (autocatalytic) mechanism. So, at low R-values, maximum ozone concentrations are low. Furthermore, there is little increase in maximum ozone concentrations as R-values increase until ozone is produced early enough in the simulation. I call this slow increase a lag phase.

### 5.6.1 Acceleration Phase

Closely following the lag phase, is an acceleration phase, where the positive feedback mechanism accelerates ozone production. In this phase, a greater relative abundance of VOC to NO<sub>x</sub> means relatively less NO to convert and  $OH^\bullet + NO_2$  termination reactions (R9) are less likely to occur (because  $VOC + OH^\bullet$  reactions are now more likely). This allows NO-to-NO<sub>2</sub> conversions to occur sooner leading to greater NO<sub>2</sub> photolysis and greater ozone production. This in turn triggers more radical initiation, accelerating VOC attack and ozone production. The acceleration phase is seen as a sharp rise in maximum ozone over a small change in R-values.

### 5.6.2 Low-NO<sub>x</sub> Saturation Phase

Finally, for simulations that have sufficiently high initial VOC to NO<sub>x</sub> ratios, the positive feedback mechanisms occur so soon that HNO<sub>3</sub> production removes enough NO<sub>x</sub> to push the system into a low-NO<sub>x</sub> regime. This results in a slowing of ozone production which in turn affects ozone concentration. I call this the low-NO<sub>x</sub> saturation phase. In Figure 5.23, I have sketched a similarity relationship and labeled the lag, acceleration and low-NO<sub>x</sub> saturation phases.

I finish the analysis by comparing the scaling break with: the ridgeline, two processed based variables ( $OH^\bullet$ -chain length and fraction of  $HO_2^\bullet$  that reacts with NO ( $f_{HO_2+NO}$ )), a physical quantity ( $OH^\bullet$  reactivity ( $k_{NO}$ )) and two environmental variables (temperature and cumulative NO<sub>2</sub> photolysis rate). I start with the most obvious link: the ridgeline and  $\beta$ .

## 5.7 Scaling Break and Ridgeline

Before exploring the relationship between the scaling break and ridgeline, the concept of ridgeline must be more carefully defined. As it will be shown below, while the ridgeline is a familiar concept, unfortunately it can be defined in more than one way. Definitions can be made from three points of view: a regulatory (or sensitivity), a geometric (or mathematical) and a process based (or physical). Other definitions exist (Sillman, 1999) and since each has a specific objective, each produces a

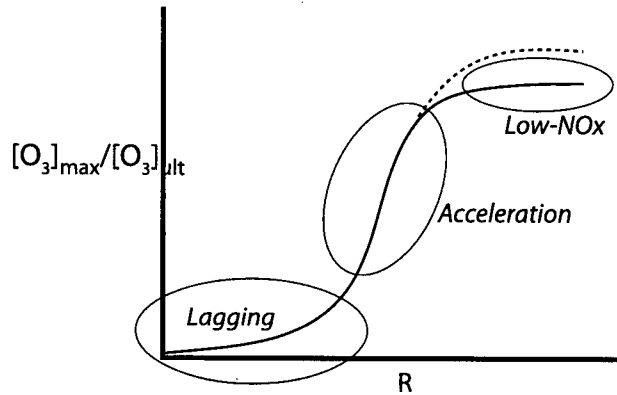


Figure 5.23: Generalized ozone profile showing Lag, Acceleration and Low-NOx regimes. Also shown is the shape of the similarity relationship in the absence of a regime shift (dotted line).

different 'ridgeline'. I will show that the scaling break is most closely aligned with the process based point of view.

### 5.7.1 Regulatory Basis for Ridgeline

Because of the importance of NOx-inhibition, a ridgeline based on ozone sensitivity to NOx is of paramount importance to regulators. Such a ridgeline should divide an ozone response surface into two regions: one where high NOx levels limit radical propagation to such an extent that *increasing* NOx concentrations *decreases* ozone levels and the other where ozone is insensitive to changing VOC concentrations but decreases with decreasing NOx. Mathematically, this requires finding the location on the response surface where ozone shows no change to changing NOx<sup>7</sup> i.e.:

$$\frac{\partial [O_3]_{max}}{\partial [NOx]_o} = 0 \quad (5.21)$$

Using the WEX model, the location where ozone sensitivity to changing NOx concentration vanishes is given by:

$$\frac{\partial [O_3]_{max}}{\partial [NOx]_o} = \gamma \left( \frac{[NOx]_o}{j_{av}/k_{NO}} \right)^{a-1} [af(R) - Rf'(R)] = 0 \quad (5.22)$$

which requires:

$$[af(R) - Rf'(R)] = 0 \quad (5.23)$$

Since the solution to 5.23 is a function of  $R$  only, it defines a straight line on an isopleth diagram. But  $R = \beta$  is **not** a solution to Eq. (5.23), indicating that the line  $R = \beta$  does not coincide with a

<sup>7</sup>While a similar definition could be made using VOC sensitivity, this definition is more broadly applicable to the remote troposphere where ozone is NOx sensitive (Sillman, 1999).

NO<sub>x</sub>-sensitivity based ridgeline. Rather, results from Chapter 4 suggest that the scaling break lies above the ridgeline on an isopleth diagram.

### 5.7.2 Geometrical Basis for Ridgeline

The advantage of a ridgeline definition based on ozone sensitivity to initial NO<sub>x</sub> concentration is ease of identification on an isopleth diagram. However, from a purely geometric point of view, this definition does not put the ridgeline in the right spot. That is, a hiker would not locate the ridgeline in this manner, but instead would set the ridgeline along the uphill path (gradient) showing the smallest slope. However, even by this definition, the ridgeline may not be correctly placed for some geometric figures. A better definition is one that sees the ridgeline as the location where contours show the maximum curvature. It turns out that these two geometric definitions put the ridgeline in different locations and both prove difficult to evaluate mathematically (see Appendix F). Finally, I would like to mention that a parameterization for the similarity relationship using only a single Weibull function, will clearly not produce a scale break but still produces a 'ridgeline' when used to produce an isopleth diagram. This further suggests that the 'ridgeline' is mainly a geometric property of a set of curves and does not necessarily reflect any change in chemical process.

### 5.7.3 Process Basis for Ridgeline

Finally, one can also formulate a definition based on the photochemical processes (Seinfeld and Pandis, 1998):

That combination of initial VOC and NO<sub>x</sub> at which all the NO<sub>x</sub> is converted into nitrogen-containing products by the end of the simulation so that there is no NO left to participate in NO-to-NO<sub>2</sub> conversions nor any NO<sub>2</sub> left to photolyze.

This definition, while chemically precise, makes ridge identification difficult on an isopleth diagram. However, this definition corresponds closely with the concepts used to explain the scaling break. There, however, the scaling break defines the combination of initial VOC and NO<sub>x</sub> at which **most** of the NO<sub>x</sub> gets converted to NO<sub>z</sub> with **little** free NO<sub>x</sub> available for NO-to-NO<sub>2</sub> conversions or photolysis. Thus the scaling break coincides most closely with a process based ridgeline.

However, Sillman (1999) points out that the actual split between VOC and NO<sub>x</sub>-sensitive is a broad transition region rather than a sharp line. Following this reasoning, I propose that the most natural division of an ozone response surface is into three regions: VOC sensitive (or NO<sub>x</sub>-saturated) region, ridge or transition region and NO<sub>x</sub>-only scaling region. I suggest that  $\beta$  marks the boundaries the VOC-sensitive/ridge regions. The NO<sub>x</sub>-only scaling region identifies that part

Species	$\beta$	$R/\beta$ at $OH^\bullet$ -chain Maximum
ALD	5.2	1.06
KET	15.3	0.98
OLI	4.5	1.11
OLT	4.2	0.96
XYLE	5.3	1.26
TOLU	10.1	0.99
HCHO	4.2	1.19
Stock	9.4	1.06
Arb	8.5	0.94

Table 5.1: Scaling break and  $R$ -value of  $OH^\bullet$ -chain maximum for seven RADM2 classes and two urban mixtures.

of the response surface where maximum ozone concentration is independent of  $[VOC]_o$ . In the next chapter, I propose a means of determining the boundary of this region using the slope of ozone isopleths.

## 5.8 Relationship between Scaling break and other parameters

To end this chapter, the scaling break is compared with the  $OH^\bullet$ -chain length; the fraction of  $HO_2^\bullet$  that reacts with  $NO$ ; the  $OH^\bullet$ -reactivity; temperature and cumulative  $NO_2$  photolysis rate.

### 5.8.1 Scaling break Ridgeline and Chain Length ( $\chi_{OH}$ )

Both Seinfeld and Pandis (1998) and Tonnesen and Jeffries (1994) suggest that the  $OH^\bullet$ -chain length is a maximum slightly above the (sensitivity based) ridgeline – in roughly the same location as the scaling break. To examine any possible connection between chain length and the scaling break, OZIPR simulations were rerun using process analysis (Tonnesen, 2000). For each simulation, average  $OH^\bullet$ -chain length ( $\chi_{OH}$ ) was calculated. It was found to depend only on  $R$  as evident in Figure 5.24A. For each RADM2 scaling class, the  $R$ -value at maximum  $\chi_{OH}$  ( $R_{OH}$ ) was determined and the ratio of  $R_{OH}$  to  $\beta$  is given in Table 5.1.

From this table we see that there is a close correlation between the location of  $OH^\bullet$ -chain maximum and the scaling break, with most values within  $\pm 10\%$  of unity. The biggest exceptions are XYLE and HCHO, which show  $OH^\bullet$ -chain maximum well below the scaling break (it must be noted that while both  $f_{HO_2+NO}$  and  $OH^\bullet$ -chain length appear to be functions of  $R$  only, there is still some scatter in the model output leading to small uncertainty in actual location of both the scaling break and  $OH^\bullet$ -chain maximum). The deviation of both XYLE and HCHO suggests that while the scaling break and maximum  $OH^\bullet$ -chain length are related, they do not occur at the same  $R$ -value.

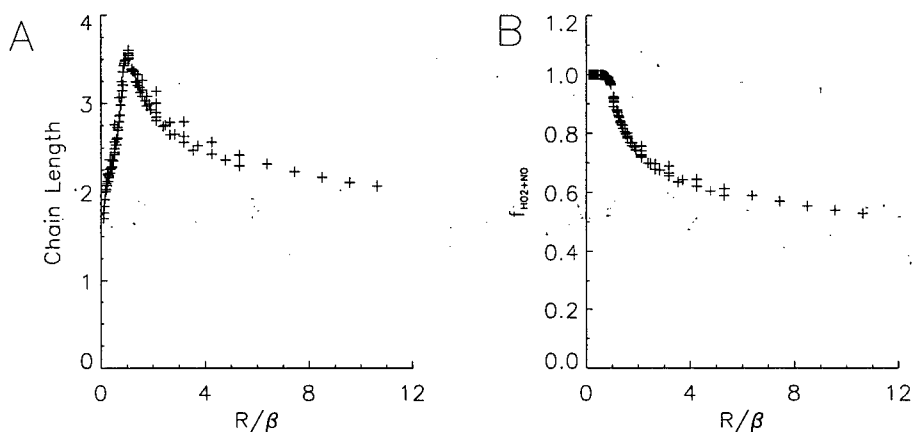


Figure 5.24:  $OH$ -chain length (A) and  $f_{HO_2}$  (B) for the Stock urban mixture as a function of  $R/\beta$ .

Species	$\beta$	$f_{HO_2+NO}$ at $R = \beta$
ALD	5.2	0.96
KET	15.3	0.97
OLI	4.5	0.95
OLT	4.2	0.97
XYLE	5.3	0.89
TOLU	10.1	0.95
HCHO	4.2	0.92
Stock	9.4	0.96
Arb	8.5	0.94

Table 5.2: Fraction of  $HO_2^*$  that reacts with  $NO$  scaling break for various RADM2 classes and mixtures.

### 5.8.2 Scaling break and fraction of $HO_2^*$ radicals that react with $NO$ ( $f_{HO_2+NO}$ )

The fraction of  $HO_2^*$  radicals that react with  $NO$  ( $f_{HO_2+NO}$ ) measures the extent to which  $HO_2^*$  radicals react with  $NO$  (in potential ozone producing reactions) or with themselves (in radical termination reactions). A value of  $f_{HO_2+NO}$  below 1.0 implies an over-abundance of  $HO_2^*$  relative to available  $NO$ ; suggesting that  $f_{HO_2+NO}$  can be used to infer when production is governed by low- $NO_x$  chemistry.

Process analysis was used to calculate average  $f_{HO_2+NO}$  for each of the 7 scaling RADM2 classes and the two urban mixtures. Again, it was found that  $f_{HO_2+NO}$  scaled with  $R$  (Figure 5.24B) and the f-values, for the RADM2 scaling classes, at  $R = \beta$  are given in Table 5.2. The Table shows that over a wide range of  $\beta$  values, there is a narrow range of  $f_{HO_2+NO}$  values at the scaling break (with the exception of XYLE) indicating that the scaling break coincides with a fixed ratio of  $f_{HO_2+NO}$  ( $\approx 0.95$ ) largely independent of VOC species.

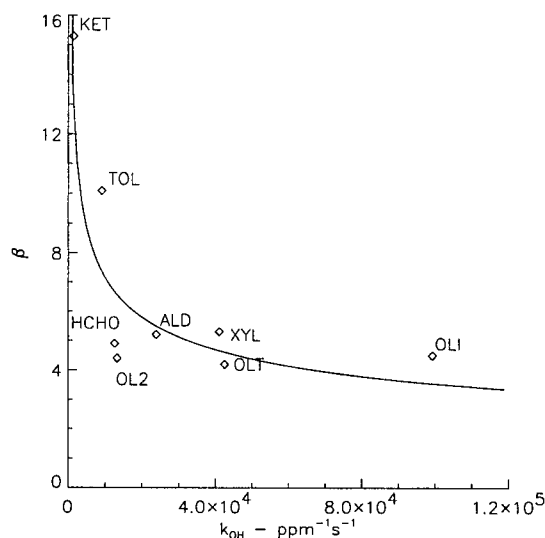


Figure 5.25: Scaling break as a function of  $OH^\bullet$ -reactivity for eight RADM2 classes and non-linear line of best fit.

### 5.8.3 Scaling break and $OH^\bullet$ reactivity ( $k_{OH}$ )

One might expect that VOCs with higher  $OH^\bullet$ -reactivities would show lower  $\beta$  values i.e. with a higher  $OH^\bullet$ -reactivity, more peroxy radicals can be produced (through  $OH^\bullet$  attack), for a given  $[VOC]_o$ , leading to low- $NO_x$  conditions (via  $NO$ -to- $NO_2$  conversions and  $HNO_3$  production) at lower R-values. However, many VOCs photolyze to produce their own (organic) source of radicals that can also initiate ozone formation. Such VOCs should have a lower  $\beta$  value than would be expected based on their  $OH^\bullet$ -reactivity alone. Figure 5.25 shows  $OH^\bullet$ -reactivity versus  $\beta$  for the seven scaling RADM2 classes. In addition, a trend line through the results has been drawn. A non-linear model was chosen to reflect the underlying non-linear feedback mechanisms involved in ozone formation. This line has  $\beta$  decreasing as reactivity increases. From the Figure, both HCHO and OL2 have  $\beta$  values lower than can be explained by their  $OH^\bullet$ -reactivity. Since formaldehyde readily photolyzes to produce hydroperoxy radicals, this photolytic source of radicals supplements its low  $OH^\bullet$ -reactivity. OL2 produces 1.6 HCHO molecules every time its peroxy radical reacts with  $NO$  (in addition to 0.2 ALD and 1.0  $HO_2^\bullet$ ) which appears to be more than the other alkenes. Both TOL and OLI have higher values than would be expected from their reactivities. Neither one directly photolyzes and their peroxy radicals (TOLP and OLIP respectively) produce few carbonyl compounds when converting  $NO$  to  $NO_2$ .

#### 5.8.4 Scaling Break and environmental conditions

In the previous chapter, I showed that the  $\beta$  dependence on total actinic flux ( $J$ ) and temperature was negative i.e.  $\beta$  decreased when either  $J$  or  $T$  increased (see Figure 4.16). I now explain this dependence. Increasing total actinic flux results in more  $NO_2$  photolysis and enhanced ozone production. Higher ozone levels and increased photolysis lead to greater radical production. This leads to more  $NO$ -to- $NO_2$  conversions, a quicker increase in  $NO_2$  followed by  $NO_3$  formation. Therefore an initial mixture of VOCs and  $NO_x$ , with  $R < \beta$ , might reach low- $NO_x$  conditions when  $J$  is increased. Thus an increase in  $J$  leads to a decrease in  $\beta$ . Similarly, since most reaction rates increase with temperature (Levine, 1978), the net effect of increased temperature is to speed up the oxidation process and allow VOC sensitive conditions to become  $NO_x$ -sensitive.

### 5.9 Summary

This chapter has provided a mechanistic understanding for the observed scaling break. I started by describing ozone formation in terms of ozone production and showed that the break stems from a regime shift in ozone production. This shift can be interpreted as a change in negative (or controlling) feedback loops associated with low- $NO_x$  conditions. Along the way, I outlined four properties that govern ozone production for VOC/ $NO_x$  mixtures. Both the WEX and IER (Johnson, 1984) are examples of models which parameterize these properties. I also used the properties to parameterize the temporal variability of ozone concentration with the WEX model.

The scaling break coincides closely with a process based definition of ridgeline and, in fact, could be used to define a new 'ridgeline'. The magnitude of the scaling break appears to be a complex function of the  $OH^\bullet$ -reactivity and the ability of the VOC to produce radicals (either directly or through the photolysis of secondary carbonyl compounds). The scaling break is also closely related to a maximum in  $OH^\bullet$ -chain length and a specific value of  $f_{HO_2+NO}$ . The next chapter examines the remaining WEX parameters from a similar mechanistic approach.

## Chapter 6

# Chemical Processes and the WEX Parameters

### 6.1 Introduction

In this chapter, I explore the relationship between the remaining WEX parameters ( $\gamma, a, \alpha_1, \alpha_2, \lambda$ ) and photochemical processes. As a reminder, the WEX model is:

$$\begin{aligned} \frac{[O_3]_{max}}{j_{av}/k_{NO}} &= \gamma \left( \frac{[NOx]_o}{j_{av}/k_{NO}} \right)^a f(R) \\ f(R) &= \left[ 1 - \exp \left\{ -\lambda \left( \frac{R}{\beta} \right)^{\alpha(R)} \right\} \right] \\ \text{where } \alpha(R) &= \frac{\alpha_2 - \alpha_1}{2} \tanh(R - \beta) + \frac{\alpha_1 + \alpha_2}{2} \end{aligned} \quad (6.1)$$

While it is tempting to speculate that each parameter is controlled by a specific chemical reaction, I will show that groups of reactions, which form sub-processes within the larger photochemical system, determine parameter size. As a result, it is best to view WEX parameters as representing the integrated effects of various reaction groups. I begin by describing how each parameter arises in the model; grouping them into two classes: scaling and geometric. The scaling parameters are  $a$  and  $\gamma$ . By scaling, I mean that these parameters are used in the scaling analysis to derive the similarity relationship (and define a power-law relationship) whereas the others are used in its parameterization.

#### Scaling parameters

One way to view the similarity relationship is as a family of curves where each simulation belongs to one member of a family. Each curve is distinguished by its initial NOx concentration. In other words, each curve relates  $[O_3]_{max}$  to  $R$  along an isomephitic path. The parameter  $a$  is used to scale  $[O_3]_{max}$ , along each curve, so that the resulting family of maximum ozone concentrations produces a common variability (the similarity relationship) independent of initial NOx concentration. Thus  $a$  measures the dependence of maximum ozone concentration on initial NOx at any given R-value.

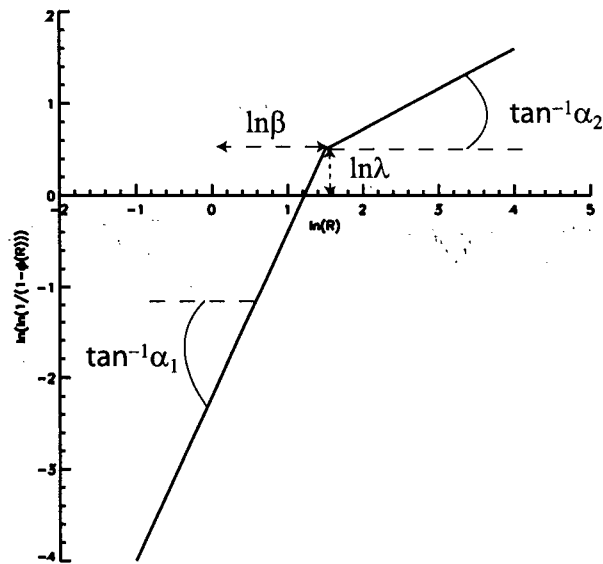


Figure 6.1: Schematic representation of the four WEX geometric parameters.

The other scaling parameter,  $\gamma$ , used to normalize the similarity relationship, relates peak maximum ozone concentration (the greatest value of maximum ozone for any given combination of initial VOC and NO<sub>x</sub>) to initial NO<sub>x</sub> concentration – a global ‘NO<sub>x</sub>-efficiency’.

### Geometric Parameters

The four geometric parameters ( $\alpha_1, \alpha_2, \beta, \lambda$ ), schematically shown in Figure 6.1, characterize two line segments in the Weibull plane;  $\alpha_1$  and  $\alpha_2$  give the two slopes while  $\beta$  and  $\lambda$  locate the intersection of the two line segments.

### Sensitivity Analysis

To examine the link between chemistry and WEX parameter values, two types of sensitivity analysis were performed. The first is a straightforward comparison between two isopleth diagrams; one produced using a set of ‘baseline’ WEX parameters, the other produced with one ‘baseline’ parameter altered (to produce a ‘modified’ parameter set). While Chapter 4 shows a wide range of parameter values for the different VOC classes and VOC mixtures, I have chosen the OLT (the RADM2 propene surrogate) parameter values as a standard (or baseline). From these baseline values, I individually perturb the parameter values (with perturbation size guided by the parameter range found in Chapter 4) and then compare isopleth plots. Table 6.1 summarizes the baseline and altered parameters values. In all, five analyses were made, one for each parameter.

Parameter	Baseline	Modified Value
$\gamma$	10.0	5.0
$a$	0.6	0.45
$\alpha_1$	2.0	4.0
$\alpha_2$	0.75	0.33
$\beta$	4.0	8.0
$\lambda$	1.0	2.0

Table 6.1: *Baseline and Modified parameters for WEX generated isopleths.*

The second investigation involves a sensitivity analysis of the RADM2 chemical mechanism in order to reveal possible relationships between specific reaction rates or reaction products and corresponding WEX parameters (after regression to the similarity relationship). This analysis is problematic; a single change to the mechanism (say a change to a specific reaction rate or reaction product) often produces changes to several WEX parameters. The resulting modified mechanism may not accurately represent ozone formation, however the intention is to explore WEX parameter sensitivity to RADM2 reaction rates and reaction products.

## 6.2 WEX Scaling Parameter $a$

The first WEX parameter to study is the scaling parameter  $a$ . It has the property of collapsing maximum ozone concentrations, taken along different isomephitic paths (when plotted as a function of  $R$ ), onto a common curve. In the extreme, when  $a = 0$ , maximum ozone along each isomephitic path is independent of initial NO<sub>x</sub> concentration and ozone isopleths become lines of constant  $R$ . However, such a situation is unrealistic – the range of  $a$ -values, found in Chapter 4, appears to lie between 0.48 and 0.75. Finally, Eq. (6.1) shows as  $a$  increases, maximum ozone concentration, along each path, becomes more dependent on underlying NO<sub>x</sub> concentration.

### 6.2.1 NO<sub>x</sub> Inefficiency

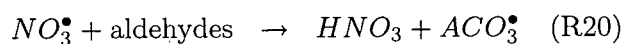
For all of the VOC and VOC mixtures analyzed in Chapter 4, the value of  $a$  was less than 1.0; implying that a doubling of initial NO<sub>x</sub> concentration does not lead to a doubling of maximum ozone concentration. Thus  $a$  quantifies the extent to which an increase in NO<sub>x</sub> is not matched by an equal increase in maximum ozone (at similar  $R$ -values) – a ‘NO<sub>x</sub>-inefficiency’

To understand this inefficiency, consider a simulation using the RADM2 (Stockwell et al., 1990) aldehyde surrogate ALD where, in the NLR, the following maximum ozone concentrations are

observed:

$$\begin{aligned} [O_3]_{max} &= 200 \text{ ppb} & \text{when } [NOx]_o &= 40 \text{ ppb} \\ (O_3)_{max} &= 402 \text{ ppb} & \text{when } [NOx]_o &= 160 \text{ ppb} \end{aligned} \quad (6.2)$$

Thus a four fold increase in initial NO<sub>x</sub>, results in only a doubling of maximum ozone. This 'inefficiency' is related to an increase in importance of NO<sub>x</sub> reactions that do not lead to ozone production (Jeffries, 1995). Consider, for example, the following reactions, important in the NLR:



where  $NO_3^\bullet$ ,  $ACO_3^\bullet$  are the nitrate and acetylperoxy radicals. With higher initial NO<sub>x</sub> concentrations, reactions *R18*, *R19* and *R20* are more likely to occur. Reaction *R18* provides a sink for both ozone and  $NO_2$  while reactions *R19* and *R20* are a sink for  $NO_2$  only. All three side reactions cause ozone efficiency (ozone produced for each NO<sub>x</sub> consumed) to decrease as NO<sub>x</sub> increases, a process consistent with field studies (Liu et al., 1987). I find that increasing NO<sub>x</sub> changes the reaction pathways in such a way that the resulting 'NO<sub>x</sub>-inefficiency' not the same for all R-values (remember, I have chosen a value for *a*, the 'NO<sub>x</sub>-inefficiency', which fits the model output best around the scaling break). At low *R*, a better fit to the 'scaled data' often has  $a \approx 0.2$ , indicating that for simulations with low R-values, doubling initial NO<sub>x</sub> results in little if any increase in ozone. It must be remembered that at low R-values, with the photochemical system radical limited, substantial NO<sub>x</sub> remains unprocessed at simulation end. Therefore, it is not surprising that maximum ozone shows little response to increased initial NO<sub>x</sub>. For very large R-values, I have found that maximum ozone often scales with an exponent closer to 0.5; suggesting that the system becomes less efficient as reactions like *R18*, *R19* and *R20* become important. The scatter in the similarity relationship, observed in region IIb (Figure 3.9), likely stems from a change in the 'NO<sub>x</sub>-inefficiency'.

### 6.2.2 Range of *a*-values

The correct value for *a* has been debated ever since Johnson first proposed that  $SP = 4.1[NOx]_o$  in his IER model (Johnson, 1984).<sup>1</sup> This linear relationship implies a constant 'NO<sub>x</sub>-inefficiency' and has been questioned by Blanchard et al. (1999) who suggest, based on numerical simulations using

<sup>1</sup>Again, SP refers to smog potential which includes ozone produced as well as NO converted to other forms of NO<sub>y</sub>. Thus SP is closely associated with odd-oxygen (*Ox*).

a typical urban mixture of VOCs, it be replaced by a non-linear relationship with an exponent of 2/3 i.e.:  $SP = [NOx]_o^{2/3}$ .

Chang and Rudy (1993) have determined that for maximum ozone, the NOx-scaling exponent should be 1/2 i.e.:  $[O_3]_{max} = \gamma[NOx]_o^{1/2}$ . While they arrive at their results using model simulations they also fit their model to smog chamber data. Finally, both Akimoto et al. (1979) (based on propene-NOx experiments) and Shen et al. (1977) (using cyclohexane experiments) also suggest a NOx-scaling exponent of 1/2.

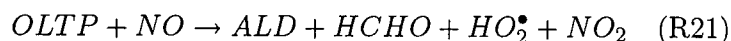
I find  $a$  shows the least variability among the WEX parameters suggesting that specific VOC chemistry plays only a minor role in its determination – a possible reason why Johnson (1984), Blanchard et al. (1999) and Chang and Rudy (1993) assumed it to be constant. I have found  $a$  ranges from a low of 0.48 (TOLU) to a high of 0.75 (HCHO). Both urban mixtures give a common value of 0.58 – midway between values found by Blanchard et al. (1999) and Chang and Rudy (1993).

### 6.2.3 Response surface sensitivity to $a$

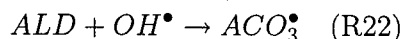
Ozone isopleths, using the baseline WEX parameter values, have been plotted in Figure 6.2A while Figure 6.2B shows ozone isopleths after reducing  $a$  from 0.6 to 0.45. The main difference lies in the transition region between VLR and NLR; lowering  $a$  makes the transition more gradual. In addition, reducing  $a$  appears to slightly reduce maximum ozone concentrations (although mainly in the higher ozone regime).

### 6.2.4 Sensitivity of $a$ to RADM2 modifications

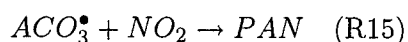
To investigate the relationship between the RADM2 mechanism and  $a$ , RADM2 was modified in an attempt to cause the greatest change in ‘NOx-inefficiency’ (while avoiding changes to the other parameters). The OLT class was used as the sole VOC in a set of smog chamber simulations using a modified mechanism. When OLT reacts with the  $OH^\bullet$  radical, RADM2 produces the OLTP peroxy radical. When this radical reacts with  $NO$ , the products include carbonyl compounds ALD and HCHO:



When ALD reacts with the  $OH^\bullet$  radical,  $ACO_3^\bullet$  is formed:



which is the sole PAN precursor in RADM2 i.e.:



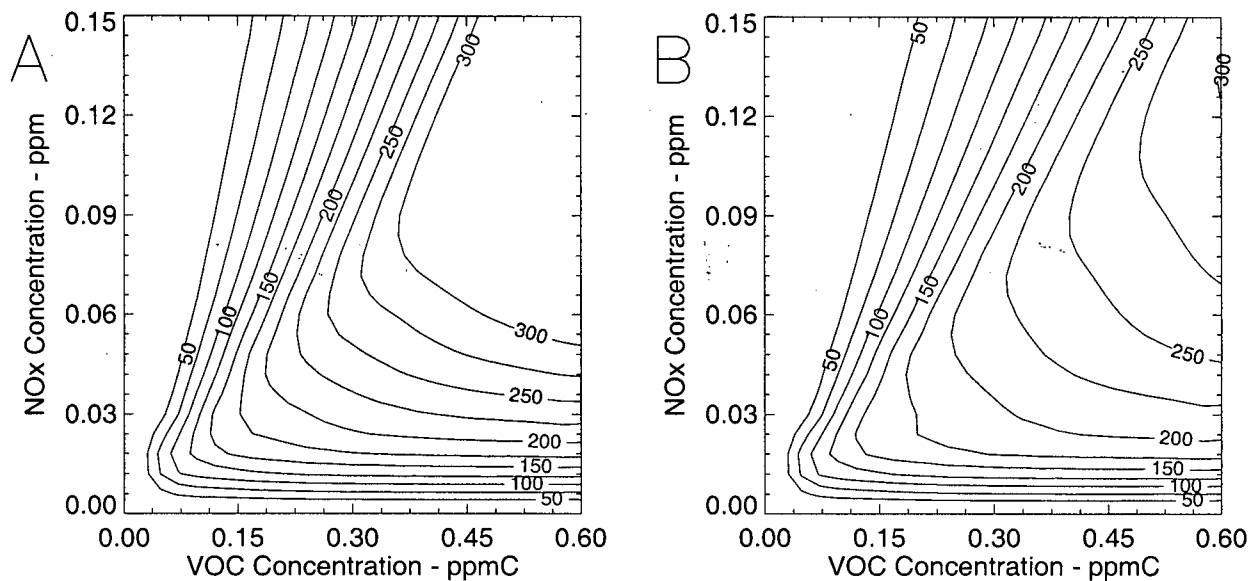


Figure 6.2: The effects of changing  $a$  on ozone response surface. Figure A shows maximum ozone concentration (in ppb) as a function of initial VOC and NO<sub>x</sub> concentration calculated using the WEX model and baseline parameter values. Figure B shows the resulting ozone isopleths (in ppb) after a reduction in  $a$  from 0.6 to 0.45 (while all other WEX parameters have been held constant).

Parameter	Original	Modified
$\gamma$	9.5	10.8
$a$	0.6	0.65
$\alpha_1$	2.2	2.2
$\alpha_2$	0.72	0.82
$\beta$	4.2	4.7
$\lambda$	0.92	0.7

Table 6.2: Comparison of OLT parameters for the original and modified RADM2 mechanism.

Reaction (R15) is a side reaction which consumes  $NO_2$  (and thereby preventing ozone formation (via R1a)) and increases 'NO<sub>x</sub>-inefficiency'. By making this reaction less likely, 'NO<sub>x</sub>-inefficiency' should decrease and hence  $a$  should increase. To test this hypothesis, RADM2 was modified so that only half an ALD molecule is formed from the OLTP+NO conversion (R21). OZIPR simulations were run with this modified mechanism and regressed to the WEX model. Table 6.2 shows the WEX parameters for OLT using the original and modified RADM2 mechanism.

From the table we see a 10% increase in  $a$ . With less ALD and  $ACO_3^*$  produced, less mass runs through R15, the system is more efficient and the NO<sub>x</sub> scaling exponent is closer to 1.0. Notice,

however, that there has been as large a change to both  $\gamma$  (increasing) and  $\lambda$  (decreasing) and a slight increase in  $\beta$ . These multiple changes suggest that WEX parameters are sensitive to many aspects of the photochemical system and no single reaction controls an individual WEX parameter. For this reason, WEX parameter should be viewed at best as describing processes within the larger reaction system.

### 6.3 WEX Scaling Parameter $\gamma$

The WEX parameter  $\gamma$  relates peak maximum ozone to initial NOx. i.e.:

$$\gamma \propto \frac{[O_3]_{peak}}{[NOx]_o^a} \quad (6.3)$$

where  $[O_3]_{peak}$  is the greatest maximum ozone concentration value for any combination of initial VOC and NOx. A higher  $\gamma$ -value means VOCs produce higher ozone maximum ozone concentrations for a given amount NOx.

#### 6.3.1 NOz speciation and $\gamma$

For a mixture of VOC and NOx which becomes NOx-limited, most of the initial NOx is converted to NOz before simulation end so that  $[NOx]_o \approx [NOz]_{final}$ . Furthermore, peak maximum ozone concentration occurs for NOx-limited conditions so  $[O_3]_{max} \approx [O_3]_{peak}$ . Thus one might expect a relationship between  $\gamma$ ,  $[O_3]_{peak}$  and  $[NOz]_{final}$  similar to Eq. (6.3) to hold for simulations with  $R \gg \beta$ . Figure 6.3 compares  $\gamma$  to  $[O_3]_{final}/[NOz]_{final}$  for 8 NOx-limited smog chamber simulations: the six RADM2 scaling classes and the two urban mixtures. In each case, there is a strong correlation between  $\gamma$  and  $[O_3]_{max}/[NOz]_{final}$  as seen by the clustering of values along a common line above the 1 : 1 line. I use the link between ozone, NOz and  $\gamma$  to describe the physical significance of  $\gamma$ .

I will show that the magnitude of a VOCs peak ozone concentrations is determined by the way final NOz is partitioned. For example, VOCs which facilitate the conversion of NOx to PAN have lower  $\gamma$ -values than those that facilitate  $HNO_3$  production. Specifically, the largest  $\gamma$ -value is 40.6 (HCHO) while the smallest is 7.5 (ALD). The products of the  $OH^\bullet$ -attack on HCHO are  $HO_2^\bullet$  and CO, neither or which is a PAN precursor, while the product of  $OH^\bullet$ -attack on ALD is the acetylperoxy radical ( $ACO_3^\bullet$ ) – RADM2's only PAN precursor. Furthermore, the relatively unreactive alkene OL2 has the second highest  $\gamma$ -value. In the RADM2 mechanism OL2 produces a large amount of HCHO upon oxidation i.e. every time the OL2P peroxy radical converts an NO to  $NO_2$ , it produces 1.6 HCHO and only 0.2 ALD molecules. This can be compared with the alkene OLI ( $\gamma = 8.0$ ), whose peroxy radical produces only 0.28 HCHO molecules but 1.45 ALD molecules

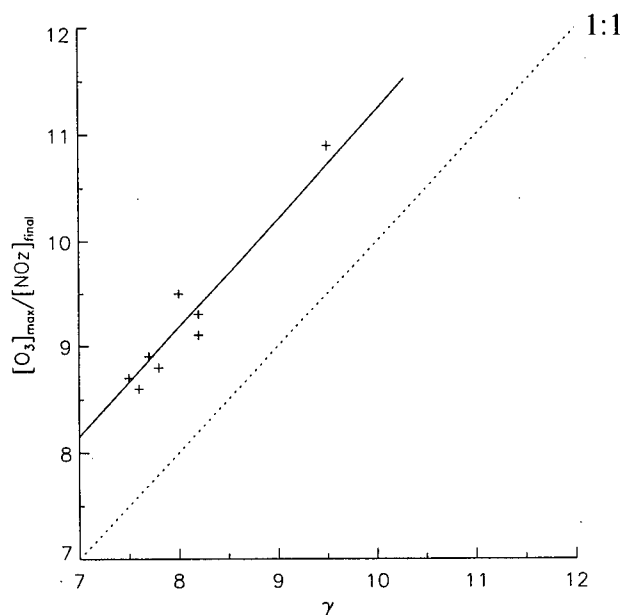
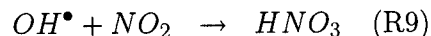
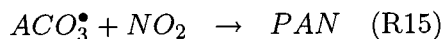


Figure 6.3: Scatter plot of  $\gamma$  versus  $O_3/NO_z$  for six RADM2 classes and two urban mixtures. Also shown is the 1 : 1 line. Due to the large values for HCHO ( $\gamma = 39.1$  and  $O_{3max}/NO_{zfinal}$ ) they have not been plotted.

for every conversion. Figure 6.4 shows the speciation of final  $NO_z$  for the 8 RADM2 classes and two mixtures in terms of  $HNO_3$ , PAN+TPAN, and ONIT.

### 6.3.2 Peak Ozone and PAN and $HNO_3$ Formation

As noted in the previous section, VOCs which create conditions favourable for PAN formation have lower peak maximum ozone levels than those that favour nitric acid formation. *Why?* The answer lies in how these two nitrogen products form:



While both reactions consume nitrogen dioxide, PAN production requires  $ACO_3^\bullet$  (produced from VOCs oxidation) while  $HNO_3$  production requires  $OH^\bullet$  radicals whose production is relatively independent of VOC (and hence R-value). Since the main source of  $OH^\bullet$  radicals is the photolysis of ozone,  $HNO_3$  production requires high ozone levels to produce sufficient  $OH^\bullet$  radicals necessary to consume all of the  $NO_x$ . Thus, VOCs which do not produce PAN precursors (like HCHO), must convert all  $NO_z$  to  $HNO_3$  and ONIT. This is consistent with Bowman and Seinfeld (1994) who,

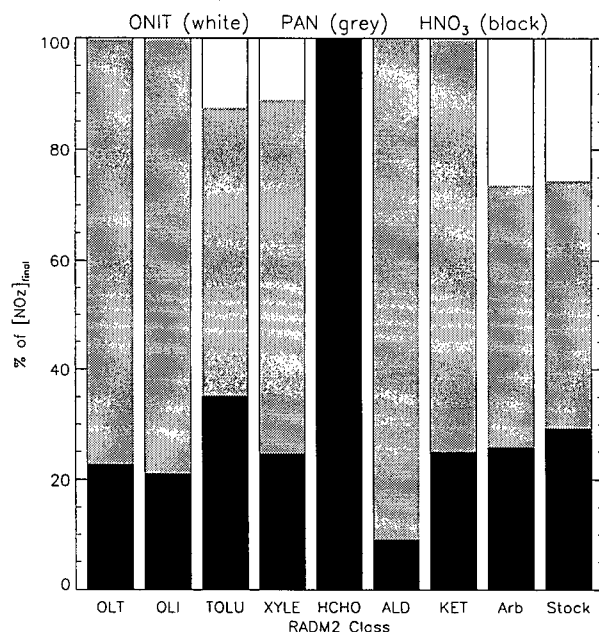


Figure 6.4: Speciation of final  $NO_z$  (organic nitrate (outline), PAN (shade) and nitric acid (dark)) for seven RADM2 classes and two urban mixtures.

using the SAPRC90 mechanism with an urban VOC mixture, find that PAN formation depends directly on a VOC's ability to produce, either directly or indirectly, the peroxyacetyl radical. In the NLR, with  $NO_2$  in short supply, ozone concentrations must rise to high levels, in order to supply the necessary  $OH^\bullet$  radicals, before nitric acid will be produced. Low PAN production also explains why the RADM2 classes with two highest  $\gamma$ -values (HCHO and ETHE) required 41 nodes – production of  $NO_z$  and final consumption of  $NO_x$  (through  $HNO_3$ ) is largely insensitive to VOC concentration and hence there is a large change in R-values between the scaling break and when maximum ozone scales with  $NO_x$  only.

### 6.3.3 Gamma and Isopleth shape

Figure 6.5A shows ozone isopleths based on the baseline WEX parameters and 6.5B shows those with  $\gamma$  reduced by 50%. Both sets of isopleths have the same shape but those with the lower  $\gamma$ -value are not as tightly spaced. (I have changed the contouring interval from 50 to 25 ppb between figures to highlight the pure scaling nature of  $\gamma$ ). In essence, changing  $\gamma$  has the same effect as changing the isopleth labels.

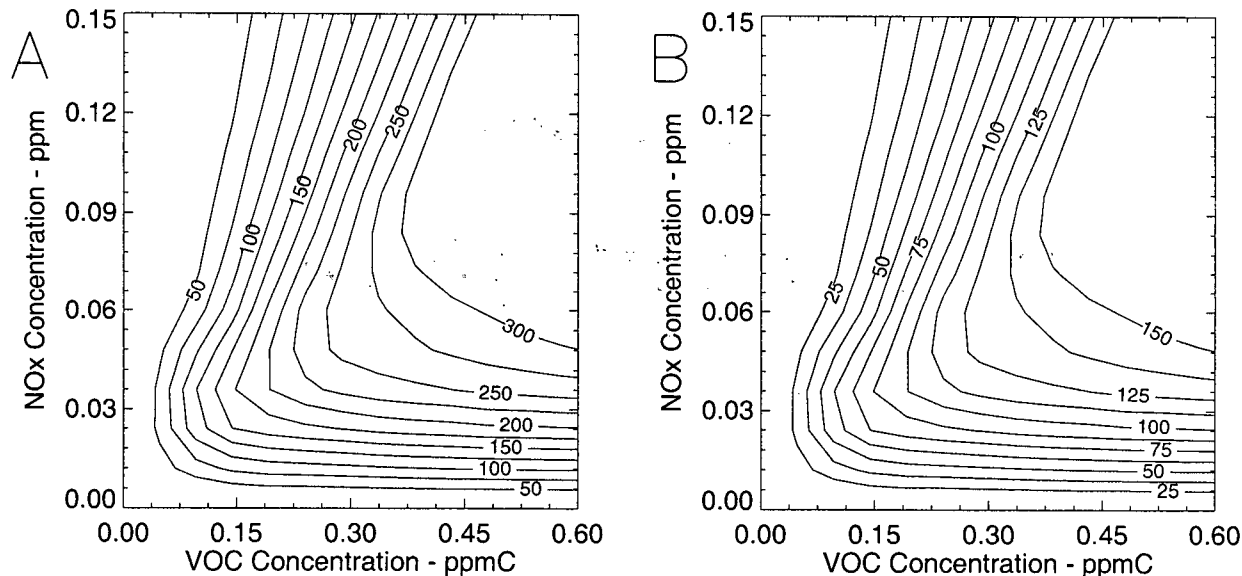


Figure 6.5: The effects of changing  $\gamma$  on ozone response surface. Figure A shows maximum ozone concentration (in ppb) as a function of initial VOC and NO $x$  concentration calculated using the WEX model and baseline parameter values. Figure B shows the resulting ozone isopleths (in ppb) after a reduction in  $\gamma$  from 1.0 to 2.0 (while all other WEX parameters have been held constant)

### 6.3.4 Variability of $\gamma$

As mentioned above,  $\gamma$  determines the highest possible ozone concentrations in the NOS regime. Johnson (1984) suggests that this value is independent of VOC species. In addition, both Blanchard et al. (1999) and Chang and Rudy (1993) do not suggest how this factor might depend on VOC species. I have found that  $\gamma$  shows a great range of variability (from a high of 39.1 for HCHO to a low of 7.5 for ALD) but is essentially constant for the two urban mixtures ( $\gamma$ -values of 8.15 and 8.16).

### 6.3.5 $\gamma$ RADM2 Experiments

The link between RADM2 chemistry and  $\gamma$  is evident from the modified RADM2 mechanism used in Section 6.2. In this mechanism, reducing ALD production (and hence  $ACO_3^*$  and PAN production) for every NO+OLTP reaction, increases  $\gamma$ . By reducing the propensity for PAN production, NO $z$  must be created by means which require higher ozone concentrations. It must be mentioned that both PAN and  $HNO_3$  production do not appear to be the sole determinants of  $\gamma$ . The reaction

$VOC + O_3$ , specific to alkenes, consumes ozone at high R-values. Since this reaction does not involve NOx, this ozone titration should not affect the 'NOx-inefficiency' (and hence  $a$ ). To see how this reaction might affect  $\gamma$ , OLT simulations were run with a modified  $OLT + O_3$  reaction rate. Specifically, the RADM2 mechanism was modified so that the original reaction rate of 0.0166 ppm  $min^{-1}$  (at 25°C) was increased to 0.236 ppm  $min^{-1}$  (identical to the OLI rate).

Table 6.3 shows the resulting WEX parameters for the original and modified mechanism. The biggest change is for  $\gamma$  and  $\lambda$  which have moved in opposite directions. As more mass runs through the  $OLT + O_3$  reaction, less net ozone is produced. The value of  $a$  is almost unchanged (0.60 versus 0.58) confirming that the  $OLT + O_3$  reaction is not a strong determinant of  $a$ .

## 6.4 Geometric Parameter $\lambda$

The next parameter to study is  $\lambda$  – the vertical coordinate of the scaling break in the Weibull plane. It measures the ratio of maximum ozone concentration when R equals  $\beta$  to the maximum in the NOS regime. This can be explained by making reference to the WEX model (Eq. (6.1)). In the NOx-only scaling region,  $f(R) \approx 1$  and maximum ozone concentration is at its ultimate value:

$$[O_3]_{ultimate} \approx (j_{av}/k_{NO})\gamma \left( \frac{[NOx]_o}{j_{av}/k_{NO}} \right)^a$$

and at the scaling break  $R = \beta$

$$[O_3]_{max} \approx (j_{av}/k_{NO})\gamma \left( \frac{[NOx]_o}{j_{av}/k_{NO}} \right)^a f(\beta)$$

So the ratio of maximum ozone at the break to maximum possible (or ultimate value) is:

$$\frac{[O_3]_{max}}{[O_3]_{ultimate}} \approx f(\beta) = 1 - \exp[-\lambda] \quad (6.4)$$

Since maximum ozone concentration in the NOS regime represents the highest ozone concentration that can be achieved from a given initial NOx (subject to environmental conditions),  $\lambda$  then quantifies the extent to which VOCs can continue to produce ozone once low-NOx conditions have been reached. VOCs (or VOC mixtures) with low  $\lambda$ -values are not able to produce much additional

Parameter	Original	Modified
$\gamma$	9.5	7.8
$a$	0.6	0.58
$\alpha_1$	2.2	2.0
$\alpha_2$	0.72	0.88
$\beta$	4.2	3.9
$\lambda$	0.92	1.3

Table 6.3: Comparison of OLI parameters for the original and modified RADM2 mechanism.

ozone when  $[VOC]_o$  is increased past the level needed to produce  $R = \beta$ . Interestingly, the largest  $\lambda$ -value is for ALD (1.7) while the lowest is for HCHO (0.14) – an exact reversal from the  $\gamma$ -values. Using Eq. (6.4), this gives a ratio of 0.82 for ALD ( $[O_3]_{max}$  is 82% of peak value at  $\beta$ ) and 0.13 for HCHO ( $[O_3]_{max}$  is only 13% of its peak value at the scaling break). Further investigation shows that for the six scaling RADM2 classes and two urban mixtures,  $\lambda$  and  $\gamma$  are the most strongly correlated pair of WEX parameters with a correlation coefficient of -0.87. This suggests  $\lambda$  is related to the way initial NO<sub>x</sub> is converted to final NO<sub>z</sub>; VOCs which do not produce PAN precursors, continue to produce substantial ozone after NO<sub>x</sub> depletion, and have a low  $\lambda$ -value.

#### 6.4.1 Sensitivity of isopleth shape to $\lambda$

The effects of doubling  $\lambda$  on isopleth shape are examined in Figures 6.6. The most striking feature is the quick transition made by the isopleths from the VLR to the NLR. If the ridge area is defined as the location where isopleths show the greatest curvature, then increasing  $\lambda$  narrows this area. Increasing  $\lambda$  also increases isopleth packing in the VLR but does not greatly affect isopleth slope in this region.

#### 6.4.2 Sensitivity of $\lambda$ to RADM2 modifications

Parameter  $\lambda$  measures the ability of a VOC to produce ozone after low-NO<sub>x</sub> conditions are reached. This appears to be largely determined by final NO<sub>z</sub> speciation.<sup>2</sup> To explore this connection, the reaction mechanism for the aromatic class XYLE, was modified in an attempt to reduce PAN formation.

After  $OH^\bullet$ -attack, XYLE produces 0.17 molecules of cresol (CSL). Cresol's main reaction pathway is with the hydroxyl radical; producing 0.9 molecules of the TPAN precursor TCO3 for every reaction. I modified the RADM2 mechanism to eliminate XYLE's CSL production after  $OH^\bullet$ -attack, with the expectation that this will allow more ozone to be produced after the scaling break. The resulting WEX parameters, regression against model output using this modified reaction scheme, are given in Table 6.4. It shows CSL elimination has reduced  $\lambda$  by 41% (while increasing  $\gamma$ ,  $a$ ,  $\alpha_2$  and decreasing  $\alpha_1$ ) and allowed more ozone production.

<sup>2</sup>However, the results of the second RADM2 experiment (section 6.3) suggest that final NO<sub>z</sub> speciation is not the sole determinant of  $\lambda$ . For alkenes, at least, increasing ozone titration by VOCs increases  $\lambda$ .

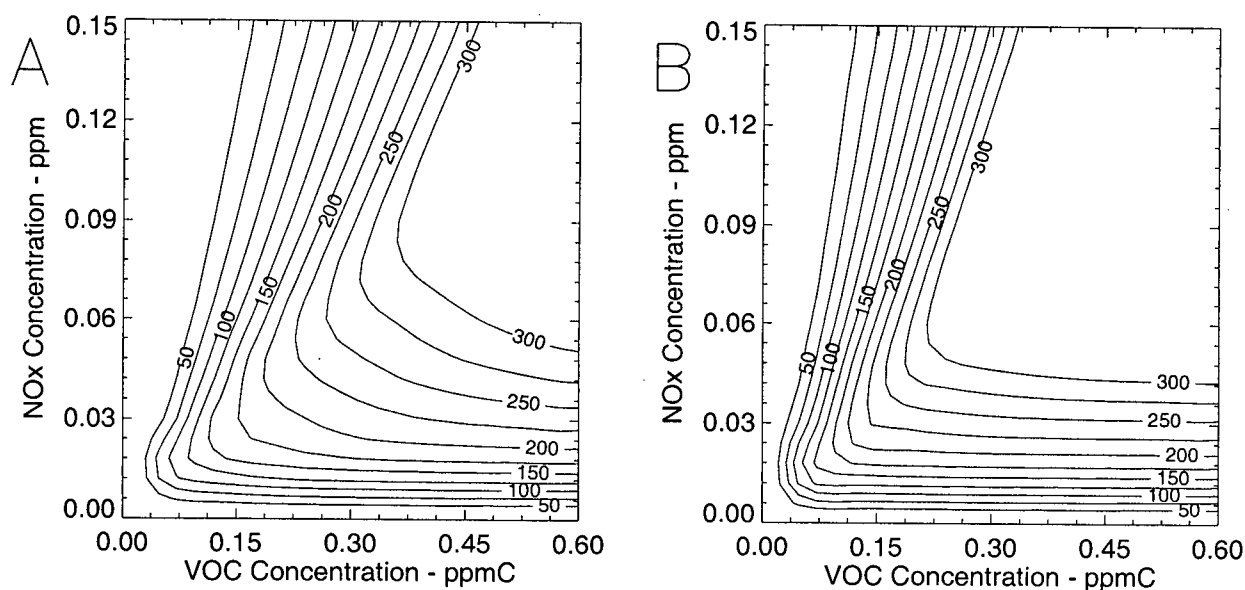


Figure 6.6: The effects of changing  $\lambda$  on ozone response surface. Figure A shows maximum ozone concentration (in ppb) as a function of initial VOC and NO $x$  concentration calculated using the WEX model and baseline parameter values. Figure B shows the resulting ozone isopleths (in ppb) after a doubling of  $\lambda$  (while all other WEX parameters have been held constant).

Parameter	Original	Modified
$\gamma$	7.6	8.5
$a$	0.56	0.64
$\alpha_1$	1.9	1.7
$\alpha_2$	0.44	0.71
$\beta$	5.3	5.4
$\lambda$	1.6	0.95

Table 6.4: Comparison of XYLE WEX parameters for the original and modified RADM2 mechanism after the elimination of CSL production.

## 6.5 Geometric Parameter $\alpha_1$

The analysis continues with  $\alpha_1$  – the slope of the lower Weibull line segment. First, I begin by examining the sensitivity of an ozone response surface to  $\alpha_1$ . This leads to an investigation of isopleth slope, which I define as the angle ozone isopleths make with the VOC axis. The relationship between isopleth slope and NO $x$ -inhibition is then considered. I finish by looking at the variability of  $\alpha_1$ , among the RADM2 classes, and its sensitivity to RADM2 modifications.

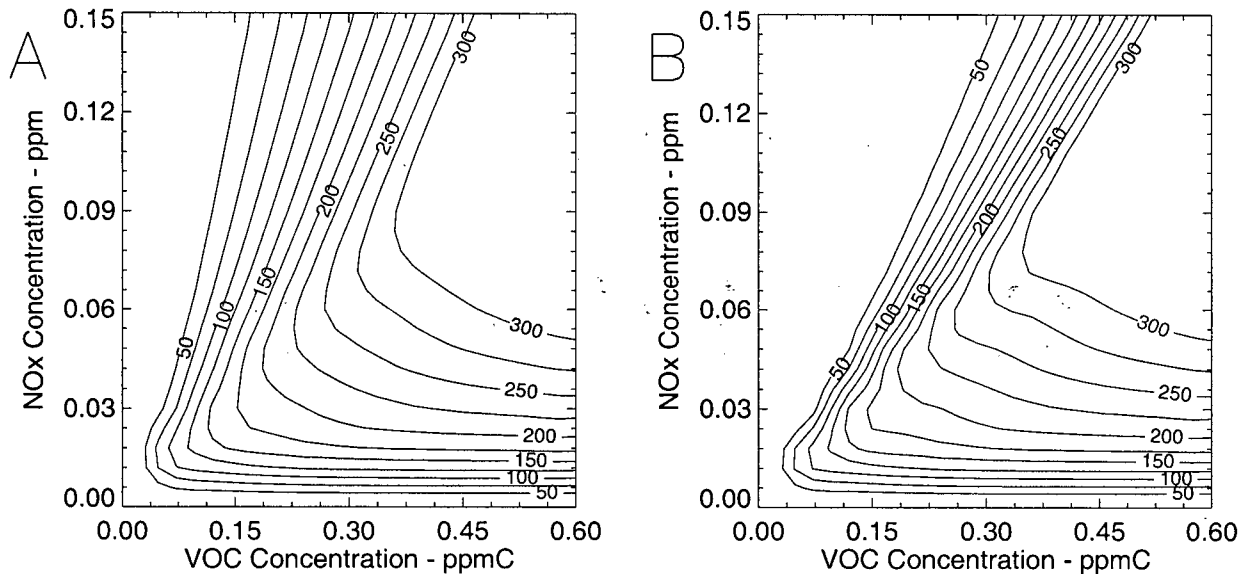


Figure 6.7: The effects of changing  $\alpha_1$  on ozone response surface. Figure A shows maximum ozone concentration (in ppb) as a function of initial VOC and NO<sub>x</sub> concentration calculated using the WEX model and baseline parameter values. Figure B shows the resulting ozone isopleths (in ppb) after a doubling of  $\alpha_1$  (while all other WEX parameters have been held constant).

### 6.5.1 Sensitivity of the ozone response surface to $\alpha_1$

Figure 6.7A and B show the effects of doubling  $\alpha_1$  from 2.0 to 4.0 (approximately going from the 2.1 of OLT to the 3.4 of TOLU) on an ozone response surface. The greatest effect is on the VLR; isopleths become more tightly packed and have a shallower slope (with respect to the VOC axis). Ozone concentrations are roughly the same everywhere and the isopleths have a similar shape around the ridge and in the NLR. I now use the WEX model to develop an expression for isopleth slope and to show its dependence on  $\alpha_1$ .

### 6.5.2 Ozone Isopleth Slope

At any location on an isopleth diagram, the angle an isopleth makes with the horizontal (VOC) axis can be defined. This isopleth slope is readily evaluated using the WEX model: Consider a unit normal  $\underline{u} = (\cos \theta, \sin \theta)$  parallel to an isopleth at some point ( $[VOC]_o, [NO_x]_o$ ) on an isopleth

diagram. By definition,  $\underline{u}$  is at right angles to the gradient i.e.:

$$\begin{aligned} 0 &= \underline{u} \cdot \nabla [O_3]_{max} \\ 0 &= (\cos \theta, \sin \theta) \cdot \left( \frac{\partial [O_3]_{max}}{\partial [VOC]_o}, \frac{\partial [O_3]_{max}}{\partial [NOx]_o} \right) \end{aligned} \quad (6.5)$$

Letting:

$$\begin{aligned} \eta &= \frac{\partial [O_3]_{max}}{\partial [NOx]_o} = \gamma \left( \frac{[NOx]_o}{j_{av}/k_{NO}} \right)^{\alpha-1} [af(R) - Rf'(R)] \\ \nu &= \frac{\partial [O_3]_{max}}{\partial [VOC]_o} = \gamma \left( \frac{[NOx]_o}{j_{av}/k_{NO}} \right)^{\alpha-1} f'(R) \end{aligned} \quad (6.6)$$

then solving Eq. (6.5) for  $\theta$  gives:

$$\begin{aligned} \theta &= \tan^{-1} \left( -\frac{\nu}{\eta} \right) \\ &= \tan^{-1} \left( \frac{-f'(R)}{af(R) - Rf'(R)} \right) \end{aligned} \quad (6.7)$$

The last expression is a function of  $R$  only, and it shows that for every line of constant  $R$ , isopleths are crossed at the same angle. In Figure 6.8A, I have used Eq. (6.7) to plot slope against  $R$  (using the baseline WEX parameters). When  $R \approx 0$  (approaching the NOx-axis), the isopleths have a slope of 90 degrees; parallel to the NOx-axis. The *ridgeline* is highlighted by the change in  $\theta$ 's sign - going from +90 to -90. As a reminder, the *scaling break* ( $\beta$ ) is 4.0 which lies to the left of the ridge in this plot (but above on an isopleth diagram). In the NOx-limited region, isopleth start to swing around and become parallel to the VOC-axis; with slope close to 0 degrees. An interesting feature of the Figure is the local minimum in the VOC-limited region. In Figure 6.8A, the minimum is  $28^\circ$  at  $R \approx 3.5$ . In Figure 6.8B, I have replotted  $\theta$  using the same WEX parameters but with a doubling of  $\alpha_1$ . In this case, the minimum occurs at roughly the same R-value but  $\theta_{min}$  drops to  $20^\circ$ . This suggests increasing  $\alpha_1$  decreases isopleth tilt in the VLR. Since, isopleths which make a shallower angle with the VOC axis show a greater change in maximum ozone concentration for a fixed decrease in initial NOx (holding initial VOC concentration constant), one would expect  $\alpha_1$  to be a measure of a VOCs NOx-inhibition, a point I address next.

### 6.5.3 NOx-inhibition and $\alpha_1$

NOx-inhibition is the phenomena by which maximum ozone concentration *decreases* when initial NOx concentration *increases*. On an isopleth diagram, this phenomena is evident in the VLR where ozone isopleths slope away from NOx axis. There are three reasons why maximum ozone concentration decreases for an increase in initial NOx concentration:

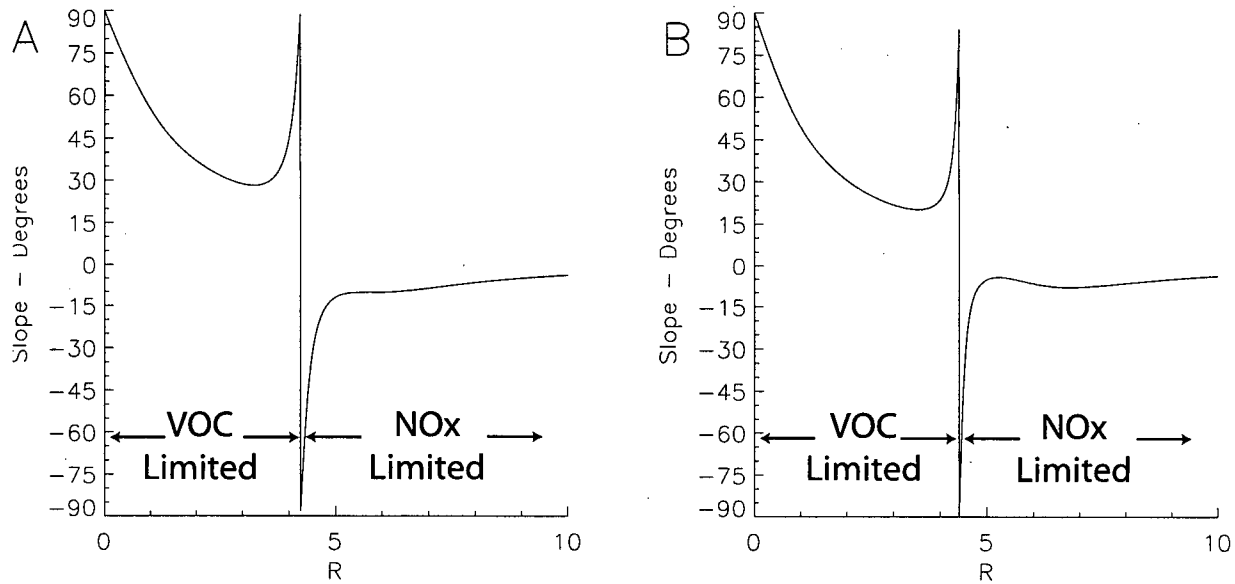


Figure 6.8: The effects of changing  $\alpha_1$  on of ozone isopleth slope. Figure A shows slopes using baseline WEX parameters while modified values were used to construct the slopes in Figure B.

1. As initial NOx increases, there is more NO available for ozone titration ( $R3$ ).
2. Secondly, by titrating ozone, radical initiation (via  $R4$ ) is also reduced, further slowing ozone formation. This has a compounding effect on production: ozone will now form later, when actinic flux starts to decline.
3. Finally, with higher  $NO_2$  concentrations, more  $HNO_3$  forms resulting in a loss of both radicals and NOx.

The above processes present another way of describing the positive feedback mechanism mentioned in Chapter 5 (although, now from the opposite point of view). While isopleth slope is one factor in determining NOx-inhibition, it does not fully determine the phenomena. For instance, a VOC which shows a small  $\theta_{min}$  (large tilting of isopleths in the VLR) but does not have very tight isopleth packing may not show the same sensitivity to changing NOx concentrations as one that has a high packing and less shallow slope. These ideas are schematically presented in Figure 6.9. Clearly both factors play a role in determining NOx-inhibition and their relative importance can be analytically quantified using the WEX model.

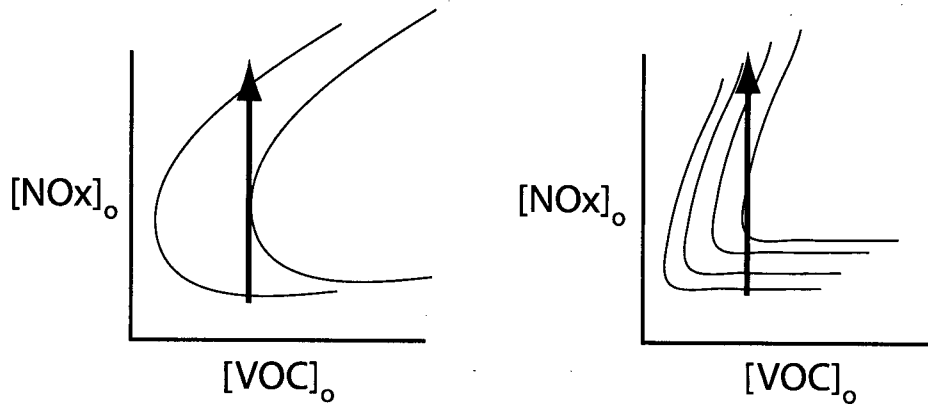


Figure 6.9: Isopleths with large tilting but low packing (A) and high packing with low tilting (B). By inspection, it is not possible to tell which shows greater NO<sub>x</sub>-inhibition.

#### 6.5.4 WEX and NO<sub>x</sub> Inhibition

To investigate the effects of both isopleth slope and packing on NO<sub>x</sub>-inhibition, I used the WEX model to evaluate the derivative of maximum ozone with respect to NO<sub>x</sub>. This is a complex function of NO<sub>x</sub> and all the WEX parameters:

$$\eta = \frac{\partial [O_3]_{max}}{\partial [NOx]_o} = \gamma \left( \frac{[NOx]_o}{j_{av}/k_{NO}} \right)^{\alpha-1} [af(R) - Rf'(R)] \quad (6.8)$$

NO<sub>x</sub>-inhibition ( $\eta$ ) depends directly on  $\gamma$ , which, as mentioned before, is related to isopleth packing. It also depends on the 6 WEX parameters in a complex way. However, since NO<sub>x</sub>-inhibition is only of concern above the ridgeline, I will ignore any dependence on  $\alpha_2$  and treat  $\alpha = \alpha_1$  independent of  $R$ . In Figure 6.10, I have plotted:

$$af(R) - Rf'(R) = a(1 - \exp[-\lambda(R/\beta)^{\alpha_1}]) - \lambda\alpha_1(R/\beta)^{\alpha_1} \exp[-\lambda(R/\beta)^{\alpha_1}] \quad (6.9)$$

versus  $R/\beta$  under three different scenarios. The plot shows the variability of Eq. (6.9) to changes in any of the three parameters ( $\lambda$ ,  $\alpha_1$ ,  $a$ ) when these are altered by 33% from a set of baseline conditions with  $\alpha_1 = 2.0$ ,  $\lambda = 1.2$ ,  $a = 0.66$ . When  $\alpha_1$  is increased to 2.67, Eq. (6.9) (and NO<sub>x</sub>-inhibition) increases for  $R/\beta > 0.45$  (i.e. Eq. (6.9) becomes more negative). Reducing  $\lambda$  to 0.9 reduces the NO<sub>x</sub>-inhibition up to  $R/\beta \approx 0.8$  and slightly increases it afterwards. Reducing  $a$  to 0.5, leads to a slight increase in NO<sub>x</sub>-inhibition for all  $R/\beta$ . While this analysis has only looked at the sensitivity of Eq. (6.9) using a single baseline set of conditions, it suggests that NO<sub>x</sub>-inhibition is more sensitive to  $\alpha_1$  than  $\lambda$  or  $a$ . It is important to note that Eq. (6.9) scales with  $R/\beta$  which is not the case with the derivative of maximum ozone with respect to  $[VOC]_o$  (Eq. (6.6)). It has a

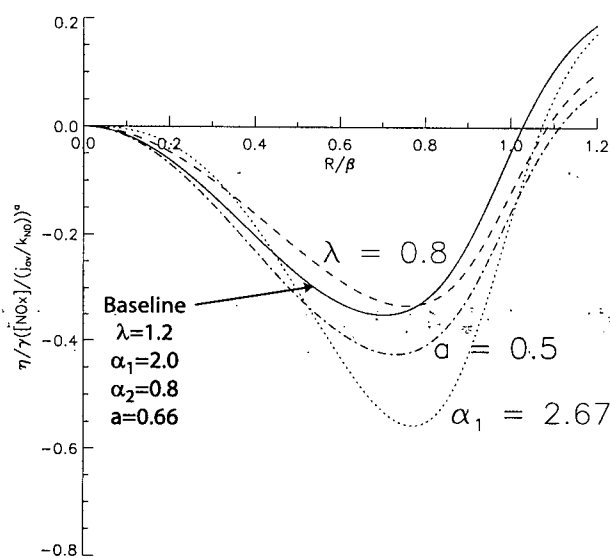


Figure 6.10: Dependence of NO<sub>x</sub>-inhibition on the three WEX parameters:  $a$ ,  $\lambda$  and  $\alpha_1$ . Each curve shows the variability of Eq. (6.9) as a function of  $R/\beta$  for a range of parameter values listed in the text.

direct  $\beta$ -dependence which leads to important differences between  $\eta$  and  $\nu$  (a matter addressed in Chapter 7).

While this is by no means a comprehensive sensitivity analysis, it shows, as expected, both  $\gamma$  and  $\alpha_1$  are important determinants of NO<sub>x</sub>-inhibition. Furthermore, since NO<sub>x</sub>-inhibition is closely related to the positive feedback mechanism (Section 5.4),  $\alpha_1$  is also a measure of the strength of the positive feedback mechanism; large  $\alpha_1$ -values produce more 's-shaped' similarity curves.

### 6.5.5 Range of $\alpha_1$ -values

I have listed the RADM2 classes by increasing  $\alpha_1$  in Table 6.5. The table shows formaldehyde having the smallest value (1.5) while TOLU has the largest (3.1). To understand the range of values and the relative ordering, recall that any VOC which has its own photolytic source of radicals can initiate radical attack without having to rely on ozone-produced  $OH^\bullet$ . Such VOC are less dependent on the autocatalytic nature of the positive feedback loop. So, I expect VOCs which readily photolyze, or those which produce more carbonyl compounds upon oxidation, will have lower  $\alpha_1$  values. Table 6.5 shows that the two lowest values are both aldehydes compounds (HCHO and ALD) which readily photolyze to produce radicals. Strangely, the carbonyl class KET, also a photolytic source of radicals, has one of the highest values for which I have no immediate explanation.

TOLU, has the highest value while the other aromatic class XYLE has an intermediate value.

RADM2 class	$\alpha_1$
HCHO	1.5
ALD	1.7
OL2	1.8
OLI	1.9
XYLE	1.9
OLT	2.2
KET	2.8
TOLU	3.1

Table 6.5: RADM2 classes ranked by  $\alpha_1$ .

Parameter	Original	Modified Mechanism
$\gamma$	9.5	9.5
$a$	0.6	0.58
$\alpha_1$	2.2	2.7
$\alpha_2$	0.72	0.52
$\beta$	4.2	10.6
$\lambda$	0.92	1.3

Table 6.6: Comparison of OLI parameters using the original and modified RADM2 mechanism.

Neither directly photolyzes but both form peroxy radicals (TOLP and XYLP respectively) that produce carbonyl compounds after reacting with NO. Every XYLP conversion produces 0.45 MGLY (methylglyoxal) and 0.806 DCB (an unsaturated dicarbonyl) both of which produce radicals upon photolysis. Every conversion of TOLP produces only 0.17 MGLY and 0.7 DCB along with 0.16 GLY (glyoxal), which results in fewer carbonyl compounds per reaction. While a more thorough comparison would calculate the fraction of total radical production coming from secondary aldehydes, this initial analysis suggests that XYLE deserves its higher ranking because of its ability to produce more radicals from secondary sources than TOLU.

### 6.5.6 Sensitivity of $\alpha_1$ to RADM2 modifications

To further examine the link between photolytic source of radicals and  $\alpha_1$ , I set the HCHO and ALD photolysis rates to zero and ran a set of OLT simulations using these modifications. Since each conversion of NO to NO<sub>2</sub> by the OLT peroxy radical (OLTP) produces one molecule of both HCHO and ALD, by halting the photolysis of HCHO and ALD, I expect to largely eliminate new radical production (from sources other than ozone) for OLT. This should strengthen the positive feedback mechanism and increase  $\alpha_1$ . Table 6.6 shows the resulting WEX parameters. As expected,  $\alpha_1$  has increased but there is also an increase in  $\beta$  and  $\lambda$  while  $\alpha_2$  has decreased.

### 6.5.7 NOS scaling regime

One could now define a new region on an isopleth diagram – the NO<sub>x</sub>-only scaling regime (NOS) – where maximum ozone concentration is largely independent of  $R$  and scales only with NO<sub>x</sub>. It is the region where isopleth slope is close to zero and roughly corresponds to the set of  $R$ -values where  $f(R) > 0.9$ . By defining this regime, an isopleth diagram can be separated into 3 regions: NO<sub>x</sub>-limited regime, a ridge area or knee region and the NOS regime. The scaling break separates the NO<sub>x</sub>-limited and the ridge area while the boundary between the ridge area and the NOS regime could be defined by a critical value in isopleth slope or  $f(R)$ .

## 6.6 Geometric Parameter $\alpha_2$

The final parameter ( $\alpha_2$ ) measures the rate at which maximum ozone concentration increases in the NLR. It is related to ozone production under low-NO<sub>x</sub> conditions. In Section 5.3, an expression for ozone production, under such conditions was given:

$$P(O_3) \approx (A[O_3] + B[VOC])^{1/2}[NO] \quad (6.10)$$

where  $A$  is a constant which accounts for the source of  $OH^\bullet$  from ozone and  $B$  is a constant which accounts for radical source from aldehydes (Sillman et al., 1990).

Equation (6.10) shows ozone production (in this regime) to have a weak VOC dependence. This is consistent with  $\alpha_2$  which has the second least variability among the WEX parameters (after the NO<sub>x</sub>-scaling exponent ( $a$ )). Equation (6.10) also shows production to be higher for VOCs with their own photolytic source of radicals. This is again consistent with the results of the RADM2 modification in Section 6.5, where removal of HCHO and ALD photolysis lead to a decrease in  $\alpha_2$ . However, the highest  $\alpha_2$  value was for OLT (0.81) and the lowest was for XYLE (0.16). Again, I cannot explain this, however, it is not likely that all the RADM2 variability can be explained by such a simple model.

### 6.6.1 Sensitivity of ozone isopleths to $\alpha_2$

Figure 6.11A and B show effects of changing  $\alpha_2$  from 0.75 to 0.33 on an isopleth diagram. Both sets of isopleths show similar shape with nearly the same magnitudes in the VLR. The greatest difference is isopleth curvature around the ridgeline – smaller values lead to greater curvature. This parameter appears to have least effect on isopleth shape.

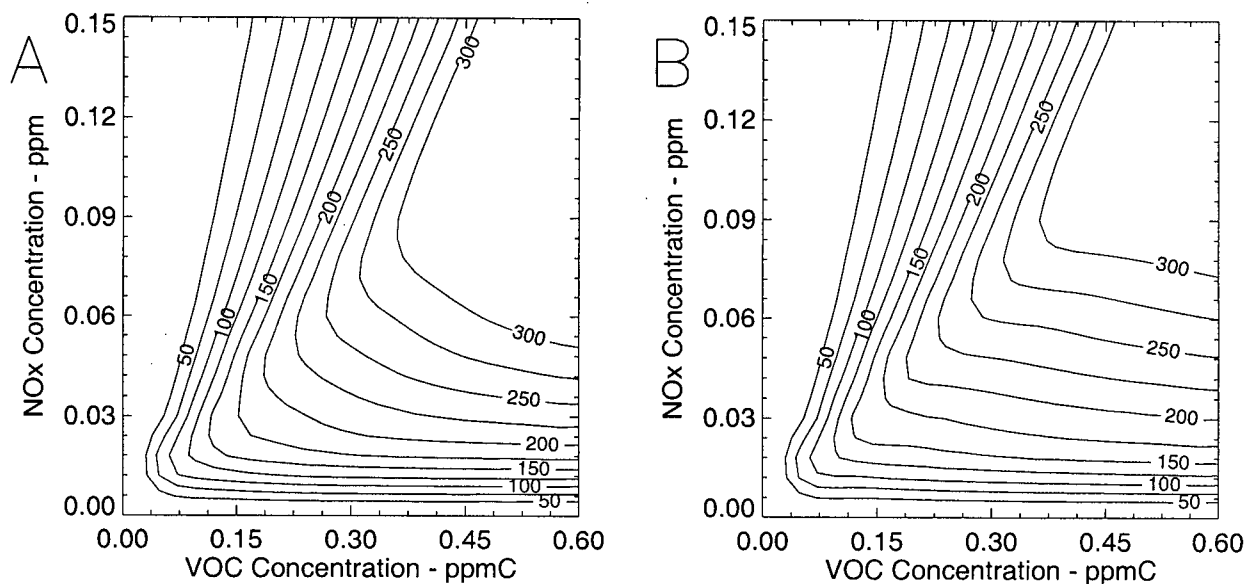


Figure 6.11: The effects of changing  $\alpha_2$  on ozone response surface. Figure A shows maximum ozone concentration (in ppb) as a function of initial VOC and NO<sub>x</sub> concentration calculated using the WEX model and baseline parameter values. Figure B shows the resulting ozone isopleths (in ppb) after a reduction of  $\alpha_2$  from 0.75 to 0.33 (while all other WEX parameters have been held constant).

## 6.7 Conclusion

In chapters 5 and 6, I have examined the relationship between WEX parameters and the underlying chemistry. I have found that while none is directly related to a measurable quantity (like  $OH^\bullet$ -reactivity or photolysis rate) each appears to quantify a sub-process within the greater photochemical system. I now summarize the significance and interpretation of each parameter:

- $\gamma$  Represents a pure scaling of maximum ozone concentration. Higher values lead to higher maximum ozone concentrations for given initial VOC and NO<sub>x</sub> concentrations. Its value is influenced by the final partitioning of NO<sub>z</sub>.
- a** This parameter is the exponent in the power-law relationship that holds between maximum ozone and initial NO<sub>x</sub> concentration. It is a measure of a VOCs 'NO<sub>x</sub>-inefficiency' – lower values imply a VOC produces less ozone per unit NO<sub>x</sub> at higher initial NO<sub>x</sub> concentrations.
- $\alpha_1$  This parameter, the slope of the WEX curve in the Weibull-plane for R-values less than  $\beta$ , is related to a VOCs 'NO<sub>x</sub>-inhibition'. Higher values imply that, in the VLR, a VOC will produce

a greater *increase* in maximum ozone for a fixed *decrease* in initial NO<sub>x</sub>. This parameter is also related to isopleth above the ridgeline and the strength of the positive feedback mechanism that controls ozone production before the scaling break – larger values imply ozone production has a greater dependence on ozone concentration.

$\alpha_2$  This parameter represents the slope of the WEX curve in the Weibull-plane for R-values greater than  $\beta$ . It is related to ozone production for R-values greater than  $\beta$  or in ‘low-NO<sub>x</sub>’ environments with higher values imply greater production rates.

$\beta$  This parameter identifies the R-value associated with the shift in the chemical regime. For precursor mixtures with initial VOC to NO<sub>x</sub> ratios greater than  $\beta$ , almost all initial NO<sub>x</sub> will be converted to stable nitrogen products by the end of the irradiation period. VOCs with higher OH<sup>•</sup> reactivities tend to have lower  $\beta$ -values.

$\lambda$  This parameter is related to the ratio of maximum ozone concentration before break to maximum ozone concentration in the NOS regime (ultimate ozone concentration). For VOCs with high  $\lambda$ -values, only a small increase in maximum ozone (relative to the concentration at  $R = \beta$ ) is achieved with higher initial VOC levels. This parameter shows a high negative correlation with  $\gamma$ .

From the list, it appears that many of the parameters are related to inorganic chemistry i.e.: NO<sub>z</sub> partitioning; ‘NO<sub>x</sub>-inefficiency’; NO<sub>x</sub> inhibition; ratio of VOC to NO<sub>x</sub> for which NO<sub>x</sub> consumption occurs before simulation end. This suggests that while VOCs play an important role supplying radicals to the photochemical system, theirs is secondary – controlling production rates or NO<sub>z</sub> speciation. This is not entirely unexpected, as NO<sub>x</sub> is the key to tropospheric chemistry: NO<sub>2</sub> photolysis is the only reaction that leads to ozone formation in the troposphere (Seinfeld and Pandis, 1998) and most of the troposphere is NO<sub>x</sub>-limited (Sillman, 1999).

Finally, WEX parameters provide an easy and concise means of comparing the relative importance of several process within the photochemical system. For instance, it is now possible to compare the relative strength of NO<sub>x</sub>-inhibition or guess the likely NO<sub>z</sub> speciation for different VOCs given their WEX parameters.

The next two chapters illustrate uses for the WEX model including: summarizing smog chamber data, investigating a simple reaction mechanism, and quantifying incremental reactivity.

## Chapter 7

# Evaluation of the WEX model using smog chamber data

### 7.1 Introduction

Up to this point, I have used dimensional analysis to describe ozone formation using power law relationships for a set of dimensionless  $\Pi$ -groups. I used model output to determine the functional relationship between maximum ozone concentration and these  $\Pi$ -groups. I have checked the consistency of these relationships using different chemical mechanisms. Further confidence in the model's ability to characterize ozone photochemistry can only be gained through direct comparison with experimental results. In this chapter, I determine if experimentally observed ozone concentrations, after suitable transformations, are consistent with the similarity relationships developed in the WEX model. To carry out these investigations, I make use of data from a set of smog chambers studies.

Before proceeding, I present an overview of smog chamber design and discuss some technical issues involving their use. This material is important for this thesis in particular, and modelers in general, because it highlights the limitations of smog chamber experiments and the difficulties in validating chemical mechanisms. As these technical issues will show, it is difficult to compare model output with smog chamber data. As a result, I do *not* use the WEX model to simulate a smog chamber and then compare with experimental observations. Instead, I fit the WEX model to smog chamber data and show that the model is both consistent with chamber observations and can collapse a wide range of results onto a single similarity relationship. While this implies the WEX model captures the variability in the chamber data, it is not an independent check of the model. Chemical mechanisms, while compared with chamber data in a slightly different manner, also suffer similar validation difficulties.

## 7.2 Smog chambers

A smog chamber is to an atmospheric chemist what an air parcel is to an atmospheric physicist: an idealization, useful for the purpose of explanation, but difficult to realize in practice. Consider the ubiquitous air parcel: a fixed volume of air bounded by a thin membrane which prevents outside mixing but offers no resistance to expansion. A smog chamber could similarly be described: a fixed volume of air bounded by a thin membrane which prevents outside mixing but offers no impedance to the transmission of sunlight and does not interfere with the photochemistry within. While similar in nature, they find different uses: air parcels are mainly used for explanations or mathematical derivations (for which they are ideally suited) while smog chambers are used to quantify both the kinetic and mechanistic properties of photochemical reactions (which they meet with varying degrees of success).

### 7.2.1 Smog chamber design

In practice, smog chambers (also called environmental chambers) are large reaction vessels into which known amounts of precursor gases are injected and uniformly mixed (Finlayson-Pitts and Pitts, 1999). The mixture is irradiated and its chemical composition continuously analyzed. Test conditions, like temperature, relative humidity and actinic flux are also measured and, if necessary, systematically varied to simulate different atmospheric conditions. There are various chamber designs, each having strengths and weaknesses, and it is important to understand how each design influences experimental results. In essence, two main design features characterize smog chambers: membrane material and light source.

#### Membrane material

The largest source of difficulty with smog chamber design is the choice of membrane (Finlayson-Pitts and Pitts, 1999). The ideal membrane should be inert, transparent and air tight. While no material meets all these criteria, two suitable materials are glass and Teflon. Glass chambers are cheap, convenient and readily available but have poor transmissivity in the ultra-violet spectrum (Doussin et al., 1997). Teflon, because of its low rates of surface deposition, good transmissivity in the ultra-violet and visibility is the membrane material used in most research centres. Chambers using Teflon membranes are varied – they can consist of fixed frames covered by Teflon films (e.g. UNC outdoor chamber (Carter and Lurman, 1991)), collapsible Teflon bags (e.g. OTC, DTC and XTC indoor chambers at the University of California, Riverside (Carter et al., 1996)) or rigid structures made of Teflon coated walls (e.g. CSIRO outdoor chamber (Hess et al., 1992a)).

## Light source

The second biggest difficulty in chamber design is the light source. While the most obvious source is natural light, it presents a number of practical problems. Principally, its intensity is altered by the presence of clouds and haze and the extent of alteration can be difficult to quantify. In addition, the use of natural light requires chambers to be placed outdoors where testing is contingent on the weather and the control of temperature and humidity more difficult. Despite these drawbacks, there are several outdoor chambers and in this chapter, I make use of data gathered from one of these – the Australian Commonwealth Scientific and Industrial Research Organization's (CSIRO) chamber in Sydney, Australia (Hess et al. (1992a), Hess et al. (1992b) and Hess et al. (1992c)).

To provide more freedom for testing and more control over environmental conditions, indoor chambers have been build which use special lamps to mimic the spectral properties of sunlight (Finlayson-Pitts and Pitts, 1999). Typically these are either specially coated mercury or xenon lamps. Often, the lamp's spectral properties are adjusted to produce a spectrum which matches that of the sun around the peak wavelength for  $NO_2$  photolysis. However, this matching can be at the expense of the spectral properties at wavelengths where photolysis of other species (for example  $O_3$  or  $HCHO$ ) may be important. Furthermore, as these lamps age, their spectra shift and regular characterization of both their spectral distribution and absolute light intensity is needed (Finlayson-Pitts and Pitts, 1999).

### 7.2.2 Chamber limitations

Smog chambers are not idealized containers that allow close inspection of free atmospheric reactions. In addition to the lighting issues, smog chambers are plagued by 'wall effects' – the sum of many processes – relating to the presence of the membrane surface which distorts the chemical transformations observed within the chamber. The most important processes include:

**Deposition** The membrane surface act as sink for various species via deposition (Simonaitis et al., 1997). Ozone, nitric acid and formaldehyde all adhere to membranes or can be adsorbed into water droplets forming on the membrane.

**Off-gassing** Closely related to deposition is off-gassing: the release of gaseous species from the chamber walls (Carter and Lurman, 1991). The most sensitive species to this process is  $NO_x$ . Chamber studies of clean air irradiation (i.e. no  $NO_x$  or VOCs) often show significant ozone formation. This photochemical production can only be accounted for by the release of organic compounds and nitrogen from the chamber walls; likely deposited during previous experiments.

**Radical sources** Smog chamber experiments produce a greater number of radicals that cannot be accounted for by the chemical kinetics (Carter et al., 1981). The presence of these excess radicals greatly limits the utility of smog chamber data. In many cases, the only way to reconcile observations with chemical kinetics is to include an extra or artificial radical sources. Figures 7.1A&B show observed ozone concentration-time profiles (open circles) from two different smog chambers (the National Institute for Environmental Studies (NIES) chamber in Japan (Akimoto et al., 1985) (Figure A) and the University of California Riverside (UCR) in the USA (Carter et al., 1996) (Figure B)). Included in each figure are two curves for predicted ozone concentrations: one without additional radical sources and one that includes these sources (lines II and I respectively). Clearly, without including artificial sources, ozone concentrations are greatly under-predicted. The exact source of this radical supply is uncertain, varies between chambers, and is difficult to characterize (Finlayson-Pitts and Pitts, 1999).

**Heterogeneous reactions** Not only can the walls act as a surface for deposition but they also serve as a site for heterogeneous reactions. Sakamaki and Akimoto (1988) propose one source for the extra radicals is the photolysis of *HONO* forming on chamber membranes by the reaction:



**Hang-up and Leakage** Finally, experiments can be contaminated by two other means: hang-up and leakage. Hang-up represents residual pollutants not completely removed from the chamber before the beginning of a new test. Generally, hang-up can be reduced by repeated filling and purging the chamber with clean air between experiments. Leakage involves both the escape of pollutants from the chamber or the infiltration of ambient air into the chamber.

To summarize, smog chamber data are confounded by many experimental uncertainties. These effects are significant, introduce distortions into the chemical transformation processes, cannot be eliminated and depend on chamber design. As a result, great care is required when corroborating chemical mechanisms with such data.

### 7.3 Comparing the WEX model to smog chamber data

Chemical mechanisms are usually developed using kinetic data and validated by comparison with smog chamber data. Since chamber data is complicated by 'wall effects', to get agreement between the two, additional expressions (or artifacts) are added to the mechanism (Finlayson-Pitts and Pitts,

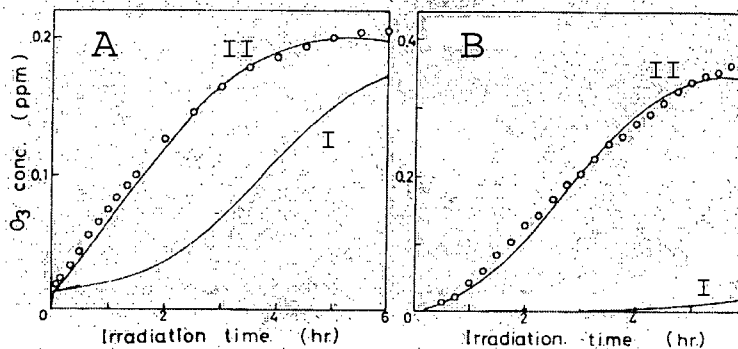


Figure 7.1: Observed and modeled ozone concentrations for two different smog chamber experiments. Figure A shows data from the National Institute for Environmental Studies (NIES) smog chamber while Figure B shows smog chamber data from the University of California, Riverside (UCR). In both figures, open circles are observed ozone concentrations, lines labeled I are modeled ozone concentrations without accounting for additional radical sources and lines labeled II are modeled ozone concentrations after the inclusion of extra radical sources (adapted from Sakamaki and Akimoto (1988)).

1999). But there is no consensus on how to characterize these artifacts (Dodge, 2000). Furthermore, these artifacts are removed when the mechanism is used in an air quality model (Jeffries et al., 1992). In essence, then, two separate models are created – and only one is validated (and not the one used for potential regulatory policy). Finally, in order to reduce wall effects, leakage and hang-up, chamber experiments are often performed at higher than ambient concentrations (Hess et al., 1992a). As a result, model validation is performed outside of the realm under which chemical mechanisms are normally used (Dodge, 2000). In general, it is estimated that while chemical mechanisms are able to simulate chamber data, the uncertainty in their predictions of remains about  $\pm 30\%$  (Dodge, 2000).

In this section, I compare the WEX model to a series of experiments from the CSIRO outdoor chamber (University of North Carolina, 2001). To reduce the difficulty in comparing smog chamber data with model output, the analysis does *not* proceed by first modeling the chamber using the RADM2 mechanism (or any other mechanism) and then finding corresponding WEX parameters which can then be used to predict chamber ozone concentrations. Instead, I fit the WEX model directly to the chamber data. I begin by expressing the chamber data using the dimensionless groups introduced in Chapter 3. Since, for reasons of cost, the facility did not perform a large matrix of experiments over a wide range of initial VOC and NO<sub>x</sub> concentrations and fixed environmental conditions, it is difficult to use *maximum* ozone concentration as a basis for comparison. Rather,

I make use of the temporal WEX model (Eq. (5.18)) to compare ozone versus time relationships. To further complicate matters, the experiments span a wide range of environmental conditions, so temperature and actinic flux dependencies (developed in Chapter 4) must be included. As an added check of the model, once I have fit the WEX model to the temporal ozone data, I can use the resulting WEX parameters to predict maximum ozone concentration as a function of  $R$ .

Finally, I also fit the data to the IER model (Johnson, 1984) for two reasons. First, it was developed using similar data from the same smog chamber and secondly, it provides a benchmark for the WEX analysis.

### 7.3.1 CSIRO Data set

In 1995 and 1996, a series of smog chamber experiments was performed at the CSIRO outdoor smog chamber facility in the North Ryde suburb of Sydney (latitude  $33^{\circ}52'S$ , longitude  $151^{\circ}13'E$ ). The facility has two separate cubical smog chambers (referred to as *Levante* (L) and *Ponente* (P)) each with a volume of  $20.4 \text{ m}^3$  and made of 0.05 mm fluorinated ethene-propene (FEP Teflon) film mounted to a rigid frame. The chambers were instrumented to measure  $NO$ ,  $NO_2$ ,  $O_3$ , temperature, ultra-violet intensity and total solar radiation flux.

Ten experiments in each of the two chambers were run using a mixture of VOCs typical of Sydney's air (Hess et al., 1992a). All of the experiments were performed without dilution and with the VOC and  $NO_x$  initially well mixed at the beginning of the experiments. Typically, the experiments started at sunrise and continued until late afternoon. Table 7.1 lists the test conditions for the 20 experiments while ozone versus time plots are given in Figure 7.2A.

### 7.3.2 IER Analysis

To fit the data to the IER model, I first rewrote it in the following form:

$$\frac{[PSP]}{[NOx]_o} = \begin{cases} zRj(t)\theta(T), & zRj(t)\theta(T) < \beta \\ \beta, & zRj(t)\theta(T) \geq \beta \end{cases} \quad (7.1)$$

where  $PSP$  represents primary smog potential (a measure of the amount of molecular oxygen dissociated by ozone producing reactions),  $z$  an unknown reactivity coefficient for the VOC mixture and  $\theta(T)$  is the model's temperature dependence factor:

$$\theta(T) = \exp \left[ -4710 \left( \frac{1}{(T_{av} + 273)} - \frac{1}{316} \right) \right] \quad (7.2)$$

For each experiment, I performed the following calculations:  $[O_3](t)$ ,  $[O_3](0)$ ,  $[NO](t)$ ,  $[NO](0)$  and  $[NOx]_o$  were used to determine  $[PSP]/[NOx]_o$ , the  $NO_2$  photolysis rate and local test time

Test name	Month	Date	$[VOC]_o$ (ppb)	$[NOx]_o$ (ppb)	R	$T_{av}$ (C)	J	$j_{av}$ ( $s^{-1}$ )
340P	September	21	200.0	19.6	10.2	22.5	228.3	0.00634
340L	September	21	200.0	19.7	10.2	22.2	227.6	0.00632
341P	September	28	200.0	53.4	3.7	18.0	231.2	0.00642
341L	September	28	200.0	24.8	8.1	17.4	226.9	0.00664
342P	October	5	100.0	54.0	1.9	22.2	248.4	0.00657
342L	October	5	200.0	55.6	3.6	21.2	250.5	0.00633
343P	October	10	400.0	53.6	7.5	21.5	250.8	0.00664
343L	October	10	100.0	54.5	1.8	21.5	247.3	0.00654
344P	October	11	200.0	44.6	4.5	26.9	251.3	0.00665
344L	October	11	400.0	46.2	8.7	26.0	253.9	0.00672
345P	October	19	200.0	100.4	2.0	28.5	250.8	0.00697
345L	October	19	400.0	97.2	4.1	28.8	245.0	0.00717
359P	March	15	100.0	30.9	3.2	25.2	174.6	0.00809
359L	March	15	50.0	28.2	1.8	25.0	187.1	0.00800
360P	March	19	50.0	31.4	1.6	22.8	215.2	0.00664
360L	March	19	100.0	30.3	3.3	22.7	221.6	0.00648
361P	March	21	100.0	17.4	5.7	22.4	225.0	0.00622
361L	March	21	100.0	31.1	3.2	22.5	230.9	0.00639
362P	March	26	50.0	19.3	2.6	25.2	241.9	0.00640
362L	March	26	100.0	18.9	5.3	24.7	237.9	0.00630

Table 7.1: Test conditions for the 20 CSIRO smog chamber experiments. The VOC is a mixture of organics typically found in the Sydney air (Hess et al., 1992a). The total  $NO_2$  photolysis rate is given by J while  $j_{av}$  is its average value over the duration of the experiment.

were used to find  $j(t)$ ,  $[VOC]_o$  and  $[NOx]_o$  were used to determine R and  $T_{av}$  for  $\theta(T)$ . Plots of  $[PSP]/[NOx]_o$  versus  $Rj(t)\theta(T)$  are given in Figure 7.2B. The IER model does a fair job at modeling  $[PSP]/[NOx]_o$  but there is still a large amount of scatter. Also included in the Figure is the IER function that best fits the data (corresponding to  $\beta = 7.50$  and  $z = 0.0112$ ). These parameters have been used with Eq. (7.1) along with the definition of PSP:

$$[PSP](t) = ([O_3](t) - [O_3](0)) + ([NO](0) - [NO](t)) \quad (7.3)$$

to calculate ozone concentrations (all of the experiments had  $[O_3](0) = [NO](t_{end}) = 0.0$ ). Figure 7.2C shows the resulting scatter plot of predicted to observed ozone concentration. Table 7.2 summarizes the scatter plot statistics. The IER model shows a bias for over prediction. One reason for this bias is the model has been developed to capture  $[PSP]/[NOx]_o$  variability and not ozone concentrations. Equation (7.3) shows that  $[PSP]$  and  $[O_3]$  differ the most when initial NO concentrations are large. In Figure 7.2B the three curves with the greatest deviation from the model (344L, 343P and 345L) all have large initial NO concentrations (53.0, 45.7 and 96.6 ppb). As a result, both the overestimation in the fitting of PSP and the high initial NO concentration lead to a large overestimation of ozone.

These results serve as a baseline for the WEX analysis; I expect the more complex WEX model to better capture ozone dependence on its precursors and environmental conditions.

Model	Slope	Intercept (ppb)	$R^2$	RMSE (ppb)	MBE (ppb)
IER	0.57	23.7	0.82	47.8	-9.1
WEX (temporal)	0.94	4.7	0.96	12.5	0.4
WEX (maximum)	0.93	5.0	0.87	20.9	4.3

Table 7.2: Summary of statistics for the IER and WEX scatter plots.

### 7.3.3 WEX Analysis of temporal ozone concentrations

Since only 20 experiments were performed over a limited range of R-values ([1.6, 10.2]), I used the temporal WEX model (Eq. (5.18)) to analyze the data. I began by expressing the data using dimensionless groups:  $\Pi (= [O_3]/(k_{NO}/j_{av}))$  for the ozone concentrations,  $\Pi_1 (= [NOx]_o/(k_{NO}/j_{av}))$  for the initial NOx concentrations,  $\Pi_2 (= [VOC]_o/[NOx]_o)$  for the relative abundance of VOC to NOx and  $\Pi_4 = \exp[-504(1/(T_{av} + 273) - 1/298)]$  for the dimensionless temperature dependence. For the  $j(t)$  dependence, I assumed that  $\beta = \beta(j(t)) = \beta'j(t)^{-c}$ . As a result, I used the following relationship for ozone concentration:

$$\begin{aligned} \frac{[O_3]}{j_{av}/k_{NO}}(j(t); R, [NOx]_o) &= \gamma \left( \frac{[NOx]_o}{j_{av}/k_{NO}} \right)^a \left( 1 - \exp \left[ -\lambda \left( \frac{Rj^c}{\beta'} \right)^\alpha \right] \right) \\ &\times \exp \left( -504 \left[ \frac{1}{(T_{av} + 273)} - \frac{1}{298} \right] \right)^b \end{aligned} \quad (7.4)$$

where  $(a, b, c)$  are the unknown exponents for the NOx, temperature and actinic flux power laws and  $(\gamma, \lambda, \alpha_1, \alpha_2, \lambda)$  are the unknown WEX parameters. Rearranging Eq. (7.5) in terms of Pi-groups yields:

$$\frac{\Pi}{\Pi_1^a \Pi_4^b} = \gamma f(\Pi_2 j^c) \quad (7.5)$$

The goal, then, is to show that by plotting  $\Pi/(\Pi_1^a \Pi_4^b)$  versus  $\Pi_2 j^c$  the data collapses onto a common curve **and** that this curve (i.e. the similarity relationship ( $f$ )) can be parameterized by a composite of two Weibull functions.

To test these two conjectures, the following steps were taken:

1. For each experiment, the total  $NO_2$  photolysis rate and total test time were used to calculate the average photolysis rate ( $j_{av}$ ).
2. The average temperature was used to determine  $k_{NO}$  and  $\Pi_4$ .
3. The initial NOx concentration was used to determine  $\Pi_1$  and the initial VOC and NOx concentrations to find  $\Pi_2$ .
4. Each measured ozone concentration was non-dimensionalized as  $\Pi$

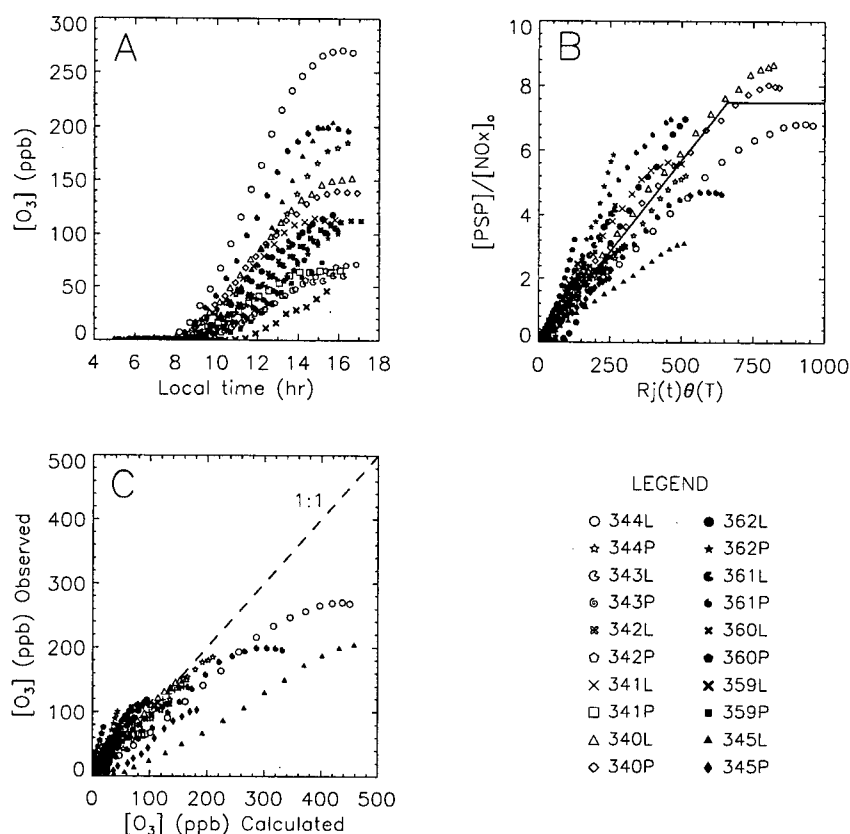


Figure 7.2: Comparison of the IER model and the CSIRO smog chamber data. Figure A shows the ozone-time profiles for the 20 experiments. Figure B shows the same data expressed as  $[PSP]/[NOx]_0$  versus  $R_j(t)\theta(T)$ . Also shown (solid line) is the IER model which has been used to calculate ozone in Figure C.

- For each ozone measurement, the cumulative  $NO_2$  photolysis rate was used to determine  $j(t)$  based on calculated local solar elevation.

The resulting dimensionless data have been grouped according to Eq. (7.5) and plotted as a function of  $\Pi_1 j^c$  in Figure 7.3A. Also shown on this plot is the WEX function  $f(R_j(t)^c)$  that best fits the data. Values for the three exponents ( $a, b, c$ ) as well as the WEX parameters are given in Table 7.3.

Before continuing with the analysis, a few comments about the parameter values in Table 7.3 are needed. The resulting  $NO_x$ -scaling exponent ( $a = 0.25$ ) is much lower than any of the values found in Chapter 4. I suspect this is a consequence of the data being weighted for low  $R$ -values – a point I return to later. The  $\gamma$ -value is larger than for the other VOCs (with the exception of HCHO) and may be a result of the low  $a$ -value ( $\gamma$  and  $a$  show a strong positive correlation of 0.89 for the

a	b	c	$\gamma$	$\alpha_1$	$\alpha_2$	$\beta'$	$\lambda$
0.25	7.6	1.5	13.1	1.4	0.88	17000	0.96

Table 7.3: WEX parameters and power law exponents used to fit the CSIRO data.

RADM2 classes). The mixture also has a low value for  $\alpha_1$  suggesting little NO<sub>x</sub>-inhibition. This finding is consistent with comments made by Tonnesen and Jeffries (1994) who argue that the GRS mechanism (developed using similar CSIRO smog chamber data) shows little NO<sub>x</sub>-inhibition when compared with the CB-IV mechanism. They worry that this low NO<sub>x</sub>-inhibition is an experimental artifact caused by additional radical sources (i.e 'wall effects') and is not an accurate characterization of ozone formation at low VOC-NO<sub>x</sub> ratios. The present analysis cannot clarify this matter. The value of  $\alpha_2$ , is greater than those found for the other VOCs studied, but this value was difficult to determine since there were relatively few data points above the scaling break. The  $\lambda$ -value is consistent with the range of values found in Chapter 4. Finally, the temperature exponent value of 7.6 is close to the 'universal' OLT value of 6.1. However, the j-exponent is almost twice as large: 1.5 versus 0.8.

The dimensionless data, after normalization and Weibull transformation are plotted in Figure 7.3B. It is difficult to see the scaling break ( $\beta' = 17000$ ) because the 'kink' in the data is slight. For a  $J$ -value of 320 (the  $J$ -value for which  $\beta$  has been tabulated in Chapter 4), the corresponding scaling break is 3.0 – only a little below the RADM2 alkene values. In Figure 7.3C, I have used the WEX model to calculate ozone concentrations and compare them with the observed values. The plot shows the WEX model fitting the data quite well – much better than the IER model (the scatter plot statistics are given in Table 7.2). The model produces the greatest discrepancies for experiments 344L (underestimating) and 341P (overestimating). There is little bias in the model.

### 7.3.4 WEX analysis of maximum ozone concentration

Finally, the WEX parameters found from the above analysis can be used to predict maximum ozone concentrations using:

$$\begin{aligned} \frac{[O_3]_{max}}{j_{av}/k_{NO}} &= \gamma \left( \frac{[NOx]_o}{j_{av}/k_{NO}} \right)^a \left( 1 - \exp \left[ -\lambda \left( \frac{RJ^c}{\beta'} \right)^\alpha \right] \right) \\ &\times \exp \left( -504 \left[ \frac{1}{(T_{av} + 273)} - \frac{1}{298} \right] \right)^b \end{aligned} \quad (7.6)$$

where  $J$  is the total cumulative NO<sub>2</sub> photolysis rate. Figure 7.4A shows the corresponding scatter plot of observed to predicted maximum ozone concentration. In general there is good agreement between the WEX parameterization and the observed ozone maximum (again the statistical summary is given in Table 7.2). In Figure 7.4B, I have also used the WEX model to generate ozone

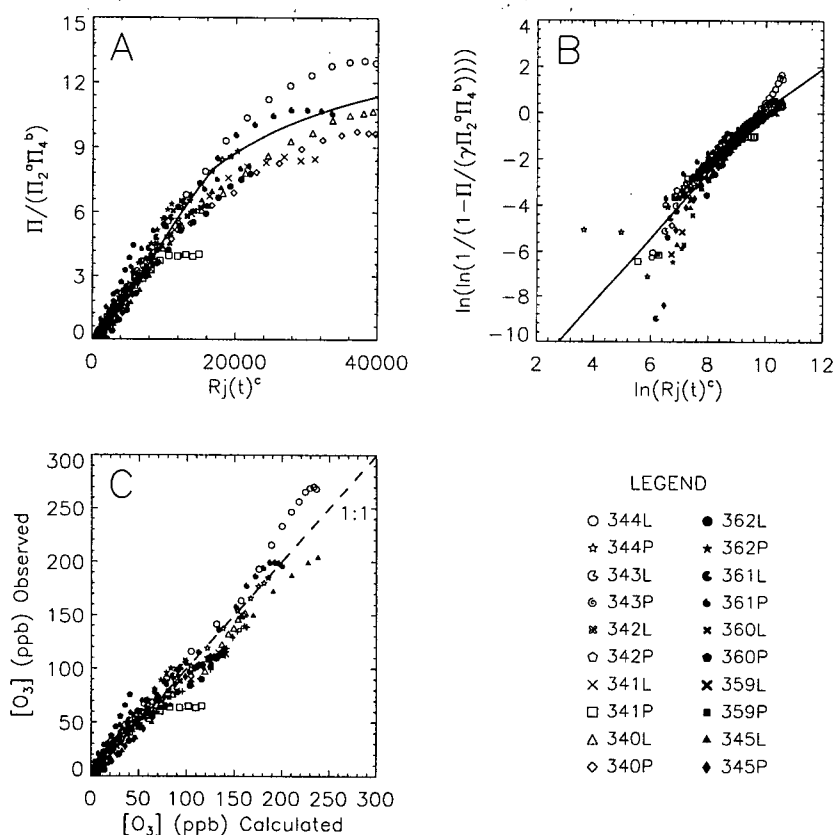


Figure 7.3: Comparison of the WEX model and the CSIRO smog chamber data. Figure A shows the non-dimensional data as a function of  $R_j(t)^c$ . Also shown (solid line) is the WEX model which best fits the data. Figure B shows the same data in the Weibull plane along with the WEX parameterization (solid line). The model has been used to calculate ozone concentrations which are compared with the actual concentrations in Figure C.

isopleths for environmental conditions of  $J = 240$  and  $T_{av} = 25^\circ\text{C}$ . Onto this plot I have marked the initial VOC and NO<sub>x</sub> concentrations for each test. However, some explanation of how these data were plotted is necessary.

Since the tests were not performed under the same conditions, I had to adjust the VOC concentrations to compensate for the differing actinic flux levels. Because the similarity relationship is a function of  $(RJ^c/\beta')$ , the adjusted VOC concentrations ( $[VOC]_o^*$ ) were made to keep this ratio

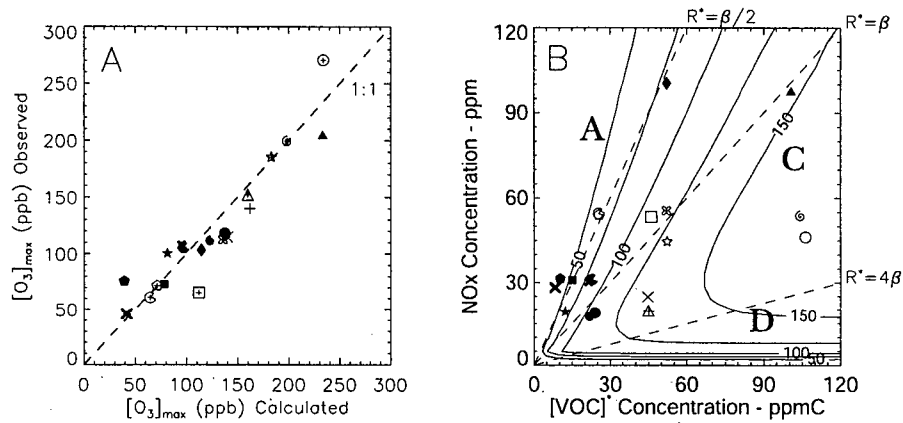


Figure 7.4: Maximum ozone concentration from the CSIRO smog chamber experiments and the corresponding WEX model. Parameters values for the WEX model are those given in Table 7.3. Figure A shows a scatter plot of WEX-predicted to observed maximum ozone concentrations. In Figure B, the WEX model has been used to generate ozone isopleths (in ppb) for  $J = 240$  and  $T = 25^\circ\text{C}$ . Also marked are the initial  $\text{NO}_x$  and adjusted VOC concentrations corresponding to the 20 experiments. The legend is the same as in Figure 7.3. Lines  $R^* = \beta, \beta/2$  and  $4\beta$  divide the plot into regions A, C and D.

constant:

$$\frac{[\text{VOC}]_o J^c}{[\text{NO}_x]_o \beta'} = \frac{[\text{VOC}]_o^*}{[\text{NO}_x]_o} \times \frac{240^c}{\beta'} \quad (7.7)$$

$$[\text{VOC}]_o^* = [\text{VOC}]_o \left( \frac{J}{240} \right)^c$$

Figure 7.4B plots maximum ozone concentration as a function of  $[\text{NO}_x]_o$  and  $[\text{VOC}]_o^*$ . Also shown in the figure are lines  $R^* = \beta$  where ( $R^* = [\text{VOC}]_o^*/[\text{NO}_x]_o$ ),  $R^* = \beta/2$  and  $R^* = 4\beta$  which divide the quadrant into sections A, C, D as defined in Section 4.1. From this figure, it can be seen that no tests lie in the  $\text{NO}_x$ -only scaling regime (D). Fifteen tests lie in region C and five in A. However, only seven lie below the scaling break and many in region C lie close to the border with region A. This suggests that there is a bias in the tests – with more tests above the scaling break and at low R-values. As mentioned in Section 4.1, the  $\text{NO}_x$ -scaling exponent in this region is  $\approx 0.2$ . Thus, the observed low a-value might be a consequence of this bias.

## 7.4 Conclusion

In this chapter, I have compared the WEX model with smog chamber data. The analysis shows the scaling relationships developed in Chapters 3 and 4 provide a means of succinctly summarizing

smog chamber observations. The similarity relationship holds over a wide range of initial precursor concentrations, temperatures and actinic fluxes. Using the WEX model to parameterize the similarity relationship, an analytic expression for ozone concentration as a function of time and maximum ozone concentration as a function of  $R$  can be developed.

The data shows a slight break in the Weibull plane but this is difficult to quantify because of the limited number of data points below the scaling break. The slight break could also reflect an inability of the chamber to simulate ozone formation at high and low  $R$ -values. The analysis shows the VOC mixture has little  $\text{NO}_x$  inhibition, consistent with models based on similar data.

While I have tested the WEX model directly against smog chamber data with good success, the chamber data may not be representative of ambient photochemistry. Thus the parameterization based on this data may not be valid for ambient use.

## Chapter 8

# VOC Reactivity – An Example of Scaling in Ozone Photochemistry

### 8.1 Introduction

Hundreds of VOCs are emitted daily into a typical urban airshed (Dodge, 2000) having a wide variety of reaction rates and reaction pathways (Atkinson, 2000). It has been long recognized that not all of these VOCs share the same propensity to produce ozone (Haagen-Smit et al., 1953). Furthermore, while controlling NO<sub>x</sub> emissions appears to be the most effective route for reducing ozone concentrations on a regional scale (National Research Council, 1991), in large urban areas controlling VOCs may be the most effective control strategy (Sillman, 1993). Of concern, then, is the best control strategy in these instances -- one that targets specific 'reactive' VOCs or one that treats all VOCs equally (Dodge, 1984). While Russell et al. (1995) show that a targeted approach can be cost effective, it can also be difficult to implement (Croes et al., 1992). Traditionally, the regulatory community has sought a middle ground between these two approaches: it has classified and regulated VOCs based on a crude two-tiered scale with most VOCs being treated as (equally) reactive while a few as completely unreactive. Examples of this approach include the 1966 Los Angeles Air Pollution control district 'Rule 66' (Dodge, 1984) and the 1992 US EPA's 'negligibly reactive' and 'reactive' classes (Dimitriadis, 1996). But it has been California's 1990 Low Emission Vehicle and Clean Fuels Regulation (California Air Resources Board, 1991) that has stimulated the greatest interest in defining VOC reactivity. These regulations allow higher tail-pipe emissions from alternative fueled vehicles provided the total 'reactivity' of these emissions is equivalent to that from conventionally fueled vehicles (Russell et al., 1995). But VOC 'reactivity' can be viewed as a scaling i.e. within a limited range of conditions, it is assumed there is a measure of ozone formation that allows the behaviour of the photochemical system to be considered independent of VOC.

In this chapter, I examine the assumptions behind such a scaling. Specifically, I examine the conditions necessary for a scaling of VOC reactivity, the range over which these conditions must

Reactivity Criteria	Proposed Scale and References
Oxidant Formation	Maximum ozone concentration (Carter, 1994), Total amount of ozone produced (Andersson-Sköld et al., 1992)
Secondary Products	Maximum odd oxygen concentration (Tonnesen, 2000), Maximum SP (Chang et al., 1999)
Biological Effects	$NO_2$ produced, PAN produced and Formation of aerosol particles (Altshuller, 1966)
Miscellaneous	Eye irritation and Plant damage (Altshuller, 1966)
	Cracking of rubber (Haagen-Smit et al., 1953), $OH^\bullet$ reactivity (Wu et al. (1976) and Darnall et al. (1976))

Table 8.1: Various measures for VOC reactivity.

hold and the corresponding measure of reactivity using the WEX model. Unfortunately, I will show that this complex subject is not amenable to an exact scaling. Nonetheless, I develop a means of assessing VOC reactivity which I compare with some simple numerical simulations and show my analysis is consistent with reactivity scales developed using more complex models. Finally, I use the WEX model to explore a simple reaction mechanism which does show a reactivity based scaling and compare it with the RADM2 chemical mechanism (Stockwell et al., 1990). I conclude this chapter with a summary of PART I.

## 8.2 VOC Reactivity

In essence, a reactivity standard is a means of ranking VOCs. Unfortunately there are different criteria for such a ranking: the ability to form oxidants, the production of secondary products and the effects on biological systems (cf. Table 8.1). While no criteria have been universally agreed upon, one commonly used is the change in maximum ozone concentration stemming from a small change in VOC concentration. This measure is intended to reflect changes to ozone concentration that occur when a regulatory strategy is introduced (Carter, 1994).

### 8.2.1 Incremental Reactivity

The sensitivity of maximum ozone concentration to initial VOC concentration, called incremental reactivity (IR) (Carter, 1994), is given by:

$$IR = \frac{\partial [O_3]_{max}}{\partial [VOC]_o} \quad (8.1)$$

Because it is impossible to make infinitesimal changes to emissions while controlling for meteorology in an airshed, this definition precludes direct measurement of  $IR^1$ . However, it can be estimated through smog chambers experiments (Carter and Atkinson (1987), Carter et al. (1995) and Kelly and Chang (1999)) or through computer modeling (Carter and Atkinson (1989), Carter (1995) and Chang et al. (1999)).

<sup>1</sup>Although Uno et al. (1985) have tried to measure IR using a combination of observed VOC concentrations, daily ozone maximums and computer modeling.

Incremental reactivity can also be calculated analytically using the WEX model:

$$IR = \gamma (j_{av}/k_{NO}) \left( \frac{[NOx]_o}{j_{av}/k_{NO}} \right)^a f'(R) \frac{dR}{d[VOC]_o} \Theta(T)^b \quad (8.2)$$

Equation (8.2) shows that  $IR$  is a complex function of: initial NOx concentration, VOC to NOx ratio and environmental conditions<sup>2</sup>. To develop a scaling of  $IR$ , a means of accounting for these competing factors must be found. To begin, I will assume that the  $T$  and  $J$ -dependences (both their magnitudes and ranges) are similar to those for maximum ozone concentration. Indeed, experimental results suggest that  $IR$  dependence on environmental conditions is not as important as its dependence on initial precursor concentrations (Kelly and Chiang, 1999). Thus, for the sake of brevity, I assume constant environmental conditions. Next, to account for the NOx-dependence, I suggest a ‘NOx-scaled’ Incremental Reactivity ( $NSIR$ ):

$$NSIR = \frac{IR}{\left( \frac{[NOx]_o}{j_{av}/k_{NO}} \right)^{a-1}} = \gamma f'(R) \quad (8.3)$$

Equation (8.3), a function of  $R$  only, provides a natural scale for VOC reactivity. It suggests that reactivities should only be compared when the relative abundance of VOC to NOx is considered. This is consistent with Carter and Atkinson (1989) who suggest that the VOC/NOx ratio is the most important factor affecting reactivity.

To see how well Eq. (8.3) agrees with  $IR$  calculated from model output, I calculated  $NSIR$  for OLT using the OZIPR program. In this numerical study, as with the previous ones, I performed a matrix of idealized smog chamber simulations (i.e. without ‘wall effects’) at a variety of OLT and NOx concentrations. Each run began with initially well mixed OLT and NOx which was irradiated, at constant temperature, for 11 hours simulating a mid-summer day (June 21<sup>st</sup>) in Vancouver B.C. To calculate  $IR$ , the OZIPR program performs three simulations at each ( $[VOC]_o, [NOx]_o$ ) pair: one with the nominal VOC concentration, another with 0.2% less and a third with 0.2% more VOC. It then calculates two  $IR$  (one using the nominal and the higher VOC run, the other using the nominal and lower VOC run) and averages the two to get a single  $IR$  (Tonnesen, 2000). In all, 121 simulations were performed. No simulations were without initial NOx or OLT, so there was no need to exclude any simulations from the analysis. In Figure 8.1A, I have plotted the OLT model output  $NSIR$  versus  $R$  which shows that  $NSIR$  is well modeled as a function of  $R$  only. I have also plotted  $NSIR$  using Eq. (8.3) where the WEX parameters are based on the regression of maximum ozone concentration versus initial precursor concentration and *not* against the  $NSIR$  model output ( $r^2 = 0.98$  and  $RSME = 0.016$ ). Equation (8.3) does an excellent job of capturing the variability

<sup>2</sup>With the actinic flux dependence arising through the  $J$ -dependence on the scaling break ( $\beta$ ).

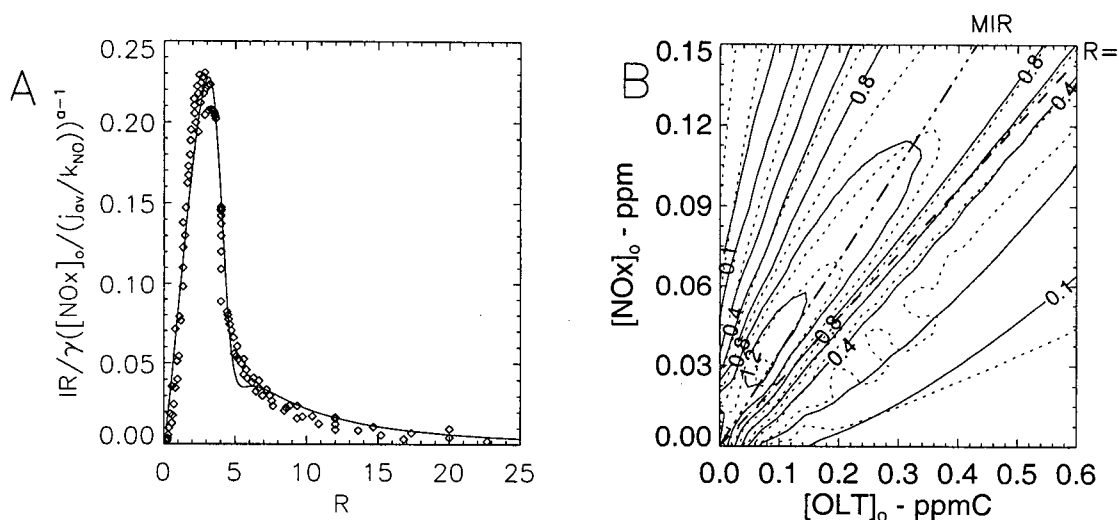


Figure 8.1: IR for OLT calculated using the RADM2 mechanism and the WEX model. In Figure A, ‘NOx-scaled IR’ is plotted as a function of  $R$  using RADM2 model output (diamonds) and the WEX model (solid line). In Figure B, isopleths of incremental reactivity have been plotted as a function of initial OLT and NOx concentration using both model output (solid isopleths) and the WEX model (dotted isopleths). Also shown are lines of  $R = MIR$  and  $R = \beta$ .

of the model output. In Figure 8.1B, the corresponding isopleths of IR have been plotted against initial OLT and NOx concentration. Again the fit between the WEX derived IR and model output is good around the line  $R = \beta$  and  $R = R_{MIR}$  but poorer for high and low  $R$ -values.

### 8.2.2 Maximum Incremental Reactivity

Figure 8.1A shows that there is an  $R$ -value where NSIR is largest; indicating the location where maximum ozone concentrations is most sensitive to initial VOC concentration. Traditionally, for any given  $[VOC]_0$ , the NOx input (initial concentration plus emissions) where IR is maximum is called the maximum incremental reactivity (MIR) (Carter, 1994). The WEX model clearly shows that this maximum, when scaled by initial NOx concentration, is a function of the relative abundance of VOC to NOx.

The WEX model can be used to determine both the  $R$ -value for the maximum ( $R_{MIR}$ ) and the

NSIR at this R-value (*NMIR*):

$$R_{MIR} \approx \beta \left[ \frac{\alpha_1 - 1}{\alpha_1 \lambda} \right]^{1/\alpha_1}$$

$$NMIR \approx \gamma \frac{\alpha_1 - 1}{\beta} \left[ \frac{\alpha_1 - 1}{\alpha_1 \lambda} \right]^{1/\alpha_1} \exp \left[ \frac{1 - \alpha_1}{\alpha_1} \right] \quad (8.4)$$

(where the above results are approximate because I have ignored the small R-dependence of  $\alpha$ ). Equation (8.4) is a function of a VOC's WEX parameters only and should therefore provide a means of ranking VOC reactivity. Unfortunately, this conclusion is limited in two ways. First of all, the ranking is valid only at one specific R-value (namely the  $R_{MIR}$ ) and secondly, since individual VOCs are never emitted in the absence of other reactive compounds, one is actually interested in the sensitivity of maximum ozone when one *component* of a mixture is changed (Bergin et al., 1998) and not when the *entire* mixture is incrementally changed.

Herein lies the problem with defining a VOC reactivity scale: VOCs produce ozone at different rates not only because they differ in  $OH^\bullet$  reactivity but also because they differ in the way they increase or reduce the radical pool, thus limiting or enhancing the reactions of other VOCs (Dimitriades, 1996). Thus, incremental reactivity is a function of the reacting environment as much as the VOC itself (Jeffries, 1993). For this reason a single IR scale can never be found – different mixtures can produce a variety of IR for any VOC. A similar problem arises in fluid mechanics where turbulent quantities are properties of the flow and not the fluid (Stull, 1988). This is also the reason why  $OH^\bullet$  reactivity has long been sought as a reactivity scale – not only does  $OH^\bullet$  attack initiate most VOC ozone forming reactions (Finlayson-Pitts and Pitts, 1999) but it is also an easily measured VOC property independent of environment. To partially compensate for the dependence on mixture composition, relative, instead of absolute reactivities are often calculated.

### 8.2.3 Relative Incremental Reactivity

One way to reduce IR dependence on mixture composition is through a relative incremental reactivity (RIR) obtained by dividing a single component's IR by the IR of the entire mixture:

$$RIR_{VOC} = \frac{IR_{VOC}}{IR_{mixture}} \quad (8.5)$$

With such a scale, while absolute values of RIR may change depending on the mixture, RIR rankings should remain constant (Carter, 1994). Another benefit of this approach is it eliminates the NOx dependence of  $RIR^3$ .

<sup>3</sup>Although the WEX model suggests this is contingent on both the VOC and mixture having the same NOx scaling exponent ( $a$ ).

Clearly, RIR is still a function of  $R$ , so to simplify matters, it is often evaluated at a specific  $R$ -value (often called ‘NOx availability’). Typically, this is the  $R_{MIR}$ , but RIR can just as easily be evaluated at other  $R$ -values and there are good reasons for doing so. First of all, RIR may change relative rankings between  $R$ -values so evaluating them at several gives an indication of the robustness of the scaling and secondly, the RIR calculated at  $R_{MIR}$  evaluates IR at relatively VOC deficient conditions typical of the Los Angeles urban area but not representative of other urban areas (Russell et al., 1995). Many urban areas are less VOC limited and so evaluation at other  $R$ -values, closer to the ridgeline, is more useful. To accommodate this, Carter (1994) defines a RIR scale at two other  $R$ -values: at the  $R$ -value giving maximum ozone concentration ( $R_{MOR}$ ) and the  $R$ -value where maximum ozone concentration is equally sensitive to changes in either NOx or VOC ( $R_{EBIR}$ ). Since IR shows little variability at large  $R$ -values (Dodge, 1984), and since these conditions are NOx-limited, scales have not been developed at higher  $R$ -values. Guided by the WEX model, I propose a new RIR, to be evaluated at the scaling break ( $R = \beta$ ), called the ‘Scaling Break Incremental Reactivity’ (SBIR) which also lies closer to the ridgeline than the MIR.

I propose a simple way of estimating a VOCs RIR (within a given mixture) is to evaluate its NSIR at the desired  $R$ -value. That is, I suggest that by ignoring the interactions between VOCs within a mixture and calculating IR for individual VOCs as if it were the only species in a mixture, the resulting IR gives an estimate of its relative incremental reactivity. So, I propose that Eq. (8.4) is proportional to a VOCs mixture-dependent RIR at  $R_{MIR}$  and:

$$NSIR(R = \beta) = \frac{\gamma \bar{\alpha} \lambda}{\beta} \exp\{-\lambda\} \quad \text{where} \quad \bar{\alpha} = \frac{\alpha_1 + \alpha_2}{2} \quad (8.6)$$

is proportional to a VOCs mixture-dependent RIR evaluated at  $R = \beta$ . To check this premise, I performed a second set of numerical experiments. Before proceeding, I must clarify one point. Earlier, I mentioned that IR is a function of the reacting system and many possible IR values can occur depending on the VOC mixture. But the analysis I propose will determine a single IR-value – fixed by its WEX parameters. What I am hoping to show, then, is that the WEX derived IR-values give a good estimate of a VOCs RIR relative to a typical urban VOC mixture. This same reasoning underlies the assigning of ‘reactivities’ to VOCs in the 1990 California regulations (Bergin et al., 1998).

#### 8.2.4 RADM2 simulations of RIR

To test the ability of Eq. (8.4) and Eq. (8.6) to predict RIR at  $R_{MIR}$  and  $R = \beta$ , I simulated ozone formation in an idealized smog chamber using the OZIPR program and the RADM2 mechanism. Each simulation used the Stock urban speciation (Stockwell et al., 1997) and then followed the same

methods as outlined section 8.2.1. For each of mixture's 12 RADM2 classes, OZIPR calculated its IR at 121 different ( $[VOC]_o, [NOx]_o$ ) combinations. The mixture IR was also calculated at these 121 pairs.

I then calculated  $R_{MIR}$  for the mixture and the 12 RADM2 classes. I then calculated the RIR for each class at  $R_{MIR}$  and at the mixture's  $\beta$ -value. In Figure 8.2A, I have plotted RIR at  $R_{MIR}$  versus Eq. (8.4) while in Figure 8.2B, RIR at  $R = \beta$  versus Eq. (8.6) is given. In both Figures, I have labeled the RADM2 classes where possible, but since the alkanes had very low reactivities, they could not be individually labeled. For both Figures, the WEX predicted and OZIPR calculated RIR are qualitatively similar ( $r^2 = 0.66$  in Figure A and  $r^2 = 0.71$  in B). The general trend in these Figures is for alkanes to have the lowest reactivities followed by aromatics, alkenes and then formaldehyde; consistent with the general understanding of ozone photochemistry (Finlayson-Pitts and Pitts, 1999). For both scales, the greatest deviation occurs for HCHO, with the WEX model greatly underestimating its RIR. It is not surprising the WEX model cannot capture the IR of HCHO, it has proved difficult to model even with more complex mechanisms (Carter et al. (1995), Russell et al. (1995)), likely due to its ability to produce new radicals via photolysis (Russell et al., 1995). I suspect that the higher radical production from HCHO greatly enhances the ozone production of other VOCs in the mixture, more so than any of the other RADM2 classes can. This enhanced interaction with the reacting environment cannot be captured through my simple analysis. To examine the correlation between the WEX model and OZIPR without HCHO, I have drawn a line of best fit through the origin and all of the other points. The new correlations are 0.93 and 0.72 respectively.

The present analysis shows WEX parameters can be used to develop a ranking of VOC reactivities but this result has been tested only under a set of very restricted conditions. Typically, an investigation of VOC reactivity involves simulations having: a changing mixed layer depth, entrainment, deposition, time varying emissions as well as different VOC mixtures. Indeed, the original MIR, MOR and EBIR scales, used in the 1990 California regulations, were based on a series of 39 box model simulations each having unique meteorological processes and using a much more detailed chemical mechanism (Carter, 1994). Using different meteorological processes and a different measure of reactivity, both Chang and Rudy (1990) and Derwent et al. (1998) calculate VOC reactivities which are consistent with IR, but Stockwell et al. (2001) caution that the MIR and MOR scales may depend on the simulation length. Typically, the influence of different environments and VOC mixture is smaller than the range of reactivities found in typical urban environments (Dimitriades, 1996). The robustness of these scales has been further tested using complex 3-D Eulerian simulations (McNair et al. (1992), Russell et al. (1995) and Hakami et al. (2004)), which give

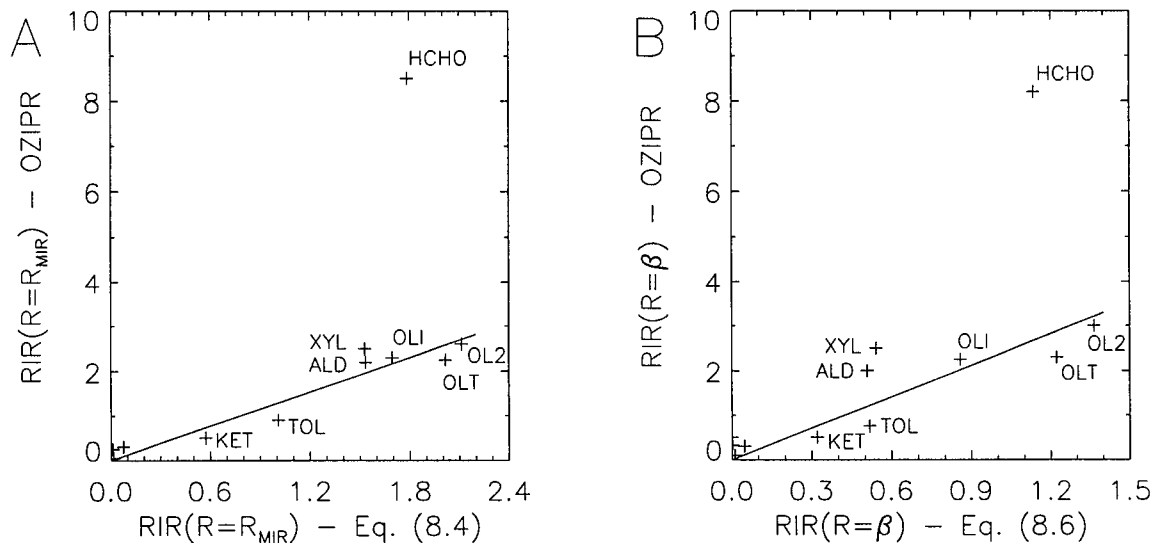


Figure 8.2: Relative incremental reactivities for the 12 RADM2 classes in the Stock (Stockwell et al., 1990) mixture based on OZIPR simulations versus RIR from the WEX model. In Figure A, the RIR has been evaluated at  $R_{MIR}$  and in Figure B at  $R = \beta$ . Also shown is a line of best fit through all of the points excluding HCHO.

results consistent with the trajectory simulations. This suggests that while my analysis ignores the effects of meteorology and emissions and examines only a single mixture, its ranking scheme should be robust. Furthermore, I believe the inclusion of atmospheric processes into the analysis, while obviously an important influence on the photochemistry, influence much more than the chemistry and only make the interpretation of reactivity scales more difficult.

### 8.3 Concerns about VOC Reactivity Scales

Regardless of criteria used to define ‘reactivity’ or meteorological processes and VOC mixture composition used in calculating these reactivities, ranking schemes are limited by uncertainties in atmospheric chemistry, based on many assumptions and derived mainly by computer modeling (Croes et al., 1992). It is not surprising that some prefer other means of establishing reactivity. For instance, Jeffries (1993) argues incremental reactivity scales are nothing more than sensitivities to model inputs and since these models cannot accurately represent all chemical and meteorological processes, it is misleading to infer causal relationships based on this type of analysis. Instead, he suggests VOC ‘reactivities’ are an issue of new radical production and that many urban air sheds

are not as radical-limited as models indicate (Jeffries, 1993). As a result, CO and methane, typically considered 'unreactive' species, can be significant contributors to ozone production ((Jeffries and Tonnesen, 1994) and (Bowman and Seinfeld, 1994)).

With this in mind, I finish this chapter by examining a simple photochemical system where a proper VOC reactivity scale can be defined. I do this for two reasons: it shows how a reactivity scale should behave and this simple scaling is most easily seen using the methods developed in the thesis.

## 8.4 GRS Mechanism – An Example of an Ideal VOC Reactivity Scale

An example of a photochemical system that shows perfect VOC scaling is the Generic Reaction Set (GRS) (Azzi et al., 1992). This highly parameterized reaction mechanism was developed to capture the essence of ozone photochemistry using the smallest number of reactions possible (Azzi et al., 1992). Its VOC reactivity scaling is merely an unintended result of the parameterization.

This chemical mechanism has been used to simulate ozone photochemistry in both smog chambers (Azzi et al., 1992) and in 3-D Eulerian grid models (Venkatram et al., 1994). In both cases, it produces results comparable with those produced using more detailed chemical mechanisms. However, the GRS mechanism has been criticized because its isopleths are too "L" shaped i.e. it does not show sufficient NO<sub>x</sub>-inhibition above the ridgeline (Tonnesen and Jeffries, 1994). Before proceeding with the reactivity analysis, I wish to make a few points regarding ozone isopleths and NO<sub>x</sub>-inhibition.

### 8.4.1 Ozone Isopleths and NO<sub>x</sub>-inhibition

While (Tonnesen and Jeffries, 1994) use a detailed process analysis to investigate NO<sub>x</sub>-inhibition in both the GRS and CB-IV mechanism, great care must be taken if using isopleth shape to determine NO<sub>x</sub>-inhibition. While there might be uncertainty regarding the correct shape of an isopleth diagram (Tonnesen and Jeffries, 1994), before this uncertainty can be resolved, the correct way to portray an isopleth diagram must be established. Isopleths can take on different characteristics depending on axis scaling – it is easy to distort a curve by compressing or expanding an axis. The only way to avoid such distortions is to plot both axes using the same physical dimension and give them both the same 'length'. For ozone isopleths, this can be achieved by scaling the VOC axis by

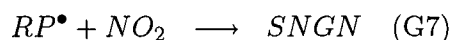
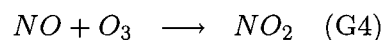
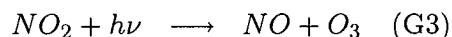
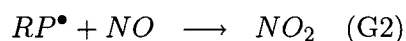
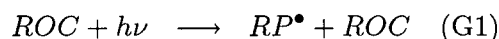
$R = \beta$ . This way, one ends up plotting on the horizontal axes:

$$\frac{[VOC]_o}{\beta} = [VOC]_o \frac{[NOx]_\beta}{[VOC]_o} = [NOx]_\beta \quad (8.7)$$

(where  $[NOx]_\beta$  is the NOx concentration along the scaling break corresponding to an initial VOC concentration  $[VOC]_o$ ). In so doing, one ends up plotting NOx concentration versus the NOx concentration at the scale break (for a given VOC concentration). If the base NOx and VOC concentrations are chosen such that the scale break lies along the  $R = \beta$  line (cf. Chapter 4), then both axes will have the same ‘length’ and the true shape of the isopleth can be revealed.

### 8.4.2 Reaction Mechanism

The GRS mechanism was developed from outdoor smog chamber data, and consists of seven reactions among seven species:



where  $ROC$  represents the reactive organic compounds,  $RP^\bullet$  the radical pool,  $SGN$  stable gaseous nitrogen products (such as  $HNO_3$ ) and  $SNGN$  is the stable non-gaseous nitrogen products (for instance nitrate particles).

Before preceding with a scaling analysis; a few observations. First of all,  $[ROC]_o$  is a conserved quantity: as  $ROC$  reacts (via  $G1$ ), an equal number of secondary compounds are produced having an identical reactivity to the parent compound. The rate constant for  $G1$  is proportional to the photolysis rate of  $NO_2$  (given by  $j_1$ ), an activity coefficient ( $a_{ROC}$ ) and an Arrhenius temperature dependence ( $A(T)$ ) (Azzi et al., 1992):

$$g_1 = j_1 \cdot a_{ROC} \cdot A(T) \quad (8.8)$$

where

$$A(T) = \exp \left\{ -4700 \left( \frac{1}{T} - \frac{1}{316} \right) \right\} \quad (8.9)$$

Reaction *G1* is a parameterization of all processes that lead to radical production. It assumes that this production depends on actinic flux and ROC concentration. Since  $[ROC]_0$  is conserved and always available to supply radicals (as long as light is available), the ROC-NO<sub>x</sub> system can never become radical limited – it can only become light limited (Tonnesen and Jeffries, 1994).

In reaction *G2*, radicals convert *NO* to *NO*<sub>2</sub> in a radical termination process having rate constant (in  $\text{ppm}^{-1}\text{min}^{-1}$ ):

$$g_2 = 3.58 \times 10^6 / T \quad (8.10)$$

In this analysis, a slightly different rate constant (in  $\text{ppm}^{-1}\text{min}^{-1}$ ) has been used based on the work of Venkatram et al. (1994):

$$g_2 = 5482 \exp \{242/T\} \quad (8.11)$$

At  $T = 298\text{K}$  the two expressions differ by only 2.7%. The equivalent RADM2 expression for this reaction ( $\text{HO}_2^\bullet + \text{NO} \rightarrow \text{OH}^\bullet + \text{NO}_2$  (R7)) has rate constant:

$$g_2 = 5440 \exp \{240/T\} \quad (8.12)$$

which is almost identical to Eq. (8.11).

Reactions *G3*, the photolysis of *NO*<sub>2</sub>, has been parameterized using the equivalent RADM2 relationships (Stockwell et al., 1990). Reaction *G4* gives the titration of ozone by *NO* with rate constant (in  $\text{ppm}^{-1}\text{min}^{-1}$ ):

$$g_4 = 9.24 \times 10^5 / T \exp \{-1450/T\} \quad (8.13)$$

Again, in this analysis a slightly different relationship was used as suggested by Venkatram et al. (1994):

$$g_4 = 2643 \exp \{-1370/T\} \quad (8.14)$$

At  $T = 298\text{K}$ , the two expressions differ by 11% with the Eq. (8.14) within 1% of the equivalent RADM2 reaction:

$$g_4 = 2643 \exp \{-1370/T\} \quad (8.15)$$

Reaction *G5* represents another radical termination reaction while reactions *G6* and *G7* are sinks for both *NO*<sub>2</sub> and radicals. Rate expressions for these reactions, all independent of temperature, are (in  $\text{ppm}^{-1}\text{min}^{-1}$ ):

$$g_5 = 1000, \quad g_6 = 120, \quad g_7 = 120 \quad (8.16)$$

I now show VOC reactivity in this system can be uniquely characterized by the activity coefficient ( $a_{ROC}$ ).

### 8.4.3 Scaling and VOC reactivity

In the GRS mechanism, different hydrocarbons are characterized by different activity coefficients. So, to study VOC reactivity in this system, a scaling analysis was performed on three ‘different’ ROCs, that is, I used the OZIPR to solve reactions *G1* to *G7* for three different values of  $a_{ROC}$ . As a baseline, I choose  $a_{ROC} = 45000 \text{ ppm}^{-1}$  since Johnson (1984) suggests that this choice reproduces the behaviour of propene. For the other two ROCs, I choose  $a_{ROC}$  to be double and half the baseline value. For each ROC, 121 smog chamber simulations were performed at constant temperature (298K) with neither dilution nor deposition and an actinic flux appropriate to Vancouver, in mid-summer (June 21<sup>st</sup>), between the hours of 7:00 a.m. and 6:00 p.m. (local time). In all three sets of simulations, *NOx* concentrations ranged from 0.0 to 0.075 ppm. To determine the appropriate range for the *ROC* concentrations, trial simulations were performed. These were done to determine if and where each ROCs produced its scaling break. Each trial simulation did, indeed, produce a scaling break and ROC ranges were chosen to produce an equal number of simulations above and below each break. The following ranges were used: 0.0 to 0.5 ppm for the baseline ROC, 0.0 to 0.25 ppm for the more reactive ROC and 0.0 to 1.0 for the less reactive ROC. Each set of simulations produced a peak maximum ozone concentration around 350 ppb.

To examine the model output using the WEX model, model output of maximum ozone concentration for each set of simulations was scaled by  $[NOx]_0^a$  and normalized. Both the baseline ROC and more reactive ROC had *NOx* scaling exponents of  $a = 0.60$  and normalizing constants of  $\gamma = 10.0$  while the low reactivity ROC  $a = 0.61$  and  $\gamma = 9.9$ . In Figure 8.3A all three sets of Weibullized model output have been plotted against  $\ln(R)$ . The scatter in the figures suggests ozone variability is not completely captured by  $[NOx]_0^a$  and  $R$ . From this Figure, it appears the only effect of changing  $a_{ROC}$  is a translation of the model output along the line  $\ln(R)$ . In fact, for each curve, the slopes ( $\alpha_1, \alpha_2$ ) and vertical offset ( $\lambda$ ) are within  $\pm 2\%$  of one another. However, there is great change in  $\beta$ . It varies from 10.1 (less reactive) to 5.2 (baseline) and 2.7 (more reactive) – almost in perfect inverse proportion to the  $a_{ROC}$ -values. This suggests scaling ROC concentration by  $a_{ROC}$  (or equivalently by  $\beta$ ), ‘different’ ROCs can be compared<sup>4</sup> on a common basis, with no need for IR or other measures of ROC reactivity.

The corresponding isopleths for the baseline (solid lines) and more reactive (dotted lines) ROC are given in Figure 8.3B. At first glance, the different isopleth patterns suggest that changing  $a_{ROC}$  produces compounds with different reactivities and photochemical pathways. But this is not the case. The observed difference arises because the VOC axis has not been properly scaled. Had

<sup>4</sup>Actually, with numerical tolerances, they become identical

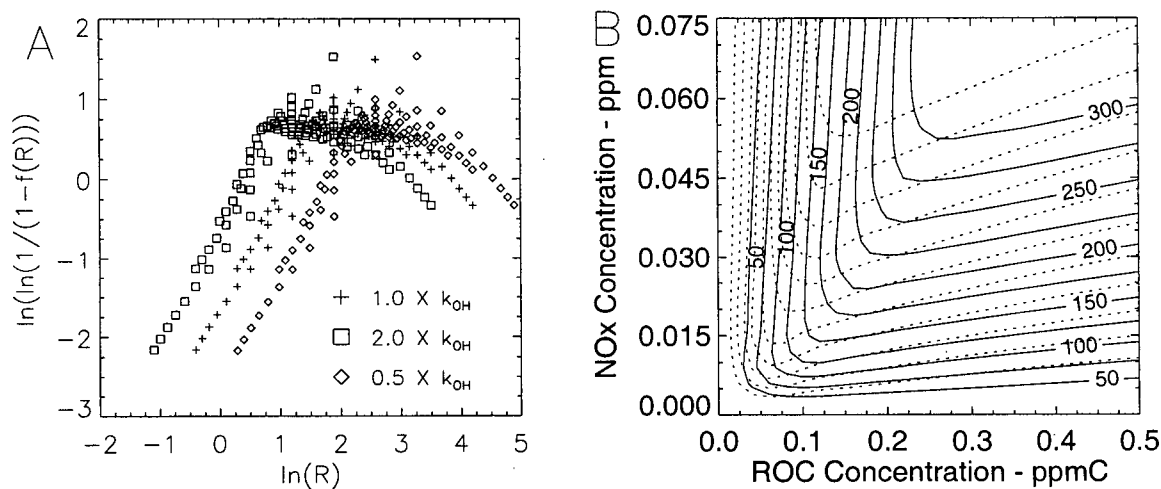


Figure 8.3: Weibull and isopleth plots for three different ROCs using the GRS mechanism. Figure A shows the Weibullized model output for an ROC with rate constant equivalent to propene (plus signs), for an ROC with twice that rate constant (diamonds) and half that rate constant (squares). In Figure B, the corresponding isopleths of maximum ozone concentration have been plotted for the propene (solid lines) and more reactive ROC (dotted lines).

the isopleths been plotted as a function of  $[ROC]_o/\beta$ , the two sets of curves would be indistinguishable. Furthermore, it was shown in Chapter 6 that VOCs with different oxidation pathways produce different WEX slopes and offsets. So, while the GRS mechanism is intended to model single hydrocarbons or complex mixtures of hydrocarbons (Azzi et al., 1992), it can really only model compounds whose reactions proceed along similar paths but have different absolute ROC concentrations. As a consequence, this model always produces a single value for  $\alpha_1$  which I have shown is a measure of NOx-inhibition. This value of  $\alpha_1 = 1.5$  is indeed lower than all of the RADM2 classes (with the exception of HCHO) studied in Chapter 4, consistent with the findings of Tonnesen and Jeffries (1994).

Finally, the  $a_{ROC}$  scaling should hold for changing environmental conditions as well. Scaling  $\beta$  by  $J$  will take into account the actinic flux dependence (since radical production is proportional to both  $J$  and  $[ROC]_o$ ) while  $g_1$  already is a product of a dimensionless temperature dependence factor ( $A(T)$ ).

Given that reaction  $G1$  represents the  $OH^\bullet$  attack on ROC, it is of interest to see if the RADM2 mechanism shows similar scaling when any of its 12 VOC classes have their  $k_{HO}$  rate constant altered. To explore this possibility, simulations were run for two classes (OLT and ALD) for three

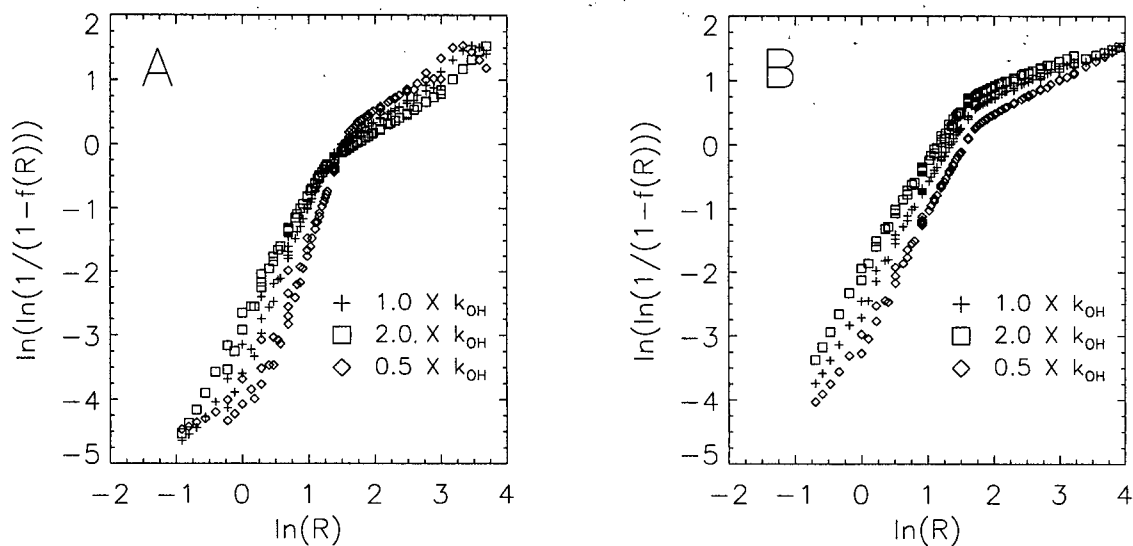


Figure 8.4: Weibullized plots of OLT and ALD with normal, twice and half the  $k_{OH}$  rate constants. Figure A shows the OLT runs and B the ALD simulations. In both figures, simulations with the original  $k_{OH}$  values are given by (plus signs), double  $k_{OH}$  values with diamonds and half with squares.

different scenarios: a baseline  $k_{OH}$ , a  $2 \times k_{OH}$  and  $0.5 \times k_{OH}$  scenario. In Figure 8.4A, I have plotted Weibullized OLT model output from these three scenarios. The three curves show very little horizontal translation with  $\beta$  ranging from 3.8 to 5.0. While this suggests that  $\beta$  decreases as  $k_{OH}$  increases, other parameters show greater sensitivity. The biggest difference is for  $\alpha_1$  – decreasing  $k_{OH}$  increases  $\alpha_1$  leading to an increase in  $NO_x$  inhibition (with range [1.8, 3.0]). The next most sensitive parameter is  $\gamma$  which suggests as  $k_{HO}$  increases, more  $OH^\bullet$  reacts with OLT and less reacts with  $NO_2$  (to form  $HNO_3$ ) so the system becomes more efficient with its  $NO_x$ .

Figure 8.4B shows the corresponding ALD results. In this case the most sensitive parameters are  $\alpha_2$  and  $\lambda$ . Interestingly, there is little change in  $\alpha_1$ , most likely because ALD has its own photolytic source of radicals and so its  $NO_x$ -inhibition is less dependent on the  $OH^\bullet$  attack. There is very little change in  $\beta$  ([5.1, 5.4]).

To summarize, for both OLT and ALD, changing  $k_{OH}$  results in a change to the chemical pathways and not simply a rescaling of VOC concentration. On the other hand, changing  $a_{ROC}$  in the GRS mechanism rescales the ROC concentration while leaving the chemical pathways unchanged.

#### 8.4.4 Radical Production and VOC reactivity

What in the GRS mechanism (and not RADM2) gives rise to the  $a_{ROC}$  scaling? There are two reasons. First, in the GRS mechanism, radical production is a function of VOC concentration and reactivity ( $a_{ROC}$ ); independent of NOx concentration. So when  $a_{ROC}$  is reduced but  $[ROC]_o$  proportionately increased, radical production remains constant. Secondly, VOC concentrations do not affect the radical reaction pathways; this partitioning is governed by NOx concentrations. That is, the fraction of radicals that react with NO to produce  $NO_2$  is independent of  $[ROC]$  and governed solely by  $[NOx]$ . For these two reasons: conservation of radical production and independence of radical pathways, maximum ozone concentration scales with  $[ROC]_o \times a_{ROC}$  (or  $[ROC]_o/\beta$ ).

In the RADM2 mechanism, an important source of radical production is ozone, not necessarily proportional to  $[VOC]_o$  or  $k_{OH}$  but strongly dependent on  $[NOx]_o$ . Furthermore, radical pathways are a function of the relative abundance of  $[VOC]$  to  $[NOx]$  and not  $[NOx]$  only. This is most evident in Figure 5.24B where the fraction of  $HO_2^*$  radicals that react with  $[NO]$  falls onto a single common curve when plotted as a function of  $R$ .

### 8.5 Conclusion

VOC reduction strategies, used to complement NOx controls, maybe more effective when reactive VOCs are more stringently controlled (National Research Council, 1991). This necessitates a means of comparing VOCs on a common ‘reactivity’ scale. While there is no universal definition for VOC reactivity, incremental reactivity (IR) is commonly used because it shows the direction emissions reductions should have on a region’s ozone concentrations (Carter, 1994). While IR is defined as the sensitivity of maximum ozone concentration to initial VOC concentration (Carter, 1994), it is highly dependent on the interactions of VOCs and VOC products with one another and with available NOx (Jeffries, 1993). As a result, no measure of absolute reactivity can be developed – they are all dependent on the reacting environment as much as the VOC species. Instead, relative IR, based on on average urban conditions are used (Bergin et al., 1998). While the WEX model, developed to parameterize the net effect of chemical interactions, cannot account for these VOC interactions, it has been used nonetheless to calculate IR for the 12 RADM2 classes. This was achieved by estimating of the *relative* IR of a VOC class using the IR of that class *in the absence of other VOCs*. The resulting scales are consistent with scales developed using more sophisticated models.

The WEX model has also been used to study the GRS chemical mechanism (Azzi et al., 1992). By making use of similarity relationships, a limitation of the GRS mechanism have been revealed:

it can only model organic compounds having a single fixed photochemical reaction sequence. In addition, the scaling analysis shows the GRS produces an ideal VOC reactivity scale which can be understood in terms of radical production and radical pathways.

## 8.6 Summary for Part I

The WEX model is an empirical parameterization for ozone formation which is not intended to accurately represent the internal workings of a photochemical system but rather to accurately reproduce the behaviour of a chemical mechanism<sup>5</sup>. As such, this high level analysis captures the essence of ozone photochemistry while excluding a great many details. This is not to say that these details are unimportant, rather, that they are not necessary for first order approximations and in many cases, they are overshadowed by uncertainties in model inputs and other aspects of ozone photochemistry.

While I have set out to build a screening tool to complement more complex photochemical models, I have accomplished much more. PART I of this thesis started with a scaling analysis of ozone photochemistry and has ended with a scaling analysis of VOC reactivity. In between, I have used scaling methods to explore many aspects of ozone photochemistry including: the scaling break (Chapter 3), which I explain in terms of competing feedback mechanisms (Chapter 5), a parameterization of maximum ozone concentration as a function of both initial precursor concentrations and environmental conditions (Chapter 4), a means of quantifying NO<sub>x</sub>-inhibition (Chapter 6), a parameterization for the temporal variability of ozone concentration (Chapter 5), the concept of isopleth slope (Chapter 6), a fundamental basis for the IER model via ozone production (Chapter 5), the link between the IER model and the WEX model (Chapter 5), a means of simplifying the presentation of smog chamber results (Chapter 7), a simple means of characterizing VOC reactivity (Chapter 8) and finally an exploration of the GRS mechanism including its scaling behaviour and its limitations (Chapter 8).

In PART II, I continue building my screening tool but, instead of using the WEX model to understand the behaviour of a photochemical system, I use it to explore the spatial and temporal variability of ozone concentration as a function of emissions and meteorological conditions in an urban area.

---

<sup>5</sup>Whether or not chemical mechanisms faithfully represent actual ozone formation is a difficult but different question (cf. Chapter 7).

## **Part II**

# **Application of the WEX Model**

## Chapter 9

# Incorporating WEX into a Photochemical Model

### 9.1 Introduction

In this chapter, I outline the steps used to incorporate the WEX photochemistry into an integrated air quality model. Discussion and interpretation of modeling results is given in the next chapter. My intention is not to produce an integrated photochemical model that will supplant existing comprehensive models but rather to create a simple model that characterizes the essential features of ozone formation on a regional scale using WEX photochemistry. Furthermore, the intent is to capture ozone formation under generic episodic conditions. Given these intentions, expectations of the model need to be defined. At a minimum, it should:

- Give the correct position of the ozone plume. I will define position in terms of the location of maximum ozone concentration and the North-South and East-West spread of the 52 ppb isopleth. This threshold was chosen for two reasons (both of which may be specific to the chosen modeling domain): it identifies the maximum desirable 1-hour ozone concentration under the Canadian NAAQO and, as I will show, it is sufficiently large to be distinguished from typical background concentrations while not representing an extreme value. To quantify correctness, I suggest a spatial tolerance based on the characteristic scales of the problem: a time scale ( $T_o$ ) of one hour (averaging time for the NAAQO) and velocity ( $\bar{U}$ ) scale of 15 km/hr (typical advection speed of the sea-breeze). Furthermore, I suggest a tighter tolerance for higher concentration isopleths proportional to the difference between the isopleth concentration and the background concentration ( $[O_3]_{isopleth} - [O_3]_{\infty}$ ):

$$\lambda = \bar{U} \cdot T_o \sqrt{\frac{[O_3]_{\infty}}{[O_3]_{isopleth} - [O_3]_{\infty}}}$$

This gives a tolerance of  $\pm 10$  km for the 82 ppb centroid and  $\pm 14$  km for the 52 ppb centroid.

- Correctly predict the maximum ozone concentration to fall into one of three categories: below 52 ppb, between 52 and 82 ppb or above 82 ppb. These thresholds, based on the NAAQO and

intended to protect human health and ecosystems, do not represent intrinsic scaling properties of the photochemistry, but are based on ecosystem effects (Federal Provincial Working Group on Air Quality Objectives and Guidelines, 1999). As I will show in this chapter, judging the modeled ozone plume by these criteria is problematic. To start, capturing the build-up of precursors in the boundary layer, prior to the modeling day, required setting initial background concentrations. But resulting ozone concentrations were sensitive to these choices, and without sufficient observations to properly characterize initial boundary layer concentrations (both at surface and aloft), selection of background VOC and NO<sub>x</sub> concentrations was partly guided by resulting **peak** ozone concentration. Secondly, for the sensitivity studies performed in the next chapter, the only possible way to judge the model is against another model's output which has not yet been done.

- And finally, produce an ozone plume responsive to emission changes. As a test of this criteria, the model should produce ozone plumes consistent with past observations when using back-casted emissions inventories. Specifically, the model should predict the correct *direction* of change (for peak concentration and plume centroid) but not necessarily the correct *magnitude* of change.

With such general requirements, the number of input parameters should be greatly reduced over those needed for comprehensive Eulerian models. Venkatram (2001) suggests that ozone concentration at a receptor can be represented using only three variables: concentration of NO<sub>x</sub>, concentration of VOC and the time over which these species are allowed to react. To complete the requirements of my model, a measure of VOC reactivity should be added.

I argue that, at a minimum, my model must account for the following process and properties:

- The advection of precursors by the mean winds.
- The volume into which pollutants are mixed.
- General spatial patterns and temporal sequence of NO<sub>x</sub> and VOC emissions (both anthropogenic and biogenic).
- Initial ozone, NO<sub>x</sub> and VOC concentrations over the whole modeling domain.
- A gross measure of VOC reactivity.
- A means of quantifying the non-linear response of ozone to precursor concentrations and environmental conditions – the WEX model.

To meet these requirements, I use a Lagrangian box model where I first calculate back trajectories from a fixed location (receptor site) and then move the box forward, along its trajectory and over the emission sources while allowing its height to vary. Since the box moves with the mean wind, there is no advection from outside; the only changes in VOC and NO<sub>x</sub> arise from surface emissions, detrainment, entrainment and deposition.

Previous work using similar techniques has mainly focused on long range and long term ozone concentrations (Eliassen et al. (1992), Leeuw et al. (1990), Simpson (1992), Stedman and Williams (1992), Simpson (1993)). Presently, I am interested in the evolution of the ozone plume over the span of a single day. What I wish to investigate is similar to Prevot et al. (1997) who used back trajectories and aircraft flights to model the evolution of pollution from the city of Milan as it is carried into the mountain valleys of the European Alps.

Finally, while the aim is to explore ozone formation under generic conditions, a specific location, the Lower Fraser Valley B.C., has been chosen to test the model. The following subsections outline the steps involved in building my model.

## 9.2 Modeling Domain

The Lower Fraser Valley is, a roughly triangular valley that spans the Canada/U.S.A. border along the 49<sup>th</sup> parallel. The valley is flanked by the Coast Mountain Ranges to the North, the Cascade Ranges to the South and the Strait of Georgia to the West (see Figure 9.1). It narrows from a width of 100 km at its Western edge to a few kilometers at its eastern boundary some 90 km inland. In the North-South direction, it extends from the major metropolitan area of Vancouver to Bellingham in northern Washington State. The characteristic size of the valley is roughly 140 km in the East-West direction and 100 km in the North-South direction.

While the Valley floor is relatively flat (the town of Chilliwack, 80 km down-valley, is less than 15 m above sea-level), the valley walls rise steeply to over 2000 m in the North and 1200 m in the South. The valley has a population of approximately 2.4 million people, the majority living in Vancouver and its surrounding communities (Greater Vancouver Regional District, 2002).

I have chosen a rectangular modeling domain encompassing the entire LFV, most of the Strait of Georgia and the Fraser Canyon to the East (see Figure 9.2). The domain was discretized into 4 km X 4 km grids with 55 cells in the East-West direction and 31 in the North-South.

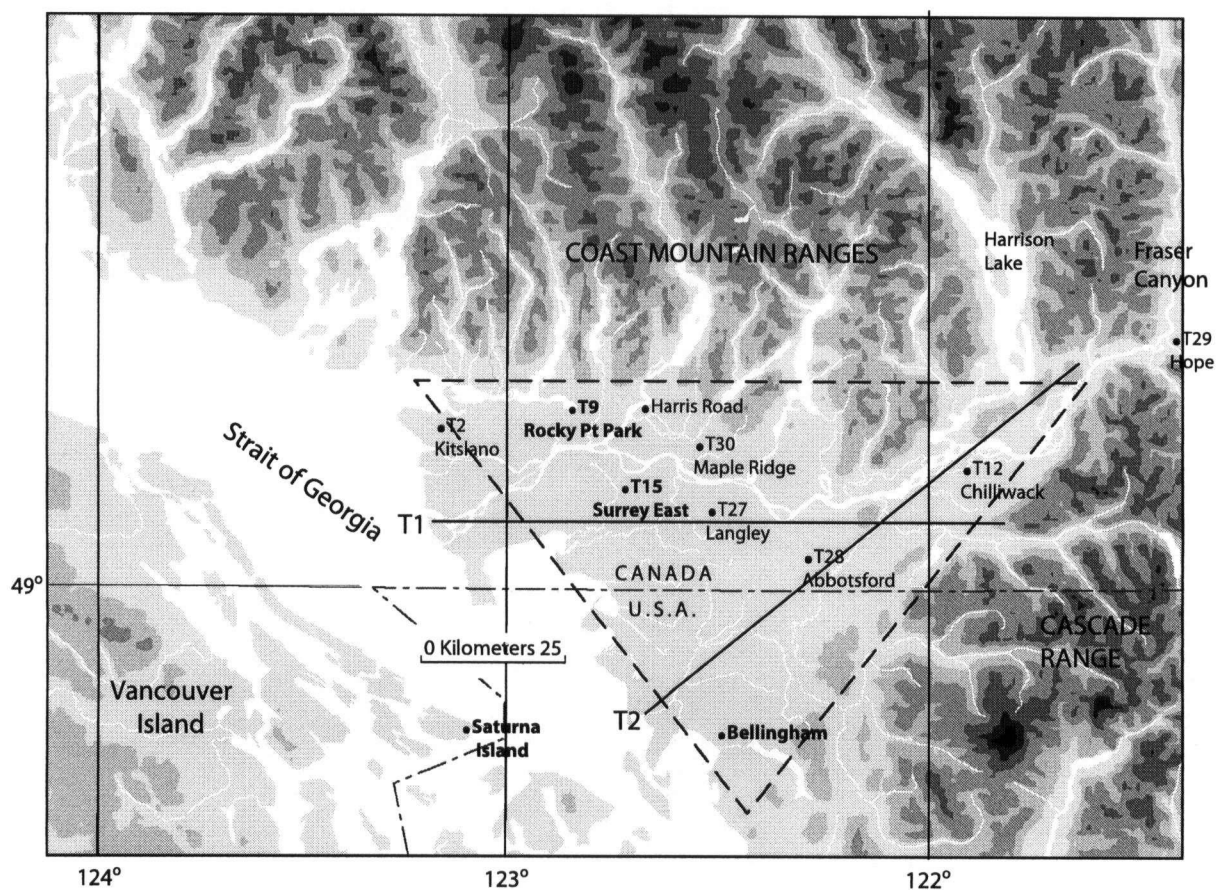


Figure 9.1: *The Lower Fraser Valley with topographic relief. The roughly triangular shape of the valley is outlined by the heavy dashed line. The valley, much narrower through its most eastern reaches, has its head at Hope. Lines T1 and T2 identify transects discussed in section 9.7. Also identified are a number of air quality stations referred to in the text.*

### 9.2.1 General Air Quality in the LFV

The LFV generally has good air quality – mean PM concentrations are lower than found in many Canadian cities (Brook et al., 1997) and comparable with Scandinavian cities (McKendry, 2000) and mean ozone concentrations usually below the NAAQO objective of 52 ppb (Federal Provincial Working Group on Air Quality Objectives and Guidelines, 1999). However, it does experience episodes of degraded air quality: high PM levels brought on by winter outflow winds from the interior (McKendry, 2000), or by occasional intrusions of Asian dust (McKendry et al., 2001) as well as episodic high ozone and associated secondary pollutant concentrations during summertime anticyclonic weather (Steyn et al., 1997). As a result, the region was identified as one of three

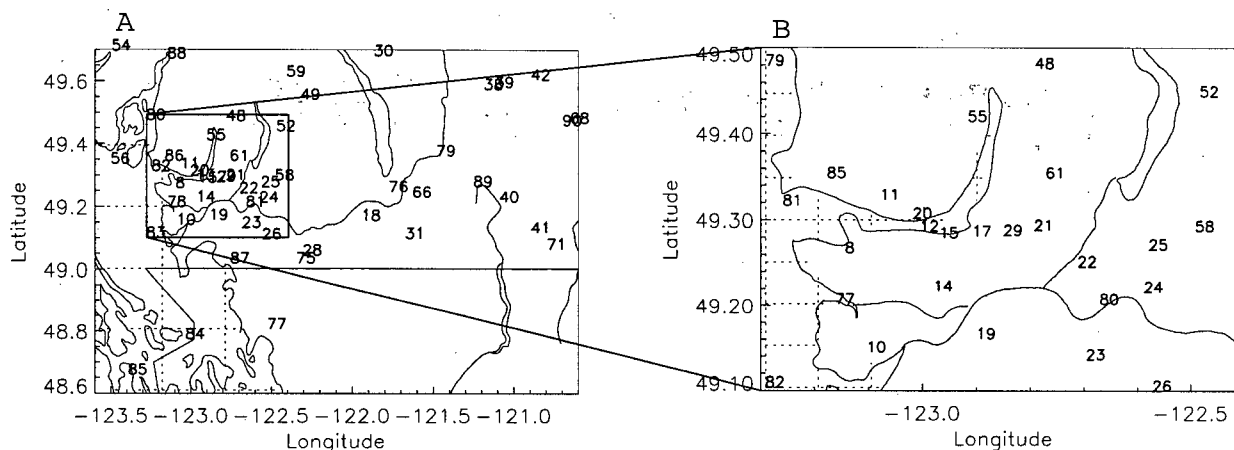


Figure 9.2: Modeling domain showing the locations of the meteorological stations used to develop wind fields. A description of each station number is given in table H.1.

'areas of concern' in Canada under the Management Plan for Nitrogen Oxides (NO<sub>x</sub>) and Volatile Organic Compounds (VOCs) (Canadian Council of Ministers of the Environment, 1990).

Because of relatively clean background air from the Pacific ocean and development of sea-breeze circulations during summertime fair-weather conditions, elevated ozone levels arise from local production (Barna et al., 2000) with highest ozone concentrations up-valley as shown in Figure 9.3. While this Figure is drawn from a specific episode, it is representative of the general pattern. For instance, at the Kitsilano measuring station (T2), on the West side of the city, not one hourly reading above 82 ppb occurred between 1992 and 1997, while at the Hope station (T29), during that same period, an average of between 2 and 16 readings above 82 ppb were recorded per year (B.C. Ministry of Environment and Parks, 1998). The principal variation of the plume is the location and value of the maximum.

A great effort has been made to reduce emissions since the mid 1980's (Greater Vancouver Regional District, 1994) when the region experienced its highest ozone reading of 212 ppb. Since then, annual NO<sub>x</sub> emissions have decreased by 15% and VOC emissions by 60% (Greater Vancouver Regional District, 2003b), the number and severity of ozone episodes has declined (see Table 9.1) and summertime peak ozone concentrations appeared to have dropped (Vingarzan and Taylor (2003), B.C. Ministry of Environment and Parks (1998)). It also appears that the location of peak ozone concentration has shifted eastward (Joe et al., 1996). The main goal of this chapter is to produce a model which captures both this spatial variability and sensitivity to changing emissions over time.

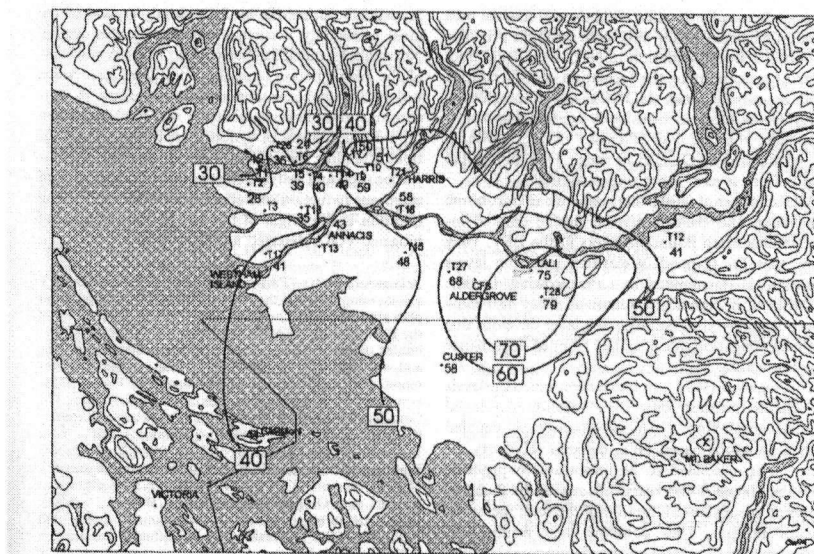


Figure 9.3: Typical ozone plume in the LFV. Shown is surface ozone concentration (in ppb), based on observations from the fixed monitoring network, at 1600 PST for an episode that occurred on August 4<sup>th</sup> 1993. Taken from Steyn et al. (1997).

### 9.3 Meteorology of Ozone Episodes in the LFV

Typically, ozone episodes occur when an upper-level ridge of high pressure is aligned with (or slightly west) of the coast while at the surface, a shallow thermal trough lies west of Vancouver, often along Vancouver Island (McKendry (1994), Taylor (1992)). These conditions produce clear skies, light winds and reduced mixed layer depths. At the surface, weak horizontal pressure gradients limit synoptic winds with most of the circulation arising from small-scale thermal forcings due to land-sea

Year	Number of Exceedances	Exceedance Hours
1987	1	36
1988	4	278
1989	1	30
1990	2	168
1991	0	2
1992	1	8
1993	0	7

Table 9.1: Occurrence of Episodes in the Lower Fraser Valley (from Environment Canada (1997)). Episodes are defined as a day when one or more measuring stations record three (or more) consecutive one-hourly averaged ozone values greater than NAAQO of 82 ppb (Concord Scientific Corporation (CSC), 1985). An exceedance day occurs when any one station records an hourly averaged value greater than 82 ppb. For every hour that a station records a value above 82 ppb, an exceedance hour is counted. It is evident from the table that episodes are infrequent events.

temperature differences (Steyn and Faulkner, 1986) or differential heating of valleys and slope walls (McKendry et al., 1998b). These conditions differ from stagnant surface anticyclone conditions typically seen in Eastern North America during high ozone episodes (National Research Council (1991), McKendry (1993)).

While the aim of the analysis is to study ozone formation under generic episodic conditions, the model uses observations from a ‘design day’ to characterize the meteorology. Future work will develop generic meteorological conditions based on a composite of observations drawn from episode days. The day selected for analysis was part of an ozone episode in August 2001, which coincided with an extensive field campaign. This campaign, which followed a similar study in 1993 (Steyn et al., 1997), used extensive ground based and airborne measurements to study the horizontal and vertical distribution of ozone and PM in the Valley (Li, 2004). The episode began on August 8<sup>th</sup> with the appearance of weak thermal trough and the development of a 500 hPa ridge west of the coast. Maximum temperatures at the mid-valley Abbotsford station (T28) jumped from 22.9°C on the 7<sup>th</sup> to 30.7°C on the 8<sup>th</sup>. By the 10<sup>th</sup>, the 500 hPa ridge was positioned along the coast (Figure 9.4) with the thermal trough extending up from the Southwestern U.S. (Figure 9.5). On the 10<sup>th</sup>, surface weather was calm and warm: the maximum temperature at Abbotsford was 30.3°C while daytime winds reached only 3.6  $ms^{-1}$  at Vancouver International Airport (YVR) and 5.6  $ms^{-1}$  at Hope (T29). These stagnant conditions lasted until the 16<sup>th</sup> when an incursion of cool marine air brought an end to the episode (Snyder, 2002).

Meteorology from August 10<sup>th</sup> was used to calculate back trajectories and mixing heights for two reasons: the meteorological patterns were consistent with typical LFV ozone episodes and the field measurements from Pacific 2001 provide additional tools for developing and testing the model. I stress that while I use detailed meteorology from a specific day, my intention is to investigate the spatial and temporal behaviour of the ozone plume for a generic episode.

## 9.4 Previous Modeling

Ozone formation in the LFV has been extensively studied using both comprehensive and trajectory modeling. Notably, Hedley and Singleton (1997) and Hedley et al. (1997) modeled ozone formation using the Mesoscale Compressible Community Model (MC2) with the CALMET preprocessor and CALGRID photochemical model. Their results show an ozone plume with two distinct peaks downwind of Vancouver; one along the North Cascade Mountains and another over the Coast Mountains. I will show my model reproduces such a plume when I reduce VOC reactivity. It must be mentioned that ozone maxima displaced from the Valley is not inconsistent with observations.



plume is an open question. <sup>1</sup> It is hoped that my model will shed more light on these matters.

## 9.5 Interpolation of the Wind Fields

A diagnostic model was used to generate hourly 2-D wind fields. The model consisted of interpolating hourly wind observations (speed and direction), taken from local meteorological stations, and smoothing the interpolated fields to reduce divergence. There were 53 surface observation stations in the domain for an average station separation of  $d \approx 23$  km. Stations were located throughout the domain, having a range of exposures with mixed reliability and were administered by a number of agencies: Environment Canada, Greater Vancouver Regional District (GVRD), B.C. Ministry of Forests, B.C. Ministry of Highways stations, B.C. Hydro and the US National Weather Service. Table H.1 lists the stations, their latitude, longitude and administering agency. Although winds fields were developed from surface observations, back trajectories based on these fields should not differ greatly from trajectories developed using mid-boundary layer winds since convective mixing that day should have lead to boundary layer winds whose direction and speed are independent of height (Arya, 1999).

### 9.5.1 Interpolation

Every hour, observed winds were interpolated component-wise onto the entire grid by an inverse distance weighting method, as suggested by Goodin et al. (1979), using the following weighting factor:

$$W(r) = \begin{cases} \frac{R^2 - r^2}{R^2 + r^2} & : r < R \\ 0 & : r \geq R \end{cases}$$

where  $r$  is the distance from a grid point to a nearby station and  $R$  is the distance at which the weighting factor goes to zero (i.e. radius of influence). To avoid interpolating localized wind patterns from a station in a mountainous region to cells in potentially different topographic locales, two different radii of influence were used. In mountainous regions, a radius of 20 km was used, whereas a 44 km radius was used over remaining grid. Cells not within a radius of influence of any

---

<sup>1</sup>A major weakness in the air pollution monitoring network is the spatial distribution of stations. In the first half of the 20<sup>th</sup> century, Vancouver's air pollution problem was one of industrial emissions in the downtown core and harbour (Oke et al., 1992), whereas today, it is ozone and secondary particulates further up-valley. Unfortunately, since the mountains and tributary valleys are sparsely inhabited, there are no regular measurements to fully characterize ozone concentrations away from the LFV. As a result, there is a bias in the network with too many stations lying along an East-West transit and too many stations close to the city core. This makes characterization of the ozone plume difficult, especially in the North-South direction.

stations were set to the all-station average for that hour's readings. This occurred principally with grid cells in the Southeast corner of the domain, over the Cascade mountains. It was reasoned that setting these grids cells to an average value would be more meaningful than to a localized value from a distant station.

To determine the radii of influence, a set of data withholding experiments was performed. In each experiment, a single observation was withheld from the analysis and the resulting interpolated value was compared to the withheld value. Experiments were performed using only the Environment Canada and US National Weather Service stations, since these were thought to be the most reliable and best sited stations. For each wind component, the sum of the errors from each experiment was calculated. It was found that setting the mountainous radius below 20 km, greatly increased the total error, while radii above did not change the error significantly. However, since the model does not include topography, when using the larger radii of influence, the wind fields tended to flow through height contours. It is suspected that errors from a few stations were dominating the total. For the valley and ocean grid cells, decreasing the radius of influence increased errors but increasing it did not. Sensitivity of the resulting ozone plume, on the radii of influence was indirectly checked by calculating trajectories based on MC2 simulations for the same time period. These results are discussed in section 9.6.

### 9.5.2 Divergence Reduction

After interpolation, hourly gridded wind fields were adjusted to reduce horizontal divergence. Following the method of Goodin et al. (1980), at each grid point, the local divergence was calculated and the  $u$  and  $v$  components of the surrounding cells were adjusted until the divergence vanished. While this method eliminates divergence at the grid point in question, new divergence is created at the surrounding points. Through an iterative procedure, however, the divergence within the field was brought below the suggested threshold of  $5 \times 10^{-6} \text{ s}^{-1}$  used by the CALMET prognostic model (Scire et al., 2000).

## 9.6 Development of Back Trajectories

Advection was handled using a set of 60 Lagrangian box models. Each box followed a trajectory calculated from the interpolated wind fields. End points (or receptor sites) were chosen to form a regular  $6 \times 10$  grid. All trajectories ended at 1800 local time and started at 0500 local time. Each box was a  $4 \text{ km} \times 4 \text{ km}$  column with height given by the mixed layer depth (discussed in the next section). Trajectory positions were calculated using 60 second time steps. Since the typical

eddy turnover times in a convective mixed layer is between 10 and 20 minutes (Stull, 1988), it was decided that trajectory positions need only be saved at 15 minute intervals.

A constant acceleration method (Stohl, 1998) was used to calculate trajectory positions. This involved an iterative approach where velocity  $\dot{X}^0$  at point  $X^0$  and time  $t_o$  was used to calculate position  $X^1$  at time  $t_1$ . Next, the velocity at  $X^1$  at time  $t_1$  ( $\dot{X}^1$ ) was averaged with the original velocity and used to calculate a new position  $X^2$ :

$$X^2(t_1) = X^0(t_o) + 0.5 \times (\Delta t)[\dot{X}^0(t_o) + \dot{X}^1(t_o)] \quad (9.1)$$

In practice, this should be repeated until subsequent iterations do not change the estimate of position. Because, I was interested in the position within a 4 km box at 15 minute intervals, I only performed a single iteration of this scheme.

### 9.6.1 Limitations of the Trajectories

While there are many errors associated with the use of back trajectories, I argue these will not prevent the model from representing the main features of the ozone plume. Some common concerns with back trajectories and reasons why these will not adversely affect the modeling are given below:

**Vertical Wind Shear** Vertical wind shear will pull the column apart limiting the duration of the simulation and size of box (Seaman, 2000). This effect, while important, should be minimized by vertical mixing in the CBL. Furthermore, trajectories last only 13-hours, most of which is during convective conditions. In addition to assuming uniform vertical wind fields, I also assume vertically uniform concentration profiles. However, Krol et al. (2000) and Galmarini et al. (1997) show that if the timescale of a chemical reaction is faster than the timescale of vertical mixing, concentration inhomogeneities can arise between updrafts and downdrafts that ultimately alter the rate of chemical transformations. While specific reactants may be affected in this way, I am concerned with gross photochemical production on the time scale of a day.

**Horizontal diffusion** Turbulent dispersion of material into and out of the column is a severe limitation of box models. While limiting the influence of vertical wind shear suggests minimizing column footprint, reducing the influence of horizontal diffusion requires a larger footprint. It is hoped that the  $4 \times 4$  km footprint will provide a sufficient compromise. The effects of horizontal diffusion provide a limit to the smallest scales that the model can resolve.

**Accumulation of errors** At each time step, errors in Eq. (9.1) accumulate. Stohl (1998) suggests these positional errors are proportional to 20% of the travel distance. On average, my

trajectories travel 81 km (with a range of 39 to 158 km). Thus the average error in position is about at 16 km or 4 grid cells at the starting point. This error also provides an estimate for the size of features that can be resolved.

To estimate the uncertainty in the back trajectories, calculations have been done using both the interpolated wind fields and model output from the MC2 meteorological model (Tanguay et al., 1990). In Figure 9.6, a comparison of four trajectories is given. These represent trajectories terminating at the western part of the valley (A), the southern part of the Valley (B), the city of Vancouver (C) and the eastern limit of the valley (D). In general, MC2 trajectories travel greater distances and tend to be straighter, partly due to the much stronger morning winds MC2 produced over the strait. As a result, once trajectories pass over the ocean, the discrepancy between them grows quickly (c.f. Figure 9.6A and C). The greatest discrepancy occurs with the trajectories that start in the mountains (c.f. Figure 9.6D). The MC2 trajectory has the air mass moving down Harrison Lake before being caught in the up-valley flow near Chilliwack while the trajectory based on the interpolated winds shows starts on top of the Coast Mountains, descends in a drainage flow before being drawn back up mountain and into the valley flow. Because neither trajectory passes over significant emission sources (see Figures 9.10 and 9.10), the large discrepancy between the two is not expected to greatly influence the ozone plume. This is verified in Chapter 10 section 10.1.5, where ozone plumes based on the two sets of trajectories are compared.

## 9.7 Parameterizing Mixed Height

During summer fair-weather conditions, temperature contrasts between cool sea surfaces warm landmasses results in onshore flow and the advection of cool air via a sea-breeze. This cool air undercuts the existing air mass – producing an thermal internal boundary layer (TIBL) – limiting vertical mixing. Interactions between the sea-breeze and the LFV's complex coastal topography create large spatial and temporal variation in the TIBL (Steyn and Oke (1982), Hayden et al. (1997), Hägeli et al. (2000) and Cai and Steyn (2000)). While Venkatram (1977) has developed a simple model for estimating TIBL depth based on entrainment of heat flux across the top of the TIBL, advection and subsidence, it has difficulty reproducing observed TIBL heights in the LFV (Hayden et al., 1997). On the other hand, Gryning and Batchvarova (1996) have developed a slightly more sophisticated model, that takes into account spatially varying land-use patterns and irregular shoreline, and have shown it reproduces observed spatial and temporal TIBL patterns as well as three-dimensional simulations with the CSU-RAMS mesoscale model (Batchvarova et al., 1999). Theirs is a slab model based on a turbulent kinetic energy (TKE) budget within the TIBL. It assumes

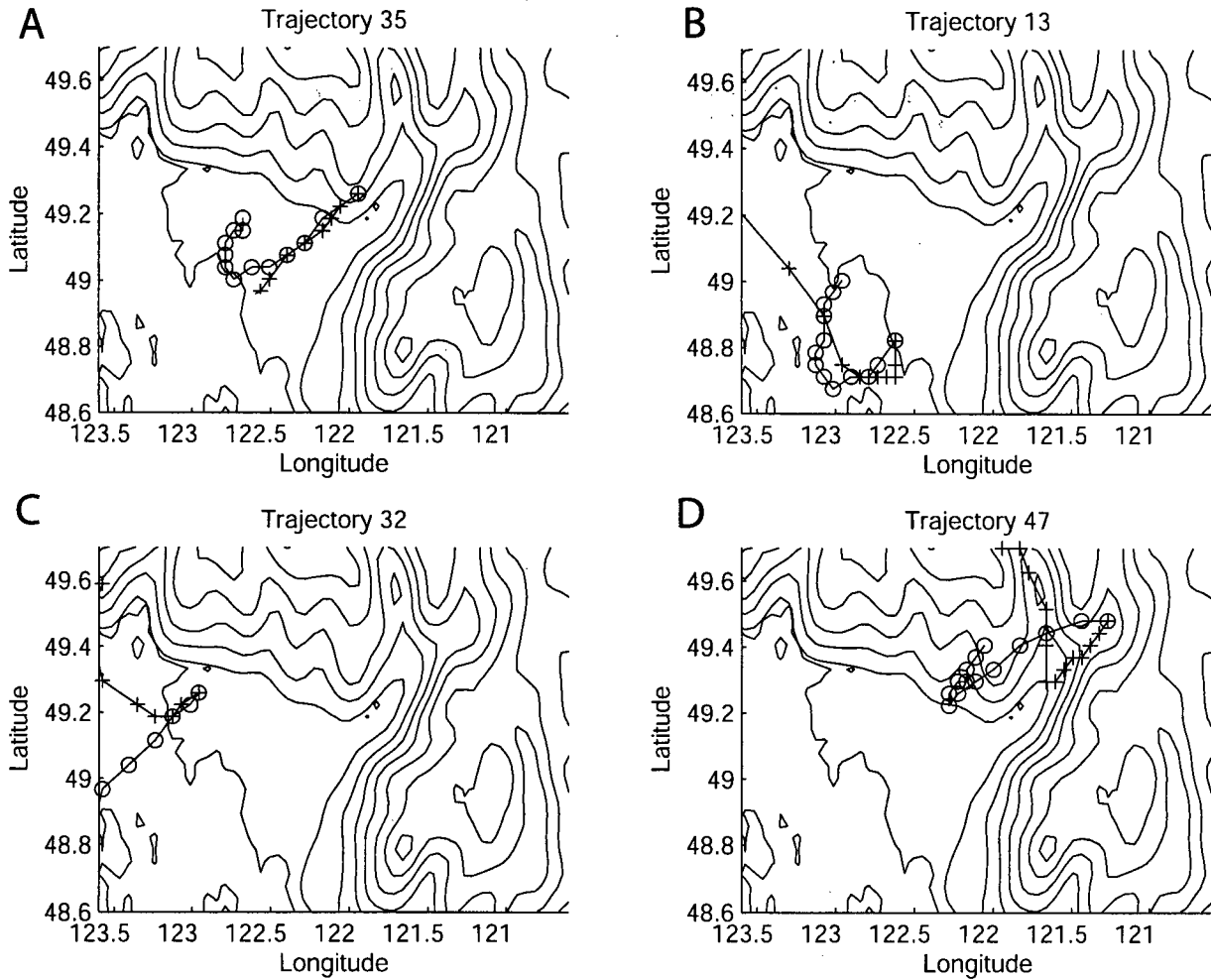


Figure 9.6: Four back trajectories derived from the interpolated wind fields (circles) and MC2 model output (plus signs). Contours give elevation in 200 m intervals.

potential temperature within the TIBL is uniform with height, the air above stably stratified with potential temperature gradient independent of height and time (Gryning and Batchvarova, 1990). Their equation for the height of the internal boundary layer ( $h$ ) is:

$$\left\{ \frac{h^2}{(1+2A)h - 2BkL} + \frac{Cu_*^2 T}{\gamma g [(1+A)h - BkL]} \right\} \times \left( \frac{\partial h}{\partial t} + u \frac{\partial h}{\partial x} + v \frac{\partial h}{\partial y} - w_s \right) = \frac{(\overline{w'\theta'})_s}{\gamma} \quad (9.2)$$

where  $u$  and  $v$  are the horizontal components of the mean wind in the  $x$  and  $y$  directions and  $k$  the von Karman constant.  $A$ ,  $B$  and  $C$  are dimensionless constants arising from the parameterization of TKE production, set to 0.2, 5.0 and 8.0 respectively. This model has been used to determine column mixing heights along each trajectory in this study.

The subsidence velocity is  $w_s$  and was assumed to increase linearly with height:

$$w_s = -\beta z \quad (9.3)$$

where  $\beta$  was set to  $7.0 \times 10^{-5} s^{-1}$ , within the range  $[10^{-4}, 10^{-6}]$  suggested by Steyn and Oke (1982), and guided by a set of observations taken at Chilliwack during Pacific 2001. The potential temperature gradient above the TIBL ( $\gamma$ ) was set to  $0.0098 K/m$  – typical for fair weather conditions in the LFV (Hayden et al., 1997).

The Monin-Obukhov length ( $L$ ), friction velocity ( $u_*$ ) kinematic heat flux  $(\overline{w'\theta'})_s$  were calculated based on land use classes and the interpolated wind fields.

### Land-use Classes

The model used only four generic land-use classes: water, forest, green-space (which includes agriculture, parks, bogs) and urban. Allocation of the landmass to these categories was achieved by taking the 27 MC2 land-use classes (Tanguay et al., 1990) and mapping them onto this smaller subset. The initial allocation of the MC2 land classes to the LFV did not include the city of Vancouver but was incorporated into MC2 by Dr. Martilli through an analysis of GIS data (Dr. Martilli, personal communication). Table H.2 lists the mapping between the MC2 classes (and the GIS based urban area) and the four generic classes. Land-use classes were also used in developing the emissions inventory, discussed in the next section.

Interpolated winds at each grid cell were used to determine local friction velocity using a set of correction factors based on the land-use classes. Similarly, sensible heat flux was scaled to a set of measured values, taken from a Vancouver site on days with a well developed sea-breeze, using a second set of land-use correction factors (D.G.Steyn, personal communication). Table H.3 lists the land-use classes and correction factors. The latter are based on results of Batchvarova et al. (1999). Finally, the friction velocity and surface heat flux were used to calculate the Monin-Obukov length.

#### 9.7.1 Mixing Height Results

Equation (9.2) was solved for the daylight hours by separating it into three parts: advection, subsidence and heating. Each was solved separately at every time step. A Bott advection scheme (Bott, 1989) was used for the advection part with time step of 60 seconds and spatial resolution of 500 m. Mixing heights over the ocean at all hours and over the entire domain during the domain, was set to a constant 50 m. Calculated mixing heights at 1000, 1200, 1400 and 1600 PST are plotted in Figure 9.7.

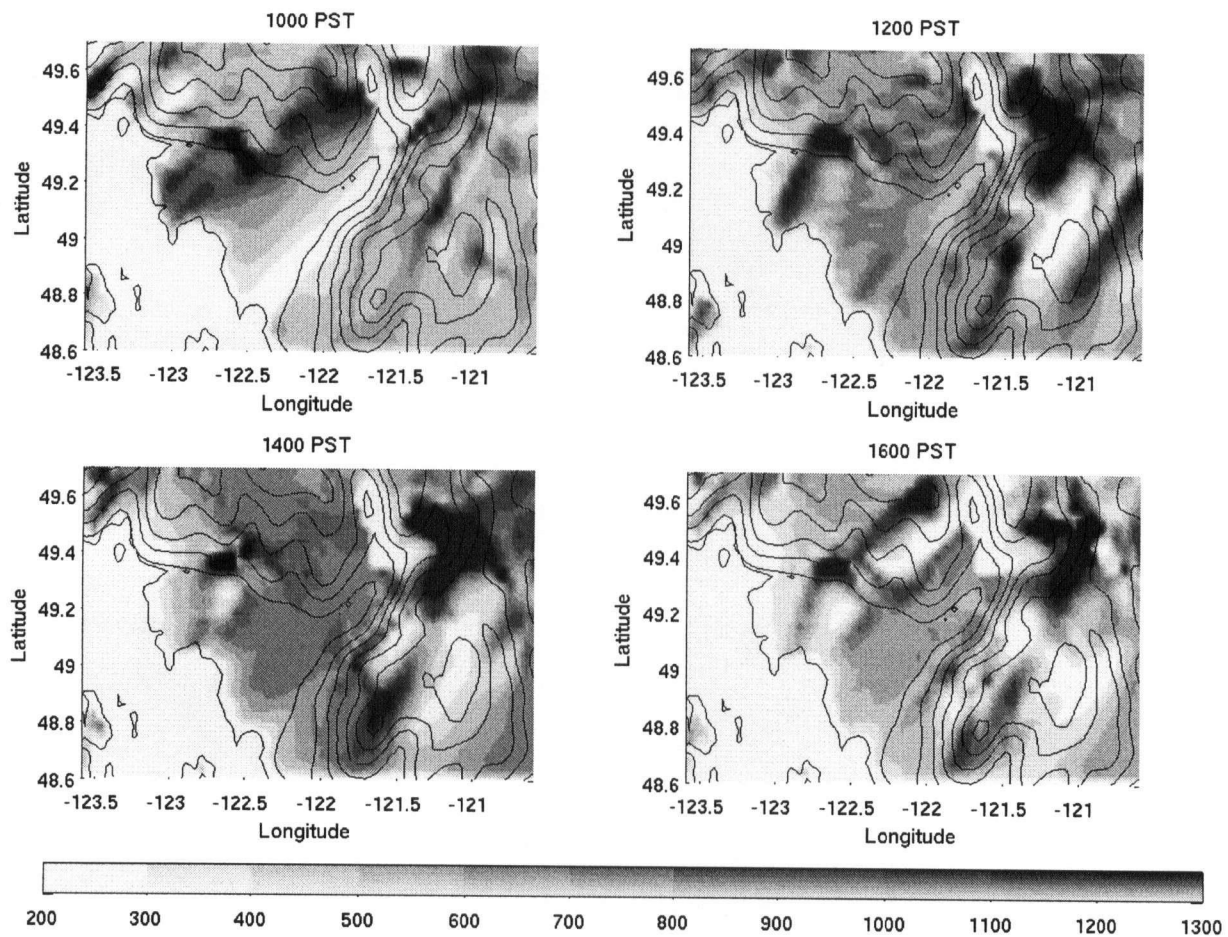


Figure 9.7: Calculated mixing heights (in  $m$ ) for four different hours based on Eq. (9.2).

The calculations produce heights over Chilliwack of  $319\ m$  at 1000 PST and  $575\ m$  at 1400 PST; very close to the observed values (based on measured potential temperature soundings) of  $325\ m$  (measured at 0933 PST) and  $600\ m$  (measured at 1346 PST).

As a check on the model, mixing heights were compared with MC2 model output (Dr. Martilli, personal communication) along transects T1 and T2 (see Figure 9.1). Mixing heights at 1000 and 1400, along transect T1 are plotted in Figure 9.8 and along transect T2 in Figure 9.9. For transect T1, the biggest discrepancy occurs at 1400 PST in the centre of the valley where the simple model gives a ‘dome-like’ structure with maximum height around  $600\ m$  whereas the MC2 model output builds the mixing height to much greater depths ( $\sim 1200\ m$ ) further inland. In addition, the morning profile based on the simple model grows quite sharply from the coast suggesting weaker onshore winds at that time. Likely, the MC2 model has started the sea-breeze circulation earlier than given

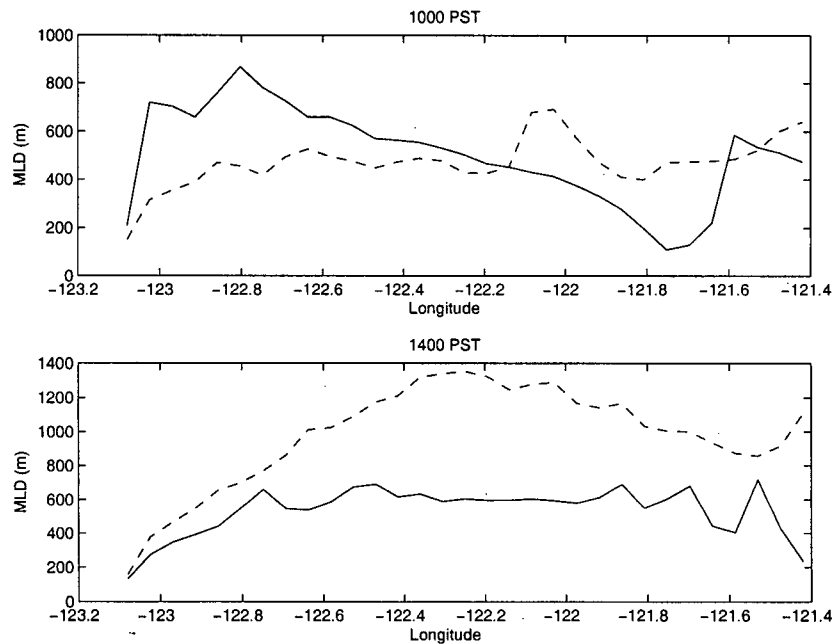


Figure 9.8: Calculated mixing heights at two different times along transect T1. Solid lines are results from the simple model of Batchvarova et al. (1999) while dashed lines from MC2 model output (Dr. Martilli, personal communication).

by the interpolated wind fields. It is interesting to speculate on the importance of catching the onset of the sea-breeze and its subsequent up-valley advection of rush-hour pollutants. By the afternoon, both models have similar profiles near the coast.

Along transect T2, both curves show strong similarities but the MC2 results are almost larger by a factor of two. Difficulties calculating latent and sensible heat fluxes (likely arising from poor representation of surface moisture) appear to be causing the extreme mixing heights in the MC2 simulations (Dr. Martilli, personal communication). This is not an issue with the simple model, since the model uses measured and not calculated heat fluxes.

## 9.8 Emissions

To explore the relationship between ozone and its precursors, a simple emissions inventory was developed using published year 2000 emission rates (Greater Vancouver Regional District, 2002). An overview of the inventory is given below with more details in Appendix G.

In essence, the task involved taking yearly VOC and NO<sub>x</sub> emission totals from the LFV and spatially and temporally allocating these using a small number of general sources. Sources were

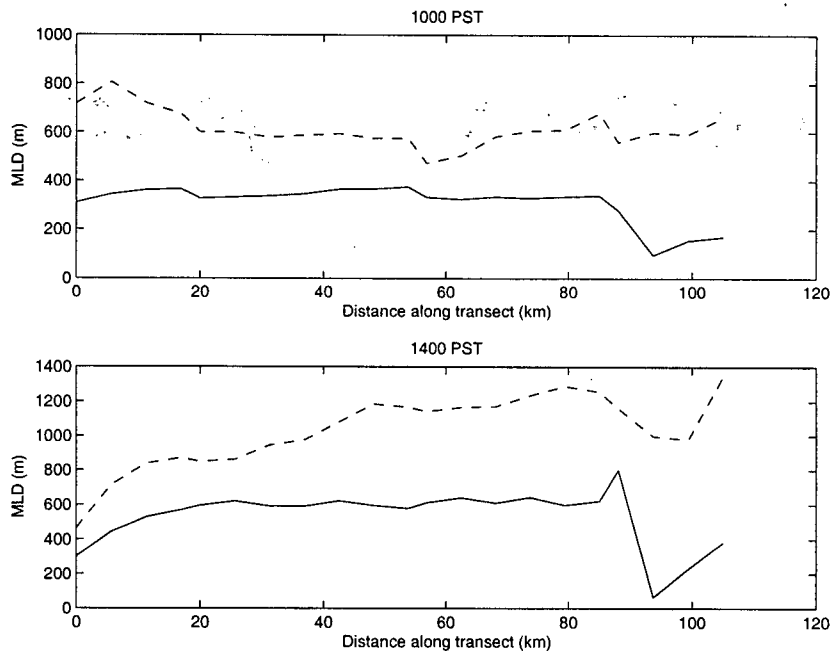


Figure 9.9: Calculated mixing heights at two different times along SW-NE transect T2. Solid lines give heights from on simple model of Batchvarova et al. (1999) and dashed lines are MC2 model output (Dr. Martilli, personal communication).

classified into three main categories: mobile, area and point with the mobile and area sources being further subdivided. Table 9.2 shows the final disaggregation of emissions along with domain-wide emissions rates for each source, during a typical summer day between the hours of 500 and 1800 local time. For each sub-category, temporal curves for monthly, daily and hourly emissions rates were used to calculate hourly emissions. These were then spatially allocated using a set of six emissions masks: sea, urban, transportation, aircraft, agriculture and biogenic all loosely based on the four land use classes. The masks were non-overlapping and covered the entire domain. Appendix G gives more details about the emission masks. Figures 9.10 and 9.11 show VOC and NO<sub>x</sub> emissions fields at 1600 LST based on the simple model. Evident is the large concentration of emissions from the city of Vancouver and its surrounding communities. This is not unexpected since the majority of emissions in the LFV are from mobile sources (Greater Vancouver Regional District, 2002) concentrated in urban areas or along transportation corridors. Characterization of these emissions is central to the development of the emissions inventory.

There are two difficulties in calculating mobile source emissions: determining their spatial distribution, and their magnitude. The former is important in determining the latter, that is, over any

General Category	Sub-category	VOC (tonnes/day)	NOx (tonnes/day)
Mobile	LDV	79	70
	HDV	3	46
	Marine	32	35
	Rail	0	9
	Aircraft	2	3
	Construction	21	35
	Agriculture	2	12
Area	Space Heating	0	0
	Evaporative	52	
	Forests	235	44
	Livestock	6	
	Crop	32	
	Miscellaneous	5	
Point		13	17
Total		484	270

Table 9.2: Emissions categories and domain wide flux for a typical summer day (in tonnes) based on the simple emissions inventory.

transportation network and at any given time, a variety of driving conditions coexist, greatly influencing vehicle emissions (especially VOC emissions which consist of both tailpipe and evaporative emissions and are highly dependent on operating conditions, vehicle maintenance and temperature (National Research Council, 2000)). Because of the difficulty in modeling vehicle operating conditions (vehicle speed, driving patterns, etc.), significant uncertainties exist even in the most detailed emissions estimates (Sawyer et al., 2000).<sup>2</sup>

Since the published values account for localized traffic flows and driving conditions (Greater Vancouver Regional District, 2003a), I should find my totals in agreement with episode specific totals (as long as I account for increased summertime traffic and evaporative emissions). Furthermore, after allocating these emissions in a general way over the urban area and rough transportation network, I do not expect the difference between the simple and episode specific inventory significant in influencing the resulting ozone plume. In essence, I am arguing the main importance of accurate, localized emission rates is in the calculation of *total* emissions and not on the photochemistry.

### 9.8.1 Comparison with a Detailed Episode Specific Inventory

As a check on the simple emissions inventory, a comparison was performed against a detailed inventory developed for the Pacific 2001 field campaign (Gauthier et al., 2003). This inventory was developed using the Sparse Matrix Operator Kernel Emission (SMOKE) modeling system (Houyoux

<sup>2</sup>While tunnel studies in the LFV show the regulatory emissions model (MOBILE) capable of predicting in-use emissions (Rogak et al., 1998), this requires more detail than is generally available (i.e. video cameras to identify vehicle type and age, road side temperatures and accurate vehicle speeds). Nonetheless, even with such detailed observations and operating under the relatively controlled tunnel conditions (hot-stabilized and roughly constant speed) VOC and NOx emissions are still under-predicted by 29% and 23% respectively (Gertler et al., 1997).

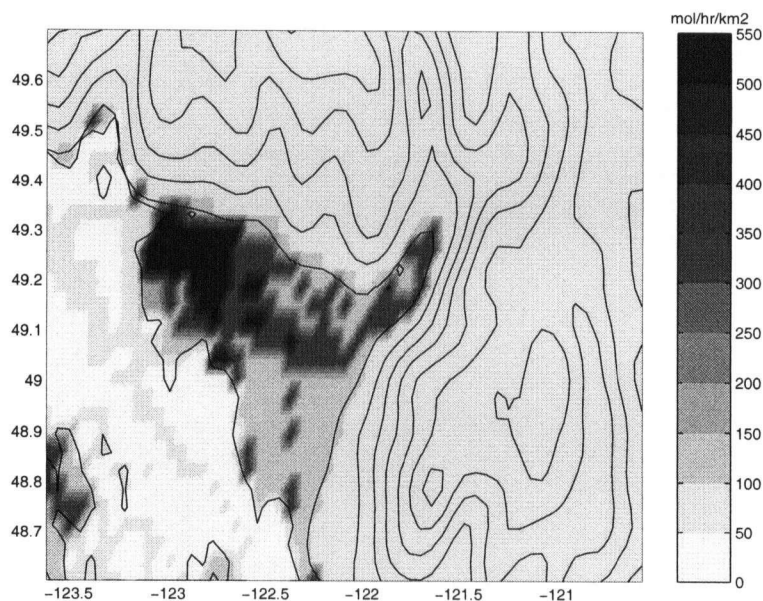


Figure 9.10: *Spatial pattern of VOC emissions (in mol/hr/km<sup>2</sup>) at 1600 LST based on simple inventory.*

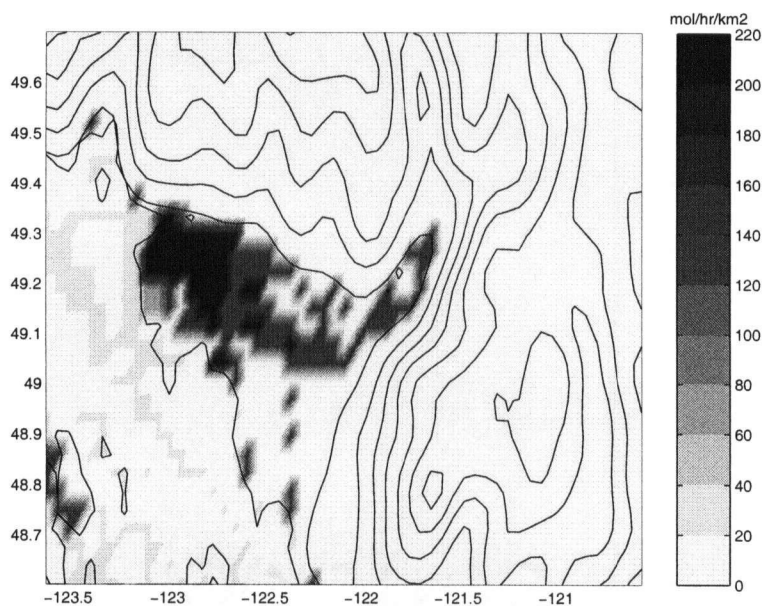


Figure 9.11: *Spatial pattern of NO<sub>x</sub> emissions (in mol/hr/km<sup>2</sup>) at 1600 PST based on simple inventory.*

and Vukovich, 1999) (which uses MOBILE and the Biogenic Emissions Inventory System (BEIS) (Pierce and Waldruff, 1991) to calculate mobile and biogenic emissions respectively) to spatially and temporally allocated emissions as well as speciate the VOCs. Figures 9.12 and 9.13 compare

domain wide emission of VOC and NO<sub>x</sub>, for the hours between 0700 and 1800 local time <sup>3</sup>. In addition, emission totals over the three mask with the highest emissions rates have been plotted. While the figures show the simple inventory produces emission which are in both quantitative and spatial agreement with the more detailed inventory, a few additional comments can be made:

- VOC emissions, from the simple inventory, along the transportation and urban masks show more pronounced morning and evening peaks due to the simple traffic patterns I used.
- The close agreement of VOC emissions over the forest mask is a little unexpected. While the published yearly values are based on output from GloBEIS3 model output (Greater Vancouver Regional District, 2003a), to calculate hourly emissions, I assumed a simple scaling with average hourly forest temperature. Drewitt et al. (1998) show, using data from field studies in the LFV, a large amount of the observed variability can be accounted for by scaling monoterpene emissions by temperature. In addition, they show isoprene emissions scale with both temperature and incident short wave radiation. Since on a clear day these two factors are not independent, it was expected a temperature-only scaling would reproduce the general biogenic profile. Whether or not the episode specific inventory, which takes episode specific meteorological conditions like cloud cover, relative humidity and solar elevation into account, scales almost exclusively with temperature or whether there are several competing influences which fortuitously cancel needs further investigation.
- For NO<sub>x</sub>, the biggest discrepancy occurs over the marine and urban masks. I suspect this arises from slight differences in the determination of the sea/land boundary between inventories. Such differences would allow marine emissions, from ships in harbour, to be allocated to the urban cells surrounding the harbour. I do not expect this to have any influence on the resulting ozone plume.

## 9.9 Speciation of VOCs

A single VOC speciation based on average LFV emissions, for a 1985 episode (Jiang et al., 1997a), was used (see Table 9.3). While a speciation based on ambient air samples would be more appropriate to use, Jaing et al. (1997) show that ambient and emissions inventory compositions in the LFV are in reasonable agreement. Finally, ambient VOC composition in the LFV between 1990 and 1996 has remained relatively constant (even though absolute concentrations have dropped)

<sup>3</sup>Problems with the SMOKE output prevented comparisons for the hours of 0500 and 0600.

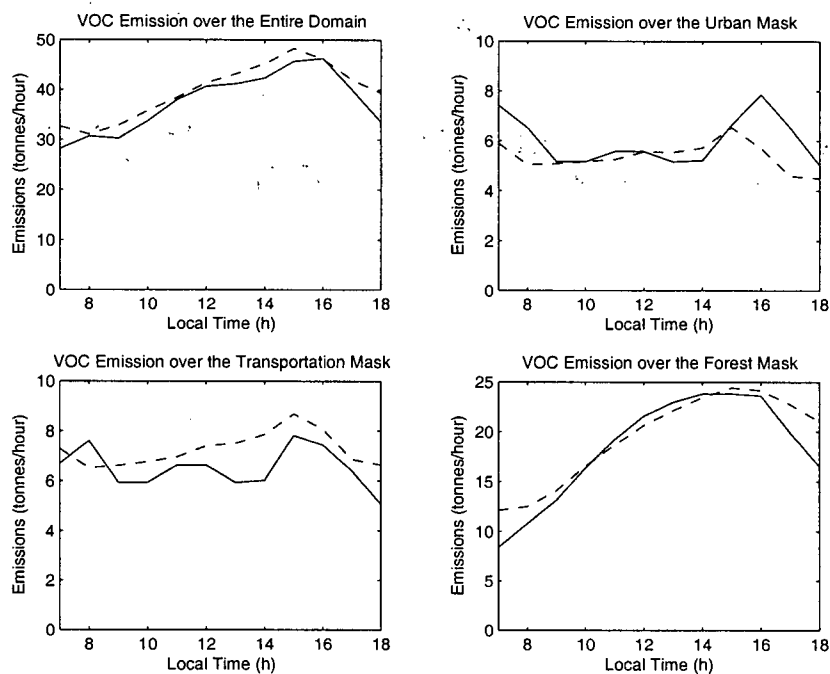


Figure 9.12: Comparison of VOC emissions between the simple inventory (solid line) and the episode specific emissions inventory (dashed line).

(Greater Vancouver Regional District, 1999), suggesting the 1985 speciation is still representative of the LFV airmass. While speciated VOC emissions were available from the SMOKE output, a domain wide averaged speciation based on these emissions was very unreactive – over a third of the mixture was assigned to the CB-IV non-reactive (NR) class. This can be compared with the ARB 29-city mixture (Jeffries et al., 1986), where the CB-IV speciation is only 9% NR<sup>4</sup>.

## 9.10 Boundary Layer Processes

### 9.10.1 Deposition

Deposition is the transfer of airborne material to the earth's surface where it is removed (Seinfeld and Pandis, 1998). Only dry deposition, the removal of material in the absence of moisture, is treated in the model. While dry deposition is known to be a function of many micro-meteorological variables including: friction velocity, wind speed, atmospheric stability, surface heat flux and turbulence

<sup>4</sup>The COND2243 chemical mechanism used for the present speciation does not specifically include a non-reactive class, although it does have two very low reacting classes: methane and alkanes whose  $OH$  are less than  $10^{-4}$  ppm<sup>-1</sup>min<sup>-1</sup> (Jiang et al., 1996)

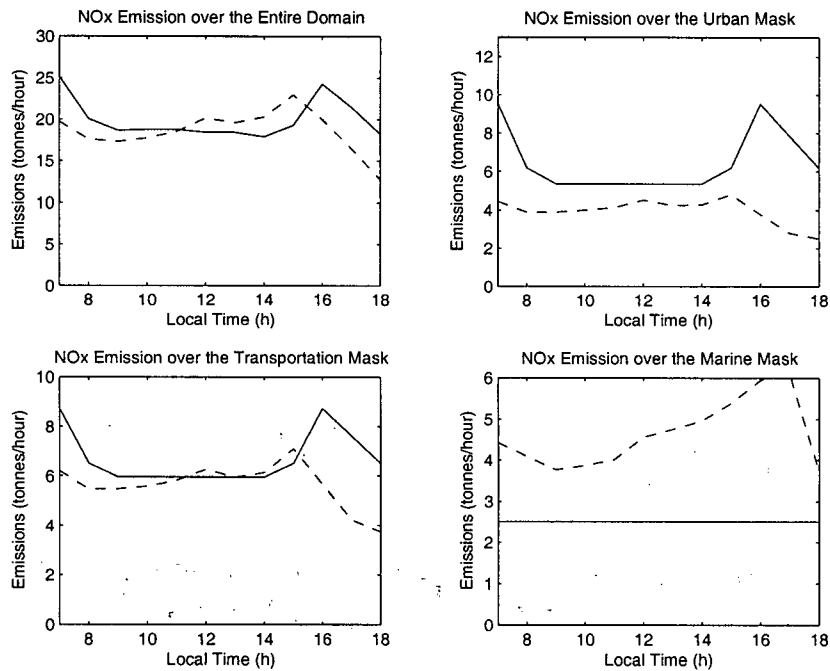


Figure 9.13: Comparison of NOx emissions between the simple inventory (solid line) and the episode specific emissions inventory (dashed line).

COND Class	Carbon Fraction
ETHE	0.040
MEOH	0.001
ETOH	0.004
HCHO	0.005
CCHO	0.002
RCHO	0.002
MEK	0.004
CRS	0.002
ALK1	0.289
ALK2	0.112
ARO1	0.075
ARO2	0.087
OLE1	0.031
OLE2	0.028
OLE3	0.318

Table 9.3: Speciation of VOCs used in the LFV photochemical simulations based on the COND2243 chemical mechanism (Jiang et al., 1997b).

(Arya, 1999), a simple parameterization using a deposition velocity ( $v_d$ ) of 0.2 cm/s was used. While such a simple parameterization ignores the effects of surface roughness, and species reactivity, Russell and Dennis (2000) suggest the details of deposition parameterization do not significantly impact modeled sensitivity of ozone to its precursors.

## 9.11 Initial Boundary Layer Concentrations

Emissions add to precursors already found in the boundary layer. These arise from existing ambient (background) concentrations and carry-over of emissions from previous days. The model's biggest difficulty is establishing initial boundary layer concentrations which vary in time and space, are quite dilute and as a result, difficult to measure. While the observation network provides hourly surface NO<sub>x</sub> concentrations, it does not provide surface VOC concentrations nor any information about the vertical structure of VOC, NO<sub>x</sub> (or ozone) concentrations. These show great variability in complex coastal regions, where they often form distinct layers of pollution, and are a well documented feature of ozone episodes in the LFV: both Pisano et al. (1997) and McKendry et al. (1998a) measured layers of high O<sub>3</sub> using tethered balloons, while Hayden et al. (1997) used an airborne downward looking lidar to observe elevated aerosol layers and McKendry et al. (1998b), using a chemiluminescent detector, found polluted layers having almost twice the ozone concentrations as air above or below along a flight path over a tributary lake in the LFV.

### Elevated Pollutant Layers

The simplest way for elevated pollutant layers to form is through the diurnal cycle of mixed layer development. While daytime convective mixing creates uniform vertical concentrations, nighttime radiative cooling creates a shallow stable boundary layer (SBL) suppressing vertical mixing (Stull, 1988). Above the SBL, a residual layer forms where pollutants are effectively cut-off from surface removal processes (such as deposition or chemical sinks from fresh emissions). Meanwhile, these same removal processes reduce surface layer concentrations leading to a vertical concentration gradient. This effect can be amplified along tributary valleys, where winds are channeled over forested side walls removing surface layer pollutants while leaving pollutant layers aloft (Banta et al., 1997). Additional processes that lead to elevated pollutant layers include: the venting of pollutants along valley side walls, from 'convective debris' (i.e. pollutants pushed above the mixed layer by convective plumes) or from coastally trapped disturbance undercutting an initially polluted mixed layer (McKendry, 2000).

Entrainment of precursors (and ozone), from elevated layers, acts as an additional emission source (or sink depending on concentration differences between the column and polluted layers) and McKendry (1997) has estimated that as much as half of the observed increase in morning and early afternoon ozone concentrations, at a mid-valley location during Pacific '93, could be attributed to down-mixing of ozone.

### 9.11.1 Residual Layer Concentrations

The presence (and effects) of pollutant layers was treated very simply in the model. Special simulations were performed in which precursors were emitted into the domain, having fixed background VOC and NO<sub>x</sub> concentrations, and allowed to build up to steady state levels. Two sets of simulations were performed, one for NO<sub>x</sub> and another for VOC, and in each, precursor emissions were advected, without chemical reactions, using the interpolated winds for five days. At the end of the first day, the build up of pollutants in the boundary layer was modeled using the 1600 PST concentrations. This field was assumed to form an overnight residual layer which was decoupled from the ongoing surface emissions and deposition processes. During the second day, surface emissions were continuously injected into the domain while precursors were either removed as mixed heights decreased or entrained, from the residual layer, as mixed heights increased. At the end of the second day, the concentration field at 1600 was used as the new residual layer concentration. This process was repeated for five days at which time the final 1600 concentration field was assumed to represent the build up of pollutants in the boundary layer. Throughout the simulation, concentrations outside of the domain were fixed at the background ambient concentration.

Unfortunately, choice of background concentrations, used to start the pollutant build up, affected the steady state residual layer concentrations (and as explained in the next section, also the initial surface concentrations) which in turn influenced final ozone concentrations. Steady state NO<sub>x</sub> concentrations were less sensitive to the initial ambient value than VOC concentrations, and so for simplicity, were set at 0 ppb<sup>5</sup>.

The resulting NO<sub>x</sub> boundary layer concentrations had a domain wide average of 4.3 ppb (consistent with rural locations (National Research Council, 1991)), an urban average of 30 ppb (consistent with observed surface concentrations and tethered balloon observations during Pacific '93 (Pisano et al., 1997) and with observations from other North American cities (National Research Council, 1991)) and maximum of 82 ppb (found over the urban area).

Ambient VOC concentrations were chosen so the resulting residual layer concentrations were comparable with previous observations and the resulting maximum ozone concentration was consistent with the maximum observed on the 10<sup>th</sup> of August. Setting the ambient level at 70 ppbC, the corresponding VOC residual layer concentrations showed a domain-average of 89 ppbC, an urban average of 159 and maximum of 316 (also found over the urban area). The urban average compares favourably with measurements taken in Vancouver, between 1989 and 1994, that show average VOC concentrations in the range of 70 to 440 ppbC (Pryor, 1998). They are also consistent with

<sup>5</sup>Typical isolate rural sites in North America have ambient NO<sub>x</sub> concentrations between 0 and 2 ppb (National Research Council, 1991).

speciated hydrocarbon measurements taken between 1990 and 1996 (Greater Vancouver Regional District, 1999).

The ambient NO<sub>x</sub> value 0 ppb and VOC value of 70 ppb may not represent true summertime LFV ambient concentrations and some of the processes leading to pollutant carry-over, not captured by the simple simulations, may be incorporated into these values.

### 9.11.2 Initial Surface Concentrations

Initial surface ozone concentrations were set to 25 ppb, typical of background values measured at Environment Canada's CAPMoN station on Saturna Island B.C. (Vingarzan, 2004). Initial surface VOC and NO<sub>x</sub> concentrations were set to the 0500 concentration fields from the five day preconditioning simulations. Calculated initial NO<sub>x</sub> concentrations compared well with the 0500 August 10<sup>th</sup> observations from the monitoring network. At the Kitsilano, Langley and Hope stations, calculated values were: 53, 28 and 9 ppb while measured values were: 83, 28 and 11 ppb. No comparable measurements were available for VOC concentrations.

## 9.12 Developing WEX parameters

Finally, to include photochemistry, a series of OZIPR runs was performed using the LFV speciation of Jiang et al. (1997b) and the modified COND2243 chemical mechanism (Jiang et al., 1997a) for an August 10<sup>th</sup> day in Vancouver starting at 0500 PST and ending at 1800 PST. Smog chamber simulations were performed at constant temperatures of: 15, 20, 25 and 30°C, with initial NO<sub>x</sub> concentrations ranging from 0 to 30 ppb and a VOC concentrations ranging from 0 to 400 ppbC. All simulations included an initial background of 25 ppb ozone and were without deposition or dilution. To calculate the WEX parameters, the background ozone concentration was removed from the final ozone concentration before performing the scaling analysis. The resulting parameterization for ozone concentration (in ppm) was:

$$[O_3] = (j_{av}/k_{NO}) \Theta(T)^b \left( \frac{[NOx]_{eff}}{j_{av}/k_{NO}} \right)^a \gamma f(R) + 0.025 \quad (9.4)$$

where

$$f(R) = 1 - \exp \left\{ -\lambda \left( \frac{R}{\beta} \right)^{\alpha(R)} \right\}$$

$$\text{and } \alpha(R) = \frac{\alpha_2 - \alpha_1}{2} \tanh(R - \beta) + \frac{\alpha_1 + \alpha_2}{2} \quad (9.5)$$

Parameter	Value
$\gamma$	10.0
a	0.81
$\alpha_1$	2.1
$\alpha_2$	0.66
$\beta$	11.3
$\lambda$	0.76
b	7.6

Table 9.4: WEX parameters used in the LFV photochemical simulations.

is the WEX parameterization and  $\Theta(T)$  is the dimensionless group that controls for temperature:

$$\Theta(T) = \exp \left[ -\frac{E_{OH}}{k} \left( \frac{1}{T_{avg} + 273} - \frac{1}{T_{ref}} \right) \right] \quad (9.6)$$

and  $E_{OH}/k = 504 \text{ K}$

Table 9.4 lists the resulting parameters values.

Up to now, the WEX parameterization has relied on all precursors being initially well mixed at the start of a simulation. To account for the initial concentrations and emissions throughout the day, effective initial precursor concentrations ( $[NOx]_{eff}$ ,  $[VOC]_{eff}$ ) were calculated. These were found by first determining NOx and VOC concentrations at each hour, without any chemistry, and weighting them against the actinic flux to which they were exposed. For example the effective NOx concentration was given by:

$$[NOx]_{eff} = \frac{1}{t_{end} - t_{start}} \frac{\int_{t_{start}}^{t_{end}} [NOx](t) \cdot j(t) dt}{\int_{t_{start}}^{t_{end}} j(t) dt} \quad (9.7)$$

This is slightly different from the approach used by Venkatram et al. (1994) with his species age, where his weighting function is simply  $t$  and not  $j(t)$ .

### 9.13 Predicted Ozone Concentrations

The resulting ozone plume based on the trajectories, mixing heights, emissions and WEX parameterization is given in Figure 9.14. In order to highlight plume shape, only isopleths starting at 52 ppb (and increasing in 10 ppb increments) are given. The resulting plume is centered between Chilliwack and Hope with maximum of 81 ppb. This can be compared with the observed plume, found by interpolating observations from 20 measuring stations and corner values arbitrarily set to background, with maximum of 82 ppb. A few observations:

- While background concentrations were adjusted to give the correct ozone maximum, no considerations were made for the location of the maximum and general plume structure. Nonetheless,

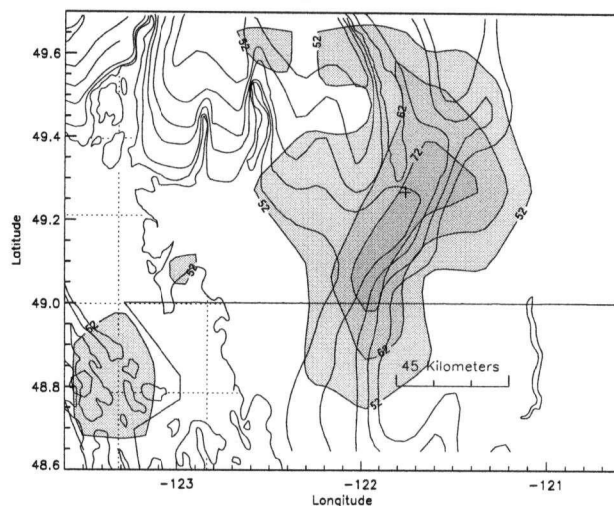


Figure 9.14: Predicted ozone concentrations (in ppb) at 1800 PST based on simple model. Unshaded contours give elevation above sea-level in 200 m intervals.

the predicted plume produces its maximum in the upper valley close to the observed maximum at Hope (T29) but produces a 72-ppb isopleth which extends further south.

- The predicted 52 ppb isopleth covers a much larger area than is observed. Some of the discrepancies are likely due to the lack of measuring stations in the North-South direction. Despite the differences in size, the plume centroids are within 12 km of one another.
- The predicted plume identifies the Gulf Islands as a location where ozone values are above 52 ppb. This feature is consistent with modeling studies (Jiang et al., 1998) and is an area of current research (Snyder, 2002).

## 9.14 Temporal Behaviour

Finally in Figure 9.16, I have plotted predicted and observed ozone concentrations, between the hours 0600 and 1800, for six measuring stations in the LFV. Included in each figure are the NAAQO thresholds of 52 and 82 ppb. In general, the model gives the correct temporal pattern with low morning ozone concentrations that rise throughout the day before peaking in late afternoon. The maximum station reading was 82 ppb at Hope (T29), which the model did not correctly predict.

<sup>6</sup> Furthermore, the model shows the more easterly stations have their peak value occurring later

<sup>6</sup>While the maximum station reading was 82, due to the sparse nature of the data, the maximum interpolated value was 77.1. Likewise, the maximum WEX calculated value was 81 but when interpolated it was only 78.

in the day, consistent with observations (Pryor and Steyn, 1995). The model misses the observed low morning ozone concentrations which are likely caused by deposition and ozone titration from nighttime emissions.

For the westerly stations of Kitsilano (T2), Rocky Point Park (T9) and Surrey East (T15), peak ozone concentrations are low: station T2 does not exceed 52 ppb while T9 and T15 barely do. The model captures these lower maxima and correctly predicts the non-exceedance at T2 but incorrectly predicts non-exceedances at T9 and T15. For the easterly stations, the model correctly predicts the higher maxima at Hope (T29), Abbotsford (T28) and Chilliwack (T12) but, again, does not catch the exceedance at Hope.

An unexpected feature of the model is the slight drop in ozone concentrations following the late afternoon peak. Interestingly, each box model can only predict a monotonic increase in ozone concentration because of the scaling with cumulative actinic flux. Modeled decreases arise from the complex patterns traced by the back trajectories each hour. This realism suggests most of the important processes leading to ozone production in the LFV are captured by the simple model.

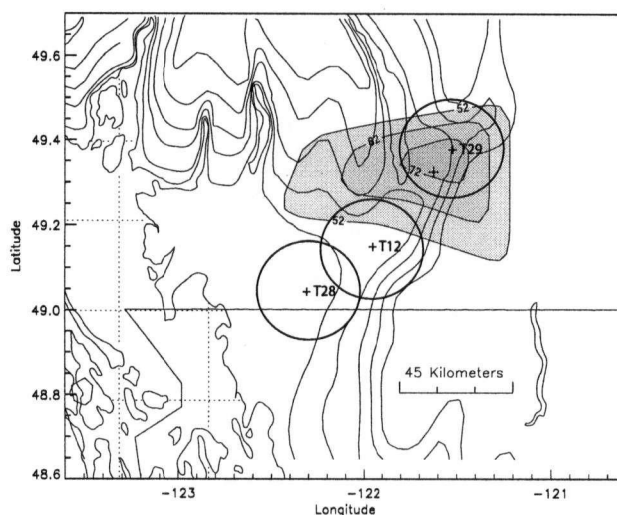


Figure 9.15: Observed ozone concentrations (in ppb) at 1800 on August 10<sup>th</sup>. Concentrations over mountainous regions are uncertain and may be quite different to interpolated values shown by isopleths. Unshaded contours give elevation above sea-level in 200 m intervals. To highlight plume uncertainty away from the valley, the three most easterly measurement stations (Hope (T29), Chilliwack (T12) and Abbotsford (T28)) are marked with a 20 km radii of influence surrounding each.

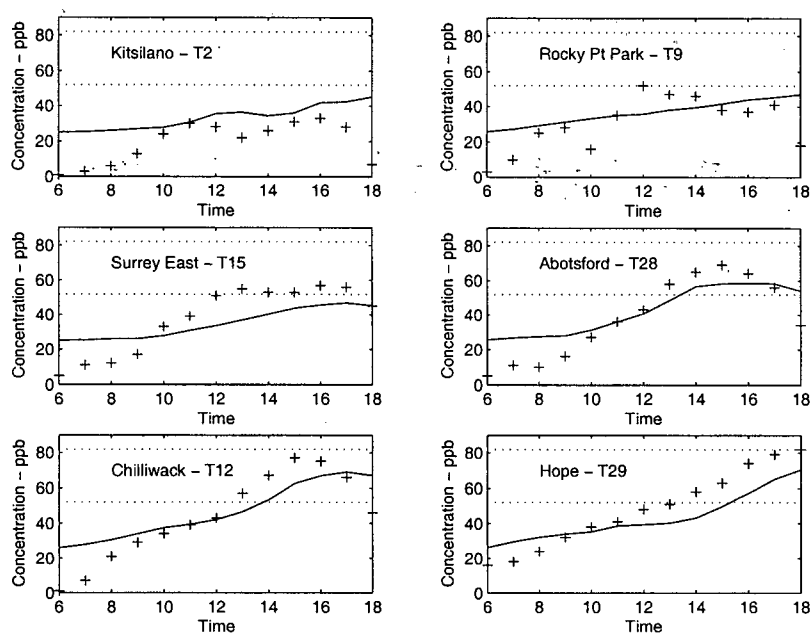


Figure 9.16: Predicted and observed (+) ozone concentrations (in ppb) between 0600 and 1800 PST at various stations on August 10<sup>th</sup> 2001.

## 9.15 Conclusions

In PART I, I studied the internal properties of the WEX model while in this Chapter I have taken a step back and shown the WEX parameterization can be applied in an air quality model. Specifically, an integrated ozone model has been developed that incorporates: a simple slab model for mixing heights, back trajectories based on interpolated wind fields, photochemistry based on the WEX model and an emissions inventory based on a simple scaling of published emissions totals. The model captures the spatial and temporal structure of an ozone plume for an episode occurring on August 10<sup>th</sup>, 2001 in the LFV, B.C. The model is sensitive to ambient precursor concentrations determined from a series of boundary layer pre-conditioning simulations. As a result, the list of properties and processes needed to characterize the essential features of ozone formation in the LFV should include:

- The effects of precursor build up on background concentrations via the storage and release of pollutants from elevated pollutant layers.

While the simple methods used to account for pollutant build-up neglect and simplify many processes, in the next chapter I show, through a series of sensitivity studies, the model reproduces the plume's sensitivity to environmental conditions and precursor concentrations and, as such,

provides a useful approximation to the complex ozone response surface.

## Chapter 10

# Model Results and Discussion

The underlying theme in this thesis can be expressed by the two questions introduced in the preface:

- How much detail is necessary to capture ozone sensitivity to VOC and NO<sub>x</sub> emissions in a particular region?
- Given that a model is only as strong as its weakest link, what level of detail is justified in each modeling component?

In response to these questions, I contend my integrated model describes photochemistry, meteorology and emissions to comparable levels of detail and, together, the integrated model captures, to first order, the LFV's sensitivity to VOC and NO<sub>x</sub> emissions.

To support these assertions, I suggest the WEX parameterization of ozone's non-linear dependence on precursors and environmental conditions, given in Chapters 3 and 4, shows ozone photochemistry has been modeled to at least first order and that the analysis in Chapter 9 (and Appendix G) indicate spatial and temporal emissions fields have also been well characterized. In the first part of this chapter I demonstrate, by means of a series of sensitivity studies, that meteorological processes have been adequately modeled. The last part of this chapter addresses the model sensitivity to VOC and NO<sub>x</sub> emissions. Model validation is not checked using quantitative point by point comparisons of predicted versus observed ozone concentrations, but rather through a series of higher level sensitivity analyses that draws on results obtained through a variety of different modeling techniques.

### 10.1 Sensitivity to Meteorological Parameters

Many studies of ground level ozone in the LFV have identified key meteorological processes influencing ozone formation (Taylor (1992), Robeson and Steyn (1990), Pryor and Steyn (1995) and McKendry (1994)). These are nicely summarized in the classification and regression tree statistical analysis (CART) by Burrows et al. (1995) which I adopt as a framework for a series of sensitivity studies used to demonstrate the modeled ozone plume responds to changes in key meteorological

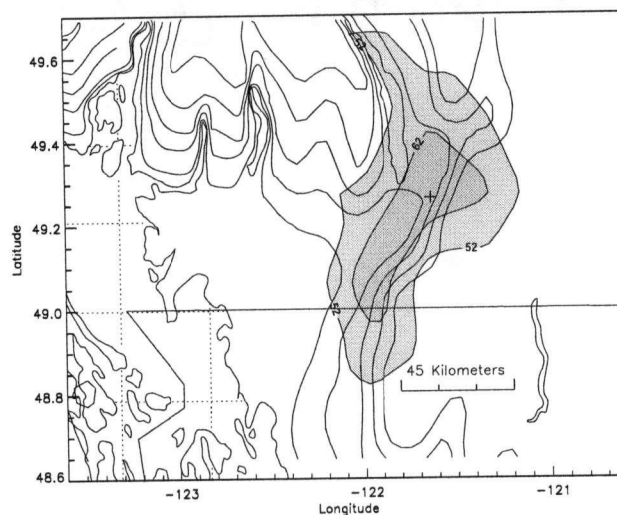


Figure 10.1: *Modeled surface ozone concentrations (in ppb) after decreasing interpolated August 10<sup>th</sup> temperatures 5°C. Unshaded contours give elevation above sea-level in 200 m intervals.*

parameters in a consistent and expected way. From this, I indirectly infer meteorological processes are handled to a sufficient degree of faithfulness for use in the integrated model.

While the CART analysis starts with a database of 57 separate predictors, only a small subset of these are needed to predict future ozone concentrations at five LFV sites (see Appendix I for a reproduction of the LFV CART regression tree) and consistent with other statistical approaches (Robeson and Steyn (1990) and Taylor (1992)), the single most important CART predictor is maximum surface temperature.

### 10.1.1 Temperature

In the CART decision tree, high ozone concentrations are effectively isolated from low values by two nodes, both depending on Abbotsford's maximum temperature: the first requires temperatures above 24.7°C, while the second requires temperatures in excess of 29.8°C. This suggests the modeled ozone plume should be responsive to temperature perturbations on the order of 5°C. The August 10<sup>th</sup> Abbotsford maximum temperature was 30.5°C, above the 29.8°C threshold, so the model was rerun with all temperatures 5.0°C cooler.

Figure 10.1 shows the resulting plume after the temperature reduction. Comparison with the baseline plume (Figure 9.14) shows the new plume has a greatly reduced area exceeding 52 ppb but the plume centroid remains in almost the same location. The general shape of the plume has not changed, even though concentrations drop by 10 ppb on average, because the simple temperature

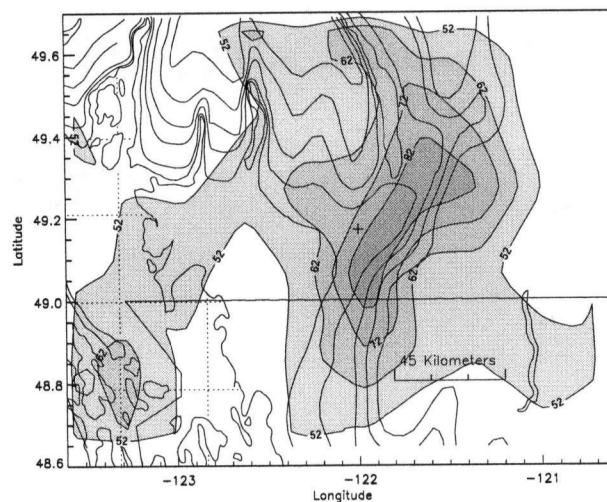


Figure 10.2: Modeled surface ozone concentrations (in ppb) after increasing interpolated August 10<sup>th</sup> temperatures 5°C. Unshaded contours give elevation above sea-level in 200 m intervals.

scaling in Eq. (9.6) gives rise to constant proportional changes in peak ozone concentrations. While the CART analysis predicts greater sensitivities, it must be acknowledged that a 5°C temperature change would likely occur in combination with synoptic and meso-scale changes (i.e. pressure gradient, mixing heights, etc.) also likely to influence surface ozone concentrations, and so the CART sensitivity represents an upper bound. A more thorough analysis would require recalculating mixing heights, using the new temperature fields, before determining ozone concentrations.

For completeness, the effects of a 5.0°C temperature increase are given in Figure 10.2. In this case, concentrations in almost the entire upper-valley exceed 82 ppb while the 52-ppb centroid has only shifted 6 km southward. The core of the plume has a roughly 10 ppb increase in peak concentrations and the 72- and 82-ppb isopleths have almost identical shapes and positions as the baseline 62- and 72-ppb isopleths.

### 10.1.2 Residual layer concentrations

The next major determinant in the CART decision tree (along the branch leading to the higher concentrations) is the previous day's ozone concentrations, suggesting pollutant carry over from one day to another is an important process in the LFV. I must point out that while McKendry (1994) and Pryor et al. (1999) show exceedances in the LFV are typically single day events closely tied to synoptic scale meteorological conditions, this does not contradict the CART analysis. Rather, it suggests episodes require a few days to build and, on average, just reach exceedance levels before synoptic conditions change. This conclusion is consistent with the boundary layer pre-conditioning

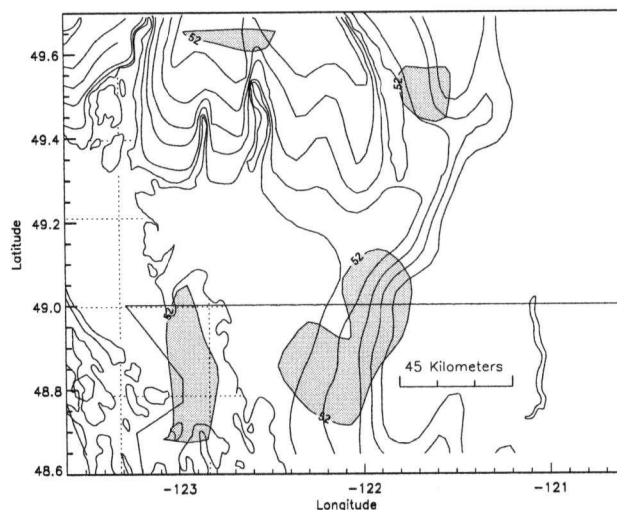


Figure 10.3: Modeled surface ozone concentrations (in ppb) using a clean residual layer. Unshaded contours give elevation above sea-level in 200 m intervals

simulations used to account for pollutant carry prior to the modeling day. Figure 10.3 shows the effects of using clean boundary layer concentrations ( $[VOC]_o = 17$  ppb and  $[NOx]_o = 2$  ppb), both at the surface and aloft, on the baseline ozone plume. These values were used by Hedley et al. (1997) to initialize their MC2-CALGRID runs in the LFV.

The main plume has disappeared completely and in its place four separate plumes, with peaks just over 52 ppb, appear: over the Cascades and Coast mountains, the southern edge of Harrison Lake and over the southern reach of the Strait of Georgia. Such a dramatic change in the shape and intensity of the ozone plume shows the central importance of pollutant build up in this model. While it is difficult to determine if actual ozone formation is as strongly dependent on pollutant carry over as these results suggests, the shape of the ozone plume invites comparisons with model output from an MC2-CALGRID simulation for a July 1985 episode (Hedley et al., 1995). Their results, reproduced in Figure 10.4, show separate maxima (albeit at much higher concentrations) predicted over the Cascades and Coast mountains (with a third maximum over the Southern Gulf Islands). Jiang et al. (1998) note that additional modeling using SAIMM/UAM-V produce similar results and agreement between models is better than with observations. They suggest the models are being systematically influenced by unknown processes. It is interesting to speculate if pollutant carryover and mixed layer/free troposphere handover mechanisms are the unknown processes.

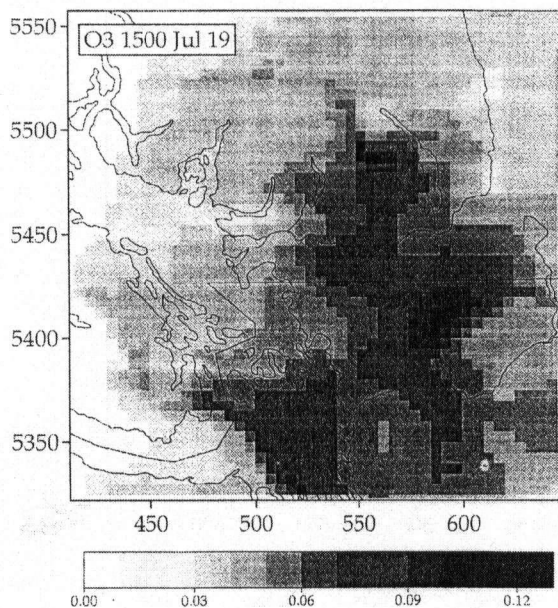


Figure 10.4: Modeled surface ozone concentrations (in ppm) at 1500 PST July 19<sup>th</sup> using the MC2-CALGRID modeling system. (From (Hedley et al., 1995))

### 10.1.3 Actinic Flux

The next level of branching on the CART decision tree involves the Julian day of the year – episodes occurring before August 27<sup>th</sup> generally lead to higher concentrations than those occurring later on. To test model response to actinic flux, OZIPR simulations were run for a September 10<sup>th</sup> day<sup>1</sup>, new WEX parameters were found and used in the integrated model while keeping mixing heights, trajectories and emissions unchanged. The resulting plume, shown in Figure 10.5, is shifted slightly north-eastward about 11 km while peak ozone concentrations have dropped by about 10 ppb.

This simple simulation suggests mid-summer episodes produce higher ozone concentrations than late or early summer ones (assuming temperature, mixing heights and winds are unchanged). Of special interest in this regard is the region's highest recorded 1-hour ozone reading of 212 ppb on September 3 1988. Steyn et al. (1999) show the meteorology of this episode to be identical to a 105-ppb July 1998 event; arguing the difference in peak concentrations can only be explained by emissions reductions in the intervening years. Their analysis did not consider the effects of reduced actinic flux and, as a result, my analysis suggests measured emissions reduction must have had an

<sup>1</sup>This represents a 14% drop in the total cumulative  $NO_2$  photolysis rate over the 0500 to 1800 trajectory travel time.

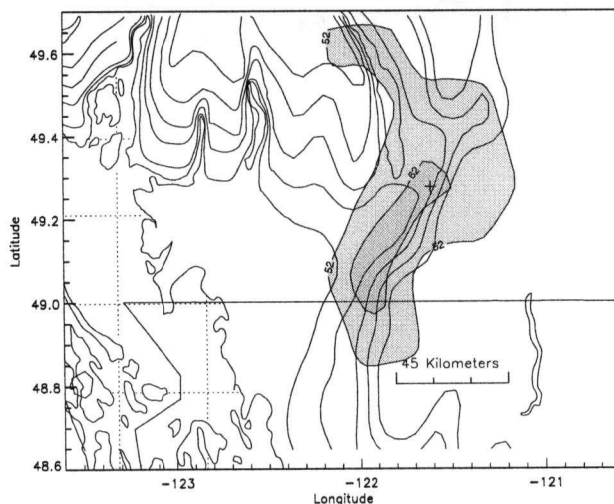


Figure 10.5: *Modeled surface ozone concentrations (in ppb) using actinic fluxes appropriate for a September 10<sup>th</sup> day. Unshaded contours give elevation above sea-level in 200 m intervals*

even greater influence on reducing peak ozone concentrations.

#### 10.1.4 Wind Fields

I now examine the influence of the wind fields on the ozone plume. The CART analysis shows wind speed and Vancouver-Hope pressure gradient<sup>2</sup> as predictors of high ozone conditions. In this section, I see how the model responds to increased wind speeds and in the next section to slight differences in wind direction through the use of different back trajectories.

To test model sensitivity to increased ventilation, a simulation was run with wind speeds increased by a factor of 1.5 and wind direction unchanged. Assuming the sea-breeze strength on August 10<sup>th</sup> is typical, then a 1.5× increase represents a little more than a one standard deviation departure from average conditions (based on the observed range of wind speeds during sea-breeze conditions in the LFV (Steyn, 1998)). The new wind fields were used to calculate new back trajectories, mixing heights, initial and residual layer concentrations. Figure 10.6 shows an eastward shifted plume, of reduced concentrations, consistent with increased venting by a strengthened sea-breeze. The second plume, on the western edge of the modeling domain, is likely caused by increased venting of pollutants from strengthened nighttime westerly winds.

<sup>2</sup>This is essentially a surrogate for wind speed. A positive Hope-Vancouver pressure gradient (often caused by a thermal trough lying along the coast) interferes with sea-breeze development, reducing inland penetration of clean Pacific air. Conversely, a negative gradient assists the sea-breeze and its associated flushing.

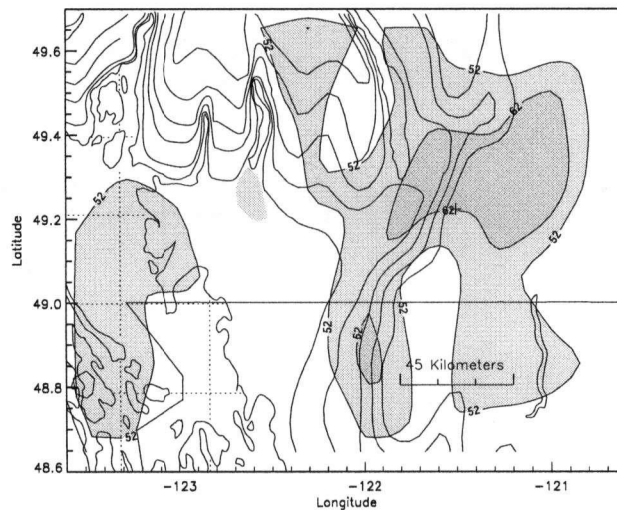


Figure 10.6: Ozone plume (in ppb) resulting from a  $1.5\times$  increasing in wind speed. Unshaded contours give elevation above sea-level in 200 m intervals

### 10.1.5 Back Trajectories

I examined model sensitivity to back trajectories by replacing trajectories from the interpolated wind fields with those developed from the MC2 wind fields. Unlike the previous sensitivity analyses where plume response to changing meteorological conditions was expected, in this case if back trajectories developed from the interpolated wind fields adequately describe the transportation processes, then the use of new trajectories, drawn from a different model but based on the same underlying meteorological conditions, should leave the final ozone plume unchanged.

Section 9.6 showed the trajectories were in greatest disagreement over the ocean and mountains. However, figures 9.10 and 9.11 show these areas to be largely free of emissions, hinting these discrepancies might have limited influence on the resulting plume. Figure 10.7 suggests this is the case, showing the 72-ppb isopleth to be in almost position, have a similar shape and cover only a slightly smaller area when compared with the baseline plume (Figure 9.14). The MC2 trajectory-based plume has the 52-ppb isopleth covering almost all of the Coast Mountains and the secondary Gulf Island plume shifted further eastward.

### 10.1.6 Mixing Depths

As a final test, model sensitivity to mixing heights was explored by substituting MC2 derived values in place of those based on Eq. (9.2). In addition, MC2 trajectories were used with new residual layer and initial concentrations calculated. Section 9.7.1 shows a large discrepancy between the

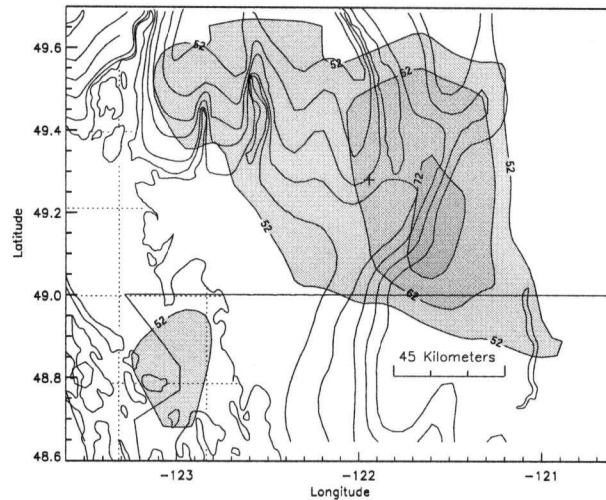


Figure 10.7: Ozone concentrations (in ppb) using MC2-based trajectories. Unshaded contours give elevation above sea-level in 200 m intervals

two models with MC2 generally predicting larger values of mixing heights. Ignoring entrainment, simple ventilation indices, showing concentrations inversely proportional to wind speed and mixing depth, would suggest the large mixing heights will produce lower precursor concentrations (and indirectly lower ozone concentrations). Figure 10.8 shows the 72-ppb isopleth has almost completely disappeared but the 52-ppb centroid is largely unmoved. I suspect the limited sensitivity arises from the model's dependence on polluted residual layers which allow a growing boundary layer to entrain precursors at a rate that almost compensates for dilution from increased volume. While this process may not be unrealistic, its importance appears to be exaggerated giving the model an unrealistic insensitivity to mixing depths.

Finally, on Figure 10.8 a second 62-ppb isopleth appears over the western edge of the coast mountains. Trajectory comparison shows the new plume is produced by trajectories that pass over the Strait before being carried upslope and that the MC2 trajectories remain over forested areas longer, receive additional VOC emissions which they use to process marine NO<sub>x</sub> emissions into higher ozone concentrations.

This secondary, off-valley peak raises an interesting question about the proper plume shape and the simple methods which I am using to characterize it. In principle, MC2 should handle local influences of terrain and micro-meteorology, in sparsely monitored areas, on the wind fields better than the interpolation procedures. As a result, it is possible the new maximum over the Coast mountains arises from this increased resolution of local conditions. Additional off-valley maximum, as observed by McKendry et al. (1998b) and modeled by Hedley et al. (1995), may

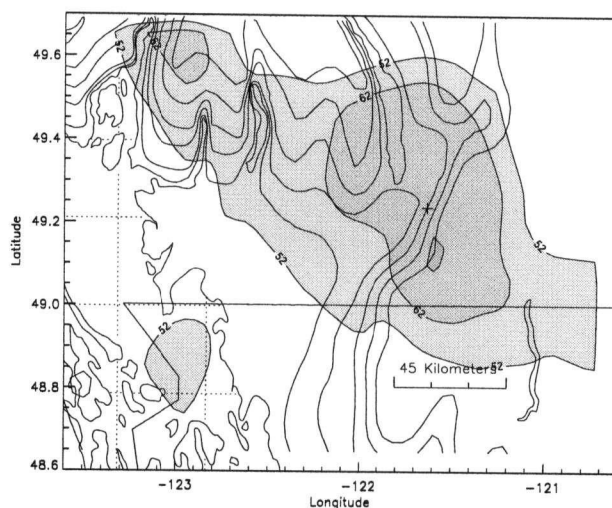


Figure 10.8: *Ozone concentrations (in ppb) using MC2-based trajectories and mixing heights. Unshaded contours give elevation above sea-level in 200 m intervals*

have also occurred on August 10<sup>th</sup> but these peaks are not being resolved, even by the MC2 based trajectories, because they are driven by transport processes occurring in tributary valleys too narrow for the box models. It is of great interest to see if a detailed chemical mechanism, when coupled to the MC2 output, produces additional off-valley maxima.

Based on the sensitivity tests, it is difficult to judge the model's ability to capture all the first order meteorological processes. Its sensitivity to temperature, actinic flux and wind speed appear correct. Furthermore, it is not overly sensitive to the specifics of the back trajectories. However, it is extremely sensitive to residual layer concentrations and, as a result, not too sensitive to mixing heights. I present some ideas that might improve this dependence in the discussion section.

## 10.2 Sensitivity to Emissions

I now explore the model's sensitivity to VOC and NO<sub>x</sub> emissions. First I test the model using previous emissions levels and show the resulting plume, which is shifted westward with higher peak value, is consistent with observations and previous studies. Next, I estimate future ozone concentrations based on expected emissions reductions before using the model to develop domain wide ozone isopleths.

### 10.2.1 Backcast emissions for 1985

Since 1985, the region's VOC emission have decreased by a factor of 1.6 and NO<sub>x</sub> emission by a factor of 1.15 (Greater Vancouver Regional District, 2003b) and peak summertime ozone concentrations have declined (Vingarzan and Taylor, 2003). Furthermore, Joe et al. (1996) show while peak ozone concentrations dropped at Rocky Point Park (T9) between 1978 and 1990, they increased at Abbotsford (T28), concluding the plume has generally shifted eastward in response to increased development up-valley. A simulation was run using 1985 emissions levels to see if the simple model develops an ozone plume having both a higher peak concentration and a westward shift. A simple scaling of all anthropogenic VOC (by 1.60) and NO<sub>x</sub> emissions (by 1.15) was used to reproduce the 1985 inventory and no attempt was made to change the spatial allocation of the emissions nor was the speciation changed. No changes were made to the biogenic emissions, back trajectories or mixing depths. Figure 10.9 shows the resulting ozone plume. The peak ozone concentration has increased to 90 ppb with a large portion of the upper valley in excess of 82 ppb. The centroid of the 52 ppb isopleth has moved westward roughly 20 km.

While the 20 km westward shift and 9 ppb increase in peak concentrations are consistent with observations, they are likely conservative results. Observations and analysis by Burrows et al. (1995), Joe et al. (1996), B.C. Ministry of Environment and Parks (1998), Steyn et al. (1999) and Vingarzan and Taylor (2003) would suggest a plume further west with higher ozone concentrations (assuming meteorology of August 10<sup>th</sup> is typical of episode conditions both then and now). Allocating emissions further westward to reflect 1985 development patterns might improve estimates of plume location and peak.

### 10.2.2 Future scenario under Tier 2 automotive standards

The LFV's primary source of anthropogenic emissions both VOC and NO<sub>x</sub> is LDV (Greater Vancouver Regional District, 2002). As of 2004, new federal LDV emission standards (called Tier 2) are expected to bring significant emissions reductions relative to the current (Tier 1) standards (National Research Council, 2000). These standards are both more stringent (i.e. they require lower emissions over the test cycle) and far reaching (i.e. they apply to all LDV regardless of weight) and are expected to greatly reduce total LDV emissions in the LFV (Dr. Robert Caton, personal communication). I have used the simple model to explore the consequences of Tier 2 vehicle standards on ground level ozone in the LFV. Because of the slow turnover rate of cars in the LFV <sup>3</sup>,

<sup>3</sup>The average age of a light duty gasoline powered vehicle in the LFV is almost 9 years (Greater Vancouver Regional District, 2003b)

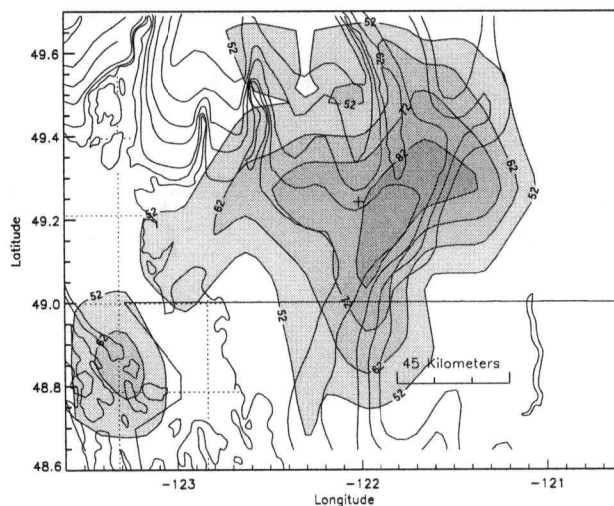


Figure 10.9: Ozone concentrations (in ppb) based on 1985 emissions levels. Unshaded contours give elevation above sea-level in 200 m intervals.

and the disproportionate influence older cars have on emissions totals (Sawyer et al., 2000), it is not expected that Tier 2 standards will significantly influence LDV emissions for a decade. However, to see the effect these standards would have on present ozone levels, I used projected LDV emissions for 2015 along with year 2000 emissions for all remaining sources. The model predicts the plume to remain essentially unchanged in position and concentration (Figure 10.10) even though LDV VOC and NO<sub>x</sub> emissions are expected to be 26% and 12% of present levels respectively (Dr. Caton, personal communication). These reductions translate in a 27% decrease in both anthropogenic VOC and anthropogenic NO<sub>x</sub> emissions. But due to the ubiquitous nature of cars, VOC and NO<sub>x</sub> emissions decrease proportionally over most areas, and the simple WEX scaling then leaves the plume in roughly the same location. Furthermore, emissions in the valley are not dominated by vehicles to the same extent as over the urban areas, so the LDV reductions have a smaller influence on the peak producing trajectories which in the case studied, mostly pass over the non-urban parts of the valley.

### 10.2.3 Speciation

To test the influence of VOC speciation on the ozone plume, a speciation based on the SMOKE emissions inventory was used. First, new WEX parameters were determined from OZIPR simulations using the CB-IV mechanism (Gery et al., 1989) and the new speciation. Modeled ozone concentrations using the new WEX parameters are given in Figure 10.11. All concentrations are greatly reduced (only a small area lies above 52 ppb), higher concentrations are found over the

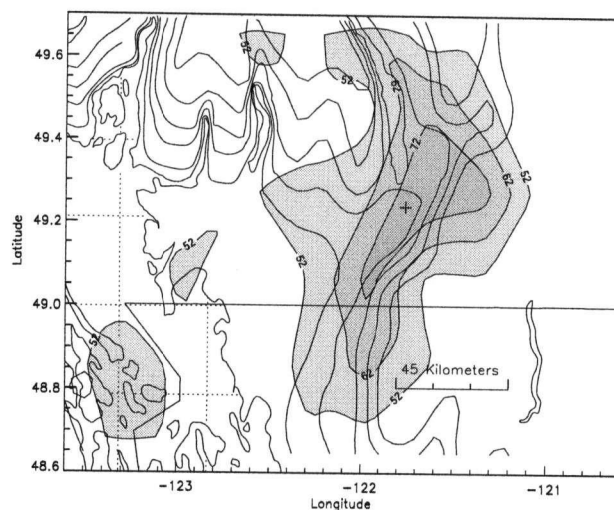


Figure 10.10: *Ozone concentrations (in ppb) based on projected future Tier 2 LDV emission standards. Unshaded contours give elevation above sea-level in 200 m intervals.*

Cascade and Coast mountains with a trough of lower concentrations lying along the valley. Although this spatial pattern is similar to the NRC results (Figure 10.4), there are two reasons why I do not think it implies an underestimation of VOC reactivity on their (NRC) part. First, I use their same speciation in my model (that is, I use their domain average speciation for all emission sources whereas they use different speciations for each source) and secondly, as mentioned before, it is believed that the VOC speciation based on the inventory is in good agreement with observations (Jaing et al., 1997). A more likely explanation for similarity between Figures 10.11 and 10.4 is either an excess of NO<sub>x</sub> emissions or deficiency in VOC emissions in the NRC modeling. Conceptually, either case (or both) lead to low  $R$  values. For the SMOKE speciation, the large proportion of non-reactive VOCs leads to a large  $\beta$  value. Since ozone concentrations scale with  $R/\beta$  the higher  $\beta$  value from the SMOKE speciation would give similar results to simulations using an inventory having high NO<sub>x</sub> to VOC ratios (i.e. low  $R$ -values).

### 10.3 LFV Ozone Isoleths

To ascertain the region's sensitivity to emissions, I performed a large number of simulations systematically varying anthropogenic VOC and NO<sub>x</sub> emissions. Guided by inventory forecasts and backcasts (Greater Vancouver Regional District, 2003b) VOC and NO<sub>x</sub> emissions were independently varied from 1.7 to 0.2 times their current levels in 10% increments for a total of 225 simulations. To include the influence of emission levels on initial and residual layer concentrations, a library of

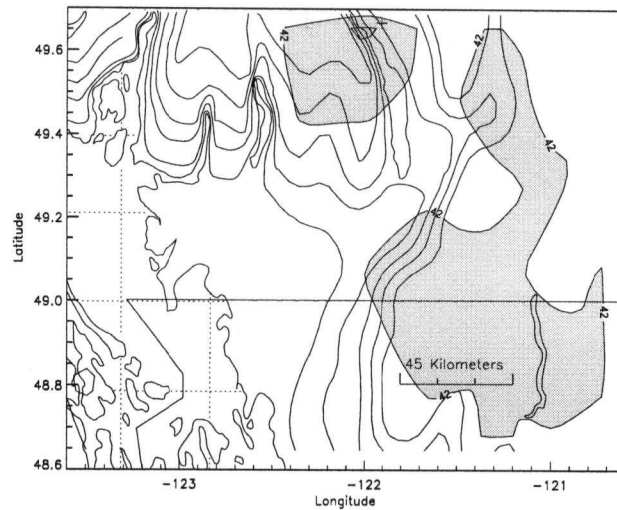


Figure 10.11: Ozone concentrations (in ppb) using WEX parameters based on SMOKE speciation. Unshaded contours give elevation above sea-level in 200 m intervals.

initial and residual layer concentrations was developed through a set of four preliminary simulations. In each simulation, emissions at one of four levels (1.5, 1.0, 0.5 or 0.2 times 2000 anthropogenic emission rates) were continuously released into an initial clean environment and advecting for a three day pre-conditioning period. The resulting library consisted of the 0500 (for the initial concentrations) and 1600 (for the residual layer) concentrations from the preliminary simulations. For each of the 225 sensitivity simulations, initial and residual layer concentrations were found from the library values through an interpolation based on that simulation's emission levels.

Figure 10.12 shows the resulting isopleths of maximum ozone concentration as a function of year 2000 anthropogenic VOC and NO<sub>x</sub> emissions. Also located on the figure are inventory estimates (Greater Vancouver Regional District, 2003b) for the years 1985 to 2020 in 5 year increments. The plot shows that since 1985, VOC emissions have been more effectively reduced than NO<sub>x</sub> (likely due to early hydrocarbon based LDV emissions controls and closure of two refineries in the LFV) and that projected emission controls target VOC and NO<sub>x</sub> emissions equally.

The figure suggests peak ozone concentrations were higher in the past<sup>4</sup> consistent with analysis of LFV ambient data over those same years (Vingarzan and Taylor, 2003). From the figure, the region appears to be VOC-limited and was closer to ridgeline in the late 1980's. Furthermore, the figure suggests projected emissions levels do not offer further reductions in peak ozone concentrations and unexpected reductions in NO<sub>x</sub> emissions could lead to increased ozone concentrations. While

<sup>4</sup>More precisely, it suggests if the August 10<sup>th</sup> meteorology were to repeat itself, higher ozone concentrations would have occurred.

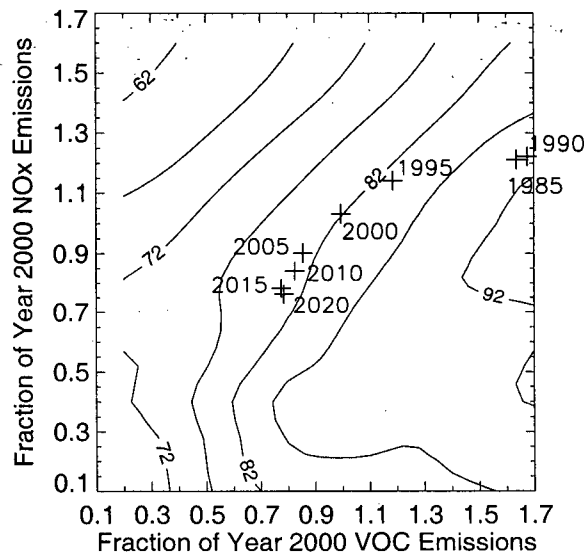


Figure 10.12: *Region wide ozone isopleths (in ppb) as a function of anthropogenic VOC and NO<sub>x</sub> emissions. Also included are maximum ozone concentrations for years: 1985, 1990, 1995, 2000, 2005, 2010, 2015 and 2020 based on forecasted and backcasted emissions inventories (Greater Vancouver Regional District, 2003b).*

this NO<sub>x</sub>-inhibition effect is well known, the latest emissions inventory carelessly lumps total VOC, NO<sub>x</sub>, PM<sub>2.5</sub>, SO<sub>x</sub> and NH<sub>3</sub> emissions into a single ‘smog forming’ pollutant category (Greater Vancouver Regional District, 2002). They project decreases in LDV ‘smog forming’ pollutants to be partially offset by increases in marine emissions, solvent evaporation and agricultural emissions. Given that marine emissions are mainly NO<sub>x</sub> and solvent emissions VOCs, future ozone levels might return to late 1980’s levels if the former are reduced instead of the latter.

Jiang et al. (1997a) also find their box model simulation to be VOC limited and based on 1985 emissions levels, ozone concentrations increase with decreasing NO<sub>x</sub> levels until these are below 40% of 1985 levels. The present analysis is consistent with this analysis but finds the transition closer to 60%. A VOC limited regime is also consistent with analysis by (Pryor, 1998). Finally, Pryor and Steyn (1995) show a trend toward higher ozone concentrations on weekends than weekdays. They show ambient NO<sub>x</sub> concentrations are typically higher weekdays whereas VOC concentrations, when scaled by incremental reactivity, are roughly constant. Again, these findings are consistent with a VOC-limited region.

## 10.4 Discussion

Despite realistic appearance of the ozone plume, many qualifications must be stressed. First, all simulations were based on meteorology taken from a single day. While the intent was to examine ozone formation under generic episode conditions, the influence of day to day variation in the local pressure gradient or strength of the sea breeze circulation must be considered. Ideally, episode days would be classified using the synoptic typing developed by McKendry (1994) and composite hourly wind fields for each episode type would be developed based on observations from all days of similar type. These fields would then be used to determine mixing heights and back trajectories. Developing generic wind fields in this manner would be consistent with the present use of measured heat fluxes averaged over sea-breeze days instead of day specific data. The final result would be a set of ozone plumes for variety of episode conditions.

Another shortcoming of the model is its sensitivity to initial and residual layer concentrations. While precursor build up and the presence of elevated pollutant layers during ozone episodes is well documented (Pisano et al. (1997), McKendry et al. (1998a), Hayden et al. (1997) and McKendry et al. (1998b)), the processes leading to the build up are varied and complex (McKendry and Lundgren, 2000) and, with the exception of a few isolated point measurements taken during field campaigns, little data exists on upper level VOC and NO<sub>x</sub> and surface concentrations. Properly incorporating the first order influence of pollutant build up into the model will require further analysis. This must include the effects of night-time chemistry, especially the conversion of NO<sub>2</sub> to N<sub>2</sub>O<sub>5</sub> and subsequent removal via heterogeneous reactions. In addition, the model prescribes both residual layer ozone and NO<sub>x</sub> concentrations but NO titration would greatly reduce ozone concentrations there. Although some of the resulting NO<sub>2</sub> would remain in the residual layer, where it could photolyze and lead to the recreation of NO and ozone, an estimate of NO<sub>x</sub> removal rates in the residual layer must be determined. Lastly, residual layer concentrations were determined from surface layer emissions being advected by the interpolated winds. However, during the night, the decoupling of the SBL from the mixed layer produces winds which vary with height and proper modeling of advection should consider vertically varying wind speed and direction.

As I see it, the final weakness of the model is its reliance on back trajectories. To reduce uncertainties stemming from back trajectories, a diagnostic model like CALMET (Scire et al., 2000), which can account for topography when interpolating wind fields, could be used. Uncertainties from the back trajectories could be removed through the use of the 1-D Eulerian model developed for the initial and residual layer calculations. This calculates transport, entrainment and deposition of precursors over the entire domain at a timescale of minutes. To mesh the Eulerian model with

the WEX chemistry (parameterized over the timescale of a day and not minutes) the species age concept Venkatram et al. (1994) could be used. To do this, I would rerun the Eulerian model tracking, at each time-step and each grid cell, the total actinic flux received by both VOC and NO<sub>x</sub>. Final VOC and NO<sub>x</sub> as well as cumulative actinic flux at each grid cell would then be used by the WEX model to calculate ozone concentrations.

The use of trajectories does have its benefits; they provide a clear (although overly simplistic) link between sources and receptors. For instance, the present analysis suggests the most important air-masses are those ending at mid-valley locations. Back trajectories show these air-masses either start over the Strait of Georgia (based on the MC2 analysis) or east of the city (based on the interpolated fields). In both cases, they do not pass over the city where high NO<sub>x</sub> emissions would inhibit ozone formation. Urban emissions only indirectly influence peak ozone through the build up of pollutants in the residual layer. It is difficult to determine the representativeness of these back trajectories until episodes with different meteorology are investigated. However, observations from a recent episode on June 21<sup>st</sup> 2004 (Figure 10.13) clearly shows the progression of the ozone plume along a path close to that given by the mid-valley back trajectories: the plume appears over Surrey East (T17) at noon, moves up-valley in a northeast direction before reaching a late afternoon maximum value of 87 ppb near Hope (T29).

The source-receptor picture presented by back trajectories also identifies several interesting issues:

- Will marine emissions, expected to increase in the following decades (Greater Vancouver Regional District, 2003b), which are primarily NO<sub>x</sub> sources west of the city, affect future ozone concentrations? <sup>5</sup>
- Or will continued residential development east of the city, couple with increased VOC emissions be a more serious concern?

Properly investigating these issues will require comprehensive Eulerian grid modeling.

Finally, the emissions inventory appears to be the least problematic aspect of the model. At first glance, this seems unexpected; after all, Russell and Dennis (2000) argue emission inventories (with errors up to a factor of three in some cases) are the dominant source of uncertainty in photochemical models. If this is the case, then wouldn't a simple model, using fairly general approximation for this most uncertain component, be further compromised? The answer is no, for the reasons outlined in section 9.8, namely, while the spatial allocation of emissions might be crude, emission totals are

---

<sup>5</sup>Of course, the issue is more complex with additional SO<sub>x</sub> emissions potentially causing higher  $PM_{2.5}$  concentrations.

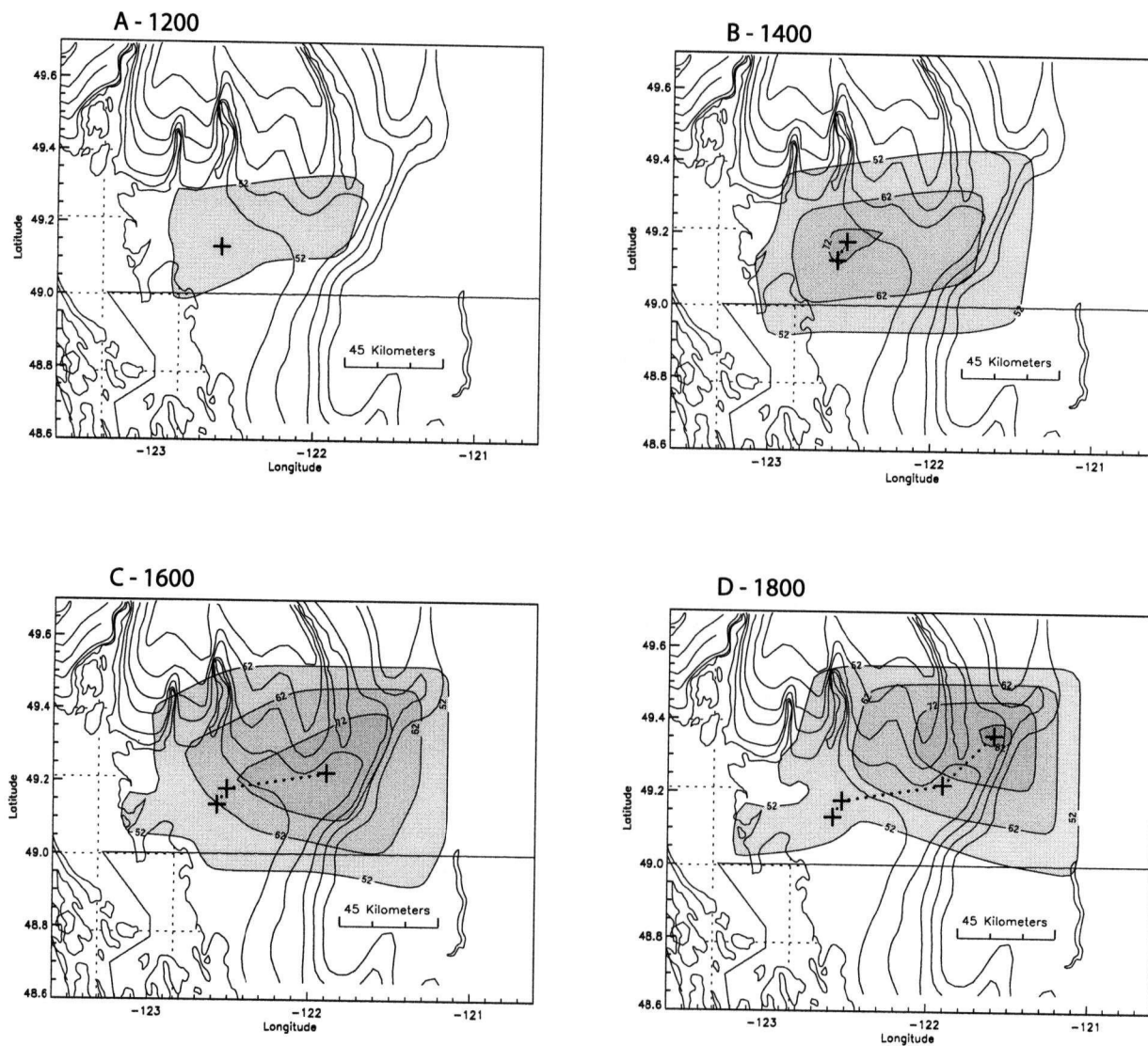


Figure 10.13: Interpolated ozone concentrations (in ppb) in the LFV based on observations at four different times on June 21<sup>st</sup>, 2004. Approximate plume centroid is marked by '+' signs and plume 'trajectory' by the dotted line. Unshaded contours give elevation above sea-level in 200 m intervals.

based on detailed emissions modeling and I believe getting emissions totals correct is more important than knowing precisely their spatial distribution. This hypothesis could easily be checked through a comparison of model output based on the simple inventory and a more detailed one.

## 10.5 Conclusions

The sensitivity analyses for temperature, actinic flux, mixing heights and wind speeds suggest meteorological properties have been captured in sufficient detail to justify their use in the integrated model. Furthermore, the integrated model's sensitivity to emissions is consistent with observations and previous research: it shows the region to be VOC limited, its show a general decrease in magnitude of peak concentrations as well as an eastward shift in plume centroid. However, the model appears to be very conservative and, except for the simulations which changed the VOC speciation and residual layer concentrations, the plume shows little spatial variability – in many cases the 52-ppb centroid is displaced less than the 15 km judged to be the characteristic scale for this isopleth. In order to model multi-day episodes, the model would have to include the effects of night-time SBL on: chemistry, vertically varying surface deposition rates and vertically varying wind fields.

While the model has been applied in a single setting, it is difficult to say how it would fare in other regions. Modeling success here might stem from ozone production being almost entirely local in origin (Hedley and Singleton, 1997) and the region's generally persistent summer weather (Oke and Hay, 1998). In fact, Burrows et al. (1995) find their statistical model for ozone formation in the LfV captures a greater amount of the observed variability than similar models for Montreal P.Q. and the Atlantic provinces because the training data from the latter two regions show more variance. This they attribute to more complicated meteorology and the need for predictors relating to long-range precursor transport.

Clearly, this model is not a turnkey system. It makes use of local expert knowledge (for instance the VOC speciation developed and checked by Jiang et al. (1997a) and Jaing et al. (1997), the modeling of mixing heights by Batchvarova et al. (1999), the surface heat flux measurements, under sea-breeze conditions, by Dr. Steyn (personal communication) and the identification of the most important meteorological processes controlling ozone formation (Burrows et al., 1995)) and is developed based on a region's specific circumstances. It is interesting to note that while comprehensive models, based on the primitive constitutive equations should, in principle, be generally applicable, often several iterations of the selected episode are required to achieve acceptable levels of accuracy (Russell and Dennis, 2000); a process that may be indirectly tuning the model to a region's specific circumstances.

## 10.6 Summary for Part II

The simple integrated model developed in these last two chapters is intended as both a screening tool, complementing comprehensive modeling efforts and a learning tool. It is designed to predict a region's sensitivity to precursor emissions by capturing the first order interactions between meteorology, chemistry and emissions. It makes use of a scaling of ozone precursor relationship presented in Part I, a simple emissions inventory developed in Chapter 9 and Appendix G, a simple model for mixing heights and a set of back trajectories based on observed surface winds.

The advantage of this modeling approach is its transparency: interactions between processes are more readily apparent than in the array of highly focused research areas found in 'black box' models, quick execution time allows many future scenarios to be explored, allowing connections between emissions (and indirectly demographics, lifestyle choices and technological innovation) and air quality to be drawn and lastly, because model assumptions and limitations are more apparent, the model is less likely to be used outside its intended limits.

Finally, the distinction between a simple model and a simplistic model must be made and I propose the following operational definitions: a simple model presents a high-level picture of a problem while remaining faithful to the underlying physics whereas a simplistic model provides an incomplete picture by overlooking important processes. There is a fine line between the two with no *a priori* means to determine when the line has been crossed. However, I suggest the sensitivity tests performed in this chapter provide *a posteriori* confirmation that my model is simple, by the above definition.

# Chapter 11

## Conclusions

Three main issues face the atmospheric science community: anthropogenically induced climate change ('global warming'), stratospheric ozone depletion ('ozone hole') and regional photochemical production of oxidants and aerosols ('urban smog'). These manifest themselves in different ways and present a variety of modeling challenges: global warming, once started cannot be halted – regardless of actions taken today, will persist for millenia and cause potentially catastrophic damage at the global scale; the ozone hole, while showing signs of improvement – as a result of recent policies – will nonetheless persist for decades impacting ecosystems on an hemispheric scale and finally, urban smog could be reduced almost at once – given a change in lifestyles and attitudes, has a lifetime of days to months and produces organism specific impacts. Because of its smaller temporal and spatial scales, regional oxidant production is better suited to detailed numerical representation than either climate change or ozone depletion. However, the stakes and complexity of this problem (and the three in general) suggest a variety of investigative approaches, in addition to comprehensive numerical modeling, are needed.

With this in mind, the goal of this thesis is to create a simple model for ozone formation that quickly determines the response of an ozone plume to changes in precursor emissions while furthering understanding about the interactions between photochemistry, meteorology and emissions. But what constitutes an understanding? Many megabytes of output from a photochemical model is no more tantamount to knowledge of ozone sensitivity than a weather forecast is to an understanding of synoptic scale meteorology. I suggest an understanding requires, among other things, knowledge of a problem's characteristic scales like time and length as well as its more generalized process scales. To this end, this thesis analyzes ozone photochemistry in terms of characteristic scales and then use these scales to build a model for ozone formation in a urban region. In this chapter, I present conclusions from this research as well as suggestions for future work.

### **Scaling analysis of ozone photochemistry**

This thesis' main effort involved distilling the non-linear interactions between ozone, its precursor and environmental conditions. Based on this analysis, the following conclusions can be drawn:

- 
- Maximum ozone concentration as a function of initial VOC and NO<sub>x</sub> concentration can be described by a single similarity curve involving two variables: initial NO<sub>x</sub> concentration and the ratio of initial VOC to NO<sub>x</sub> concentration. The similarity relationship is obtained from a scaling analysis of OZIPR model output. Parameterization of the similarity relationship (the WEX model) requires six parameters and when Weibull transformed shows a characteristic 'dogleg' or scaling break.
  - The most important variable in the WEX model ( $\beta$ ), the ratio of initial VOC to NO<sub>x</sub> at which the break occurs, defines the characteristic process scale for ozone photochemistry. While tempting to equate this break with the ridgeline, is it better viewed from the perspective of a change in governing feedback mechanisms separating low- and high-NO<sub>x</sub> chemistry regimes.
  - The remaining parameters in the similarity relationship are not related to a VOC's physical or chemical properties but instead quantify sub-processes within the photochemical system including: NO<sub>x</sub>-inhibition, isopleth slope, final partitioning of NO<sub>x</sub> as NO<sub>z</sub> and a measure of NO<sub>x</sub>-efficiency.
  - The scaling analysis, similarity relationships and parameterizations appear to be independent of chemical mechanism, hold for a variety of VOC species and mixtures and are applicable over a wide range of VOC and NO<sub>x</sub> concentrations. The analysis can be extended to include the dependence of maximum ozone concentration on temperature and actinic flux.
  - While the WEX model was shown to be consistent with smog chamber data, collapsing a wide range of results onto a single similarity relationship, an independent validation of the model, using chamber data over a full range of VOC and NO<sub>x</sub> concentrations, was not possible because of chamber limitations; especially under low NO<sub>x</sub> conditions.
  - From the point of view of ozone-precursor relationships, the fundamental basis for describing ozone formation is in terms of four rules governing ozone production ( $P(O_3)$ ) that are summarized in Section 5.3.8. Both the WEX and IER models (Johnson, 1984) satisfy these rules and using these rules, the WEX model can be extended to quantify the temporal variability of ozone using the cumulative NO<sub>2</sub> photolysis rate ( $j(t)$ ).
  - Measures of VOC reactivity constitute a form of scaling but since these are properties of the reacting system and not just the VOC, there is no single VOC reactivity scale. An estimate of one type of reactivity scale, the relative incremental reactivities (RIR), can be made using the WEX model by determining sensitivity of maximum ozone concentration

to initial VOC concentration at the scaling break. The resulting NO<sub>x</sub>-scaled incremental reactivity (NSIR) is found to be consistent with other VOC reactivity scales. Finally, because the highly parameterized Generic Reaction Set (GRS) (Azzi et al., 1992) models organic compounds having a single fixed reaction sequence, the incremental reactivity (IR) of its VOCs shows a simple scaling.

### Essential Meteorological Processes during an Ozone Episode

In describing the most important meteorological processes governing ozone formation during an ozone episode in the Lower Fraser Valley B.C., the following conclusions have been reached:

- Back trajectories, based on interpolated hourly observations of wind speed and direction, appear to adequately describe horizontal transport processes in the LFV. Final ozone concentrations are not sensitive to small discrepancies in trajectory paths over areas with few emission sources.
- Spatial and temporal variability of mixing depth, based on the simple applied slab model of Gryning and Batchvarova (1996), appear to be adequately captured for purposes of predicting ozone formation in the LFV.
- Residual layer concentrations are central to the the simple model and indirectly account for multi-day build-up of pollutants during an ozone episode. As a result of high residual layer concentrations, the simple model is not sensitive to mixing heights. The model suggests determining the build-up of residual layer concentrations and associated elevated pollutant layers represent the most significant challenge for modeling ground level ozone in the LFV.
- The model has used both observations specific to August 10<sup>th</sup> (principally wind speed and direction) and common to sea-breeze days (surface sensible heat fluxes). Ideally, the model would be internally consistent and develop wind fields using observations averaged on sea-breeze days. This would help remove episode specific features from the analysis and should lead to a better picture of the plume's characteristic features.

### Simple Emissions Inventory

Development of a simple emissions inventory, to complement the meteorological and photochemical models, produced the following conclusions:

- A simple emissions inventory, based on published emission totals, a small set of general land use categories and generic temporal curves, gives spatial and temporal emissions consistent

with a more detailed inventory. Modeling success suggests correctly quantifying total emissions is more important than spatially and temporally allocating emissions to high level of detail. This conclusion could be further checked by comparing model output based on the simple inventory against model output using a more detailed inventory.

- A single VOC speciation, developed from a detailed emissions inventory and used for every emissions source, appears to adequately represent VOC reactivity in the context of characterizing the ozone plume under episodic conditions.

### Simple Integrated Model for Ozone formation

An air quality model integrating a scaling analysis of ozone photochemistry with the simple meteorology model and emissions inventory, was used to study ozone formation in the LFV. Based on this study, the following conclusions can be drawn:

- The integrated model captures the spatial structure of the ozone plume in LFV during typical episode conditions. Furthermore, modeled plume response to increased wind speed, decreased temperature and reduced actinic flux is consistent with previous analyses. While the meteorology used in the present research was typical of a LFV ozone episode, an analysis of a variety of meteorological conditions would consolidate these results. Such an analysis could be guided by McKendry's (1994) synoptic typing of ozone episodes in the LFV. Of special interest would be the variability of meso-scale conditions, during episode conditions, under the different synoptic types.
- The temporal variability of ozone concentrations, throughout the day, can be determined by scaling peak ozone concentrations by the cumulative  $NO_2$  photolysis rate ( $j(t)$ ). For the episode considered, modeled ozone concentrations, at a selection of locations along the valley axis, generally increase throughout the day before slightly decreasing in the late afternoon. The domain wide maximum concentration increases during the day and the location of this maximum moves up-valley throughout the day. These results are consistent with observations.
- The present model shows the ozone plume generally confined to the valley but field observations and other modeling results suggests ozone maxima exist away from valley. These results are difficult to confirm with observation, due to the lack of monitoring stations away from the valley, and difficult to check using the present model, due to large sensitivities the trajectories show to wind fields in these locations. A compounding difficulty is the poor representation of the wind fields over the steep mountain topography by the observation network.

- 
- The model shows the region to be VOC limited in agreement with previous work. The model produces a westward shifted ozone plume of higher peak concentration when using 1985 emissions totals, in agreement with historical trends. However, based on past observations, the modeled peak concentration is likely too low with plume centroid too far eastward. These discrepancies could be caused by the test day meteorology not being representative of meteorology during ozone episodes or the significant Eastward shift of emissions that have occurred since 1985. In either case, trying to determine the correct magnitude of responses to changes in emissions lies beyond the scope of the current model.
  - The model shows projected emissions reductions may not provide additional improvements to present episodic concentrations and that larger than anticipated reductions in NO<sub>x</sub> emissions, without equivalent additional VOC reductions, could increase episodic concentrations. Future emissions reductions stemming from TIER 2 LDV standards, which target NO<sub>x</sub> emissions to a greater extent than VOC emissions, may not result in appreciable changes in episodic ozone concentrations. These conclusions should be used to guide future comprehensive modeling studies.
  - The model had difficulty determining boundary layer precursor concentrations (both surface and aloft) at simulation start. Ideally, the model would use observed VOC and NO<sub>x</sub> concentrations but limited data forced the modeling of initial boundary layer concentrations using pre-conditioning simulations involving a ambient (background) concentrations, emissions, deposition, advection, entrainment and detrainment. Resulting steady state concentrations were found to depend on the choice of background concentration. These were chosen to produce boundary layer concentrations consistent with the limited observations and an ozone plume with **peak** concentration within a few ppb of the observed value. Using boundary layer concentrations calculated by a comprehensive grid based model would improve the model in this regard.
  - While modeling techniques developed in this thesis should be applicable to other regions, success in the LFV may stem from the region's clean background air, limited advection of pollutants from neighbouring urban areas, persistent summertime weather and lack of industrial point sources.
  - Using the output of economic and social models to drive the simple emissions inventory would allow the simple ozone model to be used in a larger integrated assessment model.

# Bibliography

- Akimoto, H., F. Sakamaki, M. Hoshino, G. H. Inoue and M. Okuda, 1979: Photochemical ozone formation in propylene-nitrogen oxide-dry air system. *Environmental Science & Technology*, **13**, 53–58.
- Akimoto, H., H. Takagi, G. Inoue, F. Sakamaki, N. Washida and M. Okuda, 1985: Design and characterization of the evacuable and bakeable photochemical smog chamber. *Environmental Science and Technology*, **19**, 507–512.
- Altshuller, A. P., 1966: An evaluation of techniques for the determination of the photochemical reactivity of organic emissions. *Journal of the Air Pollution Control Association*, **16**, 257–260.
- Altshuller, A. P. and A. S. Lefohn, 1996: Background ozone in the planetary boundary layer over the United States. *Journal of the Air and Waste Management Association*, **46**, 134–141.
- Andersson-Sköld, Y., P. Grennfelt and K. Pleijel, 1992: Photochemical ozone creation potentials: a study of different concepts. *Journal of the Air and Waste Management Association*, **42**, 1152–1158.
- Arya, S. P., 1999: *Air Pollution Meteorology and Dispersion*. Oxford University Press, New York, USA, 310 pp.
- Arya, S. P., 2001: *Introduction to Micrometeorology*. Academic Press, San Diego, USA, 420 pp.
- Atkinson, R., 2000: Atmospheric chemistry of VOCs and NOx. *Atmospheric Environment*, **34**, 2063–2101.
- Azzi, M., G. M. Johnson and M. Cope, 1992: An introduction to the Generic Reaction Set. in *Proceedings of the 11th international Clean Air Conference*, Brisbane Australia.
- B. H. Levelton and Associates Ltd, 1993: 1990 air emissions inventory for the Lower Fraser Valley: Area sources. Technical report, B. H. Levelton and Associates Ltd, Richmond B.C.
- Banta, R. M., P. B. Shepson, J. W. Bottenheim, K. G. Anlauf, H. A. Wiebe, A. Gallant, T. Bisen-thal, L. D. Oliver, C.-J. Zhu, I. G. McKendry and D. G. Steyn, 1997: Nocturnal cleansing flows in a tributary valley. *Atmospheric Environment*, **31**, 2147–2162.
- Barenblatt, G. I., 1996: *Scaling, Self-similarity, and Intermediate Asymptotics*. Cambridge University Press, Cambridge, UK, 386 pp.
- Barna, M., B. Lamb, S. O'Neil, H. Westberg, C. Figueroa-Kaminsky, S. Otterson, C. Bowman and J. DeMay, 2000: Modeling ozone formation and transport in the cascadia region of the Pacific Northwest. *Journal of Applied Meteorology*, **39**, 349–366.
- Batchvarova, E., X.Cai, S.-E. Gryning and D. G. Steyn, 1999: Modelling internal boundary-layer development in a region with a complex coastline. *Boundary-Layer Meteorology*, **90**, 1–20.

- B.C. Ministry of Environment, L. and Parks, 1998: Air quality report for British Columbia. Technical report, Air Resources Branch, Victoria, B.C.
- Bergin, M. S., A. G. Russell, W. P. L. Carter, B. E. Croes and J. H. Seinfeld, 1998: *Environmental Analysis and Remediation*. volume 7, chapter Ozone Control and VOC Reactivity, pp. 3355–3383. Wiley and Sons, New York, USA.
- Blanchard, C. L., 2000: Ozone process insights from field experiments – part III: Extent of reaction and ozone formation. *Atmospheric Environment*, **34**, 2035–2043.
- Blanchard, C. L., F. W. Lurman, M. Korc and R. M. Roth, 1994: The use of ambient data to corroborate analyses of ozone control strategies. Technical Report STI-94030-1433-FR, Sonoma Technology Inc.
- Blanchard, C. L., F. W. Lurman, P. M. Roth, H. E. Jefferies and R. M. Roth, 1999: An introduction to the Generic Reaction Set. *Atmospheric Environment*, **33**, 369–381.
- Bluman, G. W. and S. C. Anco, 2002: *Symmetry and Integration Methods for Differential Equations*. Springer-Verlag, New York, USA, 419 pp.
- Bott, A., 1989: A positive definite advection scheme obtained by nonlinear renormalization of the advective fluxes. *Monthly Weather Review*, **117**, 1006–1015.
- Bowman, F. M. and J. H. Seinfeld, 1994: Ozone productivity of atmospheric organics. *Journal of Geophysical Research*, **99**, 5309–5324.
- Brauer, M., J. Blair and S. Vedal, 1996: Effect of ambient ozone exposure on lung function in farm workers. *American Journal of Critical Care Medicine*, **154**, 981–987.
- Bridgman, P. W., 1937: *Dimensional Analysis*. Yale University Press, New Haven, CT., USA, 113 pp.
- Brook, J. F., T. F. Dann and R. T. Burnett, 1997: The relationship among TSP, PM<sub>10</sub>, PM<sub>2.5</sub>, and inorganic constituents of atmospheric particulate matter at multiple Canadian location. *Journal of the Air and Waste Management Association*, **47**, 2–19.
- Buckingham, E., 1914: On physically similar systems; illustrations of the use of dimensional equations. *Physical Reviews*, **4**, 345–376.
- Buckingham, E., 1915: Model experiments and the forms of empirical equations. *Transactions ASME*, **37**, 263–296.
- Burnett, R. T., M. Smith-Doiron, D. Steib, M. E. Raizenne, J. R. Brook, R. E. Dales, J. A. Leech, S. Cakmak and D. Krewski, 2001: Association between ozone and hospitalization for acute respiratory diseases in children less than 2 years of age. *American Journal of Epidemiology*, **153**(5), 444–452.
- Burrows, W. R., M. Benjamin, S. Beauchamp, E. L. Lord, D. McCollor and B. Thomson, 1995: CART decision-tree statistical analysis and prediction of summer season maximum surface ozone for the Vancouver, Montreal and Atlantic regions of Canada. *Journal of Applied Meteorology*, **34**, 1848–1862.

- Businger, J. A., J. C. Wyngaard, Y. Izumi and E. F. Bradley, 1971: Flux-profile relationships in the atmospheric surface layer. *Journal of the Atmospheric Sciences*, **28**, 181–189.
- Cai, X. M. and D. G. Steyn, 2000: Modelling study of sea breezes in a complex coastal environment. *Atmospheric Environment*, **34**, 2873–2885.
- California Air Resources Board, 1991: Proposed regulations for low emission vehicles and clean fuels – final statement of reasons. Technical report, CARB, Sacramento, CA.
- Canadian Council of Ministers of the Environment, 1990: Management plan for nitrogen oxides (NO<sub>x</sub>) and volatile organic compounds (VOCs) phase I. Technical report, CCME.
- Canadian Council of Ministers of the Environment, 2000: Canada-wide standards for particulate matter (PM) and ozone. Technical report, CCME.
- Cardelino, C. A. and W. L. Chameides, 1995: An observation-based model for analyzing ozone precursor relationships in the urban atmosphere. *Journal of the Air and Waste Management Association*, **45**, 161–180.
- Carter, W. P. L., 1990: A detailed mechanism for the gas-phase atmospheric reactions of organic compounds. *Atmospheric Environment*, **24A**, 481–518.
- Carter, W. P. L., 1994: Development of ozone reactivity scales for volatile organic compounds. *Journal of the Air and Waste Management Association*, **44**, 881–899.
- Carter, W. P. L., 1995: Computer modeling of environmental chamber measurements of maximum incremental reactivities of volatile organic compounds. *Atmospheric Environment*, **29**, 2513–2527.
- Carter, W. P. L. and R. Atkinson, 1987: An experimental study of incremental hydrocarbon reactivity. *Environmental Science and Technology*, **21**, 670–679.
- Carter, W. P. L. and R. Atkinson, 1989: Computer modeling study of incremental hydrocarbon reactivity. *Environmental Science and Technology*, **23**, 864–880.
- Carter, W. P. L., R. Atkinson, A. M. Winer and J. J. N. Pitts, 1981: Evidence for chamber-dependent radical sources. *International Journal of Chemical Kinetics*, **13**, 735–740.
- Carter, W. P. L., D. Luo, I. L. Malkina and D. Fritz, 1996: The University of California, Riverside environmental chamber data base for evaluating oxidant mechanisms: Indoor chamber experiments through 1993. Technical Report EPA/600/R96/078a,b, U.S. EPA.
- Carter, W. P. L. and F. W. Lurman, 1991: Evaluation of a detailed gas-phase atmospheric reaction mechanism using environmental chamber data. *Atmospheric Environment*, **25A**, 2771–2806.
- Carter, W. P. L., J. A. Pierce, D. Luo and I. L. Malkina, 1995: Environmental chamber study of maximum incremental reactivities of volatile organic compounds. *Atmospheric Environment*, **29**, 2499–2511.
- Chameides, W. L., F. Fehsenfeld, M. O. Rodgers, C. Cardelino, J. Martinez, D. Parrish, W. Loneman, D. R. Lawson, A. Rasmussen, P. Zimmerman, J. Greenberg, P. Middleton and T. Wang, 1992: Ozone precursor relationships in the ambient atmosphere. *Journal of Geophysical Research*, **97**, 6037–6055.

- Chang, T. Y., D. P. Chock, B. I. Nance and S. L. Winker, 1997: A photochemical extent parameter to aid ozone air quality management. *Atmospheric Environment*, **31**, 2787–2794.
- Chang, T. Y., B. I. Nance and N. A. Kelly, 1999: Modeling smog chamber measurements of incremental reactivities of volatile organic compounds. *Atmospheric Environment*, **33**, 4695–4708.
- Chang, T. Y. and S. J. Rudy, 1990: Ozone-forming potential of organic emissions from alternative-fueled vehicles. *Atmospheric Environment*, **24**, 2421–2430.
- Chang, T. Y. and S. J. Rudy, 1993: Ozone-precursor relationships: a modeling study of semi-empirical relationships. *Environmental Science and Technology*, **27**, 2213–2219.
- Chang, T. Y. and M. J. Suzio, 1995: Assessing ozone-precursor relationships based on a smog production model and ambient data. *Journal of the Air and Waste Management Association*, **45**, 20–28.
- Comrie, A. C., 1997: Comparing neural networks and regression models for ozone forecasting. *Journal of the Air and Waste Management Association*, **47**, 653–663.
- Concord Scientific Corporation (CSC); 1985: Vancouver Oxidants Study, air quality analysis study update 1982-1984. Technical report, Prepared for Environment Canada, Environmental Protection Service.
- Croes, B. E., J. R. Holmes and A. C. Lloyd, 1992: Reactivity-based hydrocarbon controls: Scientific issues and potential regulatory applications. *Journal of the Air and Waste Management Association*, **42**, 657–661.
- Crutzen, P. J., 1995: *Composition, Chemistry and Climate of the Atmosphere*. chapter Ozone in the troposphere, pp. 349–393. Van Nostrand Reinhold, New York, USA.
- Darnall, K. R., A. C. Lloyd, A. M. Winer and J. N. P. Jr., 1976: Reactivity scale for atmospheric hydrocarbons based on reaction with hydroxyl radical. *Environmental Science and Technology*, **10**, 692–696.
- Delfino, R. J., A. M. Murphy-Moulton, R. T. Burnett, J. R. Brook and M. R. Becklake, 1997: Effects of air pollution on emergency room visits for respiratory illness in Montreal, Quebec. *American Journal of Critical Care Medicine*, pp. 568–576.
- Derwent, R. G., M. E. Jenkin, S. M. Saunders and M. J. Pilling, 1998: Photochemical ozone creation potentials for organic compounds in Northwest Europe calculated with a master chemical mechanism. *Atmospheric Environment*, **32**, 2429–2441.
- Dimitriadis, B., 1996: Scientific basis for the voc reactivity issues raised by section 183(e) of the Clean Air Act Amendments of 1990. *Journal of the Air and Waste Management Association*, **46**, 963–970.
- Dodge, M. C., 1984: Combined effects of organic reactivity and NMHC/NO<sub>x</sub> ratio on photochemical oxidant formation – a modeling study. *Atmospheric Environment*, **18**, 1657–1665.
- Dodge, M. C., 2000: Chemical oxidant mechanisms for air quality modeling: critical review. *Atmospheric Environment*, **34**, 2103–2130.

- Doussin, J. F., D. Ritz, R. Durand-Jolibois, A. Monod and P. Carlier, 1997: Design of an environmental chamber for the study of atmospheric chemistry: New developments in the analytical device. *Analisis*, **25**, 236–242.
- Drewitt, G. B., K. Curren, D. G. Steyn, T. J. Gillespie and H. Niki, 1998: Measurement of biogenic hydrocarbon emissions from vegetation in the Lower Fraser Valley, British Columbia. *Atmospheric Environment*, **32**, 3457–3466.
- Dutton, J. A., 1976: *The Ceaseless Wind: An introduction to the theory of atmospheric motion*. McGraw-Hill, New York, NY., USA, 579 pp.
- Eliassen, A., O. Hov, I. S. A. Isaksen, J. Saltbones and F. Stordal, 1992: A Lagrangian long-range transport model with atmospheric boundary layer chemistry. *Journal of Applied Meteorology*, **21**, 1645–1661.
- Environment Canada, 1989: Vancouver oxidants study: Control technology options and costs for volatile organic compound emissions from gasoline marketing. Technical report, Environment Canada.
- Environment Canada, 1997: Modelling of ground-level ozone in the Lower Fraser Valley. Technical report, Canadian 1996 NOx/VOC Science Assessment, Toronto, Canada, 157 pp.
- Environmental Protection Agency, 1997: National ambient air quality standards for ozone; final rule (40 cfr part 50). Technical report, US EPA, Federal Register 62 (138).
- Environmental Protection Agency, 1999: Guideline for developing an ozone forecasting program. Technical Report EPA-454/R-99-009, US EPA.
- Fast, J. D. and S. Zhong, 1998: Meteorological factors associated with inhomogeneous ozone concentrations within the Mexico City basin. *Journal of Geophysical Research*, **103**, 18,927–18,946.
- Federal Provincial Working Group on Air Quality Objectives and Guidelines, 1999: National ambient air quality objectives for ground level ozone. Technical report, Health Canada, Ottawa, Ontario.
- Finlayson-Pitts, B. J. and J. N. Pitts, 1999: *Chemistry of the Upper and Lower Atmosphere*. Academic Press, San Diego, USA, 969 pp.
- Friedman, M. S., K. E. Powell, L. Hutwagner, L. M. Graham and W. G. Teague, 2001: Impact of changes in transportation and commuting behaviors during the 1996 summer Olympic games in Atlanta on air quality and childhood asthma. *Journal of the American Medical Association*, **285**(7), 897–905.
- Galizia, A. and P. L. Kinney, 1999: Long-term residence in areas of high ozone: associations with respiratory health in a nationwide sample of nonsmoking young adults. *Environmental Health Perspectives*, **107**(8), 675–679.
- Galmarini, S., J. Vila-Guerau de Arellano and P. G. Duynkerke, 1997: Scaling the turbulent transport of chemical compounds in the surface layer under neutral and stratified conditions. *Quarterly Journal of the Royal Meteorological Society*, **123**, 223–242.
- Garrat, J. R. and B. B. Hicks, 1990: Micrometeorological and PBL experiments in Australia. *Boundary-Layer Meteorology*, **50**, 11–29.

- Gauthier, M., X. Qiu, R. B. Caton, J. W. Boulton and M. Lepage, 2003: Phase I Report: Pacific Northwest IAQMP. Technical report, Rowan Williams Davies and Irwin (RWDI) Inc., Guelph, Ontario.
- Gertler, A. W., D. N. Wittorff, R. McLaren, W. Belzer and T. Dann, 1997: Characterization of vehicle emissions in Vancouver B.C. during the 1993 Lower Fraser Valley oxidants study. *Atmospheric Environment*, **31**, 2107–2112.
- Gery, M. W., G. Z. Whitten, J. P. Killus and M. C. Dodge, 1989: A photochemical kinetics mechanism for urban and regional scaled computer modeling. *Journal of Geophysical Research*, **94**, 12925–12956.
- Gilliland, F. D., K. Berhane, E. B. Rappaport, D. C. Thomas, E. Avol, W. J. Gauderman, S. J. London, H. G. Margolis, R. McConnell, K. T. Islam and J. M. Peters, 2001: The effects of ambient air pollution on school absenteeism due to respiratory illness. *Epidemiology*, **12**(1), 43–54.
- Glickman, T. S., editor, 2000: *Glossary of Meteorology*. American Meteorological Society, Boston, Massachusetts, U.S.A., 2<sup>nd</sup> edition.
- Goodin, W. R., G. J. McRae and J. H. Seinfeld, 1979: A comparison of interpolation methods for sparse data: application to wind and concentration fields. *Journal of Applied Meteorology*, **18**, 761–771.
- Goodin, W. R., G. J. McRae and J. H. Seinfeld, 1980: An objective analysis technique for constructing three-dimensional urban-scale wind fields. *Journal of Applied Meteorology*, **19**, 98–108.
- Greater Vancouver Regional District, 1988: 1985 Lower Mainland Emissions Inventory. Technical report, GVRD Regional District, Burnaby B.C., 11 Volumes.
- Greater Vancouver Regional District, 1994: GVRD Air Quality Management Plan. Technical report, GVRD Policy and Planning Department, Burnaby, B.C.
- Greater Vancouver Regional District, 1999: Volatile organic compounds in the ambient air of Greater Vancouver 1990 to 1996. Technical report, GVRD Air Quality Department, Burnaby, B.C.
- Greater Vancouver Regional District, 2002: 2000 emissions inventory for the Lower Fraser Valley Airshed. Technical report, GVRD Policy and Planning Department, Burnaby, B.C.
- Greater Vancouver Regional District, 2003a: 2000 emissions inventory for the Lower Fraser Valley Airshed: Detailed listing of results and methodology. Technical report, GVRD Policy and Planning Department, Burnaby, B.C.
- Greater Vancouver Regional District, 2003b: Forecast and backcast of the 2000 emissions inventory for the Lower Fraser Valley airshed 1985–2025. Technical report, GVRD Policy and Planning Department, Burnaby, B.C.
- Gryning, S.-E. and E. Batchvarova, 1990: Analytical model for the growth of the coastal internal boundary layer during onshore flow. *Quarterly Journal of the Royal Meteorological Society*, **116**, 187–203.
- Gryning, S.-E. and E. Batchvarova, 1996: A model for the height of the internal boundary layer over an area with an irregular coastline. *Boundary Layer Meteorology*, **78**, 405–413.

- Guenther, A., C. Geron, T. Pierce, B. Lamb, P. Harley and R. Fall, 2000: Natural emissions of non-methane volatile organic compounds, carbon monoxide, and oxides of nitrogen from north america. *Atmospheric Environment*, **34**, 2205–2230.
- Guenther, A., P. Zimmerman, P. Harley, R. Monson and R. Fall, 1993: Isoprene and monoterpene emission rate variability: model evaluation and sensitivity analysis. *Journal of Geophysical Research*, **98**, 12609–12617.
- Haagen-Smit, A. J., 1952: Chemistry and physiology of Los Angeles smog. *Industrial and Engineering Chemistry*, **44**, 1342–1346.
- Haagen-Smit, A. J., C. E. Bradley and M. M. Fox, 1953: Ozone formation in photochemical oxidation of organic substances. *Industrial and Engineering Chemistry*, **45**, 2086–2089.
- Hägeli, P., D. G. Steyn and K. B. Strawbridge, 2000: Spatial and temporal variability of mixed-layer depth and entrainment zone thickness. *Boundary Layer Meteorology*, **97**, 47–71.
- Hakami, A., R. A. Harley, J. B. Milford, M. T. Odman and A. G. Russell, 2004: Regional, three-dimensional assessment of the ozone formation potential of organic compounds. *Atmospheric Environment*, **38**, 121–134.
- Haldane, J. B. S., 1985: *On being the right size and other essays*. chapter 1. Oxford University Press, New York.
- Harte, J., 1991: *Toxics A to Z: a guide to everyday pollution hazards*. University of California Press, Berkeley, California, USA, 479 pp.
- Hayden, K. L., K. G. Anlauf, R. M. Hoff, J. W. Strapp, J. W. Bottenheim, H. A. Wiebe, F. A. Froude, J. B. Martin, D. G. Steyn and I. G. McKendry, 1997: The vertical chemical and meteorological structure of the boundary layer in the Lower Fraser Valley during Pacific '93. *Atmospheric Environment*, **31**, 2079–2105.
- Heck, W. W. and E. B. Cowling, 1997: The need for a long term cumulative secondary ozone standard - an ecological perspective. *Environmental Manager*, pp. 23–33.
- Heck, W. W., O. C. Taylor, R. Adams, G. Bingham, J. Miller, E. Preston and L. Weinstein, 1982: Assessment of crop loss from  $O_3$ . *Journal of the Air Pollution Control Association*, **32**, 353–.
- Hedley, M., R. McLaren, W. Jiang and D. L. Singleton, 1995: Evaluation of the MC2-CALGRID photochemical modelling system. Technical Report PET-1361-95S, National Research Council of Canada.
- Hedley, M., R. McLaren, W. Jiang and D. L. Singleton, 1997: Evaluation of an air quality simulation of the Lower Fraser Valley - II. Photochemistry. *Atmospheric Environment*, **31**, 1617–1630.
- Hedley, M. and D. L. Singleton, 1997: Evaluation of an air quality simulation of the Lower Fraser Valley - I. Meteorology. *Atmospheric Environment*, **31**, 1605–1615.
- Hess, G. D., F. Carnovale, M. E. Cope and G. M. Johnson, 1992a: The evaluation of some photochemical smog reaction mechanisms - I. temperature and initial composition effects. *Atmospheric Environment*, **26A**, 625–641.

- Hess, G. D., F. Carnovale, M. E. Cope and G. M. Johnson, 1992b: The evaluation of some photochemical smog reaction mechanisms – II. initial addition of alkanes and alkenes. *Atmospheric Environment*, **26A**, 643–651.
- Hess, G. D., F. Carnovale, M. E. Cope and G. M. Johnson, 1992c: The evaluation of some photochemical smog reaction mechanisms – III. dilution and emissions effects. *Atmospheric Environment*, **26A**, 653–659.
- Hinze, J. O., 1975: *Turbulence*. McGraw-Hill Series in Mechanical Engineering. McGraw-Hill, New York, USA., 2<sup>nd</sup> edition, 790 pp.
- Holton, J. R., P. H. Haynes, M. E. McIntyre, A. R. Douglass, R. B. Rood and L. Pfister, 1995: Stratosphere-troposphere exchange. *Reviews of Geophysics*, **33**, 403–439.
- Horvath, S. M. and D. J. McKee, 1994: *Tropospheric Ozone*. chapter Acute and Chronic Health Effects of Ozone. Lewis Publishers, Boca Raton, Florida, USA.
- Hough, A. M. and R. G. Derwent, 1990: Changes in the global concentration of tropospheric ozone due to human activities. *Nature*, **344**, 645–648.
- Houyoux, M. R. and J. M. Vukovich, 1999: Updates to the sparse matrix operator kernel emissions modeling system (SMOKE) and intergration with Models-3. in *The Emissions Inventory: Regional Strategies for the Future*, Raleigh, NC. Air and Waste Management Association.
- Intergovernmental Panel on Climate Change, 2001: *Climate Change 2001: Mitigation*. Cambridge University Press, New York, USA, 752 pp.
- Jackson, P. L. and D. G. Steyn, 1994: Gap winds in a fjord, part II: Hydraulic analog. *Monthly Weather Review*, **122**, 1266–1276.
- Jacob, D., 1999: *Introduction to Atmospheric Chemistry*. Princeton University Press, Princeton, N.J., USA, 266 pp.
- Jacobson, M. Z., 1999: *Fundamentals of Atmospheric Modeling*. Cambridge University Press, New York, NY, USA, 656 pp.
- Jaing, W., D. L. Singleton, M. Hedley, R. McLaren, T. Dann and D. Wang, 1997: Comparison of organic compound composition in the emissions inventory and ambient data for the Lower Fraser Valley. *Journal of the Air and Waste Management Association*, **47**, 851–860.
- Janach, W. E., 1989: Surface ozone: Trend details, seasonal variations, and interpretation. *Journal of Geophysical Research*, **94**, 18289–18295.
- Jeffries, H., 1993: A different view of ozone formation. *Fuel Reformation*, **3**, ISSN 1062–3744.
- Jeffries, H. E., 1995: *Composition, Chemistry & Climate*. chapter 9. Photochemical Air Pollution. Van Nostand-Reinhold.
- Jeffries, H. E., M. W. Gery and W. P. L. Carter, 1992: Protocols for evaluating oxidant mechanisms used in urban and regional models. Technical report, US EPA.

- Jeffries, H. E., K. G. Sexton, J. R. Arnold and T. L. Kale, 1986: Validation testing of new mechanisms with outdoor chamber data. Volume 2: Analysis of VOC data for the CB4 and CAL photochemical mechanisms. Technical Report EPA-600/3-89-010b, U.S. Environmental Protection Agency.
- Jeffries, H. E. and S. Tonnesen, 1994: A comparison of two photochemical reaction mechanisms using mass balance and process analysis. *Atmospheric Environment*, **28**, 2991–3003.
- Jiang, R. and D. N. P. Murthy, 1995a: Modeling failure-data by mixture of 2 Weibull distributions: a graphical approach. *IEEE Transactions on Reliability*, **44**, 477–488.
- Jiang, R. and D. N. P. Murthy, 1995b: Reliability modeling involving two Weibull distributions. *Reliability Engineering and System Safety*, **47**, 187–198.
- Jiang, R. and D. N. P. Murthy, 1997: Parametric study of multiplicative model involving two Weibull distributions. *Reliability Engineering and System Safety*, **55**, 217–226.
- Jiang, R., M. J. Zuo and D. N. P. Murthy, 1999: Two sectional models involving two Weibull distributions. *International Journal of Reliability, Quality and Safety Engineering*, **6**, 103–122.
- Jiang, S. and D. Kececioglu, 1992: Graphical representation of two mixed-Weibull distributions. *IEEE Transactions on Reliability*, **41**, 241–247.
- Jiang, W., M. Hedley and D. L. Singleton, 1998: Comparison of the MC2/CALGRID and SAIMM/UAM-V photochemical modelling systems in the Lower Fraser Valley, British Columbia. *Atmospheric Environment*, **32**, 2969–2980.
- Jiang, W., D. L. Singleton, M. Hedley and R. McLaren, 1997a: Sensitivity of ozone concentrations to VOC and NO<sub>x</sub> emissions in the Canadian Lower Fraser Valley. *Atmospheric Environment*, **31**, 627–638.
- Jiang, W., D. L. Singleton, R. McLaren and M. Hedley, 1997b: Sensitivity of ozone concentrations to rate constants in a modified SAPRC90 chemical mechanism used for Canadian Lower Fraser Valley ozone studies. *Atmospheric Environment*, **31**, 1195–1208.
- Jiang, W., D. L. Singleton, D. L. Hedley and M. McLaren, 1996: Modification and evaluation of the CALGRID chemical mechanism for ozone studies of the Lower Fraser Valley, B.C. Technical Report PET-1360-95S, National Research Council Canada, Ottawa, Canada.
- Joe, H., D. G. Steyn and E. Susko, 1996: Analysis of trends in tropospheric ozone in the Lower Fraser Valley, British Columbia. *Atmospheric Environment*, **30**, 3413–3421.
- Johnson, G. M., 1984: A simple model for predicting ozone concentration of ambient air. in *Proceedings of the Eighth International Clean Air Conference*, pp. 715–713, Melbourne Australia.
- Kelly, N. A. and T. Y. Chang, 1999: An experimental investigation of incremental reactivities of volatile organic compounds. *Atmospheric Environment*, **33**, 2101–2110.
- Kleinman, L. I., 1994: Low and high NO<sub>x</sub> tropospheric photochemistry. *Journal of Geophysical Research*, **99**, 16831–16838.
- Krol, M. C., M. J. Molemaker and J. Vila-Guerau de Arellano, 2000: Effects of turbulence and heterogeneous emissions on photochemically active species in the convective boundary layer. *Journal of Geophysical Research*, **105**, 6871–6884.

- Leeuw, F. D., H. J. V. R. Leyssius and P. Bultjes, 1990: Calculation of long term averaged ground level ozone concentrations. *Atmospheric Environment*, **24A**, 185–193.
- Lelieveld, J. and F. J. Dentener, 2000: What controls tropospheric ozone? *Journal of Geophysical Research*, **105**, 3531–3551.
- Lenner, M., 1987: Nitrogen dioxide in exhaust emissions from motor vehicles. *Atmospheric Environment*, **21**, 37–43.
- Lesser, V. M., J. O. Rawlings, S. E. Spruill and M. C. Somerville, 1990: Ozone effects on agricultural crops: Statistical methodologies and estimated dose-response relationships. *Crop Science*, **30**, 148–155.
- Levine, I. N., 1978: *Physical Chemistry*. McGraw-Hill Book Company, New York, NY, USA, 847 pp.
- Li, S. M., 2004: A concerted effort to understand the ambient particulate matter in the Lower Fraser Valley: The Pacific 2001 Air Quality Study. *Atmospheric Environment*, in press.
- Lin, C.-Y. C., D. J. Jacob and A. M. Fiore, 2001: Trends in exceedances of the ozone air quality standard in the continental United States, 1980–1998. *Atmospheric Environment*, **35**, 3217–3228.
- Liu, S. C., M. Trainer, M. A. Carroll, G. Hubler, D. D. Montzka, R. B. Norton, B. A. Ridley, J. G. Walega, E. L. Atlas, B. G. Heikes, B. J. Huebert and W. Warren, 1992: A study of the photochemistry and ozone budget during the Mauna Loa Observatory photochemistry experiment. *Journal of Geophysical Research*, **97**, 10463–10471.
- Liu, S. C., M. Trainer, F. C. Fehsenfeld, D. D. Parrish, E. J. Williams, D. W. Fahey, G. Hübler and P. C. Murphy, 1987: Ozone production in the rural troposphere and the implications for regional and global ozone distributions. *Journal of Geophysical Research*, **92**, 4191–4207.
- Logan, J., 1985: Tropospheric ozone: seasonal behaviour, trends, and anthropogenic influence. *Journal of Geophysical Research*, **90**, 10463–10482.
- Lonneman, W. A., 1986: Comparison of 0600–0900 am hydrocarbon compositions obtained from 29 cities. in *Proceedings of the 1986 EPA/APCA Symposium on Measurement of Toxic Air Pollutants*. 419 pp.
- Lu, C. H. and J. S. Chang, 1998: On the indicator-based approach to assess ozone sensitivities and emissions features. *Journal of Geophysical Research*, **103**, 3453–3462.
- Lu, R. and R. P. Turco, 1995: Air pollution transport in a coastal environment - II. Three dimensional simulations over Los Angeles Basin. *Atmospheric Environment*, **29**, 1499–1518.
- McKendry, I. G., 1993: Ground-level ozone in Montreal, Canada. *Atmospheric Environment*, **27B**, 93–103.
- McKendry, I. G., 1994: Synoptic circulation and summertime ground-level ozone concentration at Vancouver, British Columbia. *Journal of Applied Meteorology*, **33**, 627–641.
- McKendry, I. G., 1997: Elevated ozone layers and vertical down-mixing over the Lower Fraser Valley, B.C. *Atmospheric Environment*, **31**, 2135–2146.

- McKendry, I. G., 2000: PM10 levels in the Lower Fraser Valley, British Columbia Canada: An overview of spatiotemporal variations and meteorological controls. *Journal of the Air and Waste Management Association*, **50**, 443–452.
- McKendry, I. G., J. P. Hacker, R. Stull, S. Sakiyama, D. Mignacca and K. Reid, 2001: Long-range transport of Asian dust to the Lower Fraser Valley, British Columbia, Canada. *Journal of Geophysical Research*, **106**, 18361–18370.
- McKendry, I. G. and J. Lundgren, 2000: Tropospheric layering of ozone in regions of urbanized complex and/or coastal terrain: a review. *Progress in Physical Geography*, **24**, 329–354.
- McKendry, I. G., D. G. Steyn, R. M. Banta, W. Strapp, K. Anlauf and J. Pottier, 1998a: Daytime photochemical pollutant transport over a tributary valley lake in Southwestern British Columbia. *Journal of Applied Meteorology*, **37**, 393–404.
- McKendry, I. G., D. G. Steyn, S. O’Kane, P. Zewar-Reza and D. Hueff, 1998b: Lower tropospheric ozone measurements by light aircraft equipped with chemiluminescent sonde. *Journal of Atmospheric and Ocean Technology*, **15**, 136–143.
- McNair, L., A. Russell and M. T. Odman, 1992: Airshed calculation of the sensitivity of pollutant formation to organic compound classes and oxygenates associated with alternative fuels. *Journal of the Air and Waste Management Association*, **42**, 174–178.
- Meadows, D. H. and J. M. Robinson, 1985: *The Electronic Oracle: Computer Models and Social Decisions*. John Wiley and Sons, Chichester, UK, 445 pp.
- Mickley, L. J., P. Murti, D. Jacob, J. Logan, D. Rind and D. Koch, 1999: Radiative forcing from tropospheric ozone calculated with a unified chemistry-climate model. *Journal of Geophysical Research*, **104**, 30153–30172.
- Milford, J. B., D. Gao, S. Sillman, P. Blossey and A. G. Russell, 1994: Total reactive nitrogen (NO<sub>y</sub>) as an indicator of the sensitivity of ozone to reductions in hydrocarbon and NO<sub>x</sub> emissions. *Journal of Geophysical Research*, **99**, 3533–3542.
- Millan, M. M., R. Salvador and E. Mantilla, 1997: Photooxidant dynamics in the Mediterranean basin in summer: Results from European research projects. *Journal of Geophysical Research*, **102**, 8811–8823.
- National Research Council, 1991: *Rethinking the Ozone Problem in Urban and Regional Air Pollution*. National Academy Press, Washington, D.C., 500 pp.
- National Research Council, 2000: *Modeling Mobile Source Emissions*. National Academic Press, Washington, D.C., USA, 239 pp.
- Oke, T. and J. Hay, 1998: *The Climate of Vancouver*. Number 50 in B.C. Geographical Series. University of British Columbia, Vancouver, B.C., 84 pp.
- Oke, T. R., M. North and O. Slaymaker, 1992: *Vancouver and Its Region*. chapter Primordial to Prim Order: a Century of Environmental Change, pp. 146–170. University of British Columbia Press.
- Ott, W., 1994: *Environmental Statistics and Data Analysis*. Lewis Publishers, Boca Raton, Fl., USA, 336 pp.

- Pannetier, G. and P. Souchay, 1967: *Chemical Kinetics*. Elsevier, 455 pp.
- Petroeschovsky, A., R. W. Simpson, L. Thalib and S. Rutherford, 2001: Associations between outdoor air pollution and hospital admissions in Brisbane, Australia. *Archives of Environmental Health*, **56**(1), 37–52.
- Pierce, T. and P. Waldruff, 1991: PC-BIES: a personal computer version of the biogenic emissions inventory system. *Journal of the Air and Waste Management Association*, **41**, 937–941.
- Pisano, J. T., I. McKendry, D. G. Steyn and D. R. Hastie, 1997: Vertical nitrogen dioxide and ozone concentrations measured from a tethered balloon in the Lower Fraser Valley. *Atmospheric Environment*, **31**, 2071–2078.
- Placet, M., C. O. Mann, R. O. Gilbert and M. J. Niefer, 2000: Emissions of ozone precursors from stationary sources: a critical review. *Atmospheric Environment*, **34**, 2183–2204.
- Prevot, A. S. H., J. Staehelin, G. L. Kok, R. D. Schillawski, B. Neining, T. Staffelbach, A. Neftel, H. Wernli and J. Dommen, 1997: The Milan photooxidant plume. *Journal of Geophysical Research*, **102**, 23375–23388.
- Pryor, S. C., 1998: A case study of emission changes and ozone responses. *Atmospheric Environment*, **32**, 123–131.
- Pryor, S. C., I. G. McKendry and D. G. Steyn, 1999: Synoptic scale meteorological variability and surface ozone concentrations in Vancouver, British Columbia. *Journal of Applied Meteorology*, **34**, 1824–1833.
- Pryor, S. C. and D. G. Steyn, 1995: Hebdomadal and diurnal cycles in ozone time series from the Lower Fraser Valley, B. C. *Atmospheric Environment*, **29**, 1007–1019.
- Pudykiewicz, J. A. and A. S. Koziol, 1999: The application of eulerian models for air quality prediction and the evaluation of emission control strategies in Canada. in *6<sup>th</sup> Conference on harmonization of models used for regulatory purposes*, Rouen, France.
- Robeson, S. M. and D. G. Steyn, 1989: A conditional probability density function for forecasting ozone air quality data. *Atmospheric Environment*, **23**, 689–692.
- Robeson, S. M. and D. G. Steyn, 1990: Evaluation and comparison of statistical forecast models for daily maximum ozone concentrations. *Atmospheric Environment*, **24B**, 303–312.
- Robinson, J. B., 1988: Unlearning and backcasting: Rethinking some of the questions we ask about the future. *Technological Forecasting and Social Change*, **33**, 325–338.
- Rogak, S. N., U. Pott, T. Dann and D. Wang, 1998: Gaseous emissions from vehicles in a traffic tunnel in Vancouver, British Columbia. *Journal of the Air and Waste Management Association*, **48**, 604–615.
- Runeckles, V., 2002: *A Citizen's Guide to Air Pollution*. chapter Effects on Vegetation and Ecosystems, p. 452 pp. David Suzuki Foundation, Vancouver, B.C., Canada.
- Russell, A. and R. Dennis, 2000: NARSTO critical review of photochemical models and modeling. *Atmospheric Environment*, **34**, 2283–2324.

- Russell, A., J. Milford, M. S. Bergin, S. McBride, L. McNair, Y. Yang, W. R. Stockwell and B. Croes, 1995: Urban ozone control and atmospheric reactivity of organic gases. *Science*, **269**, 491–495.
- Sakamaki, F. and H. Akimoto, 1988: HONO formation as unknown radical source in photochemical smog chamber. *Journal of Chemical Kinetics*, **20**, 111–116.
- Sakamaki, F., M. Okuda and H. Akimoto, 1982: Computer modeling study of photochemical ozone formation in the propene-nitrogen oxides-dry air system. *Environmental Science and Technology*, **16**, 45–52.
- Sawyer, R. F., R. A. Harley, S. H. Cadle, J. M. Norbeck, R. Slott and H. A. Bravo, 2000: Mobile sources critical review: 1998 NARSTO assessment. *Atmospheric Environment*, **34**, 2161–2181.
- Saylor, R. D., W. L. Chameides and E. B. Cowling, 1998: Implications of the new National Ambient Air Quality Standards for compliance in rural areas. *Journal of Geophysical Research*, **103**, 31137–31141.
- Schere, K. L. and G. M. Hidy, 2000: Foreword: NARTSO critical reviews. *Atmospheric Environment*, **34**, 1853–1860.
- Schroeder, M. R., 1991: *Fractals, Chaos, Power Laws: Minutes from an Infinite Paradise*. W. H. Freeman, New York, USA, 429 pp.
- Scire, J. S., F. R. Robe, M. E. Femau and R. J. Yamartino, 2000: A user's guide for the CALMET meteorological model. Technical report, Earth Tech Inc., Concord MA.
- Seaman, N. L., 2000: Meteorological modeling for air quality assessments. *Atmospheric Environment*, **34**, 2231–2259.
- Seinfeld, J. H., 1988: Ozone air quality models: a critical review. *Journal of the Air Pollution Control Association*, **38**, 616–654.
- Seinfeld, J. H. and S. N. Pandis, 1998: *Atmospheric Chemistry and Physics*. John Wiley and sons, New York, USA, 1326 pp.
- Shen, C. H., G. S. Springer and D. H. Stedman, 1977: Photochemical ozone formation in cyclohexane-nitrogen dioxide-air mixtures. *Environmental Science and Technology*, **11**, 151–158.
- Sillman, S., 1993: Tropospheric ozone: The debate over control strategies. *Annual Reviews of Energy and the Environment*, **18**, 31–56.
- Sillman, S., 1995: The use of  $NO_y$ ,  $H_2O_2$  and  $HNO_3$  as indicators for ozone- $NO_x$ -hydrocarbon sensitivity in urban locations. *Journal of Geophysical Research*, **100**, 14175–14188.
- Sillman, S., 1999: The relationship between ozone,  $NO_x$  and hydrocarbons in urban and polluted rural environments. *Atmospheric Environment*, **33**, 1821–1845.
- Sillman, S., J. A. Logan and S. C. Wofsy, 1990: The sensitivity of ozone to nitrogen oxides and hydrocarbons in regional ozone episodes. *Journal of Geophysical Research*, **95**, 1837–1851.
- Simonaitis, R., J. F. Meagher and E. M. Bailey, 1997: Evaluation of the condensed carbon bond (CB-IV) mechanism against smog chamber data at low VOC and  $NO_x$  concentrations. *Atmospheric Environment*, **31**, 27–43.

- Simpson, D., 1992: Long-period modeling of photochemical oxidants in Europe. Model calculations for July 1985. *Atmospheric Environment*, **26A**, 1609–1634.
- Simpson, D., 1993: Photochemical model calculations over Europe for two extended summer periods: 1985 and 1989. Model results and comparison with observations. *Atmospheric Environment*, **27A**, 921–943.
- Snyder, B., 2002: Meteorological summary of the Pacific 2001 air quality field study. Technical Report EC/GB 02-064, Environment Canada.
- Stedman, J. R. and M. L. Williams, 1992: A trajectory model of the relationship between ozone and precursor emissions. *Atmospheric Environment*, **26A**, 1271–1281.
- Steyn, D. G., 1996: *Air Pollution in Coastal Cities*. chapter Air Pollution Modelling and its Applications XI. Plenum Press.
- Steyn, D. G., 1998: Scaling the vertical structure of sea breezes. *Boundary Layer Meteorology*, **86**, 505–524.
- Steyn, D. G., J. W. Bottehnheim and R. B. Thomson, 1997: Overview of tropospheric ozone in the Lower Fraser Valley, and the Pacific '93 Field Study. *Atmospheric Science*, **31**, 2025–2035.
- Steyn, D. G. and D. A. Faulkner, 1986: The climatology of sea breezes in the Lower Fraser Valley, B.C. *Climatology Bulletin*, **20**, 21–39.
- Steyn, D. G. and T. R. Oke, 1982: The depth of the daytime mixed layer at two coastal sites: a model and its validation. *Boundary Layer Meteorology*, **24**, 161–180.
- Steyn, D. G., K. Ostermann and P. Bovis, 1999: Meteorology, emissions and ambient air quality during two episodes in the Lower Fraser Valley, B.C. Technical report, Atmospheric Science Programme, The University of British Columbia.
- Stockwell, W. R., H. Geiger and K. H. Becker, 2001: Estimation of incremental reactivities for multiple day scenarios: an application to ethane and dimethoxymethane. *Atmospheric Environment*, **35**, 929–939.
- Stockwell, W. R., F. Kirchner and M. Kuhn, 1997: A new mechanism for regional atmospheric chemistry modeling. *Journal of Geophysical Research*, **102**, 25847–25879.
- Stockwell, W. R., Middleton, J. Chang and X. Tang, 1990: The second generation regional acid deposition model chemical mechanism for regional air quality modeling. *Journal of Geophysical Research*, **95**, 16343–16367.
- Stohl, A., 1998: Computation, accuracy and applications of trajectories – a review and bibliography. *Atmospheric Environment*, **32**, 947–966.
- Stull, R. B., 1988: *An Introduction to Boundary Layer Meteorology*. Kluwer Academic Publishers, Dordrecht, The Netherlands, 670 pp.
- Stull, R. B., 2000: *Meteorology for Scientists and Engineers*. Brooks/Cole, Pacific Grove, CA., USA, 2nd edition, 502pp.
- Tanguay, M., A. Robert and R. Laprise, 1990: A Semi-Lagrangian fully compressible regional forecast model. *Monthly Weather Review*, **118**, 1970–1980.

- Taylor, E., 1992: The relationship between ground-level ozone concentrations, surface pressure gradients, and 850 mb temperatures in the Lower Fraser Valley of British Columbia. Technical Report PAES-92-3, Environment Canada.
- Taylor, G. I., 1950: The formation of a blast wave by a very intense explosion. II. The atomic explosion of 1945. *Proc. Roy. Soc.*, **A201**, 175–186.
- Thompson, A. M., 1992: The oxidizing capacity of the earth's atmosphere: Probable past and future changes. *Science*, **256**, 1157–1165.
- Tonnesen, G. S., 2000: User's guide for OZIPR Version 2.0. Technical report, National Research and Exposure Assessment Laboratory, U.S. EPA, Research Triangle Park, North Carolina, USA.
- Tonnesen, G. S. and R. L. Dennis, 2000a: Analysis of radical propagation efficiency to assess ozone sensitivity to hydrocarbons and NO<sub>x</sub> 1. Local indicators of instantaneous odd oxygen production sensitivity. *Journal of Geophysical Research*, **105**, 9213–9225.
- Tonnesen, G. S. and R. L. Dennis, 2000b: Analysis of radical propagation efficiency to assess ozone sensitivity to hydrocarbons and NO<sub>x</sub> 2. Long-lived species as indicators of ozone concentration sensitivity. *Journal of Geophysical Research*, **105**, 9227–9241.
- Tonnesen, S. and H. E. Jeffries, 1994: Inhibition of odd oxygen production in the Carbon Four and Generic Reaction Set mechanism. *Atmospheric Environment*, **28**, 1339–1349.
- Turco, R. P., 2002: *Earth Under Siege: From Air Pollution to Global Warming*. Oxford University Press, New York, NY, USA, 530 pp.
- United Nations Environmental Programme, 1992: *Urban Air Pollution in Megacities of the World*. Blackwell Reference, Cambridge, Mass., USA, 230 pp.
- University of North Carolina, 2001: CSIRO's outdoor chamber data for low NO<sub>x</sub> and VOC conditions. Technical report, Air Quality Research Group, Environmental Sciences and Engineering.
- Uno, I., S. Wakamatsu, R. A. Wadden, S. Konno and H. Koshio, 1985: Evaluation of hydrocarbon reactivity in urban air. *Atmospheric Environment*, **19**, 1283–1293.
- Venkatram, A., 1977: A model for internal boundary layer development. *Boundary Layer Meteorology*, **11**, 419–437.
- Venkatram, A., 2001: Challenges of air pollution modeling and its applications in the next millennium. in Gryning and Schiermeier, editors, *Air Pollution Modeling and Its Application XIV*. Kluwer Academic/Plenum Publishers.
- Venkatram, A., P. Karamchandani, P. Pai and R. Goldstein, 1994: The development and application of a simplified ozone modeling system (SOMS). *Atmospheric Environment*, **28**, 3665–3678.
- Vingarzan, R., 2004: A review of surface ozone background levels and trends. *Atmospheric Environment*, **38**, 3431–3442.
- Vingarzan, R. and B. Taylor, 2003: Trend analysis of ground level ozone in the greater Vancouver/Fraser Valley area of British Columbia. *Atmospheric Environment*, **37**, 2159–2171.
- Volz, A. and D. Kley, 1988: Evaluation of the Montsouris series of ozone measurements made in the nineteenth century. *Nature*, **332**, 240–242.

- Weibull, W., 1951: A statistical distribution function of wide applicability. *Journal of Applied Mechanics*, **73**, 293–297.
- West, G. W., J. H. Brown and B. J. Enquist, 1997: A general model for the origin of biometric scaling laws in biology. *Science*, **276**, 122–126.
- Wilks, D. S., 1995: *Statistical Methods in the Atmospheric Sciences*. volume 59 of *International Geophysics Series*. Academic Press, 467 pp.
- Wolffe, G. T. and P. E. Korsog, 1992: Ozone control strategies based on the ratio of volatile organic compounds to nitrogen oxides. *Journal of the Air and Waste Management Association*, **42**, 1173–1177.
- World Meteorological Association, 1998: Scientific assessment of ozone depletion:1998. Technical report, World Meteorological Association, Geneva, Switzerland.
- Wu, C. H., S. M. Japar and H. Niki, 1976: Relative reactivities of HO-hydrocarbon reactions from smog chamber studies. *Journal of Environmental Science and Health – Environmental Science and Engineering*, pp. 191–200, volume A11.
- Yin, D., W. Jiang, H. Roth and E. Giroux, 2004: Improvement of biogenic emissions estimation in the Canadian Lower Fraser Valley and its implication on particulate matter modeling results. *Atmospheric Environment*, **38**, 507–521.

## Appendix A

# Buckingham Pi Method of Dimensional Analysis

### A.1 Buckingham Pi Theorem

The Buckingham Pi method is a systematic approach to dimensional analysis developed by the engineering scientist Buckingham (Buckingham, 1914). The method relies on the principle of dimensional homogeneity which states that in any correct and complete equation for a physical relationship, all terms must have the same dimensions. This implies that the relationship between various physical quantities is independent of arbitrary choice of units used to describe the variables.

By means of this principle, Buckingham (Buckingham, 1915) showed that given an equation:

$$Q_0 = F(Q_1, Q_2, \dots, Q_{n-1}) \quad (\text{A.1})$$

describing a relationship among  $n$  different variables  $Q_0, Q_1, \dots, Q_{n-1}$ , it is always possible to reduce it to the form

$$\Pi_0 = f(\Pi_1, \Pi_2, \dots, \Pi_{n-k-1}) \quad (\text{A.2})$$

where each the variables  $\Pi_i$  represents a dimensionless product given by

$$\Pi_i = Q_0^a Q_1^b \dots Q_{n-1}^n \quad (\text{A.3})$$

with  $k$  being the number of independent fundamental units needed to describe the  $n$  different variables and  $f$  is an unknown function. A mathematical proof of this theorem can be found in Bluman and Anco (2002).

While the theorem gives the number of dimensionless quantities needed to describe the behaviour of a given dimensionless dependent variables, the forms of the dimensionless variables ( $\Pi_i$ ) are still unknown. The method then provides a series of steps used to determine these. Below, the method is illustrated, using the example of the growth of an atmospheric shockwave, following the approach outlined in Stull (1988). These form of reasoning was used by G.I. Taylor Taylor (1950) to deduce the approximate energy released by the first atomic bomb blast — before this information

was declassified.

### Step 1: Relevant Variables

The first and most important step is the selection of a complete set of variable  $Q_1, \dots, Q_{n-1}$  which determine  $Q_0$ . A set is complete if it contains all of the variables that effects  $Q_0$ .

For the example of a spreading shock wave, the unknown variable  $Q_0$  is the shock wave radius  $R$ . A complete set of variable which characterize  $R$  is:

$Q_1 = E$  is the energy released by the explosion

$Q_2 = t$  is the elapsed time since the explosion occurred

$Q_3 = P_o$  ambient pressure

$Q_4 = \rho_o$  ambient atmospheric density

### Step 2: Variable Dimensions

Next, the dimensions of all of the variables are expressed in terms of the fundamental dimensions. For the SI system these are: length ( $\mathcal{L}$ ), mass ( $\mathcal{M}$ ), time ( $\mathcal{T}$ ), temperature ( $\mathcal{K}$ ), electric current ( $\mathcal{A}$ ), luminous intensity ( $\mathcal{I}$ ) and species number ( $\mathcal{N}$ ).

For the shock wave problem the variables have the following dimensions:  $R$  ( $\mathcal{L}$ ),  $E$  ( $\mathcal{MLT}^2$ ),  $P_o$  ( $\mathcal{MLT}^{-2}$ ) and  $\rho_o$  ( $\mathcal{ML}^{-3}$ ).

### Step 3: Fundamental Dimensions

This step involves determining the number of different fundamental dimensions in the problem. For the shockwave problem, there are three:  $\mathcal{MLT}$ .

### Step 4: Key Variables

From the set of  $n - 1$  independent variables, a subset of  $k$  key variables are chosen subject to the following rules:

- The number of key variables most equal the number of fundamental dimensions.
- All the of problem's fundamental dimensions must be represented in the key variables.
- No dimensionless groups can be formed from any combination of the key variables.

The selection of key variables is not always unique; in many cases there can be several valid choices.

For our example, with three fundamental dimensions, the group:  $t$ ,  $E$  and  $\rho_o$  can be used. They contain the three fundamental dimensions and no dimensionless groups can be made from them.

### Step 5: Pi- Groups

In this step, the key variables are used to make dimensionless the dependent variable and the remaining independent variable by dividing each by the product of powers of the key variables. These dimensionless groups are called Pi-groups and there will always be  $n - k$  such groups.

In our example, with 5 variables and 3 fundamental dimensions, there will be two Pi-groups. The first is the shockwave radius and it is made dimensionless by:

$$\Pi = \frac{R}{\left[\frac{Et^2}{\rho_o}\right]^{1/5}} \quad (\text{A.4})$$

while the second group for pressure is made dimensionless by:

$$\Pi_1 = \frac{P_o}{\left[\frac{t^6}{E^2\rho^3}\right]^{1/5}} \quad (\text{A.5})$$

### Step 6: Alternative Pi-groups

This is an optional step which permits the creation of new Pi-groups from the original ones provided that the number of Pi-groups remains the same, all variables are still represented and no Pi-groups can be formed from any combination of the other groups.

### Similarity Relationship

The end result of the Buckingham Pi analysis is a description of the system in terms of a smaller set of variables. The analysis does not give the form of the functional relationship between the Pi-groups. This has to be found experimentally or by theoretical means.

For the shockwave problem, the analysis shows:

$$R = \left[\frac{Et^2}{\rho_o}\right]^{-1/5} f\left(P_o \left[\frac{t^6}{E^2\rho^3}\right]^{-1/5}\right) \quad (\text{A.6})$$

where  $f$  is still an unknown function. Taylor used A.6 and consecutive frames of a declassified film to determine the relationship between Pi-groups and ultimately estimate the energy released in the atomic blast.

## Appendix B

# OZIPR Trajectory Model

### B.1 Overview

OZIPR is a trajectory model which simulates complex chemical, meteorological and physical processes acting on a column of air as it advects along a wind trajectory. It is a research-oriented version of the US Environmental Protection Agency's (EPA) OZIPP (Ozone Isopleth Plotting Package) computer modeling program. While the original aim of OZIPP was to aid in the development of air quality management plans, the main goal of OZIPR is to provide a comprehensive research tool (Tonnesen, 2000).

The model is designed to be flexible. Simulation details, controlled through input files, include: the choice of chemical mechanisms, the hourly values for column temperature, humidity, pressure and mixed layer depth. In addition, elevated pollutant layer can be prescribed and entrained into the column as the mixed layer depth grows and the injection of precursors, into the column, as it passes over different emission sources can be given. Finally deposition rates for many pollutants can be set.

For an in-depth description of how the model is run, please see Gery et al. (1989). The remainder of this appendix describes the model set-up used in this thesis.

### B.2 Model Set-up

#### Simulation Modes

OZIPR can be set-up to perform a single trajectory simulation or it can perform a set of such simulations, for various fixed emission intervals, to determine the response of ozone as a function of initial precursors. This mode was used to develop ozone response surfaces for the scaling analyses. In this mode, a matrix of simulations is generated by systematically varying initial VOC and NO<sub>x</sub> emissions at fixed increments. Typically, 10% increments are used for an 11 × 11 matrix of initial conditions, but in some cases finer increments, resulting in a greater number simulations, were used.

## Chemical Mechanisms

Any chemical mechanism can be used with OZIPR once properly formatted. In this thesis, I have used OZIPR with the RADM2 mechanism (Stockwell et al., 1990), the CBM (Gery et al., 1989) and a modified version (Jiang et al., 1996) of the SAPRC 90 mechanism (Carter, 1990). Any organic compound may be included in the mechanism provided that its carbon number is specified. The model allows up to 20 VOC species (and 90 total species).

A maximum of 270 reactions are permitted. Each reaction requires a rate expression which may depend on solar zenith angle (photolysis reactions) or even other reactions. The rates of photolytic reactions can vary with solar elevation by supplying the model with rates at 10 angles which the model uses to interpolate for any angle. Up to 35 photolysis reactions may be included. Each reaction in the mechanism can include between zero and three reactants. Molecular oxygen ( $O_2$ ), nitrogen ( $N_2$ ) and generic background molecules ( $M$ ) may be used as reactants.

## Simulation Location

Each simulation requires a location (longitude and latitude) as well as time (day, month and year) in order to determine the solar zenith angle throughout the simulation. In addition, starting and ending hours for the simulation must be provided. All simulations were performed for the Vancouver B.C. region (latitude  $49.25^\circ$  and longitude  $123.15^\circ W$ ) starting at 7 : 00 a.m. and ending at 6 : 00 p.m. (local daylight savings time) for various summer days.

## Meteorological Conditions

Hourly values for column temperature, pressure, relative humidity and mixed layer height are required to characterize the meteorological conditions. For the smog chamber simulations, the mixed layer depth was held constant. Temperatures were set at a constant value throughout each simulation. Typically, the level was set at  $25^\circ C$  but a range of values from  $20$  to  $35^\circ C$  was also used. All smog chamber simulations used typical Vancouver ambient fair weather summer conditions for pressure ( $1013.25\text{ mb}$ ) and relative humidity of 50% (Steyn et al., 1999).

## Emissions

OZIPR distinguishes between three types of emissions: those emitted directly from the surface layer and which can be controlled, those which are carried into a region and cannot be controlled and emissions that result from entrainment of elevated polluted layers due to a growing mixed layer. In addition, the model allows for pollutants to be initially in the column: The speciation of VOC

compounds can be different for the surface emissions, transported emissions and the elevated layers. The ratio of NO to  $NO_2$  can also be set. The smog chamber simulations had no emissions — all precursors were assumed to be initially well mixed in the column.

### **Numerical Set-up**

The numerical solver for OZIP uses a Gear solver with a range of tolerances from 0.1 to 0.00001. All simulations used a tolerance of 0.0001. The time step for integrating the reactions varied between 5 and 10 minutes depending on the tolerance used in the Gear solver.

## Appendix C

# RADM2 Chemical Mechanism

### C.1 Overview

RADM2 is the second generation version of the Regional Acid Deposition Model (RADM1), a chemical mechanism originally used to study acid deposition on a regional scale. RADM2 provides a more complete representation of gas phase chemistry than RADM1 and is well suited for studying atmospheric chemistry. Nonetheless, because of the multitude of chemical species found in an urban atmosphere, the mechanism includes only the most significant reactions in its formulation including: the inorganic chemistry of nitrogen, ozone and sulfur containing species, a simplified treatment of organic chemistry using a small set of VOC classes and a detailed handling of radical chemistry. In total 21 photolysis reactions and 124 thermal reactions, involving 63 species, are modeled. In this appendix, a summary of the various modeled species is given. A complete description of the model, a listing of all reactions and comparisons with smog chamber data can be found in Stockwell et al. (1990).

### C.2 Stable Inorganic Species

The inorganic chemistry of nitrogen, ozone and sulphur in the troposphere is well known (Stockwell et al., 1990) and modeled using seven inorganic nitrogen species, two sulphur species as well as ozone and hydrogen peroxide. The model also includes reactions involving carbon dioxide, carbon monoxide and hydrogen gas. Table C.1 lists the inorganic species modeled in RADM2. The model includes seven photolysis reactions for stable inorganic species, the most important being the photolysis of  $NO_2$ . Included in the list of stable species is  $NO_3$ , an important sink for nitrogen at night, but short-lived during daylight hours.

### C.3 Stable Organic Species

Organic chemistry is treated in the model using 26 species lumped into seven broad classes representing: alkanes, alkenes, aromatics, carbonyl compounds, organic nitrates, organic peroxides and

Species	Definition
Nitrogen	
$NO_2$	Nitrogen dioxide
$NO$	Nitric oxide
$HONO$	Nitrous acid
$NO_3$	Nitrogen trioxide
$N_2O_5$	Nitrogen pentoxide
$HNO_4$	Pernitric acid
$HNO_3$	Nitric acid
Oxidants	
$O_3$	Ozone
$H_2O_2$	Hydrogen peroxide
Sulphur	
$SO_2$	Sulfur dioxide
$SULF$	Sulfuric acid
Carbon Oxides	
$CO$	Carbon monoxide
$CO_2$	Carbon dioxide
Other Species	
$H_2$	Hydrogen
$O_2$	Oxygen
$N_2$	Nitrogen
$H_2O$	Water

Table C.1: RADM2 Chemical Species List for inorganic compounds (based on (Stockwell et al., 1990)).

organic acids. An organic compound is placed into one of these classes based on its oxidations pathways and emissions rates. Each class is represented by several VOCs, having a range of reactivities and classes with a wider range of reactivities or more complex chemistry are represented by a larger number of VOC species. Table C.2 lists the stable organic species found in the mechanism.

For the alkanes, methane ( $CH_4$ ) and ethane (ETH) are treated explicitly while all other alkanes are represented by one of the remaining 3 alkane species (HC3, HC5 and HC8) based on  $OH^\bullet$  reactivity. For the alkenes, ethene (OL2) is treated explicitly, alkenes with internal double bonds by OLI and terminal double bonds by OLT. Isoprene (ISO) is treated separately. Aromatic chemistry is handled primarily by the TOL and XYL species with CSL being used to represent cresol and other hydroxy aromatic compounds. Carbonyl compounds, the sum of aldehydes and ketones, are modeled using HCHO for formaldehyde, ALD for acetaldehyde and higher aldehydes and KET for all ketones. Glyoxal (GLY), methylglyoxal (MGLY) and unsaturated dicarbonyls (DCB) are used to represent carbonyl compounds produced from aromatic decomposition. Three species are used to represent organic nitrogen, the most important being PAN. The five remaining classes are used for organic peroxides and acids.

## C.4 Organic and Inorganic Radicals Species

Finally, because of the importance of radicals in gas phase atmospheric chemistry, radicals reactions are treated extensively, including four inorganic and 17 organic radicals. Atomic oxygen in its singlet

Species	Definition
Alkanes	
CH <sub>4</sub>	Methane
ETH	Ethane
HC3	Alkanes with OH-rate constant between $2.7 \times 10^{-13}$ and $3.4 \times 10^{-12}$
HC5	Alkanes with OH-rate constant between $3.4 \times 10^{-12}$ and $6.8 \times 10^{-12}$
HC8	Alkanes with OH-rate constant greater than $6.8 \times 10^{-12}$
Alkenes	
OL2	Ethene
OLT	Terminal alkenes
OLI	Internal alkenes
ISO	Isoprene
Aromatics	
TOL	Toluene and less reactive aromatics
CSL	Cresol and other hydroxyl substituted aromatics
XYL	Xylene and more reactive aromatics
Carbonyls	
HCHO	Formaldehyde
ALD	Acetaldehyde and higher aldehydes
KET	Ketones
GLY	Glyoxal
MGLY	Methylglyoxal
DCB	Unsaturated dicarbonyls
Organic nitrogen	
PAN	Peroxyacetyl nitrate and higher PANs
TPAN	H(CO)CH=CHCO <sub>3</sub> NO <sub>2</sub>
ONIT	Organic nitrate
Organic peroxides	
OP1	Methyl hydrogen peroxide
OP2	Higher organic peroxides
PAA	Peroxyacetic acid
Organic acids	
ORA1	Formic acid
ORA2	Acetic acid and higher acids

Table C.2: RADM2 Chemical Species List for organic compounds (based on (Stockwell et al., 1990)).

and triplet state are modeled explicitly and are produced in ozone photolysis reactions.  $O^3P$  is also produced from the photolysis of  $NO_3$  and the quenching of  $O^1D$  upon collision with molecular nitrogen or oxygen. The mechanism also explicitly models the hydroxyl radical (HO) and the hydroperoxy radical (HO<sub>2</sub>).

The formation and reaction of organic peroxy radicals is highly parameterized due to the limited number peroxy radicals included in the mechanism and the large uncertainties in measured peroxy radical-peroxy radical reaction rates.

Species	Definition
Inorganic	
Atomic species	
$O^3P$	Ground state oxygen atom
$O^1D$	Excited state oxygen atom
Odd hydrogen	
$HO$	Hydroxy radical
$HO_2$	Hydroperoxy radical
Organic	
Peroxy radicals from alkanes	
$MO_2$	Methyl peroxy radical
$ETHP$	Peroxy radical formed from alkane $ETH$
$HC_3P$	Peroxy radical formed from alkane $HC_3$
$HC_5P$	Peroxy radical formed from alkane $HC_5$
$HC_8P$	Peroxy radical formed from alkane $HC_8$
Peroxy radicals from alkenes	
$OL_2P$	Peroxy radical formed from alkene $OL_2$
$OLTP$	Peroxy radical formed from alkene $OLT$
$OLIP$	Peroxy radical formed from alkene $OLIP$
Peroxy radicals from aromatics	
$TOLP$	Peroxy radical formed from aromatic $TOL$
$XYLP$	Peroxy radical formed from aromatic $XYL$
Peroxy radicals from carbonyl groups	
$ACO_3$	Acetylperoxy radical
$KETP$	Peroxy radical formed from ketone $KET$
$TCO_3$	$H(CO)CH=CHCO_3$
Peroxy radicals involving nitrogen	
$OLN$	$NO_3$ -alkene adduct
$XNO_2$	Accounts for additional organic nitrate formation affected by the lumped organic species
$XNO$	Accounts for additional $NO$ to $NO_2$ conversions affected by the lumped organic species

Table C.3: RADM2 Chemical List for Radicals Species (based on (Stockwell et al., 1990)).

## Appendix D

# Composite Weibull Models and the WEX Model

### D.1 Overview

In this appendix, different methods used to fit data showing a bend or 'dogleg' using Weibull distributions are discussed. These applications – used extensively in the field of reliability engineering – describe systems whose failure rates are controlled by different processes. This material is included to show first, that other methods of fitting mixed Weibull distributions exist and secondly, the one used in this thesis, the WEX model, appears to be a better method due to its ease at parameter selection. However, I must point out, there does not appear to be any direct connection between the concept of system reliability and the photochemical production of ozone.

### D.2 Weibull Distribution and Failure Rates

A variety of methods used to fit Weibull data, showing a bend or 'dogleg', can be found in the field of reliability engineering (Jiang and Kececioglu, 1992), (Jiang and Murthy, 1995b), (Jiang and Murthy, 1995a), (Jiang and Murthy, 1997), (Jiang et al., 1999). In this field, the term 'reliability' is used to express the a probability an object will perform its intended duty for a specific amount of use. Associated with this term is 'failure rate' defined as the probability that failure takes place before some level of use is reached. Examination of failure rates is often used to study the behaviour of complex systems. For many inanimate objects, living entities and complex systems, failure rates have a characteristic 'bathtub' curve. Such a curve, shown in Figure 1, is represented by an initial region of high but decreasing failure rates (wearin). These early failures are associated with inherent defects and weaknesses. As the defective and weak objects fail, they are removed from the population and failure rates decrease. The middle part of the curve shows the smallest and almost constant failure rates. Failures in this section are referred to as random failures and usually stem from unusual operating conditions as opposed to inherent defects. Eventually, the

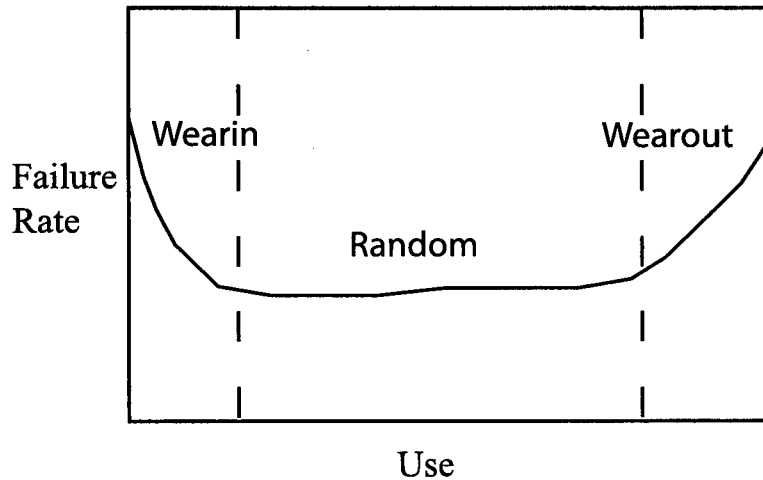


Figure D.1: A 'bathtub' curve showing changing failure rates with increasing use.

failure rates begin to rise again due to aging. These failures are caused by the cumulative effects like corrosion and are called wearout failures.

The Weibull distribution is widely used in reliability engineering because, through the proper selection of parameters, it can model wearin, wearout and constant failure rates. When using the Weibull distribution to model reliability, a system's failure rate ( $\Phi$ ) is given by a simple power law:

$$\Phi(R) = \frac{\alpha}{\beta} \left( \frac{R}{\beta} \right)^{\alpha-1} \quad (\text{D.1})$$

When  $\alpha = 1$ , a constant failure rate is modeled. For  $\alpha < 1$ , failure rates are typical of wearin phenomena and decrease while for  $\alpha > 1$ , failure rates are typical of wearout and increase. When an object shows more than one failure mode, a single Weibull distribution may not be sufficient to characterize its behaviour. In such instances, more complex methods, called multimodal analysis, are required.

### D.2.1 Three Parameter Weibull

Before examining multimodal analysis, it is worth discussing the 3-parameter Weibull model. This model uses an additional position parameter to accommodate data which vanishes at some value ( $R_o$ ) not necessarily zero (Weibull, 1951) i.e.:

$$F(R; \alpha, \beta, R_o) = 1 - \exp \left\{ - \left( \frac{R - R_o}{\beta} \right)^\alpha \right\} \quad (\text{D.2})$$

When this distribution is transformed to the Weibull plane, a concave curve is obtained. Adjusting the value of  $R_o$  has the effect of bending the curve up or down for small  $R$ . Alternatively, the

positional parameter can be thought of as an offset to be removed from all points before fitting with a standard 2-parameter Weibull. Conditioning data in this way straightens out bends for small  $R$ . However, it must be noted that for all of the ozone simulations, the presence of the 'dogleg' bend could not be removed through the use of a position parameter. This suggests the bend does not stem from an offset and a single 3-parameter Weibull cannot be used to explain the multi-mode behaviour inherent in the similarity relationship.

### D.3 Multimodal Analysis

A multimodal analysis is needed when reliability data show more than one failure mode. This is apparent when failure frequencies are plotted versus time of failure and, after Weibull transforming, the observations cluster around two straight lines. In such instances, the Weibull plot shows a bend or 'dogleg' in the data and two Weibull distributions must be used to fit the data. While there are many different techniques for combining two Weibull distributions, all accomplish the same objective: to provide a close fit to the data using a single smooth and continuous curve. Four methods used to combine two Weibulls are: the sectional model, the mixed model, the multiplicative model and the competing risk model. The suitability of these models, and the WEX model introduced in chapter 3, are discussed in the next sections using model output from OZIPR simulations using the RADM2 OLT class.

#### D.3.1 Sectional Model

In order to smoothly fit two Weibull distributions into a single distribution  $F$ , two separate distributions  $F_1(R; \alpha_1, \beta_1)$  and  $kF_2(R; \alpha_2, \beta_2)$  can be matched at break point  $R_b$ . This requires a total of six parameters:  $\alpha_1, \beta_1, \alpha_2, \beta_2, k, R_b$  but the constraints that  $F$  and  $F'$  be continuous, reduces the number of free parameters to four. This method has been used to fit the scaled ozone data from the OLT simulation and Figure D.2A shows this method fits the model output quite well. However, selection of the four free parameters is not straight forward. As a first guess, each distribution is fitted by a Weibull. These four fitted parameters  $(\alpha_1, \beta_1, \alpha_2, \beta_2)$  are then used to determine the remaining two  $(k, R_b)$ . Next, individual parameters are varied to improve the fit. This results in an iterative fitting procedure which is slow and involves a fair amount of trial and error. The model has also been judged to have no physical basis (Jiang and Murthy, 1995b).

### D.3.2 Mixed Model

For the mixed Weibull model, a weighted sum of two different distributions is used:

$$F(R) = pF_1(R; \alpha_1, \beta_1) + (1 - p)F_2(R; \alpha_2, \beta_2) \quad (\text{D.3})$$

where the unknown weighting factor  $p$  must be determined in addition to the four Weibull parameters  $(\alpha_1, \beta_1, \alpha_2, \beta_2)$ . Thus, this model requires 5 parameters. In theory, the extra parameter allows for a better fit, although in practice it is much more difficult to find the optimum choice for all five. The effect of the additional parameter, has a similar effect to using a 3-parameter Weibull for one of the two initial distributions. Figure D.2B shows the OLT data fit with the mixed model. The fit is very good but the process of finding the correct 5 parameters is slow. A physical justification for this model assumes that a collection of objects is composed of two sub-populations, in the proportions  $p$  and  $1 - p$ , having lifetimes described by  $F_1$  and  $F_2$ , respectively. As a result, the lifetimes of the entire population is a simple mixture of these two sub-populations.

### D.3.3 Multiplicative Model

The distribution function for a multiplicative model of two Weibulls is given by:

$$F(R) = F_1(R; \alpha_1, \beta_1) \times F_2(R; \alpha_2, \beta_2) \quad (\text{D.4})$$

As a physical basis for this model, consider a system with two independent failure mechanisms. Failure occurs when both mechanisms fail (i.e. the failure mechanisms act in parallel). If the time to failure ( $T_1$ ), due to the first cause, is distributed according to  $F_1$  and time to failure ( $T_2$ ), due to the second given by  $F_2$ , then system failure is given by the maximum of  $\{T_1, T_2\}$ ; modeled using  $F = F_1 \times F_2$ .

This model requires four parameters and has been fit to the OLT data in Figure D.2C. Again, the fit is excellent but the process of finding the optimum parameters values involves trial and error and the intersection of the two Weibull curves does not give the location of the scaling break.

### D.3.4 Competing Risk Model

The competing risk model uses the complement of the Weibull function ( $\bar{F} = 1 - F$ ), called the survivor function, to fit the data:

$$\bar{F}(R) = \bar{F}_1(R) \times \bar{F}_2(R) \quad (\text{D.5})$$

Again, four parameters are required and their selection requires some trial and error. A physical justification for this model involves system failure rates given by two independent mechanism acting

in series. As a result,  $F$  models the minimum of two failure times. This model always produces a concave curve in the Weibull plane (Jiang and Murthy, 1995a). Since all simulations appear to produce more convex profiles, this model does not seem suitable for parameterizing the similarity relationship.

#### D.4 WEX Model

Finally, there is the WEX model introduced in Chapter 2. The model was developed in order to produce a composite of two Weibull curves whose unknown parameters were directly determined by the geometric properties of the two line segments. Thus the four parameters are found using the two slopes ( $\alpha_1, \alpha_2$ ) and the location of the intersection ( $\beta, \lambda$ ) of the line segments:

$$\begin{aligned} F(R) &= 1 - \exp \left\{ -\lambda (R/\beta)^{\alpha(R)} \right\} \\ \alpha(R) &= \left( \frac{\alpha_2 - \alpha_1}{2} \right) \tanh(R - \beta) + \left( \frac{\alpha_1 + \alpha_2}{2} \right) \\ &= WEX(R; \alpha_1, \alpha_2, \beta, \lambda) \end{aligned} \tag{D.6}$$

Initial estimates of these values can be found by inspections or simple linear regression and subsequent parameter refinements proceed with much less trial and error. Figure D.2 shows the WEX approximation to the OLT data gives as good a fit as the other methods. Generally, each method is capable of capturing the multimodal behaviour but the WEX model has been chosen in this thesis based on its ease at parameter selection. Also, while there is no physical basis for the WEX model, by preserving the geometric properties of the line segments, it is hoped that the values for the four WEX parameters can be associated with physically important processes in the VOC-NO<sub>x</sub> photochemistry.

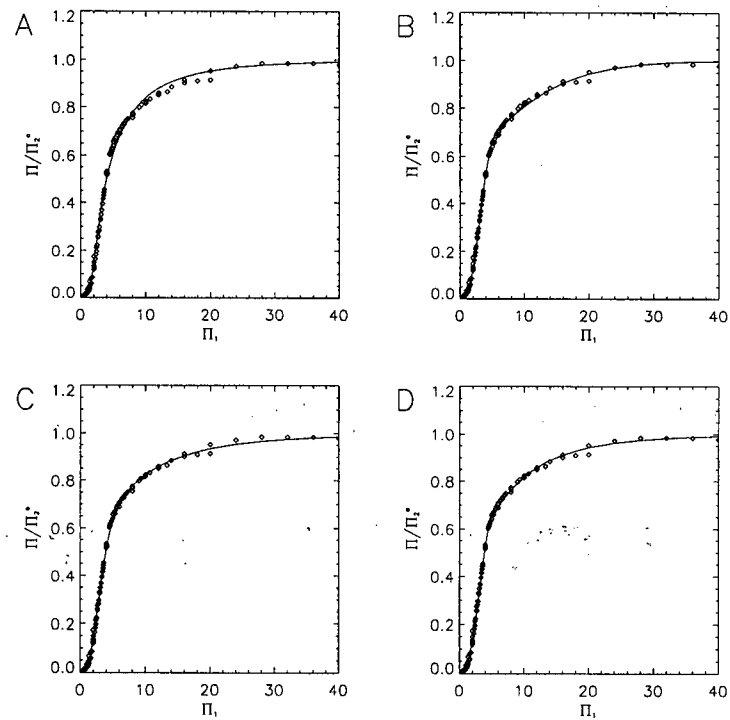


Figure D.2: A comparison of four different methods of fitting model output with different 2-Weibull models. In all Figures, scaled model output is given by the symbols and the 2-Weibull models are given by the solid lines. Model output using the RADM2 (Stockwell et al., 1990) model with OLT as the sole VOC. Figure A shows a sectional model B a mixed model C a multiplicative model and D gives the WEX model.

## Appendix E

# Weibull and Isopleths Plots for Various VOC compounds

In this appendix all Weibull and isopleth plots for the various VOC compounds and mixtures based on the RADM2, CB-IV and COND2243 chemical mechanisms are given. First plotted are results for the RADM2 classes.

### E.1 RADM2 Classes

#### E.1.1 Alkanes

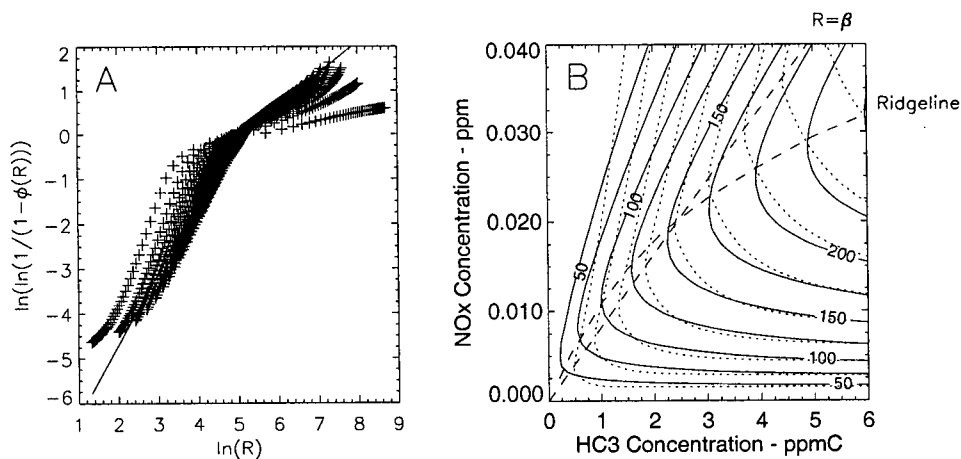


Figure E.1: Weibull transformed OZIPR model output (+) for HC3 as a function of  $\ln R$  (figure A). Solid line is WEX model. In Figure B, the same results are plotted in the more conventional form of ozone isopleths (in ppb) with OZIPR model output in solid lines and WEX model in dotted lines. The two dashed lines refer to ridgelines for the OZIPR isopleths and the WEX model. Both were found by locating the region where ozone shows no sensitivity to changing NOx.

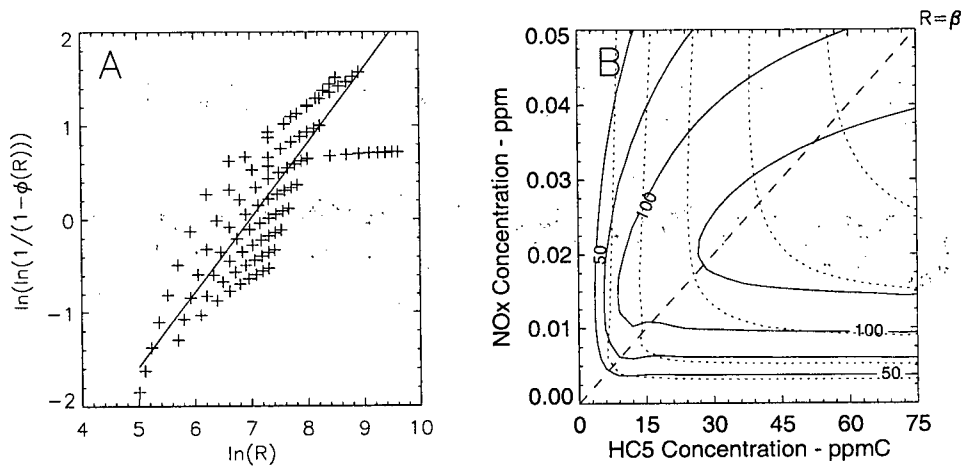


Figure E.2: Weibull transformed OZIPR model output (+) for HC5 as a function of  $\ln R$  (figure A). Solid line is WEX model. In Figure B, the same results are plotted in the more conventional form of ozone isopleths (in ppb) with OZIPR model output in solid lines and WEX model in dotted lines. The two dashed lines refer to ridgelines for the OZIPR isopleths and the WEX model. Both were found by locating the region where ozone shows no sensitivity to changing  $NO_x$ .

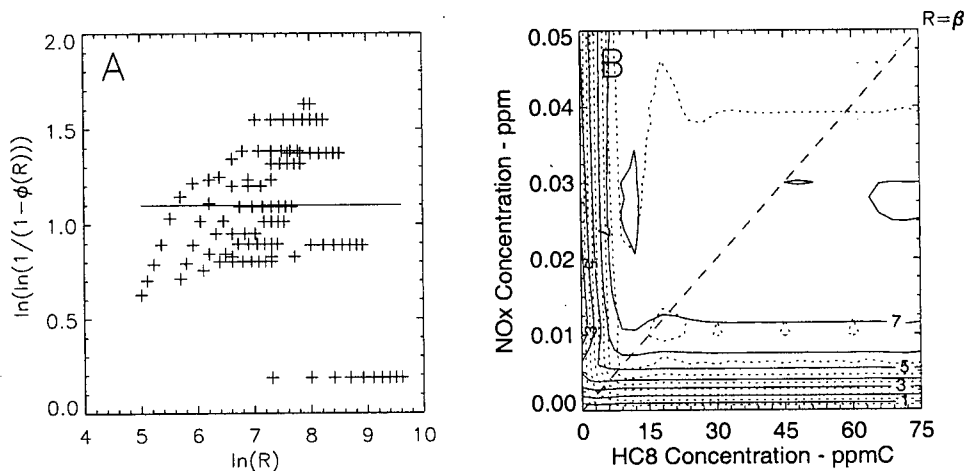


Figure E.3: Weibull transformed OZIPR model output (+) for HC8 as a function of  $\ln R$  (figure A). Solid line is WEX model. In Figure B, the same results are plotted in the more conventional form of ozone isopleths (in ppb) with OZIPR model output in solid lines and WEX model in dotted lines. The two dashed lines refer to ridgelines for the OZIPR isopleths and the WEX model. Both were found by locating the region where ozone shows no sensitivity to changing  $NO_x$ .

## E.1.2 Alkenes

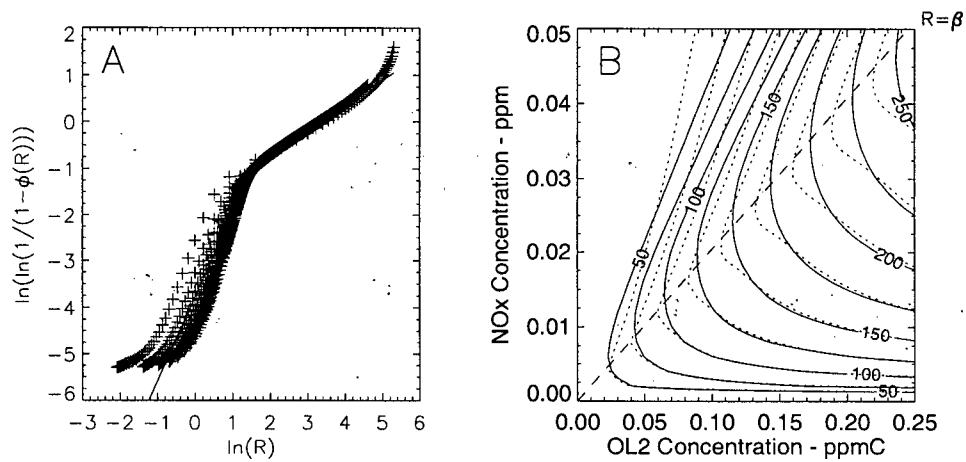


Figure E.4: Weibull transformed OZIPR model output (+) for OL2 as a function of  $\ln R$  (figure A). Solid line is WEX model. In Figure B, the same results are plotted in the more conventional form of ozone isopleths (in ppb) with OZIPR model output in solid lines and WEX model in dotted lines. The dashed line represents the scaling break  $R = \beta$ .

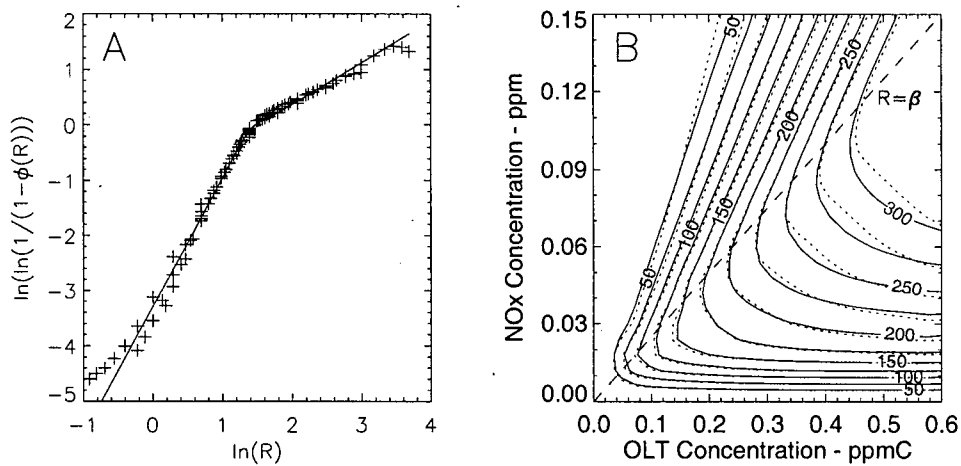


Figure E.5: Weibull transformed OZIPR model output (+) for OLT as a function of  $\ln R$  (figure A). Solid line is WEX model. In Figure B, the same results are plotted in the more conventional form of ozone isopleths (in ppb) with OZIPR model output in solid lines and WEX model in dotted lines. The dashed line represents the scaling break  $R = \beta$ .

## E.1.3 Aromatics

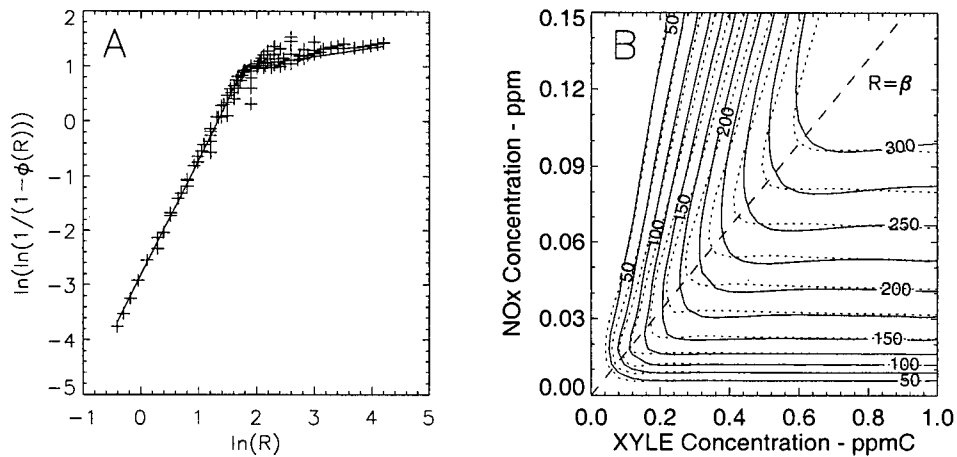


Figure E.6: Weibull transformed OZIPR model output (+) for XYLE as a function of  $\ln R$  (figure A). Solid line is WEX model. In Figure B, the same results are plotted in the more conventional form of ozone isopleths (in ppb) with OZIPR model output in solid lines and WEX model in dotted lines. The dashed line represents the scaling break  $R = \beta$ .

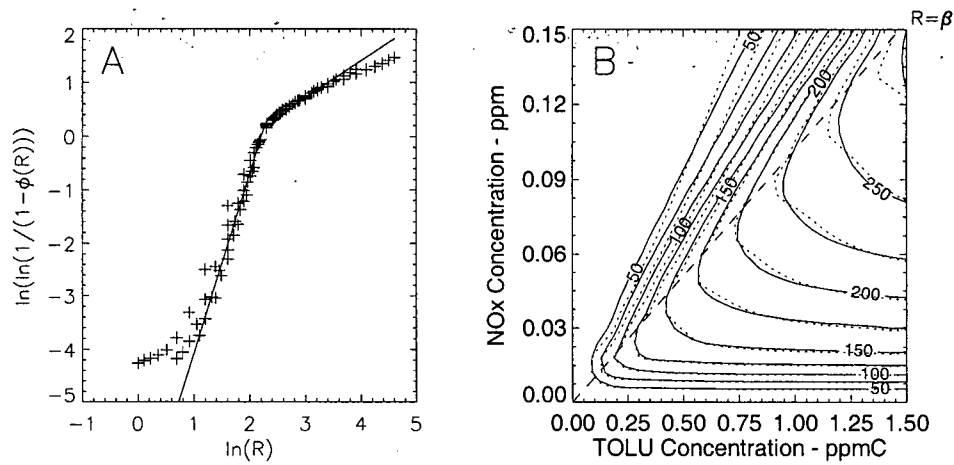


Figure E.7: Weibull transformed OZIPR model output (+) for TOLU as a function of  $\ln R$  (figure A). Solid line is WEX model. In Figure B, the same results are plotted in the more conventional form of ozone isopleths (in ppb) with OZIPR model output in solid lines and WEX model in dotted lines. The dashed line represents the scaling break  $R = \beta$ .

## E.1.4 Carbonyls

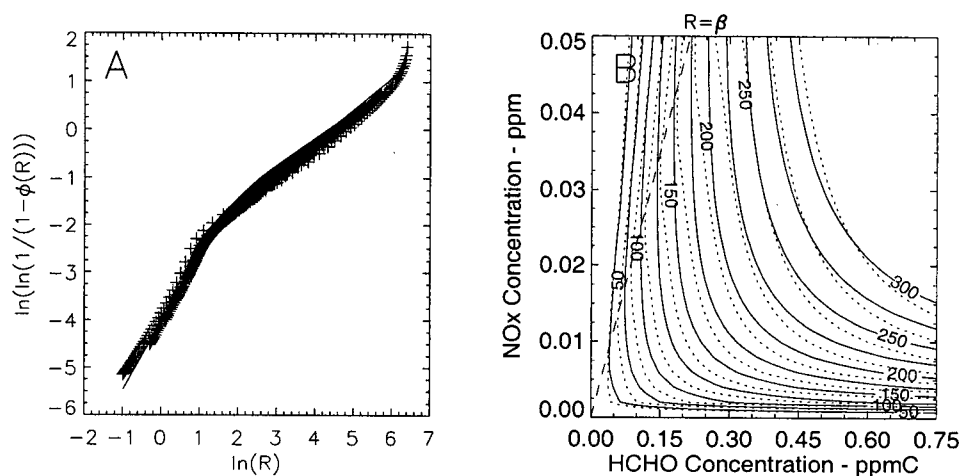


Figure E.8: Weibull transformed OZIPR model output (+) for HCHO as a function of  $\ln R$  (figure A). Solid line is WEX model. In Figure B, the same results are plotted in the more conventional form of ozone isopleths (in ppb) with OZIPR model output in solid lines and WEX model in dotted lines. The dashed line represents the scaling break  $R = \beta$ .

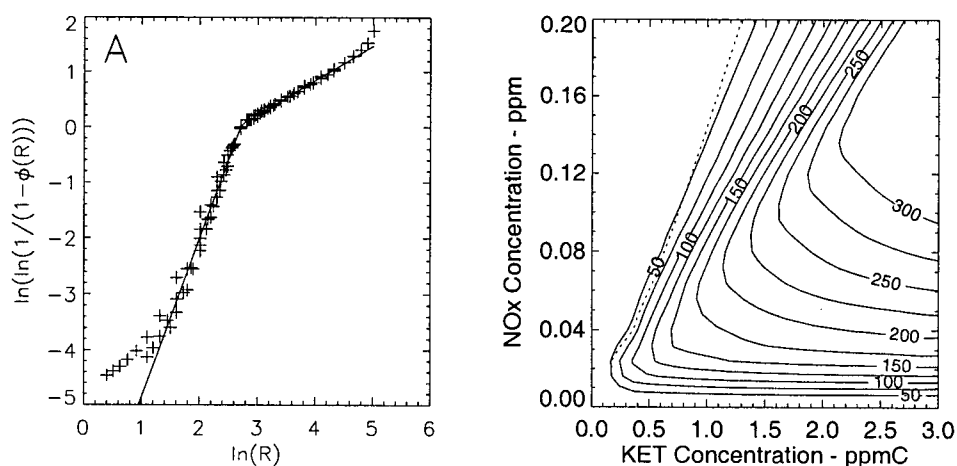


Figure E.9: Weibull transformed OZIPR model output (+) for KET as a function of  $\ln R$  (figure A). Solid line is WEX model. In Figure B, the same results are plotted in the more conventional form of ozone isopleths (in ppb) with OZIPR model output in solid lines and WEX model in dotted lines. The dashed line represents the scaling break  $R = \beta$ .

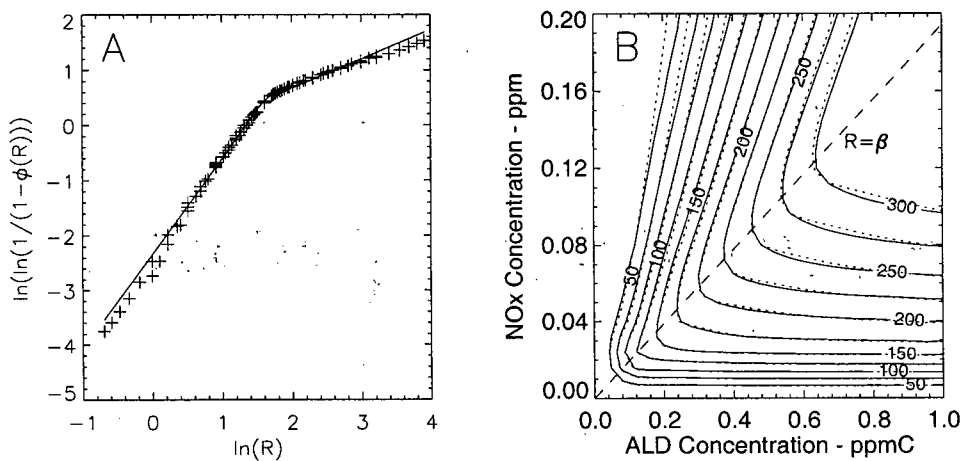


Figure E.10: Weibull transformed OZIPR model output (+) for ALD as a function of  $\ln R$  (figure A). Solid line is WEX model. In Figure B, the same results are plotted in the more conventional form of ozone isopleths (in ppb) with OZIPR model output in solid lines and WEX model in dotted lines. The dashed line represents the scaling break  $R = \beta$ .

### E.1.5 Non-reactive

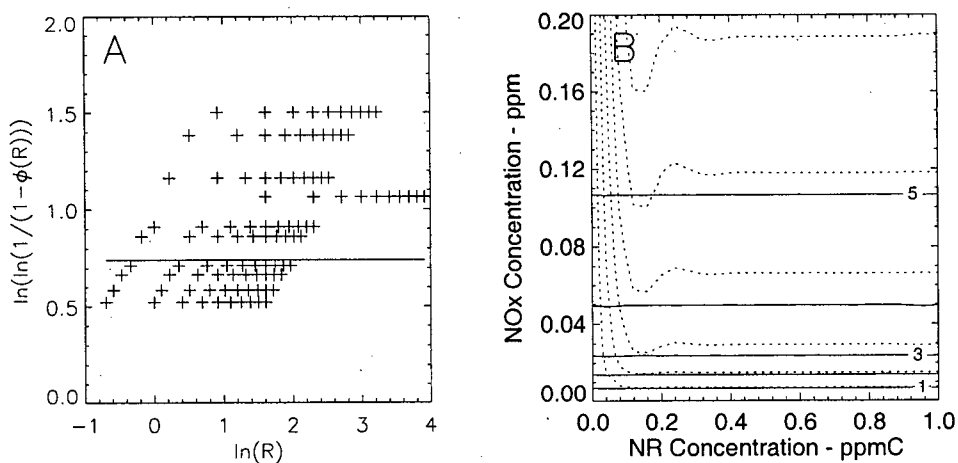


Figure E.11: Weibull transformed OZIPR model output (+) for NR as a function of  $\ln R$  (figure A). Solid line is WEX model. In Figure B, the same results are plotted in the more conventional form of ozone isopleths (in ppb) with OZIPR model output in solid lines and WEX model in dotted lines. The dashed line represents the scaling break  $R = \beta$ .

### E.1.6 Mixtures

Finally plots using an urban mixture based on the Air Resources Board (ARB) analysis of the Lonneman (Lonneman, 1986) 29 city canister study and Stockwell et al. (1997) mixture used in the RADM2 model comparisons, are given.

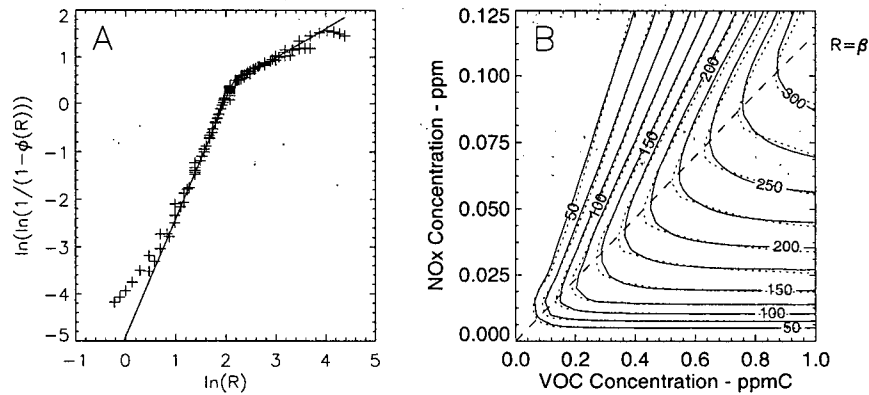


Figure E.12: Weibull transformed OZIPR model output (+) for urban mixture ARB as a function of  $\ln R$  (figure A). Solid line is WEX model. In Figure B, the same results are plotted in the more conventional form of ozone isopleths (in ppb) with OZIPR model output in solid lines and WEX model in dotted lines. The dashed line represents the scaling break  $R = \beta$ .

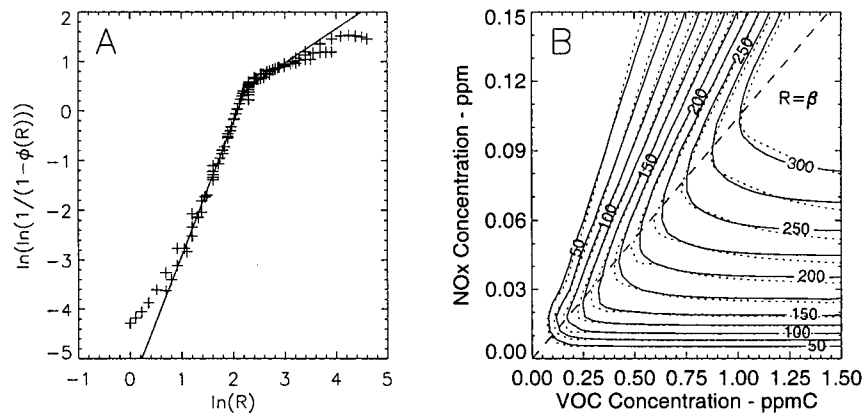


Figure E.13: Weibull transformed OZIPR model output (+) for the Stockwell (Stockwell et al., 1997) urban mixture as a function of  $\ln R$  (figure A). Solid line is WEX model. In Figure B, the same results are plotted in the more conventional form of ozone isopleths (in ppb) with OZIPR model output in solid lines and WEX model in dotted lines. The dashed line represents the scaling break  $R = \beta$ .

## E.2 CB-IV Mechanism

Results using the CB-IV mechanism for a PAR+OLE (used to represent propene) mixture and an urban mixture based on the Air Resources Board (ARB) analysis of the Lonneman (Lonneman, 1986) 29 city canister study are given in this section.

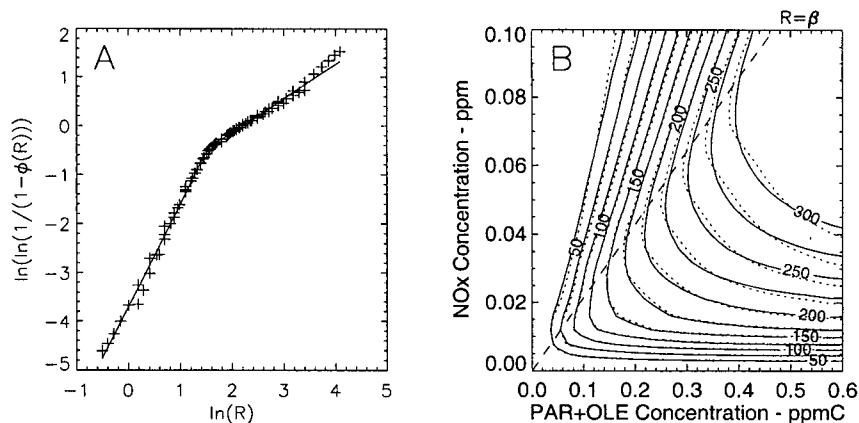


Figure E.14: Weibull transformed OZIPR model output (+) for PAR+OLE as a function of  $\ln R$  (figure A). Solid line is WEX model. In Figure B, the same results are plotted in the more conventional form of ozone isopleths (in ppb) with OZIPR model output in solid lines and WEX model in dotted lines. The dashed line represents the scaling break  $R = \beta$ .

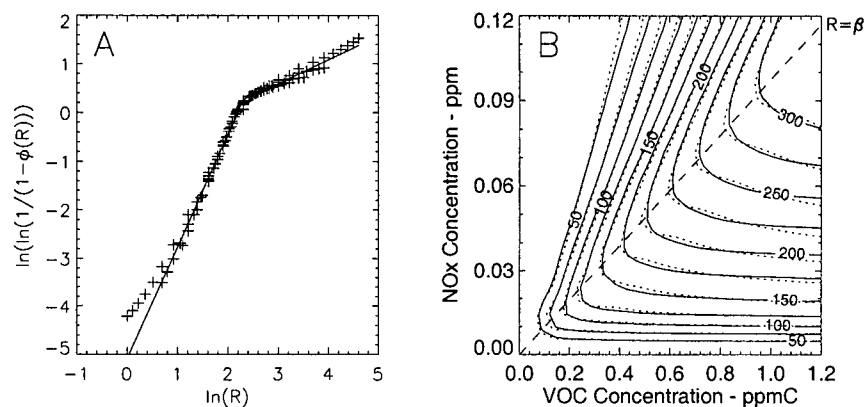


Figure E.15: Weibull transformed OZIPR model output (+) for urban ARB mixture as a function of  $\ln R$  (figure A). Solid line is WEX model. In Figure B, the same results are plotted in the more conventional form of ozone isopleths (in ppb) with OZIPR model output in solid lines and WEX model in dotted lines. The dashed line represents the scaling break  $R = \beta$ .

### E.3 NRC Mechanisms

Two plots using a modified and condensed version of the SAPRC model (Carter, 1990) developed for use in the LFV B.C. (Jiang et al., 1997b) are given in this section. The first uses the OLE1 (used to represent propene) class and the other an urban mixture typical of the LFV.

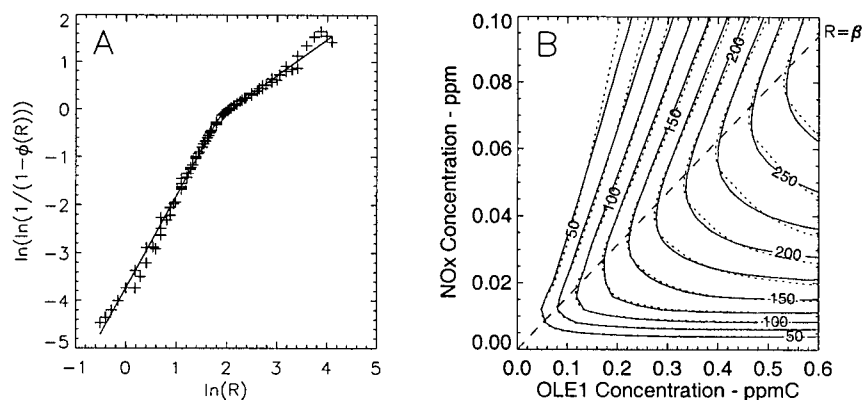


Figure E.16: Weibull transformed OZIPR model output (+) for OLE1 as a function of  $\ln R$  (figure A). Solid line is WEX model. In Figure B, the same results are plotted in the more conventional form of ozone isopleths (in ppb) with OZIPR model output in solid lines and WEX model in dotted lines. The dashed line represents the scaling break  $R = \beta$ .

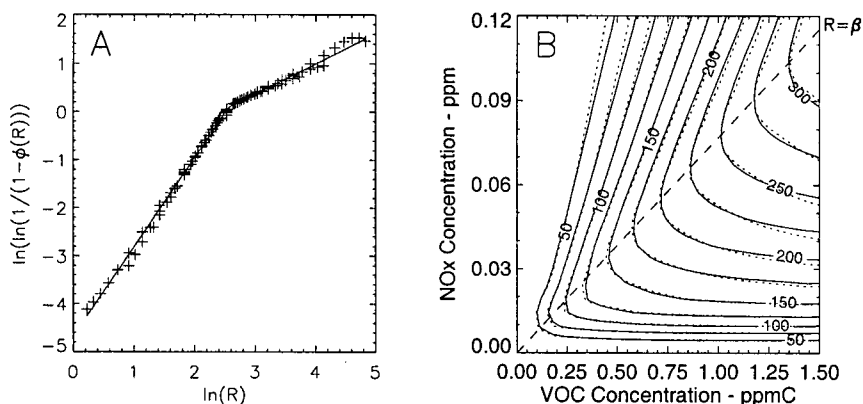


Figure E.17: Weibull transformed OZIPR model output (+) for urban mixture, typical of the LFV, B.C., as a function of  $\ln R$  (figure A). Solid line is WEX model. In Figure B, the same results are plotted in the more conventional form of ozone isopleths (in ppb) with OZIPR model output in solid lines and WEX model in dotted lines. The dashed line represents the scaling break  $R = \beta$ .

## Appendix F

# Some Mathematical Definitions of the Ridgeline

### F.1 The ridgeline

It is difficult to determine the ridgeline on an isopleth diagram – it can be defined in several ways based on either mathematical or physical reasoning. In this appendix, I provide three definitions: one based on sensitivity of maximum ozone concentration to the ratio of initial VOC to NO<sub>x</sub>; another based on the path of minimum gradient on an ozone response surface and a third on minimum isopleth curvature.

### F.2 Ridgeline based on ozone sensitivity to ratio of VOC to NO<sub>x</sub>

This concept of ridgeline is similar to the definition used in Section 5.7.1. but instead considers the sensitivity of maximum ozone to the ratio of VOC to NO<sub>x</sub> instead of NO<sub>x</sub> alone. When using the WEX model, this is a natural approach, since the similarity curve is a function of  $R$  only. A mathematical formulation of this definition would be:

**Definition I:** Given any function  $g(R, NO_x, VOC)$ , representing the ozone response surface, the ridgeline is the value of  $R$  such that:

$$\frac{\partial g}{\partial R} = 0$$

Note that if the response surface can be expressed as the product of two functions, one dependent on NO<sub>x</sub> only and the other on  $R$  only i.e:

$$g(R, NO_x, VOC) = h(NO_x) \cdot k(R)$$

then Definition I is equivalent to one given in Section 5.7.1. This can be shown by first taking the

derivative with respect to  $R$  and finding the critical points:

$$\frac{\partial g}{\partial R} = k'(R)h(\text{NOx}) + k(R)h'(\text{NOx})\frac{d\text{NOx}}{dR}$$

and when  $\frac{\partial g}{\partial R} = 0$

$$k'(R)h(\text{NOx}) = -k(R)h'(\text{NOx})\frac{d\text{NOx}}{dR}$$

And then taking the derivative with respect to NOx and finding its critical points:

$$\frac{\partial g}{\partial \text{NOx}} = k(R)h'(\text{NOx}) + k'(R)h(\text{NOx})\frac{dR}{d\text{NOx}}$$

and when  $\frac{\partial g}{\partial \text{NOx}} = 0$

$$k(R)h'(\text{NOx}) = -k'(R)h(\text{NOx})\frac{dR}{d\text{NOx}}$$

Now, in general the two partials are not equal but at the critical points, if one vanishes, then so must the other i.e. :

$$\frac{\partial g}{\partial R} = 0 \Leftrightarrow \frac{\partial g}{\partial \text{NOx}} = 0$$

So when the ozone response surface given by the product of functions dependent on NOx- and R-only, then locating the ridgeline on an isopleth diagram using definition I is equivalent to finding the location where the derivative of maximum ozone concentration with respect to NOx is zero.

Inspection of an ozone isopleth diagram shows that this Definition I puts the ridgeline in a reasonable place. However, it is difficult to justify this definition on mathematical grounds. Why should the ridgeline be located where the ozone concentrations show no change with NOx or  $R$ ? Considering that a similar definition, using the derivative with respect to VOC, would put the ridgeline in the NOx-only scaling regime, it may be that this definition provides reasonable results due to some fortunate properties of ozone isopleth diagrams.

### F.3 Ridgeline based minimum gradient along an ozone response surface

A second approach to defining the ridgeline involves finding the location where the gradient is least. A hiker would express this statement by saying: the ridgeline is the path up the hill which has the gentlest slope. In general, this definition will not produce a straight ridgeline. Mathematically, the new definition can be given by:

**Definition II:** Given any function  $g(R, \text{NOx}, \text{VOC})$ , representing the ozone response surface, the ridgeline is the locus of points where  $\|\nabla g\|$  is smallest.

To understand this definition, consider that the slope of a surface, along any unit normal  $\underline{u}$  in the direction  $\theta$ , is given by the directional derivative:

$$D_g(\nabla g) = \nabla g \cdot \underline{u}$$

Now if we choose our unit normal to lie in the direction of the gradient, then the directional derivative will give the slope of the gradient i.e.

$$D_g(\nabla g) = \nabla g \cdot \frac{\nabla g}{\|\nabla g\|} = \frac{\|\nabla g\|^2}{\|\nabla g\|} = \|\nabla g\|$$

Thus to find the ridgeline, one must minimize  $\|\nabla g\|$ . or equivalently minimize  $\|\nabla g\|^2$ . For the WEX model (with  $f$  being the similarity function), this gives:

$$\|\nabla g\|^2 \propto [NOx]_o^{2a-2} [f'^2 a^2 f^2 + R^2 f'^2 - 2aRf f'] \quad (F.1)$$

Equation F.1 is a vector valued function of both VOC and NOx and finding a minimum must be done numerically.

#### F.4 Ridgeline based minimum isopleth curvature

A final method for characterizing the ridgeline is the position on an isopleth where isopleth curvature is greatest. For a hiker, this would be the location at a fixed elevation where the topography allows the greatest range of the azimuth with an unobstructed view. The mathematical definition is:

**Definition III:** The ridgeline is the location on a isopleth where the radius of curvature ( $\rho$ ) is least.

To use this definition, the isopleths must first be parameterized as a vector valued function  $\underline{r}(t) = (VOC(t), NOx(t))$ . For such a parameterization, the radius of curvature becomes:

$$\rho = \frac{\|\underline{r}'(t)\|^3}{\|\underline{r}'(t) \times \underline{r}''(t)\|}$$

For the WEX model parameterization of the isopleths is not tractable and the whole analysis must be done numerically.

#### F.5 Conclusion

From this analysis, it can be seen that there are many different approaches to defining a ridgeline, most not tractable to mathematical analysis even when using the WEX model to parameterize the ozone response surface. Preliminary analysis, for the RADM2 OLT class, when modeling the similarity curve with a single Weibull function shows the ridgelines based on Definitions II and III are almost in the same position as the ridgeline based on Definition I.

## Appendix G

# Development of the Simple Emissions Inventory

Developing an emissions inventory is straight forward in principle but can become quite involved in practice. At its most basic level, the task involves taking published yearly emission totals and allocating them spatially over the modeling domain and temporally for each time step. Allocation proceeds by grouping emission sources into common types. At the simplest, emissions sources are divided into three general categories: point (principally large industrial facilities), mobile (i.e. vehicles, airplanes) and area (i.e. forests, landfills). These can then be further sub-divided depending on the level of detail required. This process of disaggregating emissions into more specific categories can follow down four or more levels – for motor vehicles, sources can be initially segregated by type (i.e. LDV versus HDV) followed by curb weight (i.e. station wagon versus hatchback) and further by fuel type (gasoline versus alternative fuel) then by age and finally by odometer reading. In principle, as more refinements are made, a better picture of the emission fields emerge. At some point, however, the additional resolution becomes constrained by the availability of input data. I believe that no more than a few levels of disaggregation are needed in order to capture the essential features of the ozone plume in the LFV.

The main reason for developing a simple emissions inventory was to quickly explore the relationship between emission fields and resulting ozone plume – an investigation considerably more difficult using complex inventories. For the simple inventory, only two levels of disaggregation were considered (see Table 9.2). For each emission source, temporal curves for monthly, daily and hourly emissions were used to infer hourly emissions. Emissions masks, based on land use characteristics, were then used to spatially allocate the hourly emissions. In the present model, six main masks (sea, urban, transportation, aircraft, agriculture and forest) were used along with four hybrid masks (shipping, commercial, developed and green-space). The six main masks formed a non-overlapping set, covering the entire domain.

## G.1 Spatial Emission Masks

The urban and sea emission masks were identical to the urban and ocean land-use categories respectively. The airport mask consisted of a  $2 \times 2$  grid of cells centered over Vancouver International airport (YVR). The transportation mask was developed by examining output from an emissions inventory developed specifically for the August 10<sup>th</sup> 2001 episode using the SMOKE emissions processor and detailed emissions developed for the LFV (Gauthier et al., 2003). Using mid-morning NOx emissions, I defined the transportation mask as regions with high NOx emissions (above an arbitrary threshold of  $25 \text{ mol/hr/km}^2$ ) that were neither over the ocean nor in the urban areas. This approach is justified since 83% of NOx emissions are from mobile sources in the region (Greater Vancouver Regional District, 2002). The details of the transportation mask were not sensitive to the NOx emissions threshold. The agriculture mask consisted of the green-space land-use cells not covered by the transportation mask. Similarly, the forest mask consisted of the mountain forest cells not covered by the transportation mask. The commercial mask consisted of all cells in the urban and transportation mask, while the developed mask consisted of cells in the urban, transportation and agriculture mask.

## G.2 Emission Sources

The following sections list each emission source describing the spatial and temporal allocation methods. Emission totals were based on year 2000 data and no attempt was made to adjust them to 2001 levels.

### G.2.1 Mobile Source Emissions

The LFV does not have extensive industrial facilities and as such, the majority of both VOC (52%) and NOx (85%) anthropogenic emissions are from mobile sources (Greater Vancouver Regional District, 2002) a situation that is not expected to change in the coming decades (Greater Vancouver Regional District, 2003b). Most of the VOCs emissions are from LDV while NOx emissions are roughly split between HDV, marine and non-road sources.

#### Light Duty and Heavy Duty Vehicles

Allocating the LDV and HDV emissions required vehicle speed splits in addition to spatial and temporal activity factors. Two speed classes were assumed (low speed and high speed) with low speed travel allocated to urban cells while high speed travel to the transportation cells. For both the

LDV and HDV, a baseline low/high speed split of 60/40 was used. No temperature corrections were used to account for increased evaporative losses during warm weather. Temporal profiles were based on data from the 1985 Lower Mainland Emission Inventory (Greater Vancouver Regional District, 1988) and showed traffic levels peaking during the morning and evening rush hours. Vehicle activity also increased during the summer months.

### **Marine**

Marine sources included emissions from ocean vessels, ferries and recreational boaters. Emissions were allocated using the shipping mask. It was assumed that the NO<sub>x</sub> marine emissions were from the ocean vessels operating at constant intensity year round. For the VOC emissions, recreational boaters were assumed to be the sole source with peak activity during daylight hours in the summer months (Greater Vancouver Regional District, 1988).

### **Rail**

Rail emissions were allocated on the transportation mask assuming constant activity levels year round.

### **Aircraft**

Aircraft emissions were assumed to originate exclusively from Vancouver International airport (YVR). The year 2000 inventory showed emissions from YVR and the sea-plane base on the Fraser River account for over 90% of aircraft NO<sub>x</sub> and VOC emissions (Greater Vancouver Regional District, 2002). All emissions were spatially allocated to the aircraft mask with monthly activity factors taken from the 1985 inventory (Greater Vancouver Regional District, 1988). No daily variation in activity was assumed and hourly emissions were assumed constant between 0600 and 2200 local time.

### **Non-road: Construction and Agriculture**

The final mobile source category was non-road which includes emissions from construction, agriculture and lawn equipment. I used only the first two categories; lumping lawn equipment emissions in with construction. Construction emissions were allocated using the commercial mask assuming constant monthly and daily activity. Hourly emissions were assumed constant between the hours of 0500 and 2000 local time. Similarly, agriculture emissions were allocated using the agriculture

mask assuming equal activity between March and October, no daily variation and constant hourly activity between 0500 and 2000 local time.

### G.2.2 Area Sources

Area sources include residential, light industrial and biogenic sources. For VOCs, the major contributions come from forests, agricultural crops and from solvent evaporation. For NO<sub>x</sub>, the major source is nitrifying bacteria in the top few centimeters of soils. (Yin et al., 2004).

#### Space Heating

Space heating emissions were not an important source for the August 10<sup>th</sup> inventory. Based on heating degree day data from the 1985 LOMEI inventory (Greater Vancouver Regional District, 1988), only 0.1 % of the year heating total occurs during the peak summer months of July and August. Space heating emissions were allocated using the urban mask.

#### Evaporative

Evaporative emissions consisted of VOC emissions from solvent use (e.g. painting, dry cleaning), gas marketing (e.g. vehicle refueling and distribution of gasoline) and miscellaneous sources stemming from landfills and burning. These were allocated on the commercial mask using temporal profiles taken from the Vancouver Oxidants Study (Environment Canada, 1989).

#### Forests

The forest emissions had to be scaled up from the published inventory because the modeling domain differs from that used by the GVRD (Greater Vancouver Regional District, 2002). The monthly fraction of the yearly emissions total was determined using factors based on estimated of daily VOC flux from vegetation in the LFV (B. H. Levelton and Associates Ltd, 1993). A simple scaling, based on average temperature, was used to develop hourly VOC emissions while no attempt was made to adjust NO<sub>x</sub> emissions with temperature. While hourly biogenic emissions are a function of: above canopy temperature, relative humidity, wind speed, species composition and land-use characteristics (Guenther et al., 2000), a much simpler allocation scheme, based on average forest temperature, was used. Although biogenic VOC emissions are known to scale with both light intensity and temperature (Guenther et al., 1993), it was assumed that to first order scaling by ambient temperature would capture some of the variability associated with shortwave radiation. Drewitt et al. (1998) show that for monoterpenes, emissions are mainly a function of temperature.

Using the average forest temperatures, emissions were scaled by  $\exp(\beta(T_{avg} - T_{ref}))$  where  $T_{avg}$  is the average hourly forest temperature in  $^{\circ}C$ ,  $T_{ref}$  is a reference temperature taken to be  $30^{\circ}C$  and  $\beta = 0.09K^{-1}$  is an empirical constant. Finally, the forest emissions were allocated using the forest mask.

### **Livestock**

Livestock emissions consisted of VOC from cattle, pigs, horses and sheep. Emissions were assumed to be continuous throughout the year and allocated using the agriculture mask.

### **Crop**

Crop emissions consisted of VOC emissions over crop land and were treated in a similar fashion to the forest emissions. Monthly temporal factors were based on estimated of daily VOC flux from vegetation in the LFV (B. H. Levelton and Associates Ltd, 1993). No daily variation in emissions was assumed and the forest hourly temporal factors were used for hourly activity levels.

### **Miscellaneous**

This last source included VOCs from bakeries, smoking, meat cooking and cutback asphalt. They were allocated using the urban mask with temporal factors based on data from the Vancouver Oxidants Study (Environment Canada, 1989).

### **G.2.3 Point Sources**

As can be seen from Table 9.2, the contribution of point sources a sources is small in the LFV. Because of the coarse nature of the trajectory model, it was decided to allocate their emissions using the commercial mask. Temporal activity was assumed constant year round.

General Category	Sub-category	Spatial Allocation
Mobile	LDV	Urban and transportation
	HDV	Urban and transportation
	Marine	Sea
	Rail	Transportation
	Aircraft	Airport
	Construction	Developed
	Agriculture	Agriculture
Area	Space Heating	Urban
	Evaporative	Commercial
	Forests	Forests
	Livestock	Agriculture
	Crop	Agriculture
	Miscellaneous	Urban
Point		Commercial

Table G.1: *Spatial allocation of emissions in the simple emissions inventory using the emission masks.*

## Appendix H

# Physical Geography of the Modeling Domain

Stn Number	Station Name	Administering Agency	Latitude	Longitude
8	T002,Kitsilano	Greater Vancouver Regional District	49.261	-123.164
10	T017,Richmond South	Greater Vancouver Regional District	49.142	-123.108
11	T026,Mahon Park	Greater Vancouver Regional District	49.324	-123.083
13	T023,Capitol Hill	Greater Vancouver Regional District	49.288	-122.986
14	T018,Burnaby South	Greater Vancouver Regional District	49.216	-122.982
15	T004,Kensington Park	Greater Vancouver Regional District	49.279	-122.971
17	T014,Burnaby Mountain	Greater Vancouver Regional District	49.281	-122.909
18	T012,Chilliwack Airport	Greater Vancouver Regional District	49.156	-121.941
19	T013,North Delta	Greater Vancouver Regional District	49.158	-122.901
20	T006,Second Narrows	Greater Vancouver Regional District	49.302	-123.021
21	T032,Douglas College	Greater Vancouver Regional District	49.288	-122.792
22	T020,Meadowlands Elementary School	Greater Vancouver Regional District	49.245	-122.709
23	T015,Surrey East	Greater Vancouver Regional District	49.133	-122.693
24	T030,Golden Ears Elementary School	Greater Vancouver Regional District	49.215	-122.582
25	417,UBC Research	BC Ministry of Forests	49.265	-122.573
26	T027,Langley Central	Greater Vancouver Regional District	49.096	-122.566
28	T033,Central Abbotsford	Greater Vancouver Regional District	49.043	-122.310
29	T009,Rocky Point Park	Greater Vancouver Regional District	49.282	-122.850
30	407,Big Silver	BC Ministry of Forests,	49.692	-121.860
31	419,Chwk Nursery	BC Ministry of Forests	49.098	-121.663
38	GT BR,Great Bear	BC Ministry of Transportation and Highways	49.583	-121.167
39	COQSUM,Coquihalla Summit	BC Ministry of Transportation and Highways	49.590	-121.097
40	FND MI,Foundation Mines	BC Ministry of Transportation and Highways	49.217	-121.067
41	ALLIS2,Allison Pass Remote	BC Ministry of Transportation and Highways	49.117	-120.867
42	2007,Thynne	BC Ministry of Forests	49.615	-120.867
48	CQM,Coquitlam R. above Lake	BC Hydro	49.480	-122.790
49	STA,Stave R. above Stave Lk.	BC Hydro	49.550	-122.320
52	GOC,Gold Ck.	BC Hydro	49.447	-122.475
54	CLO,Clowhom Falls	BC Hydro	49.708	-123.522
55	SEY,Mtn. Seymour	BC Hydro	49.417	-122.917
56	46146,Halibut Bank	Environment Canada Marine	49.340	-123.528
58	ALU,Alouette Lake forebay	BC Hydro	49.287	-122.484
59	STV,Stave R. Upper	BC Hydro	49.625	-122.411
61	COQ,Coquitlam Lake forebay	BC Hydro	49.350	-122.770
66	WAH,Wahleach (Jones) Res.	BC Hydro	49.232	-121.619
68	RDBRWS,Red Bluffs	BC Ministry of Transportation and Highways	49.475	-120.619
71	2045,Allison Pass	BC Ministry of Forests	49.063	-120.767
75	Abbotsford	Environment Canada	49.017	-122.350
76	Agassiz	Environment Canada	49.250	-121.767
77	Bellingham WA	U.S.National Weather Service	48.800	-122.533
78	Vancouver International Airport	Environment Canada	49.200	-123.167
79	Hope	Environment Canada	49.367	-121.467
80	Howe Sound	Environment Canada	49.483	-123.300
81	Pitt Meadows	Environment Canada	49.200	-122.667
82	Point Atkinson	Environment Canada	49.317	-123.267
83	Sand Head	Environment Canada	49.100	-123.300
84	Saturna Island	Environment Canada	48.767	-123.050
85	Victoria International Airport	Environment Canada	48.650	-123.417
86	West Vancouver	Environment Canada	49.350	-123.183
87	White Rock	Environment Canada	49.017	-122.767
88	Squamish	Environment Canada	49.683	-123.167
89	Hope Slide	Environment Canada	49.267	-121.233
90	Princeton	Environment Canada	49.467	-120.667

Table H.1: Meteorological Stations within the modeling domain: their locations and administering agency.

RPN Landuse Class	Description	WEX Landuse Class
0	water	0
1	ice	0
2	inland lake	0
3	evergreen needleleaf trees	1 or 2
4	evergreen broadleaf trees	1 or 2
5	deciduous needleleaf trees	1 or 2
6	deciduous broadleaf trees	1 or 2
7	tropical broadleaf trees	1 or 2
8	drought deciduous trees	1 or 2
9	evergreen broadleaf shrub	1 or 2
10	deciduous shrubs	1 or 2
11	thorn shrubs	1 or 2
12	short grass and forbs	1 or 2
13	long grass	1 or 2
14	crops	1 or 2
15	rice	1 or 2
16	sugar	1 or 2
17	maize	1 or 2
18	cotton	1 or 2
19	irrigated crops	1 or 2
20	urban	3
21	tundra	1 or 2
22	swamp	1 or 2
23	desert	1 or 2
24	mixed shrubs	1 or 2
25	mixed wood forests	1 or 2
26	urban (GIS)	3

Table H.2: Mapping of RPN Landuse classes to WEX landuse classes. The WEX-landuse classes are: 0 water, 1 mountain-forest, 2 greenspace and 3 urban. Entries labeled 1 or 2 imply landuse is either greenspace or mountain forest depending on the elevation.

Landuse Class	Fraction between $u_*$ and wind speed	Fraction between measured $(w'\theta')_s$ and local sensible heat flux
Water	0.01	0.00
Mountain Forest	1.25	0.10
Greenspace	1.00	0.13
Urban	0.13	2.00

Table H.3: Land use corrections for friction velocity and kinematic heat flux.

## Appendix I

# CART Decision tree for the LFV

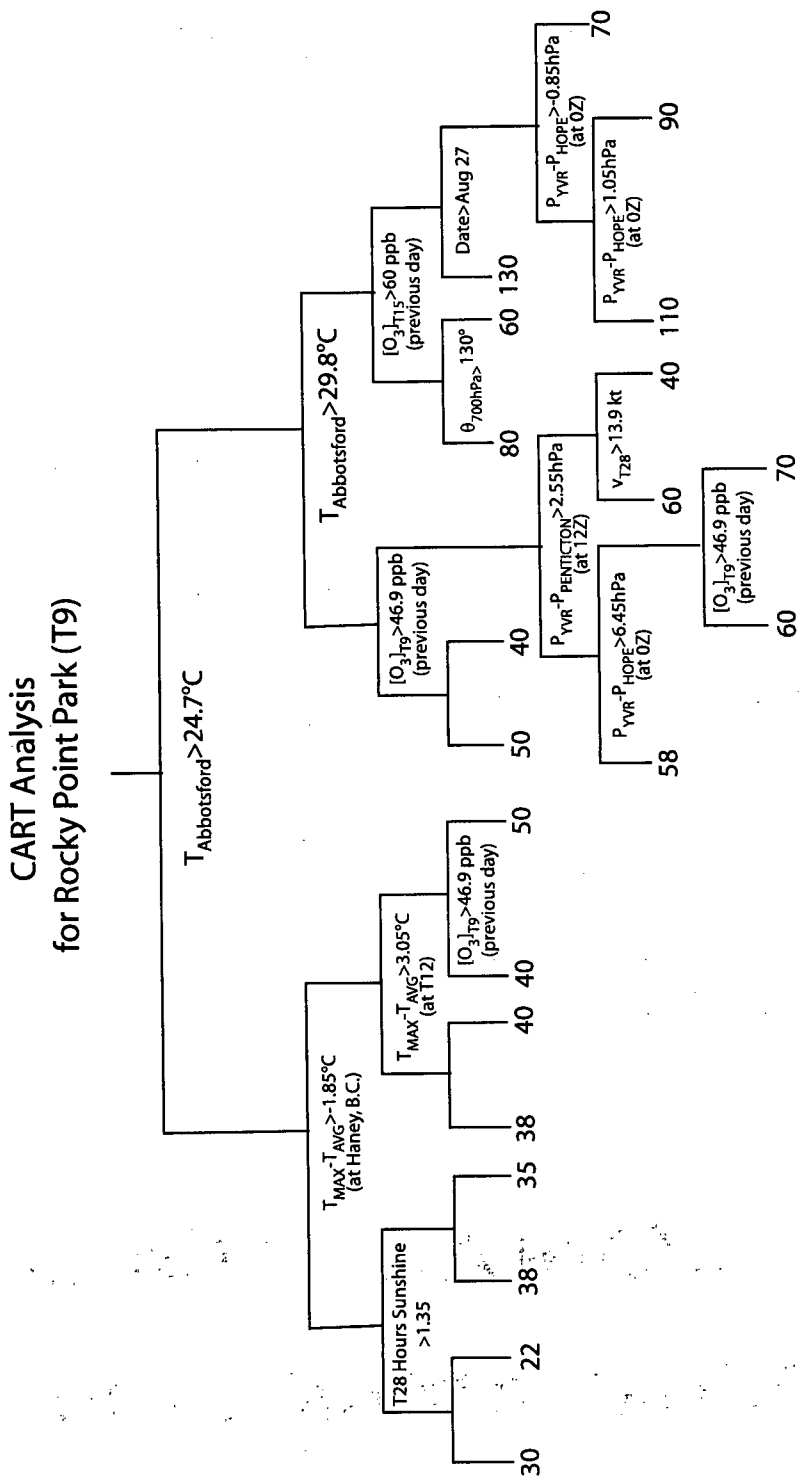


Figure I.1: CART regression tree for Rocky Point Park (T9) based on Burrows et al. (1995). Final concentrations are in ppb. Branching proceeds to right the if decision rule at node is true. For clarity, only branching rules that are simple expressions of a single predictor have been included.

## Appendix J

# Glossary of Acronyms and Abbreviations

**ARB** Acronym for Air Resources Board, a California state agency legislated to protect and improve the state's air quality.

**AQI** Acronym for Air Quality Index, an overall measure of air quality achieved by comparing concentrations of various pollutants against their respective air quality objectives and then converting these relative concentrations to a number on an AQI scale.

**BEIS** Acronym for Biogenic Emissions Inventory System. A computer program designed to calculate biogenic emissions based on meteorological conditions and land cover characteristics.

**CAAR97** Acronym for Clean Air Act Revision (1997). It is the latest revision of the original Clean Air Act table in 1970 by the U.S. congress. Among other things, it sets a new ozone standard of 82 ppb averaged over 8 hours for the third highest reading averaged over 4 years.

**CALGRID** A comprehensive Eulerian grid based model used to numerically simulate ozone photochemistry.

**CALMET** A meteorological preprocessor designed for use with the CALGRID photochemical model.

**CAPMoN** Acronym for Canadian Air and Precipitation Monitoring Network. This is an extensive network of non-urban air quality monitoring stations.

**CART** Acronym for Classification And Regression Tree. A decision-tree statistical analysis used to related a response variable to a set of predictor variables based a set of rules.

**CBL** Acronym for Convective Boundary Layer. A boundary layer characterized by convectively driven turbulence and vertically uniform potential temperature, wind speed and pollutant profiles.

- CB-IV** Acronym for Carbon Bond version IV chemical mechanism. It uses a lumped structure approach, where VOCs are broken into smaller reaction elements based on carbon bounds, to model VOC reactions.
- CSIRO** Acronym for Australia's Commonwealth Scientific and Industrial Research Organization.
- CSU-RAMS** Acronym for the Colorado State University Regional Atmospheric Modeling System, a comprehensive meso-scale meteorological model.
- CWS** Acronym for Canada Wide Standard. A new set of Canadian air quality guidelines to be implemented by 2010.
- EBIR** Acronym for Equal Benefit Incremental Reactivity. Refers to value of Incremental Reactivity at which ozone sensitivity to changing VOC concentrations is equal to its sensitivity to changing NO<sub>x</sub> concentrations.
- EPA** Acronym for the U.S. Environmental Protection Agency.
- GRS** Acronym for Generic Reaction Set. A highly parameterized chemical mechanism consisting of seven reactions among seven species.
- GVRD** Acronym for Greater Vancouver Regional District, a regional level of government in the Lower Fraser Valley B.C.
- HC** Acronym for hydrocarbon.
- HDV** Acronym for Heavy Duty Vehicles. These are usually diesel powered trucks.
- IER** Acronym for Integrated Empirical Rate model. A set of functional relationships describing ozone formation based on smog chamber data.
- IR** Acronym for Incremental Reactivity. A measure of the change in peak ozone concentration stemming from a small change in VOC concentration.
- LDV** Acronym for Light Duty Vehicles. These are usually gasoline powered automobiles.
- LFV** Acronym for Lower Fraser Valley B.C.
- LIDAR** Acronym for Light Detection and Ranging. A remote sensing instrument that uses the backscattering of light from molecules and aerosols to study the boundary layer.
- MC2** Acronym for Mesoscale Compressible Community. A non-hydrostatic semi-implicit, semi-Lagrangian meteorological model developed by Environment Canada.

- MIR** Acronym for Maximum Incremental Reactivity. The maximum value of a VOC's incremental reactivity.
- MLD** Acronym for Mixed Layer Depth. Vertical extent of mixing in the boundary layer.
- MOBILE** Name given to the Mobile Source Emissions Factor model. A computer program used to determine emissions from mobile sources based on vehicle activity and vehicle fleet characteristics.
- NAAQO** Acronym for National Ambient Air Quality Objectives.
- NRC** Acronym for National Research Council, a Canadian federal research institute.
- NSIR** Acronym for NO<sub>x</sub> Scaled Incremental Reactivity. A measure of VOC reactivity, based on the WEX model, which takes into account the dependence of NO<sub>x</sub> concentration on incremental reactivities (IR).
- NO<sub>x</sub>** Abbreviation for oxides of nitrogen which includes nitrogen dioxide (NO<sub>2</sub>) and nitric oxide (NO).
- NO<sub>y</sub>** Abbreviation for total reactive nitrogen. It is comprised of NO<sub>x</sub> and all species which are the oxidation products of NO<sub>x</sub>.
- NO<sub>z</sub>** Abbreviation for reactive nitrogen products. It is comprised of all NO<sub>y</sub> other than NO<sub>x</sub>.
- OBM** Acronym for Observationally Based Methods. A class of model used to predict ozone sensitivity and local production rates by making use of ambient measurements.
- OZIPR** Research version of the Ozone Isopleth Plotting Package (OZIPP). A computer program designed to simulate ozone photochemistry in a Lagrangian framework.
- PAN** Acronym for Peroxyacetyl Nitrate. A product of the oxidation of NO<sub>x</sub>, an eye irritant and common component of urban smog.
- PBL** Acronym for Planetary Boundary Layer and synonymous with boundary layer.
- PM,PM10,PM2.5** Acronyms for Particulate Matter, Particulate Matter with aerodynamic diameter less than 10 microns and Particulate Matter with aerodynamic diameter less than 2.5 microns.
- ppbC** Parts per billion of carbon (ppbC) is the volume mixing ratio of a VOC multiplied by the number of carbon atoms per molecule.

- PSP** Acronym for Primary Smog Products. This is a term developed by Johnson (1984) to describe the amount of molecular oxygen dissociated by ozone producing reactions.
- RADM2** Acronym for the Regional Acid Deposition Model - Version 2. It is a detailed gas phase chemical mechanism used for modeling atmospheric chemistry on a regional scale.
- Richardson Number (Ri)** A dimensionless quantity measuring the tendency for turbulence to be suppressed by buoyancy to turbulent being produced by vertical wind shear.
- RIR** Acronym for Relative Incremental Reactivity. It is a reactivity scale defined by dividing the Incremental Reactivity of a single component of a VOC mixture by the Incremental Reactivity of the entire VOC mixture.
- SAIMM/UAM-V** Acronym for Systems Applications International Mesoscale Model/ Urban Airshed Model - Version V.
- SAPRC90** Acronym for Statewide Air Pollution Research Center 90 chemical mechanism.
- SEM** Acronym for Semi-Empirical Model. A model of a complex system using a small set of variables based on simple functional relationships.
- SBL** Acronym for Stable Boundary Layer. An atmospheric layer where temperature is statically stably stratified.
- SMOKE** Acronym for Sparse Matrix Operator Kernel Emissions (SMOKE) Modeling System. A computer model designed to create gridded, speciated, and hourly emissions for input into air quality models.
- SO<sub>x</sub>** Abbreviation for oxides of sulphur including sulphur dioxide ( $SO_2$ ) and sulphur trioxide ( $SO_3$ ).
- TIBL** Acronym for Thermal Internal Boundary Layer. A boundary layer caused by the advection of air across a surface with a temperature discontinuity.
- TIER 2** New vehicle emission standards to be phased in starting in 2004.
- TKE** Acronym for Turbulent Kinetic Energy. The kinetic energy associated with turbulent eddies in a fluid flow.
- UVA,UVB,UVC** Acronyms for ultra-violet A,B and C, three separate bands of near ultra-violet radiation. UVA (0.32-0.38  $\mu\text{m}$ ) is relatively harmless, UVB (0.29-0.32  $\mu\text{m}$ ) causes sunburn while UVC (0.25-0.29  $\mu\text{m}$ ) severely damages most lifeforms.

---

**VKT** Acronym for Vehicle Kilometers Traveled. A measure of distance average vehicle travels over a given period of time. It is used in spatially and temporally scaling mobile source emissions.

**VOC** Acronym for Volatile Organic Compounds. These consist of compounds containing both hydrogen and carbon as well as other species (such as oxygen) which are reactive with respect to  $OH^\bullet$  radical. Methane is an important hydrocarbon **not** consider a VOC.

**WEX** Acronym for Weibull-Exponential. The name given to the parameterization of the similarity relationship produced when dimensionless ozone concentration is plotted against the ratio of initial VOC to  $NO_x$  concentration. While the model uses two Weibull functions to parameterize the similarity relationship, one of the Weibull distributions has shape parameter less than one, and so can be considered a generalization of the exponential distribution.

**YVR** The IATA 3-letter location code for the Vancouver international airport.